

Morphology and electronic structure of graphene supported by metallic thin films

Matteo Jugovac

Schlüsseltechnologien / Key Technologies

Band / Volume 224

ISBN 978-3-95806-498-0

Forschungszentrum Jülich GmbH
Peter Grünberg Institut (PGI)
Elektronische Eigenschaften (PGI-6)

Morphology and electronic structure of graphene supported by metallic thin films

Matteo Jugovac

Schriften des Forschungszentrums Jülich
Reihe Schlüsseltechnologien / Key Technologies

Band / Volume 224

ISSN 1866-1807

ISBN 978-3-95806-498-0

Bibliografische Information der Deutschen Nationalbibliothek.
Die Deutsche Nationalbibliothek verzeichnet diese Publikation in der
Deutschen Nationalbibliografie; detaillierte Bibliografische Daten
sind im Internet über <http://dnb.d-nb.de> abrufbar.

Herausgeber und Vertrieb: Forschungszentrum Jülich GmbH
Zentralbibliothek, Verlag
52425 Jülich
Tel.: +49 2461 61-5368
Fax: +49 2461 61-6103
zb-publikation@fz-juelich.de
www.fz-juelich.de/zb

Umschlaggestaltung: Grafische Medien, Forschungszentrum Jülich GmbH

Druck: Grafische Medien, Forschungszentrum Jülich GmbH

Copyright: Forschungszentrum Jülich 2020

Schriften des Forschungszentrums Jülich
Reihe Schlüsseltechnologien / Key Technologies, Band / Volume 224

D 464 (Diss. Duisburg, Univ., 2020)

ISSN 1866-1807
ISBN 978-3-95806-498-0

Vollständig frei verfügbar über das Publikationsportal des Forschungszentrums Jülich (JuSER)
unter www.fz-juelich.de/zb/openaccess.



This is an Open Access publication distributed under the terms of the [Creative Commons Attribution License 4.0](https://creativecommons.org/licenses/by/4.0/), which permits unrestricted use, distribution, and reproduction in any medium, provided the original work is properly cited.

Contents

Zusammenfassung	v
Synopsis	vii
Introduction	ix
1 Graphene: properties, application and synthesis	1
1.1 Graphene	4
1.1.1 Electronic properties	4
1.1.2 Mechanical and thermal properties	5
1.1.3 Applications	5
1.2 Synthesis methods	5
1.2.1 Top-down synthesis	6
1.2.2 Bottom-up synthesis	7
1.3 Insight into the CVD method	9
1.4 Current state of the art and scope of the thesis	10
2 Methods	13
2.1 Photoemission spectroscopy	13
2.1.1 Modelling the photoemission process	14
2.1.2 Strongly correlated materials	17
2.1.3 Spin-orbit coupling	17
2.1.4 Quantum well states	18
2.2 Low energy electron diffraction - LEED	20
2.3 LEEM-IV	22
2.3.1 A representative example: stacking faults in Ag films	23
3 Instrumentation and setup	29
3.1 NanoESCA PEEM at Elettra	29
3.2 Nanospectroscopy LEEM at Elettra	33
4 Ferromagnetic films on W(110): morphological and electronic properties	37
4.1 Fe/W(110)	37
4.2 Ni/W(110)	40
4.3 Co/W(110)	42
4.3.1 Co wedge	42

4.3.2	Thick Co film	56
5	CVD growth of graphene on cobalt: an in-situ study	63
5.1	Low temperature growth - formation of Gr-A	63
5.1.1	Ethylene exposure at low temperature	63
5.1.2	Transformation from Gr-A to Gr-B	67
5.2	High temperature growth - formation of Gr-C	73
5.2.1	Ethylene exposure at high temperature	73
5.2.2	Transformation from Gr-C to Gr-D	79
5.3	Characterization of the graphene transformation procedure	86
5.4	Exposure of the graphene/cobalt interface to air	88
6	Modification of the graphene/cobalt interface: atomic substitution and intercalation	91
6.1	Oxygen exposure	91
6.2	Nitrogen substitutional doping	102
6.3	Intercalation of an Au monolayer	104
	Summary and conclusions	109
	Outlook	113
	Appendix	115
A	Theoretical methods	115
A.1	Density functional theory - DFT	115
A.2	Dynamic mean field theory - DMFT	117
B	Image processing of spin-resolved momentum maps	120
C	Graphene on Fe(110) films	123
D	Graphene on Ni(111) films	126
	Abbreviations	127
	Publications and conference contributions	131
	Bibliography	151

Zusammenfassung

Die steigende Nachfrage nach Datenspeicherkapazität und die ökologische Nachhaltigkeit elektronischer Speichergeräte erfordern den Einsatz innovativer Technologien. Die umfangreiche Produktion solcher Geräte stößt auf ein wirtschaftliches Hindernis, bei der niedrige Produktionskosten für eine nachhaltige Produktionskette von grundlegender Bedeutung sind. Die Verwendung von Graphen sowohl als funktionalisierende als auch als passivierende Schicht hat sich als eine Lösung herausgestellt, die den oben aufgeführten Anforderungen entspricht. Im letzten Jahrzehnt verlagerte sich das Interesse der Wissenschaft auf die Optimierung des Graphenwachstums, wobei eine Vielzahl verschiedener Ansätze zum Einsatz kam.

Diese Arbeit beschäftigt sich mit der umfangreichen Charakterisierung von Monolagen-Graphenwachstum auf ferromagnetischen Unterlagen. Vor dem Graphenwachstum ermöglichte die Charakterisierung des temperatur- und schichtdickenabhängigen Verhaltens der dünnen Metallfilme die Optimierung ihrer Qualität, gefolgt von der Untersuchung von deren elektronischen Eigenschaften. Sowohl aus geometrischen Gründen, *d. h.* aus Gründen der Gitterfehlpassung, als auch wegen der besseren Eignung für den verwendeten Versuchsaufbau wurde Cobalt als Substrat ausgewählt. Mit orts aufgelösten Messmethoden wurde der bekannte martensische Phasenübergang von Co in Abhängigkeit von der Temperatur beobachtet und charakterisiert.

Auf den Cobaltsubstraten wurde die chemische Gasphasenabscheidung zur Bildung einer Graphenmonolage unter Verwendung von Ethylen als Kohlenstoffquelle verwendet. Die kristallographische Qualität von Graphen variiert in Abhängigkeit von der Wachstumstemperatur und zeigt unterschiedliche azimutale Ausrichtungen bezogen auf das Substrat. In dieser Arbeit wird jedoch gezeigt, dass ein Austauschprozess von Kohlenstoff mit dem Substrat die Umwandlung der verschiedenen Konfigurationen in eine epitaktisch ausgerichteten Graphenmonolage ermöglicht. Die anschließend erfolgte Charakterisierung der elektronischen Struktur zeigt, dass die spinpolarisation in der Nähe des Fermi-Niveaus, die sich bei der Adsorption von Graphen auf Cobalt bildet, ein generelles Merkmal der Grenzfläche ist, unabhängig von der relativen Orientierung zwischen Graphen und Kobalt.

Die Kontrolle der epitaktischen Beziehung zwischen dem Graphen und dem Cobaltsubstrat ermöglicht die Modifikation der Graphen-Substrat-Wechselwirkung entweder durch kontrollierte, substituierende Implantation von Fremdatomen in das C-Gitter oder durch deren Interkalation. Daher wurden in dieser Arbeit die Stickstoffsubstitution in das Graphengitter sowie die Sauerstoff- und Goldinterkalation zwischen Graphen und Co untersucht. Die Abbildung des Impulsraums zeigt, dass die Modifikation der Graphen-Kobalt-Wechselwirkung zum Verschwinden der spin-polarisierten Bänder in Graphen führt.

Synopsis

The increasing demand for data storage capacity and the environmental sustainability of electronic storage devices ask for the use of innovative technologies. Extensive production of such devices encounters an economical barrier, where a low production cost is fundamental for a sustainable production chain. The use of graphene both as functionalizing and as passivating layer emerged as a solution matching the demands listed above. It shifted the interest of the scientific community in the past decade towards the optimization of graphene growth, using a variety of different approaches.

In this thesis, a multi-technique characterization of single-layer graphene growth on top of ferromagnetic supports is reported. Preceding the graphene growth, characterization of the temperature-dependent thickness behavior of thin metallic films allowed for the optimization of their quality, followed by the investigation of the electronic properties of the metal films. The substrate was chosen as cobalt both from geometrical reasons, *i.e.* lattice mismatch, as well as better suitability to the experimental setup used. Using spatially resolved techniques, the well-known Co martensitic phase transition as a function of temperature has been observed and characterized.

On top of the cobalt support, the chemical vapor deposition growth has been used for the formation of a graphene monolayer, using ethylene as the carbon supply. The graphene crystallographic quality varies as a function of growth temperature showing different azimuthal alignments with respect to the substrate. However, in this thesis, it is demonstrated that a transformation involving carbon exchange with the substrate allows reverting the different configurations in an epitaxially aligned graphene monolayer. The subsequent characterization of the electronic structure reveals that the single spin-polarized feature near the Fermi level, forming upon graphene adsorption on cobalt, is a general characteristic of the interface, independent on the relative orientation at the graphene-cobalt interface.

Having control over the epitaxial relation between the graphene and the cobalt substrate, modification of graphene-substrate interaction can be achieved either by controlled substitutional implantation of exospecies into the C lattice mesh or by intercalation of foreign species. Therefore, in this thesis the nitrogen substitution within the graphene lattice as well as oxygen and gold intercalation at the graphene-Co interface have been studied. The momentum mapping unravels that the modification of the graphene-cobalt interaction leads to the disappearance of the single spin-polarized band in graphene.

Introduction

Carbon-based materials constitute one of the most studied branches within material science because of their many allotropic forms. Carbon is primarily present in nature in its amorphous form or in ordered structures such as diamond or graphite, materials that have been known and used for millennia. Until Lavoisier's work on diamond [1] and Scheele's studies on graphite [2], however, it was unknown that these materials are made of carbon atoms. More recently, there has been a significant increase in the study of new allotropic carbon forms. Kroto pioneered the laser ablation of graphite as synthesis of fullerene, a discovery that led to the 1996 Nobel Prize in Chemistry [3]. Remarkably, the experimental work on graphene, a hexagonally arranged monoatomic layer (2D) of carbon atoms, and carbon nanotubes appeared only a few years later. Interestingly, in the theoretical work performed in the middle of the 20th century, the properties of graphene had already been predicted. The first one to explore the electronic structure of single-layer graphite was Wallace (1947) [4], while McClure (1956) proposed a model for the electron wave function in graphene [5]. Semenoff (1984) theoretically found that the conduction electrons in graphene follow Dirac's equation for massless fermions [6].

Nonetheless, the turning point in graphene-related science was set in 2004 with the publication of the work by A. Geim and K. Novoselov [7]. They were able to obtain graphene sheets by mechanical exfoliation from solid graphite using an adhesive tape. This exfoliation procedure, repeated multiple times, allowed the isolation of a monoatomic thick graphite layer, called graphene. Afterward, the characterization of the so-isolated graphene layer revealed extraordinary characteristics, especially regarding the electron transport properties accompanied by high in-plane mobility of the charge carriers. Consequently, the Nobel Prize in Physics was assigned to Novoselov and Geim *"for groundbreaking experiments regarding the two-dimensional material graphene"* [8].

The discovery of such groundbreaking properties of this abundant material led to extensive studies regarding different pathways of its synthesis. It emerged that the peculiar electronic properties are sensitively dependent on the crystalline quality. This motivated the search for a synthesis technique suitable for large-scale graphene production, characterized by a good crystallographic quality. Several methods were employed, leading to the emergence of chemical vapor deposition (CVD) technique as one of the most versatile and promising procedures to obtain extended graphene sheets. The CVD technique, based on the decomposition of hydrocarbons on a metal surface, has been employed, among others, on copper [9, 10] and nickel [11]. These substrates emerged as suitable materials for large-scale graphene production due to their low cost and accessibility, as well as their compatibility with transfer methods to place graphene on different supports [12].

Recently, the coupling of graphene with magnetic materials has come under focus within the

field of spintronics, where the spin angular momentum adds another degree of freedom to the electric transport [13, 14]. Among the magnetic materials, cobalt is a promising candidate for this purpose, as it is one of the very few elemental ferromagnets at room temperature and it has a good epitaxial match to the graphene lattice. It is well known that the presence of graphene induces in general an enhanced perpendicular magnetic anisotropy in cobalt films, a sizable tunnel magnetoresistance [15], Néel-type chiral magnetic structures [16, 17, 18, 19], and chiral spin interactions at the graphene/cobalt interface [20]. However, a full understanding of these graphene-induced magnetic modifications in cobalt films is still lacking. Therefore, in this thesis we focus on this system, as well as its structural variants in Fe and Ni, which we will also present in the following.

From the electronic structure point of view, it was reported that the presence of the cobalt support leads to a pronounced modification of the graphene overlayer. The strong interaction at the interface leads to the downward shift of the graphene π bands, with the band crossing (*i.e.* Dirac point) found at about 2.8 eV below the Fermi level at the K point. Importantly, a peculiarity of the graphene/cobalt interface lies in the region near the Fermi level at the same point in the Brillouin zone. Possibly due to the hybridization of the Co and C bands, an additional 2D band with a conical dispersion (which will be termed as *minicone* throughout the thesis) forms in the proximity of the Fermi level [21]. The peculiarity of this band lies in its single-spin character and therefore possibly it plays a role in the magnetic phenomena mentioned above.

Moreover, there is no clear report of the presence of the minicone feature in relation to the graphene crystallographic orientation. The formation of the minicone band was reported only for graphene oriented along the cobalt lattice vector [21], without reliable information on other rotational variants of the graphene layer. In order to investigate the dependence of the electronic structure on the graphene orientation there is need for samples of elevated crystallographic quality, both of the substrate and of graphene. Therefore, a big effort in this thesis went into the optimization of the substrate quality and the subsequent graphene CVD synthesis. This calls for a real-time characterization technique, capable of laterally resolving the surface morphology. Thus, Low Energy Electron Microscopy (LEEM) and PhotoEmission Electron Microscopy (PEEM) are employed in this work. After obtaining a reproducible recipe for the growth of graphene with improved crystallographic quality, the study of the spin-resolved band structure is performed using the PEEM microscope operating in the angle-resolved photoemission spectroscopy mode (termed as *k-mode*).

Furthermore, in order to reveal the origin of the spin-polarized minicone feature and its dependence on the graphene-cobalt hybridization, intercalation of different atomic species and substitutional doping is also performed. For this purpose, oxygen and gold are employed as intercalants, while nitrogen is used to substitute the carbon atoms in the graphene network.

The thesis is structured as follows. In **Chapter 1** an overview of graphene properties and production methods is given. Among them, the CVD synthesis technique is described in detail, focusing the attention to works performed using ferromagnetic substrates. In the last part, the motivation standing behind this work is presented in further detail.

The description of the phenomena underlying the experimental surface investigation techniques used is presented in **Chapter 2**. These methods are implemented in two different setups, namely NanoESCA and Nanospectroscopy, which are introduced in **Chapter 3**.

The growth and electronic properties of the pristine metal films, mainly of Co, but also of Fe and Ni, on the W(110) surface is reported in **Chapter 4**, with special emphasis on the

structural transition of cobalt as a function of temperature. Dedicated DFT and DMFT calculations, performed by collaborators from ICTP and University of Hamburg are used as an auxiliary tool for the identification of the electronic features in the valence band. The surfaces of Fe, Ni and Co are used as the support for the CVD graphene growth, which is described subsequently. **Chapter 5** gives the peculiar growth and transformations of graphene on cobalt films, as well as the electronic characterization of the resulting graphene/cobalt interface. The characterization of the graphene/Fe and graphene/Ni films are given in the Appendix sections.

Finally, the intercalation of oxygen and gold at the graphene/substrate interface and substitutional nitrogen doping are reported in **Chapter 6** with the important conclusion that the minicone feature is an intrinsic property of the graphene/cobalt interface. The last part of the thesis presents an outlook based on the conclusion of this work.

Chapter 1

Graphene: properties, application and synthesis

Graphene is a monoatomic thick crystal composed by carbon atoms organized in a honeycomb matrix and interconnected by covalent σ bonds. The symmetry is not exactly hexagonal, since the hexagonal symmetry is obtained only by applying a di-atomic basis to the hexagonal Bravais lattice, allowing for the formation of two hexagonal sublattices. Therefore, the graphene unit cell contains two atoms, A and B located at a nearest neighbor distance (C - C) of 1.42 Å (Fig. 1.1a). The two real space vectors are defined as follows:

$$\mathbf{a}_1 = \frac{a}{2} \begin{pmatrix} \sqrt{3} \\ 1 \end{pmatrix}; \quad \mathbf{a}_2 = \frac{a}{2} \begin{pmatrix} \sqrt{3} \\ -1 \end{pmatrix}, \quad (1.1)$$

where a is the in-plane lattice constant equal to 2.456 Å. In reciprocal space instead, the two unit vectors are defined as:

$$\mathbf{b}_1 = \frac{2\pi}{\sqrt{3}a} \begin{pmatrix} 1 \\ \sqrt{3} \end{pmatrix}; \quad \mathbf{b}_2 = \frac{2\pi}{\sqrt{3}a} \begin{pmatrix} 1 \\ -\sqrt{3} \end{pmatrix}. \quad (1.2)$$

These vectors define the first Brillouin zone (FBZ) of graphene (Fig. 1.1b), characterized by the symmetry points Γ (located at the center), K and K' (located at the edge of the Brillouin zone), and M (middle point of an edge).

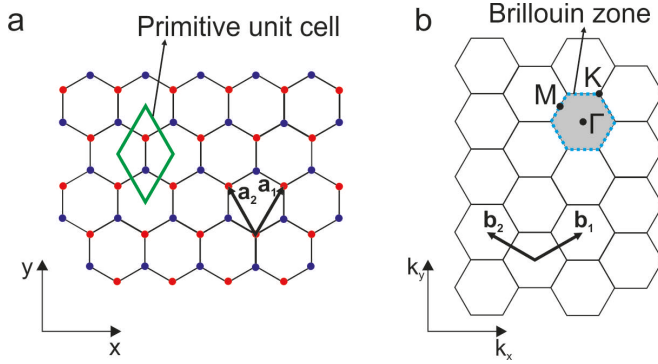


Figure 1.1: a) The periodic lattice of graphene consisting of the unit cell of two carbon atoms. b) Reciprocal lattice of graphene with the highlighted Brillouin zone along with the high symmetry points. The coordinates of the high symmetry points of the 2D (k_x, k_y) Brillouin zone are: $\Gamma = (0, 0)$, $K = (4\pi/3a, 0)$, $M = (\pi/a, -\pi/\sqrt{3}a)$. The distances between the center of the Brillouin zone and high symmetry points are: $\Gamma K = 4\pi/3a$ and $\Gamma M = 2\pi/\sqrt{3}a$.

In a strict sense, graphene is a 2D material, made of monoatomic thick layer carbon atoms. However, in the literature, it can be often found the notation of multilayer graphene, corresponding to a stack of several layers of graphene (up to 10), mutually connected by van der Waals forces. Beyond that, thicker layers are denoted as graphite. The mutual stacking between graphene layers can be of different types. This includes in bilayer graphene the AB stacking (Fig. 1.2b), while in a multilayer there is the Bernal stacking ABA (Fig. 1.2c), which is predominant in most of the carbon allotropic forms, and the rhombohedral stacking ABC (Fig. 1.2d). The interplane distance between neighboring planes is 3.35 Å.

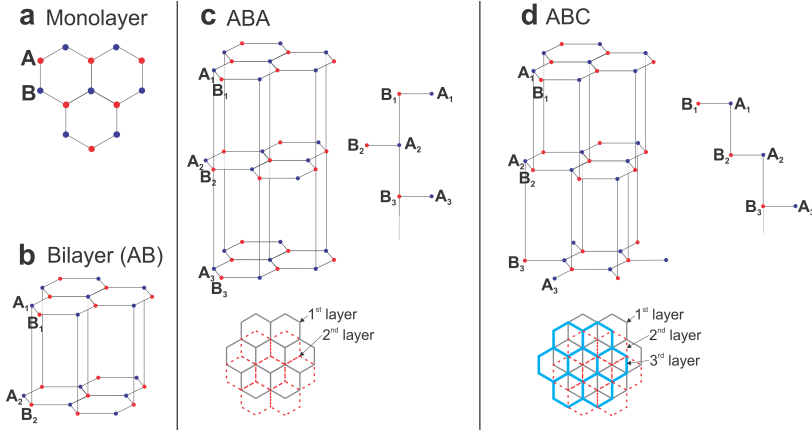


Figure 1.2: Lattice structures of a) monolayer graphene, b) AB-stacked bilayer graphene, c) ABA-stacked multilayer graphene and d) ABC-stacked multilayer graphene.

The electronic configuration of carbon is $1s^2 2s^2 2p^2$. In graphene, like in diamond and graphite, one electron from the $2s$ orbital is transferred to the $2p$ orbital, leading to the formation of a hybrid sp^2 orbital. These sp^2 orbitals are trigonal planar, with bonds respectively oriented at

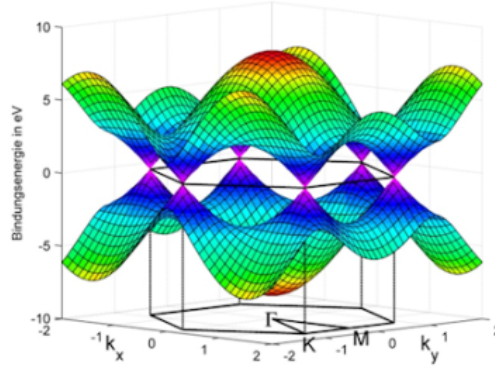


Figure 1.3: Graphene π and π^* band structure over the complete Brillouin zone. Adapted from [22].

120° in the plane pointing to three closest neighbors. They form strong σ and σ^* bonds, which are responsible for the enhanced network cohesion in the graphene plane. The fourth electron forms the C $2p_z$ orbital, which is perpendicular to the graphene plane and creates the π and π^* bonds, responsible for the peculiar properties of graphene. The graphene band structure is composed by π (valence) and π^* (conducting) bands touching at six points (K and K' points), at the edges of the Brillouin zone. For free-standing and undoped graphene, the valence band is completely filled while the conduction band is empty, therefore the Fermi level is found at the intersection of the two bands (K and K'). In the proximity of the Fermi level the dispersion of the π bands is linear and can be written as follows:

$$E(\mathbf{k}) = \pm \hbar v_F |\mathbf{k}|, \quad (1.3)$$

with $v_F = 10^6$ m/s the Fermi velocity. This linear dispersion implies that the charge carriers have the same speed independent of their energy. This means that the behavior of the charge carriers in graphene is similar to that of photons, with a speed about 300 times less than that of light. Indeed, it turns out that these electrons obey the Dirac equation for massless fermions, rather than that of Schrödinger [23, 24].

The peculiar valence band of graphene can be reproduced using a simple tight-binding approach, including both first and second nearest neighbor contributions, in the form of non-zero overlap parameters. Using the notation introduced by Castro Neto *et al.* [25], the tight-binding Hamiltonian can be expressed as:

$$H = -t \sum_{\langle i,j \rangle, \sigma} (a_{\sigma,i}^\dagger b_{\sigma,j}) - t' \sum_{\langle\langle i,j \rangle\rangle, \sigma} (a_{\sigma,i}^\dagger a_{\sigma,j} + b_{\sigma,i}^\dagger b_{\sigma,j}) + H.C., \quad (1.4)$$

with $a(b)$ and $a^\dagger(b^\dagger)$ annihilation and creation operators of an electron on the A (B) sublattice with spin σ , t and t' being the hopping parameters for first and second nearest neighbors, respectively, and with the two summations running over the first ($\langle i,j \rangle$) and second ($\langle\langle i,j \rangle\rangle$) nearest neighbors. $H.C.$ is instead the hermitian conjugated operator of the terms expressively written.

The resulting energy-momentum curve therefore becomes:

$$E_{\pm}(\mathbf{k}) = \pm t \sqrt{3 + f(\mathbf{k})} - t' \sqrt{f(\mathbf{k})}, \quad (1.5)$$

with $f(\mathbf{k})$ being defined as:

$$f(\mathbf{k}) = 2 \cos(\sqrt{3}k_y a) + 4 \cos\left(\frac{\sqrt{3}}{2}k_y a\right) \cos\left(\frac{3}{2}k_x a\right). \quad (1.6)$$

By expanding up to the first order the equation 1.5 in terms of the parameter q/k (defined from \mathbf{q} , the momentum vector taken from the K point, normalized to the K point vector modulus = 1.703 \AA^{-1}), a conical behavior of energy *vs.* momentum can be deduced. This means that the linear dispersion of its bands is limited to a momentum region close to the K point, in order for the first order expansion to be reasonable, and quantitatively being equal to $\approx 1 \text{ eV}$, as determined by Blake *et al.* [26]).

The expansion to higher-order terms leads to:

$$E_{\pm}(\mathbf{k}) = 3t' \pm v_F q + \left(\frac{9t'a^2}{4} \pm \frac{3t'a^2}{8} \sin(\theta_q) \right) q^2, \quad (1.7)$$

where θ_q is equal to:

$$\theta_q = \arctan(q_x/q_y). \quad (1.8)$$

The second order expansion in equation 1.7 leads to the breaking of the electron-hole symmetry and of the full rotational symmetry of the dispersion around the K point, by means of θ_q , bringing a different group velocity depending on the selected directions in the reciprocal space (effect known as trigonal warping [27]).

1.1 Graphene

1.1.1 Electronic properties

The above-mentioned peculiarities of the graphene band structure reflect in particular on its electronic properties. The most prominent one is the very high electronic mobility in single-layer graphene, which can be as high as $\mu \approx 230\,000 \text{ cm}^2/(\text{V}\cdot\text{s})$ at room temperature in the case of mechanically exfoliated graphene suspended between two electrodes [28], nearly 200 times the mobility reached in silicon. This mobility is, however, strongly dependent on the structural properties of graphene (presence of defects, domain boundaries, number of layers) and of the support (substrate). For example, if a mechanically exfoliated single-layer graphene is deposited onto a silicon substrate, the electronic mobility at room temperature reduces by a factor 15 down to $\mu \approx 15,000 \text{ cm}^2/(\text{V}\cdot\text{s})$ [23]. If instead hexagonal boron nitride (hBN) is used as a support, the electronic mobility is only halved, becoming $\mu \approx 100\,000 \text{ cm}^2/(\text{V}\cdot\text{s})$ [29]. For graphene synthesized by chemical methods on metallic substrates the electron mobility at room-temperature is in the order of $\mu \approx 5,000$ to $15,000 \text{ cm}^2/(\text{V}\cdot\text{s})$ [30, 31]. For a multilayer film, obtained by chemical methods on a nickel support, the mobility varies between $\mu \approx 200 \text{ cm}^2/(\text{V}\cdot\text{s})$ and $\mu \approx 3500 \text{ cm}^2/(\text{V}\cdot\text{s})$ [32, 33]. Graphene also allows the observation of particular quantum phenomena such as

anomalous quantum Hall effect, being the only material exhibiting it at room temperature [25, 34], with the conductivity having semi-integer values:

$$\sigma_{Hall} = \pm \frac{4e^2}{h} \left(N + \frac{1}{2} \right), \quad (1.9)$$

with N being the Landau level index.

1.1.2 Mechanical and thermal properties

The mechanical properties of a freestanding graphene layer were measured by Lee *et al.* [35] by nano-indentation using an atomic force microscope, finding that the Young's modulus of graphene is 1.0 TPa, about 5 times that of steel. The breaking strength of graphene is as high as 130 GPa. The thermal properties of freestanding graphene have been studied using Raman spectroscopy. By varying the power of the laser, the position of the characteristic G band of graphene (C-C vibrational stretching) has been recorded, observing that the center of the band is linearly dependent on the temperature [36]. Then, considering this temperature dependence, and knowing the power of the laser, the value of thermal conductivity of graphene can be obtained being 5300 W/mK for an exfoliated single-layer graphene [36]. That of a graphene monolayer obtained by chemical methods on copper is about 2500 W/mK [37]. For comparison, the thermal conductivity of a single-walled carbon nanotube is about 3500 W / mK [38] and about 400 W/mK for a bundle of nanotubes. [39].

1.1.3 Applications

Over the past decade, it has been demonstrated that graphene has great potential for applications, especially in the field of electronics, energy storage, and composite materials. The exceptional performance of graphene, especially concerning the electronic conductivity, makes graphene, at first sight, a suitable competitor to succeed silicon in the field of electronic components. However, the technological maturity at these days is still far from being reached. Progress is observable in the graphene high-frequency transistor design capable of achieving frequencies of 26 GHz [40], 100 GHz [41] and 300 GHz [42]. One of the issues is that freestanding graphene has a zero forbidden band, therefore introducing the need to create a non-zero band-gap. In addition, the realization of electronic components using graphene requires a homogeneous graphene and very good structural quality which remains still a challenge to the nowadays researchers, particularly regarding its mass production with a relatively low production cost.

1.2 Synthesis methods

The synthesis of graphene can be performed following two different approaches, the bottom-up and the top-down, respectively. Bottom-up methods have in common the fact that the synthesis of graphene is performed using alternative carbon sources while top-down approaches involve the separation of stacked graphite layers with the goal of obtaining single graphene sheets (Fig. 1.4).

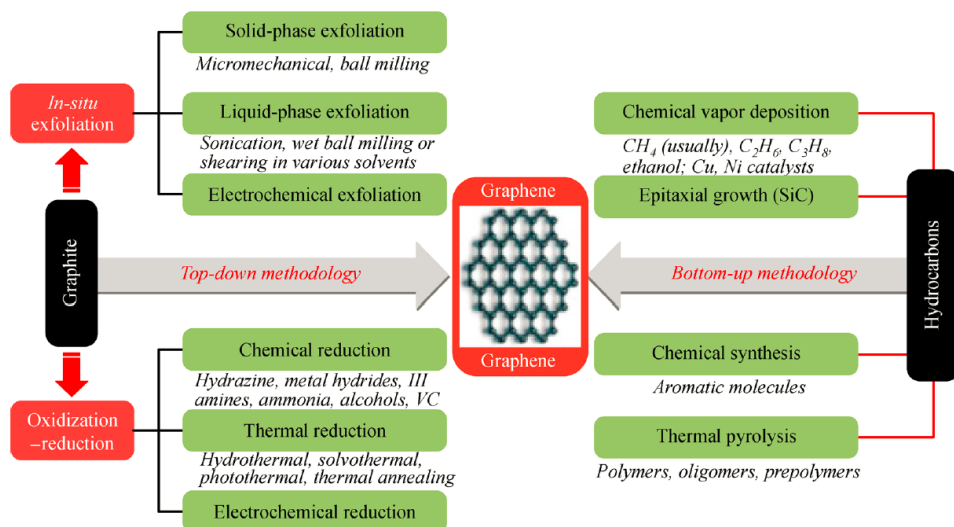


Figure 1.4: Schematic representation for graphene synthesis through top-down and bottom-up approaches. Adapted from [43].

1.2.1 Top-down synthesis

Liquid phase exfoliation

The term graphite liquid-phase exfoliation includes techniques using wet chemical dispersion followed by sonication-induced exfoliation with or without surfactants in suitable solvents. The technique is based on the use of magnetic Fe₃O₄ nanoparticles as "particle wedge" to ease the delamination of graphitic layers (Fig. 1.4). It was found that exfoliation using particle wedges can be an appropriate method for reducing ultrasonication time and suppressing structural defects deriving from long-term sonication procedures. An efficient and green method for large-scale synthesis of few-layer graphene in pure water without the use of chemicals or surfactants has recently been reported [44]. Atomic force microscopy (AFM) pictures showed that the thickness of so-obtained flakes was approximately 2.24, 0.52 and 1.76 nm, corresponding to six-layer, single-layer, and four-layer graphene. The statistical evaluation of more than 100 flakes showed that >25% of the graphene flakes are monolayer (<1 nm in thickness) with a lateral size ranging from 0.5 to 2.5 μm. The method opened the way for the cost effective and environmentally friendly production of graphene-based materials with significant potential for real-life applications. The authors of another study [45] have demonstrated a high-yield method to produce defect free few-layer graphene by exfoliation of graphite in a chemically modified degradable water-soluble polymer. They were able to obtain high-quality graphene with a production rate of 6 g/h. The transmission electron microscopy (TEM) images of the exfoliated graphene reveal that the graphene sheets are transparent under the electron beam, suggesting a low thickness of graphene sheets, as also confirmed by AFM analysis.

Electrochemical exfoliation

Electrochemical exfoliation of graphite into graphene consists in the use of carbon sources (graphite or highly oriented pyrolytic graphite rods, graphite foils) as electrodes which are dipped into an aqueous or non-aqueous electrolyte solution. Recently, a cost-effective electrochemical approach to produce graphene by electrochemical exfoliation of graphite rods in acidic electrolytes has been reported [46]. Munuera *et al.* studied an easy method for the preparation of ready-to-use and low oxygen content graphene material based on electrochemical delamination of graphite in an aqueous medium using sodium halides as electrolyte [47]. The halide-derived graphenes were tested as dye adsorbents, adsorbents for oils and non-polar organic solvents and as electrodes for supercapacitors and displayed comparable or even better performances than that of other types of graphene.

A novel electrochemical exfoliation mode was accomplished to effectively prepare graphene sheets with prospective applications in transparent conductive films [48]. A concentrated sodium hydroxide solution was used as an electrolyte and the graphite electrode was coated with paraffin to maintain electrochemical exfoliation in confined space. The tests were performed at low voltage (3 V) to prepare graphene with reduced quantities of defects and enhanced yield. A high-yield technique for generating low-defect graphene nanosheets by electrochemical exfoliation of graphene from natural graphite electrodes in the presence of sulfate ions under constant voltage and constant current models has been established, as reported in [49]. Based on the experimental results, their approach may constitute an industrial scalable processing method for producing high-yield and low-defect graphene products. In contrast to the above works, the direct electrochemical reaction between graphite powder and metallic Li in 1 mol/L lithium hexafluorophosphate/propylene carbonate electrolyte has been used to continuously exfoliate graphite with a high yield of 80% without any consumption of electrical energy [50]. The SEM and TEM studies suggest that the non-electrified electrochemical exfoliation method can produce few-layer graphene nanosheets of high quality similar to the typical electrochemical exfoliation route.

Chemical reduction of graphene oxide

Graphene oxide (GO) chemical reduction is an effective technique for producing graphene in terms of expenses and large-scale production. A disadvantage of this technique is that reduced graphene sheets tend to agglomerate. In addition, the chemical reduction process generally uses toxic reduction agents such as hydrazine or sodium borohydride. The use of green reduction agents over toxic chemicals is now one of the appealing subjects in the field of graphene [51, 52, 53]. All the reducing agents have been demonstrated to be environmentally friendly and the products generated are extremely dispersible and biocompatible and therefore helpful in one manner or another.

1.2.2 Bottom-up synthesis

Epitaxial method

The thermal decomposition of SiC is a promising technique of preparing high-quality graphene, and the epitaxial graphene produced in this manner can be implemented directly without

transferring to graphene-based electrical systems, as it has been demonstrated recently by Qin *et al.* [54].

A new method was investigated for producing uniform epitaxial graphene on C-face 6H-SiC substrates with a sputtered SiC film by annealing temperatures ranging from 1400 to 1900 °C under Ar atmosphere. Using Raman mapping and low-energy electron microscopy, bi-layer graphene of about 95% was found in a $75 \times 75 \mu\text{m}^2$. Their conclusion was that this novel technique is very promising for the manufacture of analog high frequency devices [55].

Chemical synthesis from aromatic molecules

It is possible to synthesize graphene starting from aromatic hydrocarbons. Similarly to the CVD process, there is the partial catalytic decomposition of the aromatic hydrocarbon on the surface. Thanks to thermal treatments of the surface, the molecular fragments can aggregate in graphene structures with high crystalline quality.

Moreno *et al.* reported a bottom-up method to synthesize nanoporous graphene formed in separate steps [56]. An innovative, single-pot synthesis was demonstrated instead for the chemical production of graphene/polyaniline nanocomposites. In a one-pot reaction, both graphene and polyaniline were chemically synthesized from benzene and aniline. After characterization, the films with distinct polyaniline/graphene proportions were employed in supercapacitors as the active layer [57].

Chemical vapor deposition - CVD

This method exploits the catalytic decomposition of hydrocarbon molecules on metallic surfaces, allowing for the accumulation of carbon which afterward rearranges in graphitic layers. In practice, a hydrocarbon such as methane (ethylene, propane, etc.) is brought to the surface of a metal substrate in a variable temperature range. The hydrocarbon molecule is adsorbed, dissociated and/or dehydrogenated on the catalytic metal surface. Since the process is performed at elevated temperature (between 350 °C and 1100 °C), the carbon atoms deriving from the catalytic decomposition are mobile and can form graphene following two possible processes, which are distinguished by the level of carbon solubility in the metal.

In the case of metals for which the carbon solubility is low, such as copper (0.01 % at 1000 °C), the carbon atoms adsorbed on the surface after the decomposition of the methane are reorganized into graphene with a surface limited process (Fig. 1.5 top). This surface-limited process allows for the growth of a maximum full single layer of graphene, since the surface afterward becomes inert from the catalytic point of view. As reported by Li *et al.* [58], graphene on Cu presents less than 5% of regions covered by graphene multilayers.

In the case of metals for which the solubility of carbon is high, such as nickel (1.2% at 1000 °C), the formation mechanism is different. Carbon atoms adsorbed on the surface after the decomposition of the methane diffuse in the volume of catalyst because, at this high temperature, the solubility of C is sufficiently high. During the cooling of the Ni substrate, the solubility of C decreases, causing a segregation/precipitation phenomenon of C atoms on the surface and subsequent graphene nucleation (Fig. 1.5 bottom). This phenomenon of segregation/precipitation controls the growth of additional graphene layers and the metal substrate becomes a reservoir of C atoms supplying growth. This is why multilayer graphene formed by CVD is easily achievable

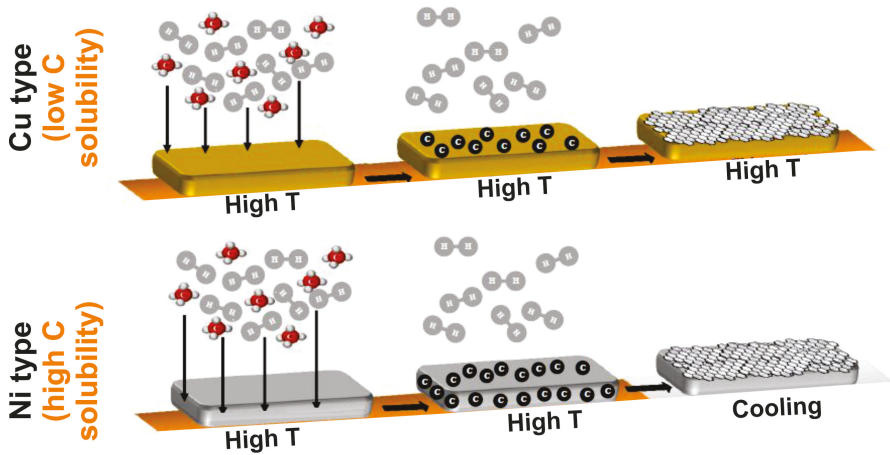


Figure 1.5: Graphene-growth mechanisms using both high and low carbon solubility metals. Adapted from [59].

on metals with high C solubility.

1.3 Insight into the CVD method

As referred to earlier, CVD growth yields graphene with a low amount of structural defects. However, the layer is supported by a substrate, which should be removed in order to make use of the CVD-grown graphene, *i.e.* transfer it onto other supports. The transfer procedure is not an easy task since it is essential to limit the damage of the graphene layer and its contamination. Two methods are mainly used to transfer graphene formed by CVD. The one that is frequently used consists in the deposition of a polymethyl methacrylate (PMMA) layer on graphene, followed by the dissolution of the metal support. Afterward, graphene is separated from PMMA via an acetone solution, which however, induces contamination in the graphene layer.

Another technique which can be employed is the insertion of an inert material at the graphene/substrate interface, allowing for a weakening of the interaction force between them. This can be achieved by thermal intercalation of gold layers, or by the growth of carbidic structures, using the bulk carbon as a reservoir.

The growth of graphene by CVD has been achieved for a large number of metals in a wide range of experimental conditions. Though the use of Cu and Ni is predominant, graphene can be grown also on Co [60, 61, 62], Fe [63], Ir [64, 65], Rh [66], Pt [67], Re [68], Au [69]. For each of these metals, according to the value of C solubility, the growth follows the model of a surface adsorption process (Cu type), which allows for the formation of predominantly monolayer graphene or via a segregation/precipitation process (Ni type), which allows for the formation also of multilayer graphene. The properties of the material used as a substrate do influence not only the type of growth mechanism but also the metal-graphene interaction, which substantially modifies the graphene electronic structure. In the case of metals with strong metal-graphene interaction, such

as Ni, Ru or Co, there is a chemisorption type interaction at the interface. The distance between graphene and those substrates is small (order of 2.0-2.2 Å) leading to the remarked modification of the electronic structure of graphene [70]. The structure of graphene is strongly related to that of the substrate during growth. In the case of metals with low metal-graphene interaction, such as Cu or Ir, there is physisorption at the interface, with a metal-graphene distance in the order of 3.3 Å [71]. In this case, the structure of the CVD grown graphene is not altered, being more similar to the free-standing case.

1.4 Current state of the art and scope of the thesis

Among the few "missing" properties of graphene, the absence of extended magnetic behavior of the layer can be mentioned as a lacking characteristic. One of the first reasons of this behavior may be that no d and f shell electrons are present, which are responsible for the magnetic coupling in ferromagnetic materials. Isolated cases of magnetic behavior can be found when looking at the microscaled features in the 2D carbon layer. For example, the so-called *zig-zag* configuration of graphene edges induces the presence of localized magnetic moments [72]. Moreover, point defects in the graphene lattice, such as *vacancies* and *adatoms* allow the existence of localized states with magnetic behavior [73, 74].

Therefore, one of the challenges in the community is the capability to obtain a "magnetic graphene", which combines the exceptional properties of the freestanding graphene with an extended magnetic order. As one of the possible solutions, the synthesis of graphene can be performed on top of ferromagnetic substrates. In order to take advantage of the magnetic behavior of graphene and therefore apply this property in technological devices, the ferromagnetic behavior should be guaranteed in a temperature range around room temperature. Accordingly, the choice of materials narrows to only a few. Considering that the materials should provide also catalytic behavior in order to facilitate the CVD synthesis, the choice is restricted to only three pure materials: Fe, Ni and Co.

As it will be discussed in the fourth chapter, a study of the spin-resolved band structure mapping has been performed for the films of the three above-listed materials. Subsequently, CVD graphene synthesis has been done on top of Fe, Ni and Co. Considering the experimental setup used for the analysis of such systems and the observed behavior of the graphene/ferromagnetic interfaces, the choice has been restricted to cobalt, on top of which the most of the preparations of this thesis were performed.

Compared with the number of works on copper or nickel, there are relatively few studies about the CVD growth of graphene using cobalt as a substrate. These studies use a variety of methods, and their results highlight a few interesting points about graphene synthesis on cobalt. It has to be noted that the carbon solubility in cobalt is quite high (1.2% at 1000 °C). The work of Ramon *et al.* [62] exploited the influence of thickness of the cobalt film on the monolayer graphene overlay rate. The CVD process has been done using low hydrocarbon (acetylene) pressure ($1.5 \cdot 10^{-8}$ Torr) with a sample temperature of 800 °C, followed by rapid temperature quenching. Cobalt films of 100, 200, and 300 nm thickness were deposited onto a SiO₂/Si substrate. It emerged that graphene completely covers the cobalt surface with a non-uniform thickness. In thinner cobalt films the amount of monolayer graphene is predominant, while in thicker ones multilayer growth is favored. This is due to the cobalt volume which acts as a reservoir of carbon for CVD growth, allowing

for the accumulation of only a little dose of carbon in thinner films, therefore, tending to form monolayer graphene.

Acting on the thickness of the thin film is not the only way to reduce the number of layers of the graphene film and improve its uniformity. Ago *et al.* [60] studied the influence of the structural quality of the cobalt film on the graphene quality by comparing the synthesis of graphene on cobalt films of 200 nm thickness deposited on SiO₂/Si and on sapphire, at 900 and 1000 °C. The thin cobalt film deposited on SiO₂/Si is atomically rough, and polycrystalline graphene forms on this substrate (Fig. 1.6a), exposing domains with different numbers of layers, and a large number of grain boundaries. The cobalt film deposited on the sapphire monocrystal allows for the formation of an epitaxial graphene film of good structural quality with limited roughness (Fig. 1.6 b). At the synthesis temperature of 1000 °C, a uniform monolayer graphene film is obtained.

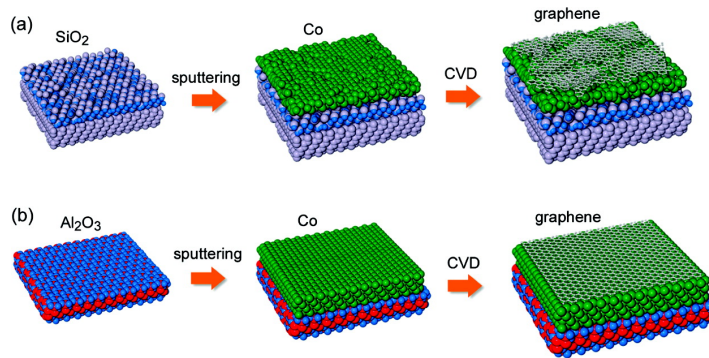


Figure 1.6: Schematics of the CVD growth of graphene over Co films deposited on SiO₂/Si (a) and sapphire c-plane (b) substrates. (a) Polycrystalline Co film is formed on the SiO₂ surface, which gives disordered graphene with a broad layer thickness distribution and randomly oriented small domains. (b) On the other hand, a crystalline Co film is formed on sapphire c-plane and assists the growth of uniform, well-defined graphene with controlled orientation. Reprinted with permission from [60]. Copyright 2010 American Chemical Society.

In their work, Eom *et al.* [75] reported that upon epitaxial graphene formation on the cobalt substrate, the band structure of the interface exhibits peculiar properties. Upon adsorption, two main features are observed for epitaxially aligned graphene while looking at the K point of the FBZ: the crossing of graphene π bands, upon strong chemisorption, is found at about 2.8 eV binding energy, while a conelike feature appears in the proximity of the metallic Fermi level.

In 2015, Usachov *et al.* [21] reported that this conelike feature (minicone) originates only in epitaxially aligned graphene, while in graphene with moiré patterns it is absent. The origin of this feature is formed by a mixture of C $2p_z$ and Co $3d$ states, and their nature is two-dimensional. The peculiarity of this state is that it is a 100% spin-polarized interface state (at least in theory), with an energy-dispersion relation that is an order of magnitude less with respect to the main Dirac cone, so that the charge carriers have a speed in the order of 10^5 m/s. The apex of this minicone is parabolic, indicating that the charge carriers are not massless. Moreover, the combination of the angle-resolved photoemission results with density functional theory calculations allowed one to determine that the minicone behavior in terms of position and parabolic apex corresponds exclusively to an “*fcc-top*” adsorption geometry.

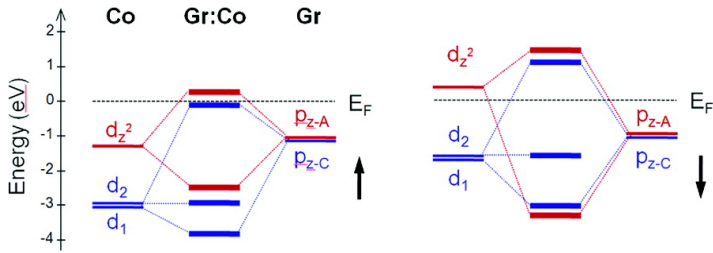


Figure 1.7: Schematic illustration of the electronic coupling between cobalt d- and carbon p_z -states near the K-point in the surface BZ for majority- and minority-spin states (left and right). Fermi energy indicated. Reprinted with permission from [75]. Copyright 2009 American Chemical Society.

Considering the above-listed works present in the literature, an extensive characterization of the graphene growth on the mesoscale is still missing. This characterization can be performed via microscopical techniques such as LEEM and PEEM, which thanks to their enhanced lateral resolution, combined with an appropriate photon source, allow to spatially resolve the microsized structures on the sample surface. The capability of such instruments to perform video-rate imaging, allowed us to real-time follow the graphene growth process, which still have not been performed using cobalt as a substrate to date. In addition, considering the ferromagnetic nature of the interface, the use of spin-resolved techniques has been employed only in few works, therefore the imaging of the electronic structure during all the preparation steps is fundamental to understand the nature of resulting spin-polarization and to study the potential modifications for tuning the properties of the interface.

Chapter 2

Methods

2.1 Photoemission spectroscopy

The photoemission process is driven by the interaction of the solid material with an electromagnetic wave field $\mathbf{A}(\mathbf{r}, t)$ [76]. The evolution of the wave function of the photoelectrons in the solid can be expressed via the time-dependent Schrödinger equation:

$$i\hbar \frac{\partial}{\partial t} \psi(\mathbf{r}, t) = \left[\frac{1}{2m} \left(\frac{\hbar}{i} \nabla - \frac{e}{c} \mathbf{A}(\mathbf{r}, t) \right)^2 + V(\mathbf{r}) \right] \psi(\mathbf{r}, t) = H\psi(\mathbf{r}, t), \quad (2.1)$$

where $\psi(\mathbf{r}, t)$ is the wave function of the single electron and the solution of this equation describes the dynamics of the electron under electromagnetic field. In the dipole approximation, the A^2 term is neglected, while the linear term becomes $\mathbf{A} \cdot \nabla + \nabla \cdot \mathbf{A}$, being the kinetic energy of the system. Considering that the boundary between the semi-infinite potential well and vacuum, at the surface level, the term $\nabla \cdot \mathbf{A}$ reduces to 0 [77]. This assumption allows one to express the transition rate from an initial ($\psi_i(\mathbf{r}, t)$) to a final electronic state ($\psi_f(\mathbf{r}, t)$) using first order time-dependent perturbation theory:

$$w_{i \rightarrow f} = \frac{2\pi}{\hbar} |\langle \psi_f(\mathbf{r}, t) | H | \psi_i(\mathbf{r}, t) \rangle|^2 \cdot \delta(E_f - E_i - \hbar\nu), \quad (2.2)$$

where H is the photoexcitation Hamiltonian, while the delta function guarantees the energy conservation. Considering the commutation relation between ∇ and \mathbf{A} , and that $\mathbf{p} = -i\hbar\nabla$, the matrix element can be expressed as:

$$M_{i \rightarrow f} = \langle \psi_f(\mathbf{r}, t) | \mathbf{p} \cdot \mathbf{A} | \psi_i(\mathbf{r}, t) \rangle. \quad (2.3)$$

In the case of an electron, the following relationship holds: $\mathbf{p} = \hbar \mathbf{k}$. This allows, in first order perturbation theory, to approximate the interaction Hamiltonian as:

$$H \approx \frac{\hbar e}{mc} \mathbf{A} \cdot \mathbf{k}. \quad (2.4)$$

By taking into account that the excitation source is usually in the range of UV and soft X-ray, the variations of \mathbf{A} are very small over atomic distances, the matrix element becomes:

$$\mathbf{M}_{fi} \approx -\frac{ie}{c} A_0 (E_f - E_i) \langle \psi_f(\mathbf{r}, t) | \hat{\mathbf{P}} \cdot \hat{\mathbf{k}} | \psi_i(\mathbf{r}, t) \rangle, \quad (2.5)$$

where A_0 is the amplitude of the vector potential and $\hat{\mathbf{P}}$ the electric polarization. The matrix element (2.5) in that form can be analyzed concerning the symmetries of initial and final states, being able to extract the selection rules for allowed/forbidden electronic transitions.

The above-described model of photoemission is, however, only a single electron model. Real electronic systems consist of multiple electrons with mutual interaction. Therefore, the initial and final electronic state should be substituted by many-particle wave functions, describing the electron system in its ground and excited state, respectively. Supposing a photon beam removing a single electron from a band, the rest of the electrons surround the photohole, therefore locally shielding it and changing the potential.

Approximating the many-particle situation requires the introduction of a spectral function $A(\mathbf{k}, E)$, leading the photocurrent to be [76]:

$$I \propto \sum_{f,i,\mathbf{k}} |\langle \psi_{f,E_{\text{kin}}} | r | \psi_{i,\mathbf{k}} \rangle|^2 A(\mathbf{k}, E). \quad (2.6)$$

The spectral function describes the probability of removing or adding an electron with momentum \mathbf{k} and energy E from or to an interacting N-electron system, respectively. In the case of interacting systems instead, the spectral function becomes:

$$A(\mathbf{k}, E) = \frac{1}{\pi} \frac{\Im(\Sigma(\mathbf{k}, E))}{(E - E_{\mathbf{k}}^0 - \Re(\Sigma(\mathbf{k}, E)))^2 + (\Im(\Sigma(\mathbf{k}, E)))^2}, \quad (2.7)$$

where a complex-valued self-energy $\Sigma(\mathbf{k}, E)$ has been introduced. The term $E_{\mathbf{k}}^0$ represents the energy of the non-interacting electrons.

2.1.1 Modelling the photoemission process

In order to theoretically treat the photoemission process in experiments, several models have been proposed. A phenomenological description in which the photoemission process is splitted into three steps has been developed by Berglund and Spicer [78] in 1964. In this approach, optical excitation between two Bloch states (namely initial and final), transport of the electron to the surface, and escape of the electron into the vacuum are treated separately. More recently, the photoemission is described as a one-step process [79]. Excitation occurs between the initial single-electron Bloch state into the so-called "time-reversed LEED state" that is free-electron like in vacuum, while it decays in the crystal.

Considering the three-step model, in the first step, the electrons are excited from their ground state $|\psi_i(\mathbf{k})\rangle$ to a final state $|\psi_f(\mathbf{k})\rangle$. Considering that energy and momentum have to be conserved, the following relations persist:

$$E_f = E_i + h\nu, \quad (2.8)$$

$$\mathbf{k}_f = \mathbf{k}_i + \mathbf{G}, \quad (2.9)$$

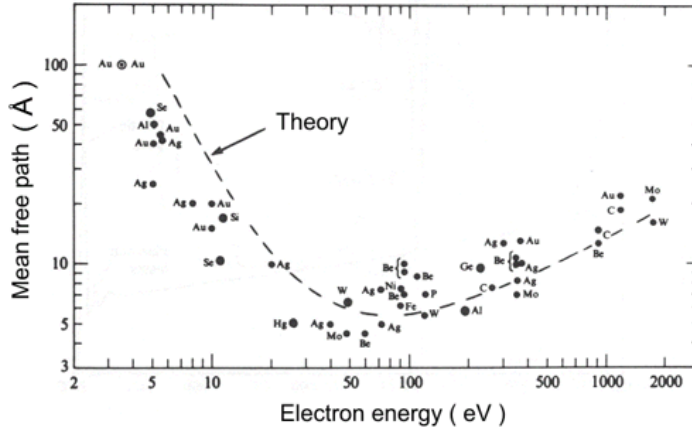


Figure 2.1: Dependence of material inelastic mean free path. The theoretical model is plotted, characterized by an equation: $\lambda = 143/E_{kin}^2 + 0.054 \cdot \sqrt{E_{kin}}$.

where \mathbf{G} is a reciprocal space vector characteristic of the system. Since usually, the excitation source is in the range of soft X-rays, the momentum carried by the photon is negligible.

After being excited, the photoelectrons propagate in the solid, as described in the second step of the photoemission process. The transmitted photoelectrons undergo elastic and inelastic scattering processes with electrons, phonons, and defects.

The electron inelastic mean free path (*i.e.* length that the electron can travel in a material without being inelastically scattered), is a quantity which depends on the kinetic energy of the excited electron. For typical incident photon beams, being in the UV and soft X-ray range, the mean free path is in the order of few nm, which depending on the local atomic arrangement, can probe up to ~ 10 atomic layers. The inelastically scattered electrons instead, lead to the appearance of a broad background, which has a quadratic dependence on the kinetic energy.

Finally, the third step describes the transmission of the photoelectrons through the surface. Since the periodic potential present in the solid is broken upon surface crossing, the momentum component perpendicular to the surface is not conserved. When a photoelectron is emitted from the surface, its energy-momentum dependence can be approximated with a free-electron dispersion. This allows one to rewrite the momentum conservation law in the system as:

$$\mathbf{k}_{\parallel} = k_{x,\parallel} + k_{y,\parallel} = \sqrt{\frac{2m}{\hbar^2} E_{kin}} \cdot \sin(\theta), \quad (2.10)$$

$$\mathbf{k}_{\perp} = \sqrt{\frac{2m}{\hbar^2} (E_{kin} \cos^2(\theta) + V_0)}, \quad (2.11)$$

where θ is the emission angle of the photoelectron. V_0 is the inner potential, an intrinsic characteristic of the material, corresponding to the lowest energy level of the valence band with respect to the vacuum level.

The above-considered model has, however, several limitations. The first is that the influence of the surface is not taken into account, resulting in no distinction between photoelectrons coming

from bulk layers and surface ones. This problem is more accurately solved starting from the equation 2.3, and considering all the photoemission steps within a single quantum-mechanical process, the one-step model. This model also overcomes the issue of the single-particle excitation of the three-step model. As introduced above, the final state is a time-reversed LEED state. In vacuum, it consists of a plane wave with the \mathbf{k} vector pointing in a particular direction of the half-sphere on the vacuum side of the sample. At the surface, a match of the electronic states of the sample is required, accompanied by continuous amplitude and first derivative of the wave function. This matching condition results in the conservation of the surface parallel wave vector component. If the vacuum plane wave can be matched to the electronic states derived from the bulk at the final state energy, the photoelectron wave function extends in the sample and the probing depth is determined by the inelastic mean free path distribution. If there are no matching bulk electronic states at the final state energy, the wave function decays exponentially in the sample, denoted as evanescent wave, which also contributes to the photoemission current.

On the other hand, in the perpendicular direction the momentum component is not conserved. This implies that the Bloch waves with any value of \mathbf{k}_\perp can couple to the vacuum part of the final state, being strongest at particular \mathbf{k}_\perp values. The electronic states in a solid are found at tens of eV above the vacuum level, having a free-electron like dispersion. The occurrence of band gaps at Brillouin zone boundaries rigidly shifts the bands to lower energies. This shift derives from the difference of the electric potential in a solid respect to the vacuum. The difference in the two potentials is the so-called inner potential (U_i), being equivalent to the height of the surface barrier, with an additional contribution from exchange interaction between electrons.

In angle-resolved photoemission experiments, the resulting spectra are composed of intensity maxima at specific values of \mathbf{k}_\parallel and E_{kin} . These intensities can be due to direct transitions between ground state electronic bands in the valence band and unoccupied bands at the final state energy, meaning that either the initial or final state density should have a local maximum. Since the only controllable quantities in the experiment are \mathbf{k}_\parallel , E_{kin} and $h\nu$, transitions involving $A(\mathbf{k}_\parallel, \mathbf{k}_\perp, E_i)$ and $A(\mathbf{k}_\parallel, \mathbf{k}_\perp, E_i + h\nu)$ are possible for any value of \mathbf{k}_\perp vectors ($\mathbf{k} = \mathbf{k}_\parallel, \mathbf{k}_\perp$), where $\mathbf{k}_\perp(E_f, \mathbf{k}_\parallel)$ is determined by direct transitions to the unoccupied electronic band structure, while \mathbf{k}_\parallel is selected by the experiment.

In photoemission resonances involving transitions from bulk electronic states, a common approximation used is to replace the final state band dispersion by the dispersion of a free electron:

$$E_f(\mathbf{k}) = E_f(k) = \frac{\hbar^2 k^2}{2m} + (E_{vac} - U_i) . \quad (2.12)$$

This equation describes a sphere in k -space and a parabola for the energy depending on the absolute value of k . The photoelectron may undergo scattering in the crystal, altering the wave vector k by a reciprocal lattice vector \mathbf{G} :

$$E_f(\mathbf{k} + \mathbf{G}) = \frac{\hbar^2}{2m} \left((k_{\parallel,x} + G_{\parallel,x})^2 + (k_{\parallel,y} + G_{\parallel,y})^2 + (k_\perp + G_\perp)^2 \right) + (E_{vac} - U_i) . \quad (2.13)$$

This equation sets the center of the k -sphere around the Γ point, while the energy position of the minimum of the parabola is $E_{vac} - U_i$. As it will be presented in the method section, the acquisition of momentum resolved images is performed at constant E_f . This condition constitutes

a k-sphere, intersecting the Brillouin zone at a particular \mathbf{k}_\perp value. The radius of the so formed circular surface is given by:

$$r_{k,max} = \sqrt{\frac{2m}{\hbar^2} (E_{kin} + U_i)}. \quad (2.14)$$

2.1.2 Strongly correlated materials

In strongly correlated materials, electron-electron interactions play a fundamental role in material properties, giving rise to a variety of peculiar phenomena. The Hubbard model emerged as suitable for the description of such phenomena, being able to reproduce the band-gap observed at the Fermi level for such systems. Moreover, Landau proposed that the collective behavior after photoexciting an electron system can be separated in high-energetic collective oscillations of the electron sea (plasmons) and the low-energetic excitations of single electrons accompanied by a response of the surrounding electrons. This leads to a photoexcited electron with well-defined energy and two main characteristics: the excitation energy is shifted with respect to an independent-electron description and the energy spectrum of the excited electron has an increased linewidth. The quantification of these quantities requires the introduction of the self-energy of the system, denoting the photoexcited electron as a quasiparticle.

2.1.3 Spin-orbit coupling

A more detailed description of a real electronic system needs the introduction of an additional angular momentum degree of freedom, which could assume the values $\pm\hbar/2$. This variable is defined as electronic spin, which derives from a relativistic approach to the quantum mechanical problem of electron dynamics.

When passing from a classical description to a relativistic one, in the equation of the relativistic particle:

$$E^2 = c^2 (p^2 + m^2 c^2), \quad (2.15)$$

the energy is substituted by the Hamiltonian operator $H = i\hbar \frac{\partial}{\partial t}$, and the momentum, by its operator $\mathbf{p} = -i\hbar \nabla$. Since this substitution leads to the presence of the second derivative of the wavefunction with respect to the time, Dirac proposed a linearization of the equation 2.15:

$$\left[i\hbar \frac{\partial}{\partial t} + i\hbar c \left(\alpha_x \frac{\partial}{\partial x} + \alpha_y \frac{\partial}{\partial y} + \alpha_z \frac{\partial}{\partial z} \right) - \beta mc^2 \right] \psi = 0, \quad (2.16)$$

where 4x4 matrices $(\alpha_x, \alpha_y, \alpha_z, \beta)$ and a 4 component wave function ψ has been introduced.

However, in the case of radial potentials, the angular momentum does not commute with the Hamiltonian of the system, therefore not being a conserved quantity. This implies that an additional quantity \mathbf{s} should be introduced so that the so formed quantity $(\mathbf{1} + \mathbf{s})$ can commute with the Hamiltonian, being, therefore, a conserved quantity. The quantity \mathbf{s} is defined as the observable of the electron spin. A simple electronic picture as discussed above is further developed in the presence of electric and magnetic fields, which in the nonrelativistic limit reduces to:

$$\left[\frac{1}{2m} \left(\mathbf{p} - \frac{e}{c} \mathbf{A} \right)^2 + e\phi - \frac{e\hbar}{2mc} \boldsymbol{\sigma} \mathbf{B} + i \frac{e\hbar}{4m^2 c^2} \boldsymbol{\epsilon} \mathbf{p} - \frac{e\hbar}{4m^2 c^2} \boldsymbol{\sigma} (\boldsymbol{\epsilon} \times \mathbf{p}) \right] \psi = W\psi, \quad (2.17)$$

where W is the electron energy excluding its rest mass and ϵ the vacuum permittivity. The first two terms are equivalent in the case of a particle in an electromagnetic field. The third term includes the interaction of the electronic spin defined as $\mathbf{s} = (\hbar/2) \boldsymbol{\sigma}$, with the external magnetic field. The fifth term treats the spin-orbit coupling. The fourth component in equation 2.17, in the non-relativistic limit can be reduced to a two component term, being able to describe the electron spin (with a two-component wave function). Along a particular quantization axis, the measurement of the spin can be expressed using the Pauli matrix operator.

In the case of spin-orbit coupling, the electron wave function can be expressed as a sum of two orbital wave functions multiplied each with the appropriate spin state along a quantization axis:

$$\psi(\mathbf{k}) = |a\rangle|\uparrow\rangle + |b\rangle|\downarrow\rangle. \quad (2.18)$$

The spin-orbit coupling preserves time-reversal symmetry since when going from t to $-t$, the fifth term in equation 2.17 does not reverse its sign. If no external magnetic field is supplied, the energy eigenvalues obey the rule $E(\mathbf{k}, \uparrow) = E(-\mathbf{k}, \downarrow)$. When time and space reversal are symmetry operators of the system, also $E(\mathbf{k}, \uparrow) = E(\mathbf{k}, \downarrow)$, leading to a degeneracy of the bands for the two spin channels. The inversion symmetry can be violated in the case of noncentrosymmetric crystals or at crystal surface, at the vacuum barrier, leading to the splitting of surface states.

In the case of photoemission measurements on magnetic surfaces, dichroic effects can be observed in the experiments performed at varying polarization of the excitation source. The magnetic dichroism manifests in the spectra as a change in photoemission intensity upon inversion of the magnetization direction.

2.1.4 Quantum well states

When going from an infinite bulk crystal to a thin film of discrete dimension, the electronic states change their character. Due to the periodic structure of the bulk solid, the continuous behavior of the perpendicular component of the energy is broken up when considering a thin film, obtaining a discrete set of states along the perpendicular direction. The number of states per band is correlated to the thickness of the film, *i.e.*, the number of atomic layers present. The projection of the energies of the discrete states on the continuous bulk band dispersion allows one to obtain regularly spaced points in the momentum direction perpendicular to the film, leading to a quantized momentum in this direction. These discrete states are often denoted as quantum well states since the electrons are confined in a potential well of finite dimensions along the perpendicular direction of the thin film.

Usually, quantum well states are studied in thin films grown on top of single crystalline surfaces. These studies aim to enter in the quantum regime, where major changes are expected when passing from a bulk crystal to a thin film. In this sense, the study of the electronic structure of these confined metallic systems is crucial, since the electronic states near the Fermi level are the ones responsible for peculiar magnetic and transport behavior.

The interface between the substrate and the film and the vacuum barrier introduce the boundary conditions at the edges of the periodic potential. The confinement assumed in the case of a free-standing film can be substituted by an energy-dependent reflection probability, with an appropriate complex phase, for the electron waves in the perpendicular direction.

For an ideal interface, the energy-dependent reflection probability is only a property of the electronic structure of the substrate, implying two important consequences. First of all, the

reflectivity needs to be high enough to produce observable quantum well modulations of the bulk derived bands. Full confinement can be obtained when the electron waves are Bragg-reflected in bulk band gaps of the substrate, but away from those gaps, the reflectivity is not always guaranteed. In the latter case, the so-formed discrete states are labeled as quantum well resonances, since there is a finite transmission across the interface. On the other hand, in magnetic substrates, the two spin channels are energetically splitted, being able to obtain different sets of quantum states and/or resonances. This leads to the formation of spin-polarized quantized states also in non-magnetic films deposited on top of magnetic substrates [80].

The study of these systems is performed in angle-resolved photoemission experiments for probing the filled states lying below the Fermi level or in inverse photoemission experiments for the study of empty states. The number and energy position of such states depends on the film thickness, increasing in density with the increment of the atomic layers, within a fixed energy range.

Thin film states owe a two-dimensional character, therefore being, in a limited photon energy range used, almost independent on the energy of the probing excitation source, therefore showing no dispersion in the perpendicular direction. Instead, the relative intensity of the quantized states depends on the photon energy used, a fact that is ascribed to matrix element effects.

The observation of quantum well-states, however, strongly depends on the preparation, therefore being limited to highly perfect heteroepitaxial systems. This implies that a layer-by-layer growth is required, allowing for a uniform thickness of the film on an atomically smooth substrate.

For a deeper analysis of the photoemission spectra, the knowledge of the electron wave function in the quantum well states is required. The wave function in a quantum well can be described as a rapidly oscillating carrier wave Bloch function derived from the closest edge of the discretized band (wave vector \mathbf{k}_{edge}), modulated by a slowly oscillating envelope function (wave vector \mathbf{k}_{env}) with total wave vector being:

$$\mathbf{k}_{tot}(E) = \mathbf{k}_{edge} \pm \mathbf{k}_{env} . \quad (2.19)$$

In the case of bulk-like potential in the film, the total wave vector follows the bulk band dispersion, being $\mathbf{k}_{tot} = \mathbf{k}(E)$. This means that at fixed energy, \mathbf{k}_{env} is given by the bulk bands since \mathbf{k}_{edge} is known. This model allows one to relate the Bloch oscillations to the inner structure of the thin film, whereas the envelope function is determined by the properties of the quantum well (total thickness and boundary conditions). The quantization rule determining the spectrum of discrete states inside a quantum well is therefore applied only to the envelope function. This rule can be obtained with a total phase shift accumulated by the wave in a round trip within the confined region of film thickness d :

$$\psi_V(E) + \psi_S(E) + 2k_{\perp}(E)d = 2\pi n , \quad (2.20)$$

with n the n -th quantum well state, $\psi_V(E)$ and $\psi_S(E)$ the phase jumps at film/vacuum and film/substrate interfaces, respectively. The values of the phase jumps can be evaluated by the following equations:

$$\psi_V = \pi \left(\sqrt{\frac{3.4\text{eV}}{E_V - E}} - 1 \right) , \quad (2.21)$$

$$\psi_S = 2 \arcsin \sqrt{\frac{E - E_{\text{low}}}{E_{\text{up}} - E_{\text{low}}}} - \pi, \quad (2.22)$$

where E_V is the energy of the vacuum level, E_{up} and E_{low} the upper and lower energies, respectively, of the substrate band gap where the quantum well states can be found.

The observation of quantum well states has been reported for various combinations of noble metal and transition metal heterostacks. The validity of the envelope model mentioned above has been demonstrated in the coupling of Ag quantum well states through a gold spacer [81].

However, the most intriguing properties of the quantized states in thin films are manifested in stacks of magnetic/non-magnetic solids. As discussed above, the physical quantities in the film depend on the thickness, in most of the cases, in an oscillatory manner. The oscillatory nature has been shown to enhance electric conductivity, Hall effect, superconductivity, and magnetic anisotropy [82, 83, 84, 85]. In the particular case of electric conductivity, the energy shift of the quantum well states across the Fermi level leads to an oscillating DOS.

2.2 Low energy electron diffraction - LEED

LEED is a surface sensitive technique committed to the determination of structural properties in a solid. Since low energy electrons are used in LEED (typically 50 - 500 eV) their wavelength corresponds to the atomic lengths of almost all the materials, therefore being sensitive to the atomic arrangement. Low-energy electrons are also characterized by a limited inelastic mean free path, therefore limiting the probing depth to the first subsurface layers. Consequently, the inspection of a LEED pattern provides the means to study the surface lattice symmetry, the lattice constant and the presence of contaminants. A schematic diagram of a LEED optics, along with an example of a LEED pattern is shown in Fig. 2.2.

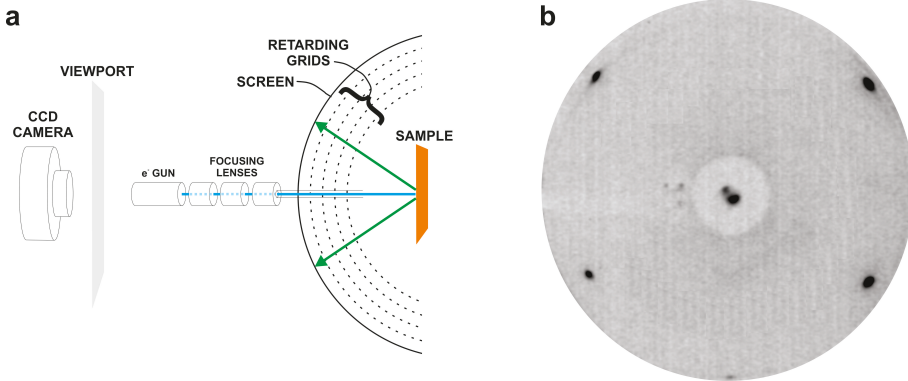


Figure 2.2: a) Scheme of a LEED apparatus b) Example of a LEED pattern of clean W(110) acquired at $E_{kin} = 55$ eV.

The electron gun generates an incident electron beam of selected energy. The electrons usually impinge on the sample at normal incidence and undergo elastic/inelastic scattering. Elastically back-scattered (diffracted) electrons pass through three hemispherical concentric grids

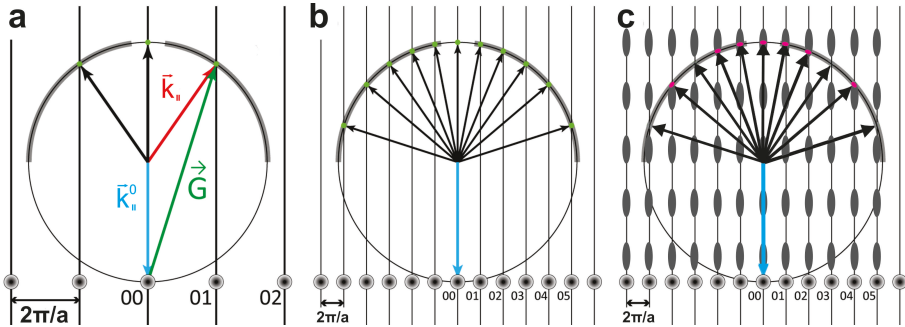


Figure 2.3: The Ewald sphere construction. The sphere has a radius k^0 , and due to the LEED geometry (electron beam with normal incidence) the incident wave vector k^0 lies parallel to the vertical 00 rod. The spots (rods) are numbered by their hk value, deriving from the geometry of the periodic lattice of the specimen. The points where the rods cross the sphere fulfill the Laue condition for the scattering. a) Spots are formed on the screen at these points of constructive interference. b) at higher kinetic energies, the Ewald sphere radius is larger, and therefore more rods cross the sphere, thus more LEED spots (green circles) are visible. c) Construction of the Ewald sphere for the elastic scattering of a realistic surface.

and afterwards are detected by a phosphor screen. The two grids close to the sample are grounded, therefore providing a field-free region. The third grid is held at a determined potential allowing for filtering out the inelastically scattered electrons.

From a LEED experiment, qualitative and quantitative information about sample surface can be extracted. The qualitative analysis is performed by visual inspection of the electron diffraction pattern, being able to provide information on the size and symmetry of the surface unit cell. Quantitative analysis instead involves the examination of intensity variations of the diffracted beams, usually through IV-curves (intensity *vs.* voltage), where the diffracted intensity is plotted as a function of the incident electron energy. Theoretical modeling of these curves, with a suitable electron scattering code, provides accurate information on atomic positions and relative stacking in the subsurface layers.

According to Bragg's elastic scattering theory, the presence of diffraction spots can be observed if the momentum of the system fulfills:

$$K_{\parallel} = k_{\parallel}^0 - k_{\parallel} = G_{\parallel}, \quad (2.23)$$

where K_{\parallel} is the difference between parallel component to the surface of incident scattering vector (k_{\parallel}) and scattered vector (k_{\parallel}^0). G_{\parallel} is the parallel component to the surface of the reciprocal vector \mathbf{G} . In Figure 2.3, the explanation of the LEED principle is shown. The Ewald sphere is the sphere having a radius equal to $|\mathbf{k}| = k^0$. Equation 2.23 is fulfilled for every point at which the sphere crosses a reciprocal lattice rod. For 2D systems, the restriction on k_{\perp} (third Laue law) can be relaxed; and therefore the diffraction condition is satisfied more frequently with respect to 3D systems. For a real surface, the bulk contribution cannot be neglected since primary electrons penetrate more than the first atomic layer, resulting in a modulation of the respective LEED pattern. A realistic model which takes into account the contribution from surface and bulk is presented in Fig. 2.3c. If a diffracted vector \mathbf{k} crosses a reciprocal lattice rod, the corresponding spot intensity will be weak, whereas if \mathbf{k} crosses a thicker region of the rods, the intensity of the

spot will be strong.

In order to relate the observed intensities in the LEED pattern, especially in the case of intensity *vs.* voltage curves, to the real crystalline structure of the surface, a suitable theory modeling the scattering (electron-matter) process should be used. The kinematic theory is suitable for the description of X-ray Diffraction, because of the weak interaction between the incident radiation and the scattering sites. In LEED multiple scattering occurs (as indicated above), therefore strongly modifying the diffraction intensity. Thus, an appropriate theory is required, namely the dynamical LEED theory. A full dynamical analysis is needed for a complete description of the spectrum structures. A complete description of the theoretical treatment of the scattering process can be found in Pendry and van Hove textbooks [86, 87].

2.3 LEEM-IV

The probe of the laterally resolved surface crystalline structure of a specimen can be performed using Low Energy Electron Microscopy (LEEM). By acquiring laterally resolved electron reflectivity curves (*i.e.* measure the backscattered electron current as a function of incident energy), combined with a suitable theory modeling the scattering process of the electrons with the surface atoms, the information about sample crystalline structure can be obtained. In practice, a series of images are acquired by step-wise changing the electron energy, corrected for the image drift induced by a possible misalignment of the sample and subsequently stacked into an image sequence. By selecting a region of interest, energy-dependent electron reflectivity can be extracted. This technique allows for determination of the local structure on the surface/subsurface, the identification of structures with different chemical environment as well as the determination of stacking differences (stacking faults).

LEEM-IV	Conventional LEED
Real time, <i>in situ</i> , direct imaging	Reciprocal space patterns
Reflectivity of only (00) beam	Many beams in diffraction patterns
Electron beam energy: 5 - 100 eV	Electron beam energy: 50 - 500 eV
Spatial resolution: 5 nm	Intensity averaged over several μm^2

Table 2.1: Major differences between LEEM-IV and conventional LEED techniques.

The main differences between LEEM-IV and the conventional LEED-IV technique are compared in Table 2.1. Despite the significant advantage of the LEEM-IV technique in its high lateral selectivity over the classic LEED technique, two main differences impose severe challenges to the dynamical analysis of the intensity: a relatively low electron kinetic energy in LEEM compared to LEED, and limited electron kinetic energy range in LEEM experiments. The electron kinetic energy in LEEM experiments (5 - 100 eV) is lower than that typically used in LEED IV (50 - 500 eV), complicating the quantitative analysis, because within about 50 eV of the vacuum level the mean-free path of electrons in solids is strongly energy-dependent. Consequently, in calculations of the electron reflectivity, the inelastic damping potential (*i.e.* the imaginary part of the inner potential V_{im}) cannot be assumed to be constant as in a conventional LEED-IV analysis.

2.3.1 A representative example: stacking faults in Ag films

As it will be shown in the following, LEEM-IV analysis of the surface can be employed in the study of structural determination of the surface. In particular, the possibility to correlate energy-dependent electron reflectivity to small changes in the stacking sequence during the growth of thin metallic films, where, depending on the material, stacking faults can be formed during growth.

The means for the characterization of stacking fault structures are scarce since the phenomenon is not easy to observe. Several studies were performed using transmission electron microscopy, being able to identify the stacking faults only at a post-growth stage. A real-time identification during the growth process implies the use of surface sensitive techniques using low energy electrons as a probe. However, stacking faults are usually formed by a martensitic process which preserves the reciprocal space symmetry of the system, therefore, leading to the formation of an identical low energy electron diffraction (LEED) pattern. LEEM-IV instead, capable of laterally resolving the electron reflectivity is a suitable technique for the identification of stacking differences, since it has been demonstrated that the electron reflectivity has a strong dependence on the electronic band structure of the material, due to the opening of band (Bragg) gaps at the edge of the Brillouin zone, therefore enhancing the reflectivity. However, especially for *fcc* crystals, it has been shown that the reflectivity curve in the region of Bragg gaps presents two distinct peaks, which is not only related to the band structure of the material, but also on geometrical configurations regarding the local arrangement of the atoms.

In order to study the capability of the LEEM-IV technique for the identification of stacking faults, an inert oxidized surface has been prepared. A clean W(110) has been exposed to oxygen pressure of $5 \cdot 10^{-7}$ mbar, while keeping the sample temperature at 1200 °C, until a self-terminated oxide surface is prepared, with a $(1 \times 1) \times 12$ reconstruction, as verified by μ -LEED [88]. Afterward, Ag has been deposited on top, allowing for the formation of silver nanodisks.

As visible from Fig. 2.4b, after the deposition of a certain amount of Ag on top of the oxidized tungsten surface, the formation of three-dimensional islands can be observed. The so-formed islands present different shapes with an arbitrary alignment of their edges towards the substrate. With increasing Ag deposition time, a 3D expansion of the islands occurs (Fig. 2.4b-f). By real-time LEEM imaging at fixed start voltage, it can be noted that the image contrast inside the island contours changes during deposition. The plot of the LEEM intensity during Ag deposition acquired on the two islands (as indicated by the two circles in Fig. 2.4d), plotted in Fig. 2.4g, shows that the contrast variation is discretized. As indicated by the capital letters on the right side of the plot, 4 main levels of intensity can be denoted, spanning from a maximum indicated by the A letter, to a minimum as indicated by the D letter, passing through two intermediate intensities B and C.

Regarding the behavior of the substrate, it can be noted from the LEEM image sequence in Fig. 2.4 that the image contrast outside the Ag nanodisks does not change. This is due to the large mobility of the deposited silver atoms/clusters on the oxidized tungsten surface, leading to the accumulation only at the Ag nanodisks. By integrating the overall area, we determined that only the $3.0 \pm 0.9\%$ of the surface is covered by silver nanodisks, leading to the accumulation of the material deposited on the overall surface area only at that small amount of surface area. Therefore, since the deposited material is not volatile, the time needed for the completion of a monolayer of Ag on the island surface is reduced by a factor 30, allowing for a 1 ML coverage in

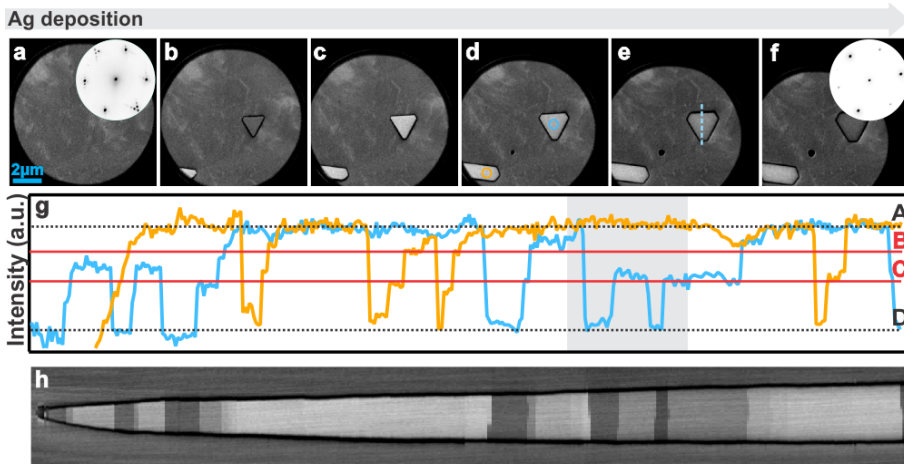


Figure 2.4: a-f) LEEM image ($V_{st} = 22$ V) sequence acquired during the deposition of Ag on O/W(110). Inset in a) represent μ -LEED pattern acquired on the oxidized surface (corresponding to a $(1 \times 1) \times 12$ reconstruction of the W(110) surface), while the one in f) represent the μ -LEED pattern acquired on the island as indicated by the blue circle in d). g) LEEM intensity vs. time during the deposition of silver, acquired on the two islands, as indicated in d). The presence of discrete levels of intensity can be noted, ascribed to different stacking of the top surface layers of Ag islands. h) LEEM profile extracted along the line in e), representing the stacking "history" of the deposited Ag layers.

only 20 seconds.

The evidence of a layer-by-layer growth can be observed in the selected LEEM image sequence as depicted in Fig. 2.5, extracted from the restricted region indicated by the gray rectangle in Fig. 2.4. As visible from the comparison of the first two frames in Fig. 2.5, the formation of a structure with different contrast, covering partially the triangular Ag island, can be noted (Fig. 2.5b). After the completion of the structure of different contrast (Fig. 2.5c), covering the whole surface of the island, the contrast changes again in the same way, i.e. by partially covering the island surface.

The origin of different image contrast on the Ag islands during deposition derives from the relative difference in electron reflectivity. As visible from the LEEM image in Fig. 2.6a acquired after growth, the two islands present different contrast. This difference derives from the variation of electron reflectivity of the two structures, as visible from the LEEM-IV curves in Fig. 2.6b.

In order to correlate the observed behavior in LEEM, IV reflectivity simulations were performed by our collaborators from the University in Cottbus. The AQuLEED package [89], based on existing Barbieri/Van Hove packages [90], which include the phase shift calculation package and the symmetrized automated tensor LEED (SATLEED) package was employed. The layer doubling extension by Materer [91] is also employed.

The comparison between LEEM-IV experimental data and simulations is presented in Fig. 2.7. The quadratic island, having a reflectivity curve characterized by two well distinct peaks in the region between 10 and 30 V, is plotted together with the simulated IV curve obtained from an Ag *fcc* stacked slab (Fig. 2.7a). The agreement between the experimental and simulated curves is quite good regarding peak positions. It can be noted that, except for the relative intensities, all the peaks observed in the experiment are well-reproduced in the simulations. The lower intensity at higher electron energies can be attributed to the energy-dependent electron transmission in the

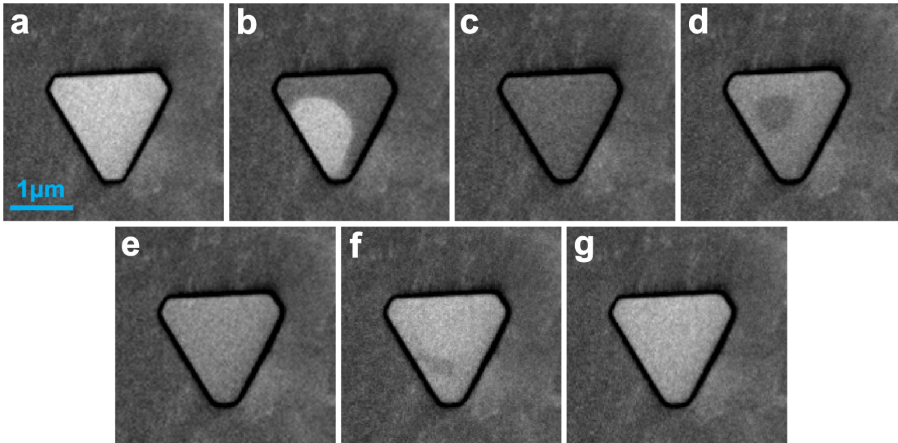


Figure 2.5: a-g) LEEM image sequence of ($V_{st} = 15$ V) of a zoomed area of Fig. 2.4, representing an Ag island growth, during a period as indicated by the gray rectangle in Fig. 2.4g. It can be observed that the growth occurs layer-by-layer, as the formation of a new contrast layer takes place after the completion of the one underneath.

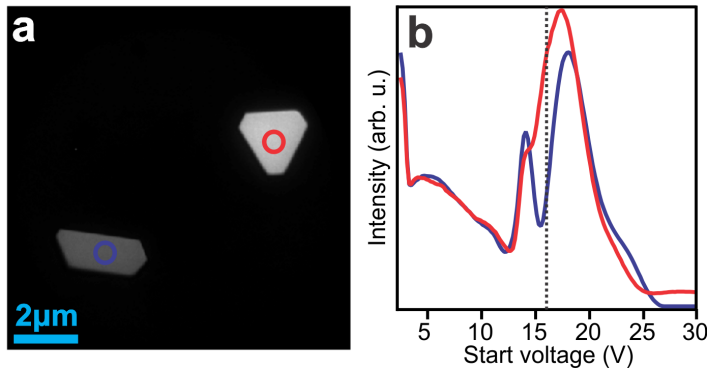


Figure 2.6: a) LEEM image ($V_{st} = 18$ V) acquired after growth of the two islands in Fig. 2.4, showing a different contrast. b) LEEM-IV curves acquired on the two islands after growth, where a clear difference in reflectivity in the two cases can be observed.

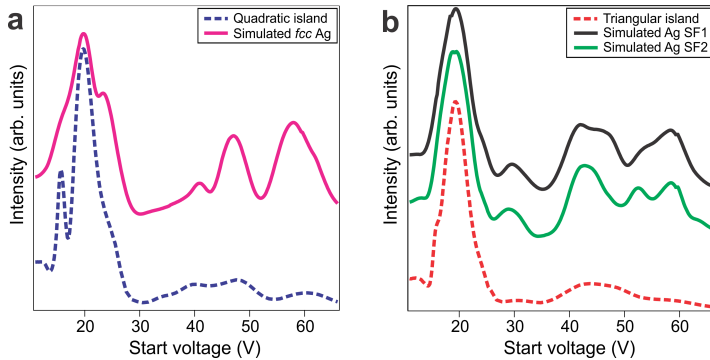


Figure 2.7: a) Comparison of experimental (bottom) and simulated IV curve (*fcc* stacking) for the quadratic island. b) Comparison of experimental (bottom) and simulated IV curves (two stacking fault configurations) for the triangular island.

LEEM microscope, therefore being different from the simulated intensities. The triangular island instead, is characterized by a single peak in the 10 - 30 V region with an additional double peak forming a saddle in the region between 40 and 50 V. In order to reveal the stacking of this island, two different configurations were considered. In the first (SF1), on top of a bulk *fcc* Ag crystal, a layer of *hcp* stacked Ag has been considered. In the second (SF2) instead, on top of a bulk *hcp* Ag crystal, a layer of *fcc* stacked Ag has been considered. By comparing the experimental curve with the simulations (Fig. 2.7b) for the two stacking fault configurations (SF1 and SF2), it can be revealed that the SF1 configurations reproduce better the experimental data. Despite the fact that in the 10 - 30 V region, no differences can be noted, the comparison in the 40 - 50 V region allows to identify the stacking of the Ag triangular island.

Therefore, the shape of the reflectivity curve in the low energy region 10 - 60 V, along with a dedicated theoretical model for the multiple scattering occurring in the surface layers, allows to discriminate the stacking sequence of the surface layers. This result is even more significant considering that an *hcp* and a *fcc* stacked layers differs only by a planar translation ($1/3$ of the lattice constant), therefore maintaining the in-plane symmetry of the system.

The validity of the approach is demonstrated also when considering different *fcc* stacked materials. As visible from Fig. 2.8, the shape of the reflectivity curve in the low-energy region is similar also for the considered *fcc*(111) materials: Co, Ni bulk crystals and in Ag films deposited on top of a Pt(997) crystal. Therefore, this rule of thumb regarding the single or double peak shape of the Bragg peak can be used for discriminating the stacking of the layers between *hcp* and *fcc* arrangements.

This representative example demonstrates that the LEEM-IV technique can be successfully employed for the real-time stacking characterization during the growth of layered structures as well as for post-characterization of spatially separated grains with varying stacking, as it will be shown in Chapter 4.

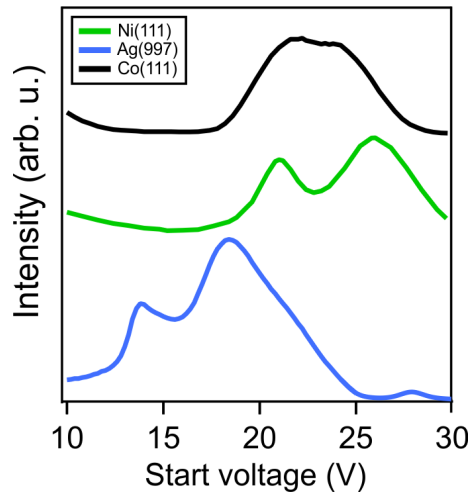


Figure 2.8: LEEM-IV curves of different *fcc* stacked materials: Co(111), Ni(111) and Ag films grown on top of a stepped Pt(997) single crystal.

Chapter 3

Instrumentation and setup

3.1 NanoESCA PEEM at Elettra

Photoemission electron microscopy (PEEM) is a surface sensitive imaging technique that uses local variations in electron emission for the generation of image contrast. The detection of emitted electrons upon excitation allows for a comprehensive characterization of the investigated sample. PEEM is a full-field imaging technique, able to collect the photoemitted electrons from selected microscopic areas of the sample. After the emission, electrons are accelerated by a strong electric field through the first lens, the objective, where a magnified image of the specimen is produced. The presence of a strong electric field at this point is crucial since the imaging resolution of the microscope is inversely proportional to the applied high voltage [92].

The excitation in PEEM is usually obtained by UV or X-ray sources (usually synchrotron radiation) with a variable energy range. This allows one to image surfaces and study interfaces and thin films with high sensitivity to their chemical and magnetic state, as well as their electronic structure. However, a severe limitation of this technique is the need for ultra-high vacuum (UHV) in order to optimize its operation, since the mean free path of the electrons exponentially depend of the local pressure between the specimen and the microscope.

Most of the measurements of this thesis were performed using the electrostatic energy-filtered PEEM at the NanoESCA beamline situated at the Elettra synchrotron in Trieste [94]. This endstation is equipped with a modified instrument based on the Focus NanoESCA concept, which is capable of performing measurements with a good energy resolution (better than 70 meV) along with a suitable spatial resolution (better than 150 μm). In particular, the microscope is composed of an optical column collecting the photoemitted electrons from the sample, which are afterward energy filtered in the double-hemispherical configuration (IDEA) and finally projected onto a 2D detector through an imaging optical column (Fig. 3.1).

The objective is the first lens which is placed in front of the sample along its normal direction, which magnifies a portion of the sample surface. In order to extract the electrons from the sample, a strong voltage is applied to the objective lens, whose magnitude affects the overall spatial resolution of the microscope. The extracted electrons are then projected into the optical column where the first intermediate image is created at the position of the iris aperture. The iris is an adjustable aperture, which allows for the selection of a determined portion of the surface area from which the photoelectrons are collected. In their further trajectories, the photoelectrons

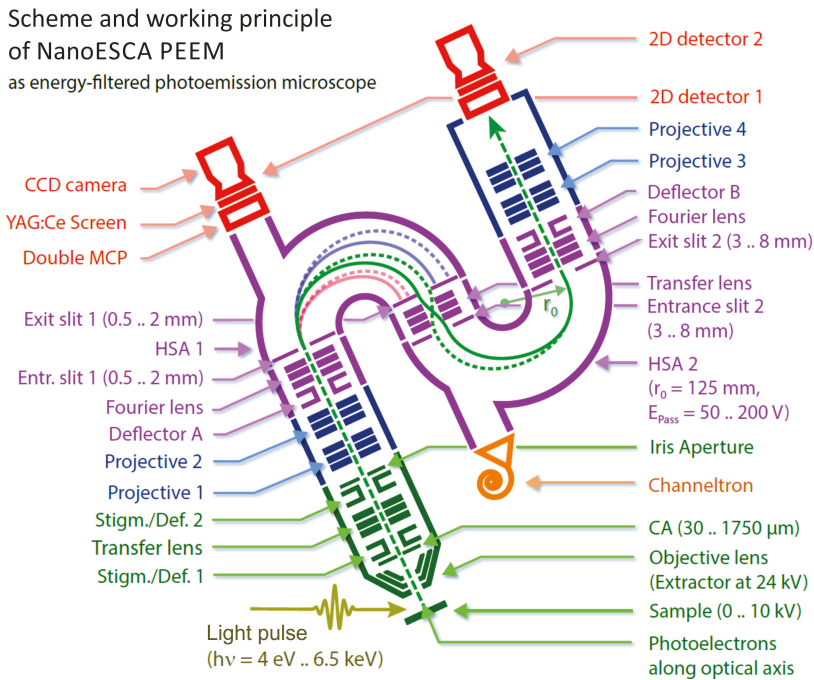


Figure 3.1: Scheme of the NanoESCA photoemission microscope. The photoemitted electrons travel through four main instrument parts: objective, first projection column, energy-filter and second projection column, until they reach the imaging detector. Two extra measurement modes are available: PEEM mode, where electrons are projected onto a 2D detector without the energy-filter. In the latter mode, photoemitted electrons are filtered only by the first HSA and collected in a channeltron, losing the spatial information. Adapted from [93].

are projected on the back-focal plane of the microscope, where the angular distribution of the photoelectron can be limited by a contrast aperture of varying size. This aperture allows for the selection of a limited angular spread of the photoelectrons centered around the optical axis, increasing the spatial resolution of the microscope, with a lowered transmission and therefore lower signal at the detector. A different combination of the voltages applied to the electrostatic lenses allows for the projection of either the momentum distribution of the photoelectrons or its real space counterpart on the entrance of the energy analyzer (decelerating them to the pass-energy used), therefore allowing for two different imaging modes of the microscope:

- **Real space mode:** by projecting the angular distribution of the photoelectrons to the entrance of the energy filter, the information about the spatial resolution is preserved after the energy filter. Depending on the excitation source used, work-function and chemical mapping with lateral resolution can be performed.
- **Reciprocal space mode:** the projection of the real space image onto the entrance of the energy filter allows for the preservation of the angular distribution of the emitted photoelectrons after the energy filter. This operation mode allows one to access the electronic structure of solids.

Real space operation

Depending on the excitation source used, the NanoESCA microscope is capable of obtaining laterally resolved information from the sample in exam. Once the sample is excited either by UV radiation or X-ray source, the energy spectrum of photoelectrons in a laterally-resolved manner can be measured. Since photoemission is a quantitative technique, with the intensity depending on the number of surface emitters, PEEM provides a quantitative estimate of the local coverage of a certain adsorbate. In addition to the intensity, binding energy or core electrons might undergo a shift due to different chemical environments causing contrast variations and, therefore, permitting the identification of chemically non-equivalent atoms of a given species.

X-ray imaging: In this mode, the excitation source (which is detailed in the following section) is focused, therefore being able to probe a limited specimen area.

In XPS, the photon energy is fixed and the photoelectron energy is measured through an energy analyzer. In the experiment, the binding energy (E_B) of the photoemitted electrons is derived from equation $E_K = h\nu - E_B - \Phi$, where E_K is unknown and is replaced by a bias voltage applied to the sample, and Φ is the work function difference between sample and analyzer. By calibrating the kinetic energies, using the Fermi level as a reference, it is possible to determine the electron binding energies accurately. By acquiring images at different sample bias values, it is possible to measure the energy spectrum of photoelectrons in a laterally-resolved manner.

The specificity of binding energies in XPS concerning the selected element or its chemical environment allows one to characterize the chemical composition of surfaces extensively. By setting the energy of the band-pass filter it is possible to select electrons with well-defined binding energy, constructing a PEEM image carrying the information about the lateral distribution of the corresponding emitters, with the intensity being proportional to the abundance of a particular element on the surface.

In XAS, instead, the intensity of secondary electron emission yield (usually at E_{kin} less than 5 eV) is measured as a function of the photon energy. The energy resolution is limited by the x-ray

monochromator, and no energy analyzer is required. Moreover, the large electron inelastic mean free path at low kinetic energies allows us to probe buried layers and interfaces down to a depth of more than 5 nm. Moreover, the use of circularly polarized light allows us also to laterally probe the magnetic state of the surface by means of XMCD measurements.

UV-source imaging: The NanoESCA microscope is equipped with a high-pressure lamp, in which an electric arc through vaporized mercury is used to produce light. The beam spot is large with a non-monochromatic spectral distribution. The mercury lamp has a maximum energy of $h\nu \approx 5.4$ eV, therefore leading to the emission of secondary electrons, which carries the information about the surface work function. Thanks to the beam spot broadness, it is possible to laterally map the surface work function differences of the sample, which can be then referenced to a known value.

Reciprocal space operation

As stated above, the NanoESCA microscope permits one to angularly and energetically resolve the photoemitted electrons. This allows for the determination of the electronic structure of the sample. In the NanoESCA, at fixed photon energy, the in-plane momentum of the photoemitted electrons can be measured in one-shot, making it different from a classical ARPES setup, where the measurement is performed by scanning the azimuthal and polar angles. The wide angular acceptance of the objective lens, at an extractor voltage of 12 kV, allows probing the entire Brillouin zone of most materials, *i.e.* $\pm 2 \text{ \AA}^{-1}$. By varying the kinetic energy of the photoemitted electrons, the acquisition of 2D momentum map series is possible. Accordingly, the band dispersion along high-symmetry directions can be determined by extracting intensity profiles within such image stacks.

Spin-resolved imaging

Since in a photoemission experiment the electrons are the information carriers, the filtering of the electrons depending on their spin helps to draw a complete picture of the electronic related phenomena in a sample.

The spin resolved imaging presented in this thesis has been performed using a LEED type spin detector. In this type of spin-filter, the spin-dependent specular electron reflectivity of a high Z single crystal with large spin-orbit coupling is exploited for obtaining images with spin information. In our setup, a W(100) single crystal is used, with the [001] direction aligned to the scattering plane of the NanoESCA microscope. The crystal is inserted in the electron optical path immediately after the second HSA (see Figure 3.2), where electrons entering the spin optics are decelerated from the pass energy to lower scattering energies [15, 50] eV before impinging the W target. The incident angle of the electron beam on the target is 45° , with the spin quantization axis (P) normal to the scattering plane. The image information (either in real or reciprocal space) is preserved upon the 90° specular reflection and projected onto a dedicated 2D detector. The reflectivity at such a crystal has been estimated to be 0.012, therefore reducing the signal in a spin resolved image by a factor 80 with respect to a spin-integrated image.

Since W(100) is used as a scattering target for the photoemission signal, the reflectivity curve is a crucial parameter to judge the quality of the spin-resolved experiments. As determined in the paper by Tusche *et al.*, two scattering energies (26.5 and 30.5 eV) are the points where the electron

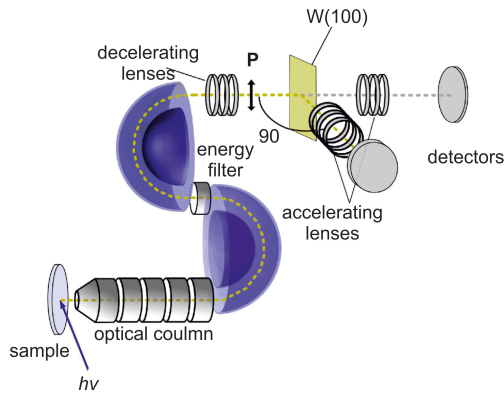


Figure 3.2: Experimental setup of the imaging spin filter installed at the energy filtered PEEM, consisting of the sample illuminated by synchrotron light, the PEEM optics, and the imaging energy filter. Electrons are decelerated and accelerated by electrostatic lenses before and after scattering at the W(100) mirror. Images are collected at the detectors in straight and mirrored geometry. The quantization axis, P , is normal to the scattering plane. Adapted from [95].

reflectivity present local maxima with similar intensity. Interestingly, the highest asymmetry in spin dependent electron reflection are observed when comparing those two energies. Therefore, by acquiring two images at those two scattering energies of the sample, it is possible to discriminate the spin of the electrons either in a real space image (where magnetic domains are observed) or reciprocal space image (where spin-dependent electronic structure can be measured). In order to maximize the efficiency of spin detection, the features in exam should have their spin lying in plane and aligned with the optical axis of the microscope, since the spin filter is sensible only to the projection of the spin along that axis [95].

After obtaining two images at the two scattering energies a dedicated image processing procedure allows for obtaining the information about spin polarization [95], as in detail described in Appendix B.

3.2 Nanospectroscopy LEEM at Elettra

LEEM is a cathode lens microscopy technique suitable for the characterization of atomically flat surfaces and real-time observation of surface-related phenomena (e.g. surface reconstructions, epitaxial growth, step dynamics, self-organization, etc.), using low-energy elastically back-scattered electrons as information carriers. LEEM adds structure sensitivity to the capabilities of synchrotron-based PEEM, providing several complementary methods for surface characterization of the materials, especially with the employment of micro-probe acquisition methods.

A LEEM apparatus with superimposed the basic scheme is shown in Fig. 3.3. The electrons are emitted from an electron gun (LaB_6) and accelerated to an energy of 15-18 keV. The beam separator deflects the electron beam, which acquires afterwards a trajectory normal to the sample surface. The deceleration of the electron beam before reaching the sample surface allows for a low energy impact of the electrons with the surface/subsurface layers. After the interaction with the surface (at varying bias voltages of the sample), the electrons are back-scattered and then re-accelerated through the objective lens, following the same pathway in reverse. The objective lens produces a

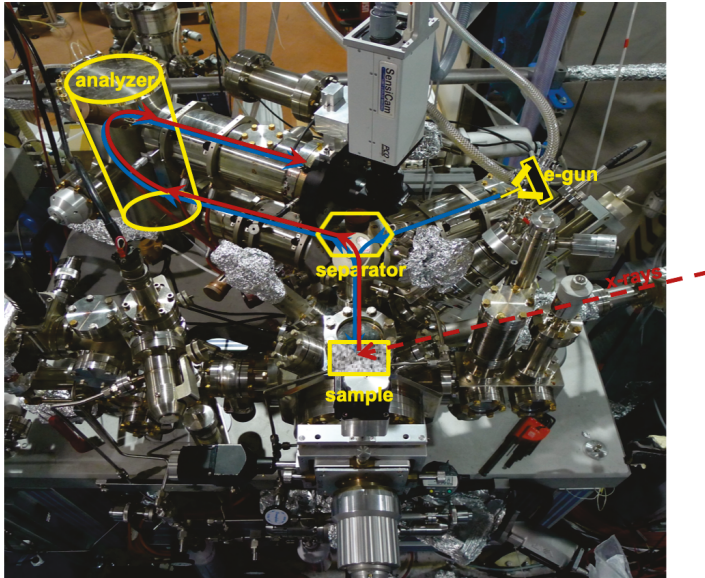


Figure 3.3: Nanospectroscopy SPELEEM with superimposed the schematic representation of the electron path in the microscope. Courtesy of T. O. Mentş.

magnified image of the sample at the beam separator, which is then magnified with a series of additional magnetic lenses, which are part of the imaging column of the microscope. After passing the last projective lens, the electron beam impinges the detector composed by a micro-channel plate/phosphor screen/CCD camera. By projecting the back-focal plane image, formed after the beam separator, the microscope can perform reciprocal space imaging, therefore acquire LEED patterns from limited portions of the sample surface.

Two different imaging contrast modes can be used for image acquisition in LEEM:

- **Diffraction contrast:** the back-scattered electron intensities and their energy dependence with the bias may vary considerably depending on differences in structure and crystal orientation, presence of an ordered adsorbate phase, etc. Therefore, the modulation of the back-scattering current (electron reflectivity) is frequently a unique fingerprint of a certain surface structure.
- **Bright- and dark-field imaging:** an aperture located in the back-focal plane (where a reciprocal space image is formed) can select a desired part of the back-scattered electron intensity. When the zero-order diffraction spot is selected, only the electrons with a normal trajectory can pass, allowing for the LEEM imaging of ordered surface structures (bright-field imaging). If a particular diffraction spot is selected with the aperture, only those electrons will contribute to the real space LEEM image, therefore allowing for the spatial identification of structures with distinct diffraction patterns (dark-field imaging).

A simple scheme of the operating principle of BF and DF imaging modes is shown in Figure 3.4.

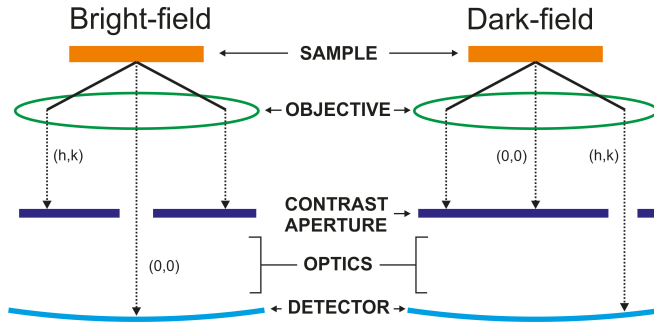


Figure 3.4: Simplified scheme of brightfield/darkfield operation mode.

The Nanospectroscopy beamline endstation is equipped with a spectroscopic photoemission and low energy electron microscope (SPELEEM), which with the aid of a toroidal electron energy analyzer, allows for both LEEM and PEEM imaging modes. The SPELEEM is a versatile instrument which allows for imaging (LEEM) and micro-probe diffraction (μ -LEED), if the sample is excited by an electron beam, and for microprobe-spectroscopy (μ -XPS), if photons are used. The regions of interest are selected using small apertures inserted in the optical column of the instrument.

In the SPELEEM, the electron kinetic energy is controlled by biasing the sample with a negative potential (commonly known as start voltage - V_{st}). The kinetic energy of scattered (or emitted) electrons is equal to $E_{kin} = V_{st} - \Delta W_{a-s}$, the latter being the difference in work function between the analyzer (a) and the sample (s).

By imaging the dispersive plane of the analyzer onto the 2D detector, it is possible to acquire wide (up to 8 eV) photoemission spectra within a single shot. In this operation mode, the microscope reaches its best energy resolution, which can be as low as ~ 110 meV.

The microscope is provided with apertures, to be inserted in the image plane located at the beam splitter, allowing for the reduction of the size of the electron/photon beam, favoring to illuminate very small surface regions for imaging/spectroscopy. Three illumination apertures with diameters of 0.5 mm, 1 mm and 5 mm are available.

Photon source

The NanoESCA and Nanospectroscopy beamlines are two branches of the same low energy and high flux photon beamline located at the Elettra synchrotron in Trieste (Italy). Two Sasaki type undulators with a period of 10 cm, phased by an electromagnetic modulator, are used for electron wiggling, being able to provide elliptically polarized radiation, as well as vertical and horizontal linear polarization. The beamline employs a high throughput monochromator based on the variable line spacing (VLS) grating scheme, optimized for the energy range between 40 to 1000 eV, and a spherical grating for energies between 20 and 40 eV. The use of a deflecting mirror located after the monochromator exit slit allows for the deflection of the photon beam at the selected branch. Each branch features a refocusing section with two bendable elliptical mirrors arranged in the Kirkpatrick-Baez configuration. They permit a strong demagnification of the source, achieving a micron-sized illumination spot at the microscope focus (around $20 \mu\text{m}$ wide), matching the typical working conditions. A scheme of the beamline is shown in Figure 3.5.

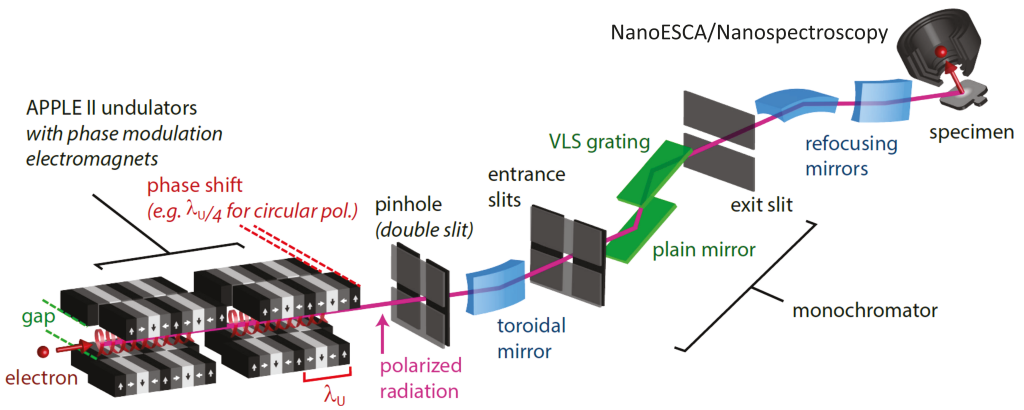


Figure 3.5: Scheme of the NanoESCA/Nanospectroscopy beamline at Elettra. The gap and the phase shift of the two undulator columns can be adjusted to generate photons with a specific energy and polarization (vertical linear, horizontal linear, left or right circular). Unwanted radiation is stopped by the pinhole and the transmitted beam is demagnified by a toroidal mirror before it enters the monochromator. The angle of the plain mirror and the grating can be adjusted to reflect a nearly monochromatic beam with the desired photon energy onto the exit slit. The width of the exit slit determines the final energy resolution. The refocusing mirrors finally produce a small beamspot on the specimen. Adapted from [96].

Chapter 4

Ferromagnetic films on W(110): morphological and electronic properties

As stated in the first chapter, the scope of the thesis was to render the graphene layer magnetic, by growing it on top of a ferromagnetic substrate exhibiting magnetic properties at room temperature. Therefore, before graphene growth we performed the optimization of the crystalline films of Fe, Ni, and Co and the study of their electronic structure in order to understand the substrate changes after graphene capping.

In order to study the electronic property of a material, the crystalline order is a crucial parameter which has to be optimized before measuring the band structure of the system. The crystalline quality is a parameter which depends on the temperature used in the preparation and on the effective volume of the specimen. This is especially true in the study of layered materials which are deposited on top of a support. First of all, a good crystallinity and cleanliness of the substrate allow for a good contact with the deposited material, which reduces the possibility of defect formation at the interface. Secondly, the temperature used both during the deposition of the material and/or during the post-growth treatment are crucial parameters, which have to be monitored in order to obtain a specimen with optimal quality. However, these treatments can induce structural transitions in the material, which can reflect in an orientation change of the surface layer or, a change in the stacking sequence of the surface and bulk layers.

The metal films have been deposited on top of the *bcc* W(110) surface, which provides a high melting point, allowing for a facilitated cleaning by flashing off deposited layers. The intermixing of the deposited material with W(110) occurs only at elevated temperatures, therefore during thermal treatments of the film, one should not exceed those temperatures. The surface energies of the ferromagnetic metals of interest here, Fe, Ni and Co are sufficiently lower than that of W therefore a quasi-Frank–van der Merwe growth is expected when depositing the metal films on the tungsten crystal kept at room temperature.

4.1 Fe/W(110)

Iron in its bulk form is characterized by a *bcc* arrangement of the atoms in the unit cell. When it is deposited on top of the W(110) crystal, however the difference of 9% in lattice constant with

respect to W ($a_{Fe} = 2.8665 \text{ \AA}$, $a_W = 3.1652 \text{ \AA}$), does not favor the epitaxy at the interface. Therefore, the formation of a two-layer meta-stable pseudomorphic (ps) film is observed. With growing film thickness ($\Theta > 10 \text{ ML}$), the tension at the interface is relaxed by a 2D modulation of the lattice (Fig. 4.1b). This modulation can be removed by thermal annealing of the film, allowing one to obtain a flat surface exposing the *bcc* (110) surface plane (Fig. 4.1c).

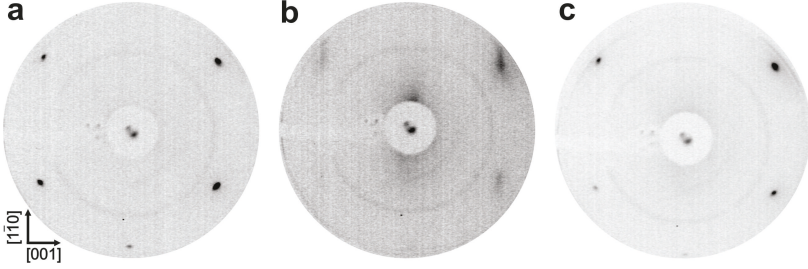


Figure 4.1: LEED patterns ($E_{kin} = 63 \text{ eV}$) during 40 ML Fe film growth: a) clean W(110) b) after Fe deposition c) after annealing to $400 \text{ }^\circ\text{C}$.

After optimizing the Fe film growth, our studies were focused on the electronic structure of iron films. Particular attention was dedicated on the mapping of the valence states in the region near the Fermi level. Upon graphene growth, the iron states (Fe 3*d*) present in the region near the Fermi level can hybridize with the graphene states (π), inducing an arbitrary spin polarization on the graphene bands. Consequently, to reveal the character of the bands in this region, we performed a spin-resolved mapping of the band structure, allowing us to unambiguously assign the character to the observed bands.

To do so, we deposited a thin iron film of about 15 ML (30 \AA), magnetized along the $[1\bar{1}0]$ direction of the tungsten substrate. For such a thickness the Curie temperature is well above room temperature. The easy magnetization axis lies along the $[1\bar{1}0]$ direction, instead of the $[100]$ in bulk iron. However, at a certain critical film thickness, reported in the range from 40 \AA to 140 \AA , a spin reorientation transition occurs, depending strongly on film preparation conditions [97, 98, 99]. Therefore, using a film of 30 \AA , we ensure that the magnetization lies in plane along the $[1\bar{1}0]$ direction, as demonstrated in the spin-resolved measurements.

The spin-integrated momentum map near the Fermi level is plotted in Fig. 4.2a and b, for two cuts containing different high-symmetry points of the lattice. The presence of a thin iron film on top of tungsten allows for the formation of the quantum well states. Its presence can be observed in the 2D momentum map in Fig. 4.2c as straight lines parallel to the ΓN direction. This appearance of the quantum well states, which are not isotropic in the k_{\parallel} plane, implies that along the ΓN direction the electrons behave like flat bands, as for the case of strongly correlated 4*f* and 5*f* compounds. By contrast, in the perpendicular direction ΓH , the quantum well states present a parabolic dispersion, with a nearly free-electron character of the quantized states.

The strong exchange coupling in Fe induces a splitting of the valence band states by about 2 eV, which at the same time hybridize due to the spin-orbit coupling. Therefore, spin-resolved mapping allows one to clearly assign the band character to the observed intensities in the surface momentum mapping in the region near the Fermi level. As visible in Fig. 4.2d and e, the character of the bands can be identified regarding its majority and minority spin character.

The agreement between the experimental spin-resolved maps with the DFT+GGA calculations (Fig.

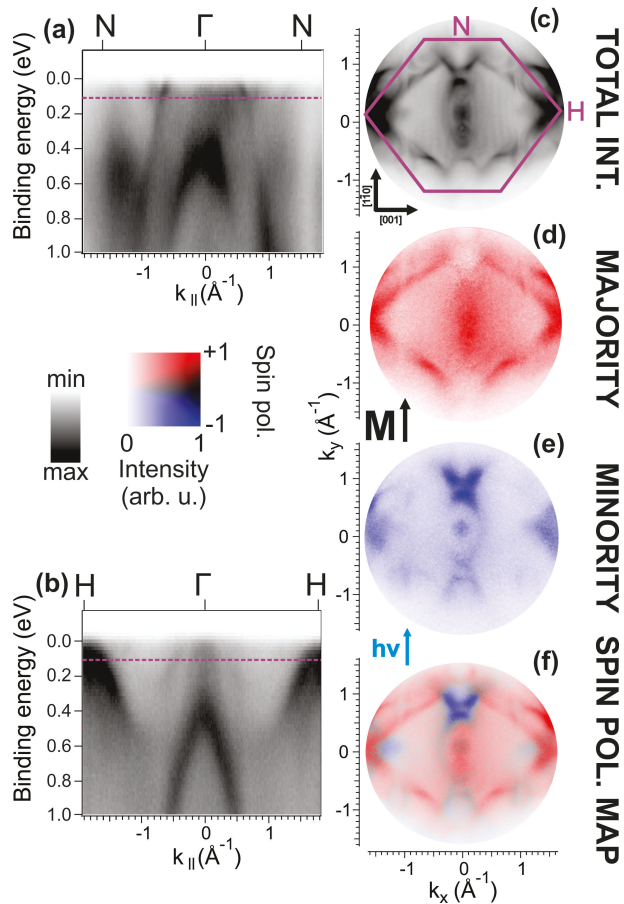


Figure 4.2: Energy *vs.* momentum map of a 15 ML Fe film taken along N Γ N (a) and H Γ H (b) directions. (c) Spin integrated 2D momentum map taken at 0.05 eV binding energy (dashed line in (a)). (d-e) Spin-resolved 2D momentum map of the image in (c). (f) 2D spin polarization map of the image in (c). The arrow below image in (c) indicates the magnetization direction of the sample before performing spin-resolved measurements, while the blue one indicates the direction of light incidence. $h\nu = 55$ eV, $T = -140$ °C.

4.3) performed by Schäfer *et al.* [100] is quite good. It can be noted that the quantum well states, visible as faint intensity in Fig. 4.2d, have exclusively a majority spin character. The character of the tubular states, connecting the N and H point of the BZ, is clearly spin-up, with +87% of measured spin polarization. In the center of the BZ, around the Γ point, a superposition of the bands with both spin characters can be observed. While in the majority spin channel the band presents an oval shape, elongated along the Γ N direction, in the minority channel a circular band emerges, centered at the Γ point. The bands forming a contour of the circular state at Γ present a minority spin character (with a measured value of -80% spin polarization) as well as the bands with a triangular shape originating at the H point of the BZ.

However, as it is shown in the Appendix C, the symmetry-mismatch between the substrate

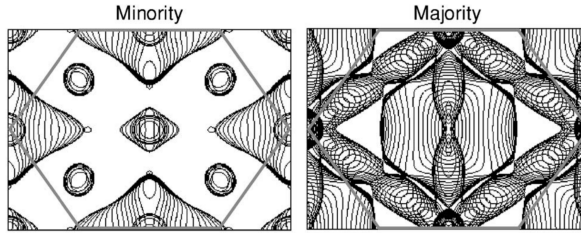


Figure 4.3: Calculated spin-resolved Fermi surface for Fe, projected on the [110] interface plane. Reprinted with permission from [100]. Copyright 2007 by the American Physical Society.

(rectangular) and graphene (hexagonal) does not allow to have a single-domain graphene lattice, therefore as it will be shown in the following, a substrate with better symmetry/lattice constant with respect to graphene is preferred.

4.2 Ni/W(110)

Nickel on top of W(110) grows in its bulk configuration, *i.e.* $fcc(111)$, therefore with a hexagonal symmetry and a lattice constant $a_{Ni} = 2.49 \text{ \AA}$, being very close to the graphene one. Thus, in the following, the optimization of the growth and the study of the electronic structure of nickel films grown on W(110) will be presented.

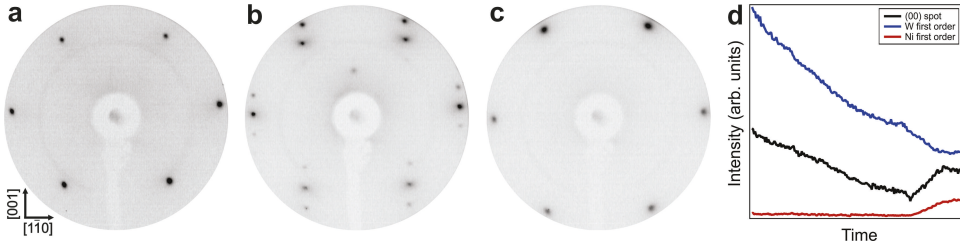


Figure 4.4: LEED patterns ($E_{kin} = 71 \text{ eV}$) during Ni film growth: a) clean W(110) b) after 1 ML Ni deposition c) after 8 ML. d) LEED intensity plot of the zero and first order spots during initial deposition stage.

The growth of Ni on W(110) starts with the formation of a single pseudomorphic layer. The completion of the ps layer is characterized by a local minimum in the intensity of the (00) spot in LEED. This ps layer is characterized by an eight-fold superstructure along the [001] direction of the W(110) substrate, as observed in LEED (Fig. 4.4b), with the appearance of additional spots along the [001] direction. The periodicity along the [1 $\bar{1}$ 0] direction is preserved, with no additional spots observed in the LEED pattern in this direction. The atomic density of the ps layer is lower with respect to the density of a layer in a bulk Ni crystal, therefore, in order to complete a full layer, further material has to be provided. Further deposition causes a raise in intensity of the (00) spot in LEED, until a local maximum is reached upon the completion of a full close packed layer. This oscillation in intensity of the reflected (00) spot is used for the calibration of the deposition rate, valid also in the case of other metals such as Co and Cu (Fig. 4.4d).

Upon further deposition, a layer-by-layer growth occurs, allowing for the formation of a uniform

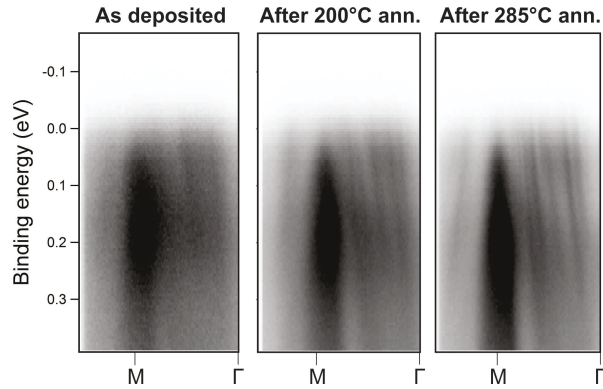


Figure 4.5: Dependence of the quality of the momentum maps (extracted along ΓM direction of the SBZ) upon annealing of a 9ML nickel film: as deposited (left), after annealing up to 200 °C (center) and after annealing up to 285 °C (right). $h\nu = 52.5$ eV.

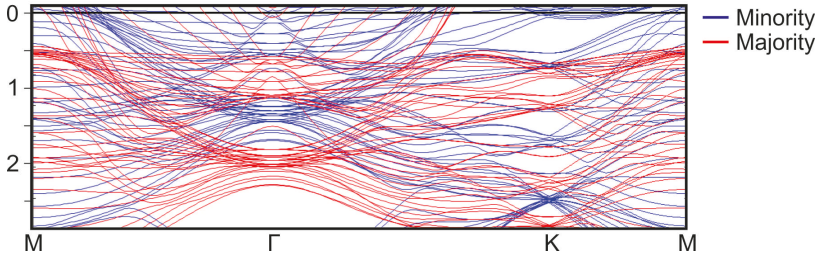


Figure 4.6: GGA calculations for a 10 ML nickel slab.

film in thickness. However, after deposition of the nickel film at room temperature, the momentum maps are not well-defined, as visible in the left part of Fig. 4.5. The crystallographic order and therefore the sharpness of the features in the region near the Fermi level improves by post-growth annealing. As visible in Fig. 4.5 center and right, the features in the valence band region become sharper upon reaching 285 °C, a temperature high enough to order the film and prevent the de-wetting (breaking apart). The effect of improved crystalline order reflects in a more pronounced way onto the quantum well states, which are visible as almost vertical lines between the Γ and M point. From a situation where they are barely visible (Fig. 4.5 left) they become sharp and more intense after the thermal treatment (Fig. 4.5 right).

The easy magnetization axis of thin nickel films deposited on top of clean W(110) is the [001] direction, as determined previously [101]. Therefore, before momentum mapping, the films have been magnetized along the easy axis. Considering the NanoESCA experimental geometry, using vertically polarized (p-pol) light, a magnetization of the sample parallel to the direction of the incoming light, leads to the formation of left-right asymmetries in the momentum maps, accordingly to the right-hand rule. The slope of the quantum well states is isotropic, with a behavior similar to free electrons, as observed along the ΓH direction in the iron films. The reduced exchange coupling with respect to iron reduces the energy splitting between majority and minority bands. As visible from Fig. 4.6, GGA calculations, which does not account for

spin-orbit effects, for a 10 ML nickel slab reveal that the split between the opposite spin bands is about 0.7 eV. This implies that an overlap of the majority and minority spin bands can be hypothetically present in the momentum maps (Fig. 4.7). This effect is clearly visible in the region near the Fermi level (around the Γ point), where the quantum well states with minority and majority character overlap. The spin-resolved momentum mapping allows for the determination of the spin character of the bands in the proximity of the Fermi level.

The measured values of spin polarization ranges up to +42% majority channel, which is found at the d states in Fig. 4.7j, while the minority channel yields a -40% of spin polarization, found at the states in Fig. 4.7i. These values are affected by the low value of spin-orbit coupling in this system, which leads to a mixing of the majority and minority bands, thereby reducing the measured spin polarization.

On the contrary to what is observed in the previous paragraph in the Fe films, the experimentally measured quantum wells does not display a single spin character. The same behavior is observed also in the d states near the Fermi level and in proximity of the K point of the BZ have majority and minority spin channels overlapped. Consequently it can be stated that with the present experimental resolution, a clear identification of the bands is impeded. The motivation standing behind the spin intermixing of the bands is that the separation between the majority and minority spin channel is much lower with respect to DFT predictions. By focusing the attention on the sharp and quite intense doublet of sp bands, which present an opposite spin character, the determination of the majority/minority splitting near the Fermi level is possible. This splitting is however energy- and band-dependent and therefore varies depending on the selected band. In Fig. 4.8a, the two sp bands crossing the Fermi level are marked. By fitting their position with respect the binding energy, their E vs. k dependence is determined (Fig. 4.8b). In that manner, a separation of 225 meV is found for those bands. This value is much lower from the one determined through DFT calculations (about 700 meV), difference which derives from the presence of strong electron correlation effects, leading to a reduced splitting between the two channels.

As stated in the beginning of the chapter, the goal of the thesis was to make graphene magnetic by using a suitable ferromagnetic substrate. Considering the behavior of nickel, the study of the electronic structure and therefore of the hybridization scheme between graphene and the substrate, would be very intricate. As a consequence, the choice of a ferromagnetic material with an enhanced exchange coupling, but maintaining a close match of the lattice constant, is highly desirable. Accordingly, our needs were met using cobalt as a substrate, as it will be explained in the following.

4.3 Co/W(110)

4.3.1 Co wedge (2-15 ML) and thin film regime

In cobalt, the different atomic density of the W(110) and of the close packed Co layer induces a compressive strain of 1.2% in the $[001]$ direction and a tensile strain of 3.1% along the $[1\bar{1}0]$ direction, with respect to a close packed ($hcp(0001)$) Co layer $[102]$.

By increasing the coverage on top of the initial layer, the strain is released at around 4 ML, resulting in a relaxed $hcp(0001)$ configuration. The orientation of the layers corresponds to the Nishiyama-Wassermann orientation of fcc crystals with the $[0001]Co||[1\bar{1}0]W$ and $[11\bar{2}0]Co||[001]W$

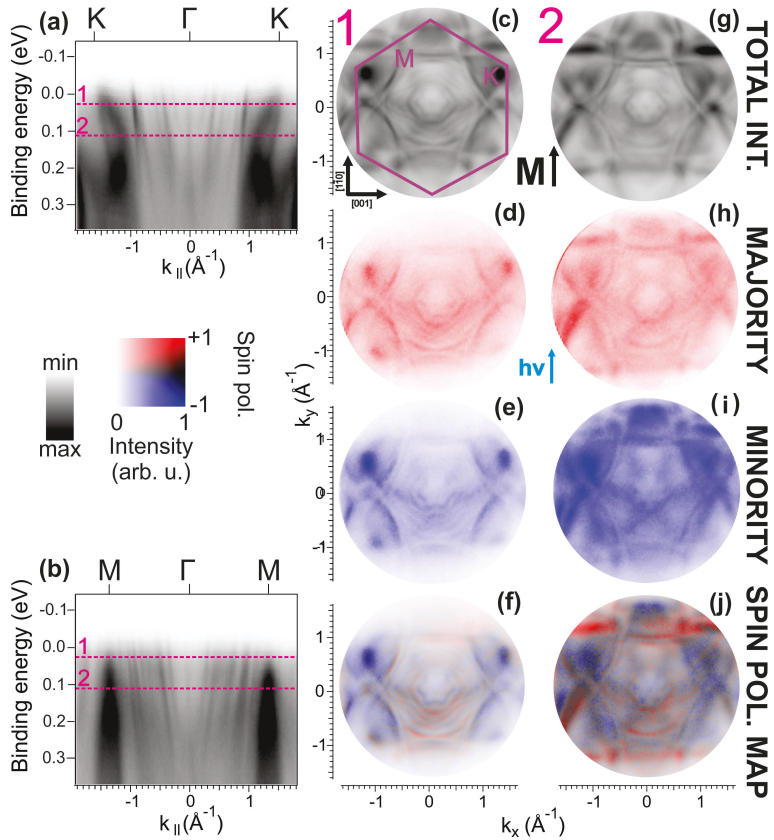


Figure 4.7: Energy vs. momentum map of a 9 ML Ni film taken along K Γ K (a) and M Γ M (b) directions. (c) Spin integrated 2D momentum map taken at 0.025 eV binding energy (dashed line 1 in (a) and (b)). (d-e) spin-resolved 2D momentum map of the image in (c). (f) 2D spin polarization map of the image in (c). (g) Spin integrated 2D momentum map taken at 0.11 eV binding energy (dashed line 2 in (a) and (b)). (h-i) spin-resolved 2D momentum map of the image in (f). (j) 2D spin polarization map of the image in (f). The arrow below image in (c) indicates the magnetization direction of the sample before performing spin-resolved measurements, while the blue one indicates the direction of light incidence. $h\nu = 52.5$ eV, $T = -140$ °C.

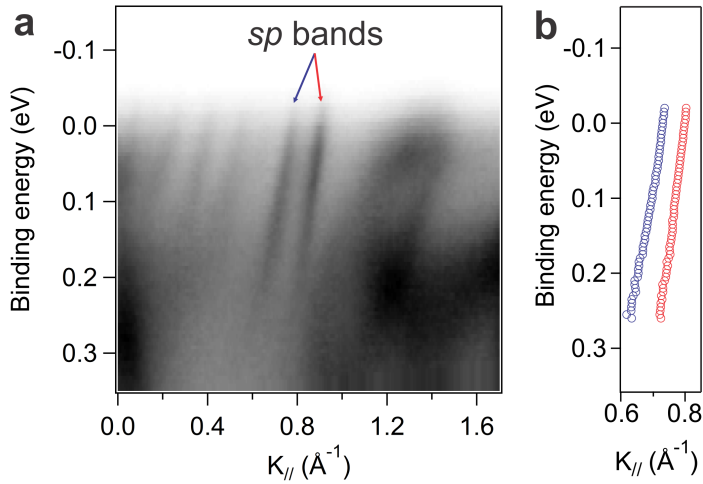


Figure 4.8: (a) Energy *vs.* momentum map of a 9 ML Ni film taken along ΓK direction. $h\nu = 52.5$ eV, s-polarization. (b) Fitted position of the *sp* bands marked in a). The color corresponds to the spin character.

orientation. The atoms in the second layer can occupy two different equivalent sites, leading to the twinning of the Co film. Therefore, the growth of Co proceeds in two different domains with a close packed regime.

The observed μ -LEED pattern upon growth of a thin Co film is often not sharp. The diffraction spots are blurred and, very often, a superstructure can be observed after growth. Since those films are very sensitive to the environment used during film growth, the presence of contaminants (such as O_2 , H_2O , etc.) leads both to a lower crystalline quality and to the formation of a surface structure on top. Therefore, a post-treatment of the film is needed before studying the properties of the grown film. After growth, the presence of a (2×2) superstructure in μ -LEED can be observed, deriving from a physisorbed oxygen phase on top, which, as it will be shown in the following, can be removed by thermal hydrogen treatments.

The further improvement of the crystallinity of the cobalt film can be achieved by annealing the film to higher temperatures. However, during this treatment particular attention has to be paid to the possible de-wetting (*i.e.* breaking apart) of the cobalt film. Moreover, in cobalt, particular care has to be applied since at elevated temperatures (about 420°C in bulk) the material undergoes a phase transition, and changes its stacking from *hcp* to *fcc*.

Accordingly, to study the stability of thin Co film upon annealing, a cobalt wedge has been prepared on top of the W(110) surface. In practice, following the surface changes using LEEM imaging, a complete close layer has been deposited at higher temperature (150°C), where the best epitaxy at the interface can be obtained. Afterwards, Co layers were deposited through a PMMA mask positioned close to the sample surface. The presence of a sharp edge in the mask allows for the formation of a wedge on the sample surface, with continuous variation of the thickness over a $30\ \mu\text{m}$ spatial range.

As it has been stated in the third chapter, low energy electron reflectivity allows characterizing the crystalline arrangement of the atoms in the subsurface layers, with very high spatial resolution.

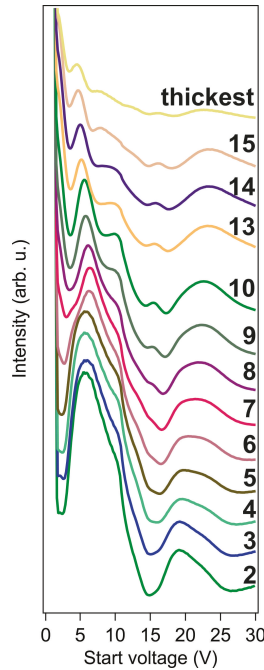


Figure 4.9: Dependence of the low energy electron reflectivity curves (LEEM-IV) on cobalt film thickness (wedge), measured after the RT deposition. The correspondent thickness is indicated on top of the curves on the right.

Therefore, we performed LEEM-IV measurements of the cobalt wedge and studied its evolution in temperature. In Fig. 4.9 the plot of the IV curves at different cobalt film thicknesses, acquired on the wedge, can be found. It is clear that the curves exhibit several peaks, with the number and position in energy being thickness-dependent. The peaks derive from the quantum confinement of the electrons in the potential well created by the thin film, leading to different phase shift (ϕ) of the reflected electron waves, depending on the film thickness (t) as:

$$\phi = \frac{2t}{\hbar} \sqrt{2m(E_{kin} + V_0)}, \quad (4.1)$$

with E_{kin} electron kinetic energy and V_0 the inner potential.

Therefore, by differentiating the reflectivity curves, the thickness of the film can be determined precisely, as visible in Fig. 4.10. The energy (Fig. 4.10a) is transformed into k_{\perp} vector (Fig. 4.10b) through the $E = (\hbar^2 k^2)/2m$.

Starting from thicknesses greater than about 3 ML, the formation of a characteristic peak can be observed at electron energies between 20 and 25 eV. This peak corresponds to the first Bragg peak in Co, in analogy to the case of similar *hcp* stacked materials, which present a broad single peak at similar electron energies [103]. The intensity of this peak, with respect to the background signal, is a measure of the crystalline quality of the film. In our case, it can be observed that in the as-grown sample, at thickness of about 15 ML, corresponding to the thickest layer in the Co wedge, the Bragg peak is less prominent, being consistent with the observed μ -LEED pattern, which was

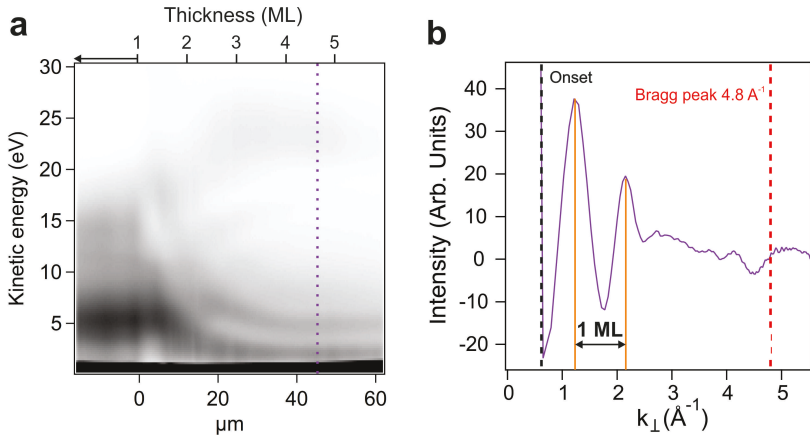


Figure 4.10: a) LEEM-IV map acquired along the cobalt wedge, showing the evolution of the low energy surface reflectivity depending on the film thickness. b) First derivative of the LEEM-IV curve acquired along the dashed line in a), showing the procedure used for the calibration of the film thickness. The Bragg peak and the onset of the curve are indicated, while the oscillations in between can be related to the thickness of the deposited film, in function of the reciprocal (perpendicular direction) wave vector.

characterized by blurred diffraction spots. Therefore, in order to improve the crystalline quality of the film, the sample has been subjected to annealing, while monitoring the changes in LEEM at fixed energy. Upon annealing, the intensity of the back-scattered electrons rises, indicating a better arrangement of the atoms, therefore being able to remove defects and improve the crystalline quality in the film. The cobalt wedge has been annealed up to 250 °C, after observing a plateau in the electron back-scattered signal.

After cooling down to room temperature the sample has been characterized by LEEM-IV, whose thickness dependent curves are plotted in Fig. 4.11. It can be observed immediately that the Bragg peak becomes more prominent, indicating a better crystalline order of the film. This is more evident in the thickest layer, where the quantum oscillations are no longer distinguishable, however a prominent Bragg peak can be observed. By careful inspection of the curve relative to the thickest film, it can be noted that at slightly lower electron energies with respect to the Bragg peak, an additional feature arises, the position of which in energy does not change with varying thickness. The presence of such a feature can be correlated to the presence of a different stacking of the material, using as a reference the reflectivity curve of Ag as discussed in the second chapter and the shape of the curves in other *fcc*(111) materials [104]. Therefore, we can suppose that the annealing of the surface leads to the *hcp-fcc* transition, which is known to occur in bulk Co at elevated temperatures. Since the appearance of this additional peak falls in the same energy range where the peaks related to the finite size of the slab occur, the contributions can easily overlap, leading to a wrong interpretation of the experimental data. Therefore, as it will be presented in the following, the phase transition is studied in thicker films, in which no oscillation in the low energy electron spectra are observed.

The temperature stability of the Co wedge has been tested by annealing the sample to temperatures above 250 °C. At around 320 °C, a dendritic change in the surface morphology is observed, starting in the films with lower thickness. This phenomenon can be ascribed to the

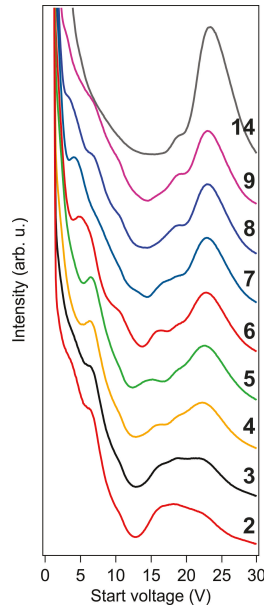


Figure 4.11: Dependence of the LEEM-IV curves on cobalt film thickness (wedge), measured after annealing to 250 °C. The correspondent thickness is indicated on top of the curves on the right.

intermixing between the Co film and the underlying W(110) crystal, a non-reversible process that creates a Co/W alloy. At the final annealing temperature of 460 °C, the alloying proceeds up to a thickness of about 12 ML, guaranteeing the film integrity of thicker films, but with no information about the surface chemical composition, which can undergo to a intermixing/alloying at the interface. LEEM-IV measurements performed at high temperature show that on the thickest part of the film, which remained intact after the annealing, the Bragg peak changed its shape, becoming splitted. The μ -LEED pattern acquired on the same region shows a threefold symmetry, indication either of an atomic flattening of the sample (leading to the formation of *hcp* terraces having a threefold symmetry) or a phase transition in the film, showing therefore an *fcc*(111) surface phase. After lowering the temperature, we observed a change in image contrast on the thicker region, accompanied by a change also in the IV curve, becoming similar to the curve observed after a 250 °C treatment. This behavior suggests that the observed changes on the surface can be ascribed to the phase transition occurring in cobalt.

The investigation of the electronic structure of the cobalt wedge has been performed as follows. First of all, two cobalt monolayers have been deposited on top of a clean W(110) surface and successively annealed up to 200 °C. The so-prepared sample has been measured in the NanoESCA chamber, using photoelectron spectroscopy ($h\nu = 90$ eV) at the W $4f_{7/2}$ core level (to calibrate the thickness and verify the integrity of the film) and momentum resolved photoemission spectroscopy (using p-polarized light of $h\nu = 56$ eV and scanning through the first Brillouin zone). The preparation procedure applied to the thickness of two monolayers was repeated in successive phases, where at each stage two additional layers were deposited, annealed at temperatures dependent on the thickness (Fig. 4.12a) and afterward photoemission measurements were carried

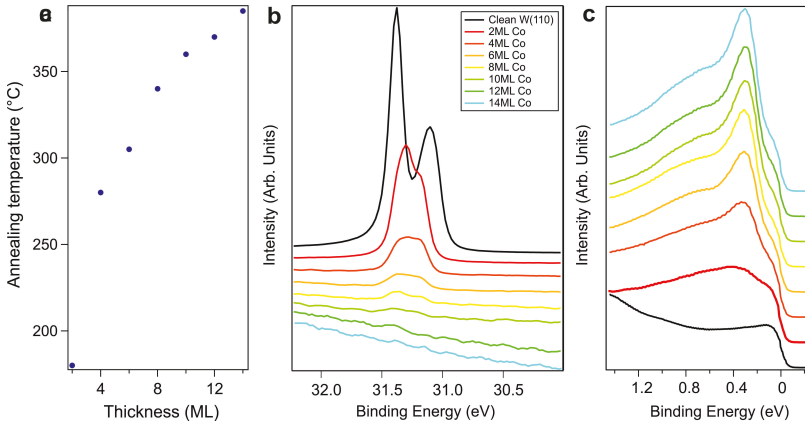


Figure 4.12: a) Annealing temperature of the cobalt film with varying thickness during preparation, before the measurement of the electronic structure. b) W $4f_{7/2}$ photoemission spectra acquired during the preparation of cobalt films with varying thickness, as specified in the inset legend. The spectra were acquired using $h\nu = 90$ eV photon energy. c) VB spectra of cobalt films with varying thickness, acquired with $h\nu = 56$ eV p-polarized photons. The color code corresponds to the spectra in b).

out as mentioned before.

In Fig. 4.12b the W $4f_{7/2}$ core level spectrum is plotted for increasing cobalt film thickness, together with the reference spectra acquired on the clean substrate. The clean spectrum is characterized by a peak at 31.4 eV binding energy, assigned to the emission of electrons in the bulk, while the one at 0.28 eV lower binding energy, is ascribed to the emission of electrons from the topmost surface layer. After the deposition of 2 cobalt monolayers the bulk tungsten peak, as expected, does not exhibit any shift in position, but only a decrease in intensity due to the screening induced by the presence of cobalt on top. Instead, the appearance of a new peak centered at 31.33 eV is observed, which we tentatively assign to the emission from tungsten atoms in contact with the atoms in the first cobalt layer (interface feature).

The momentum maps acquired along KTK direction are plotted in Fig. 4.13, in the binding energy window from -0.2 to 0.7 eV. As observed above, the quantum confinement of the electrons in the thin film regime leads to the formation of the quantum well states. Starting from the 4 ML thick layer (Fig. 4.13c), the appearance of the quantum well bands is observed, whose number rises with the thickness of the deposited cobalt film (Fig. 4.13b-h).

The evolution of the system is even better appreciated in the 2D momentum maps acquired at 150 meV from the Fermi level, as depicted in Fig. 4.14, together with the image acquired at the same energy on the clean W(110). In the 2D momentum map acquired at a sample thickness of 2 ML (Fig. 4.14b), we observe the coexistence of the features deriving from the clean W(110) (Fig. 4.14a) and the appearance of additional features from the cobalt layer. The features appearing after the deposition of cobalt have both hexagonal and rectangular symmetry. The hexagonal symmetry derives from the close packed arrangement of the cobalt atoms in the unit cell, while the rectangular one resemble the symmetry of the *bcc*(110) lattice of tungsten. The latter can be assigned to the formation of an interface state which can be ascribed to the symmetry mismatch between the Co and W unit cells. This state is observed up to a thickness of 8 ML, meaning that the strain induced at the interface is released only after such amount of cobalt monolayers. The

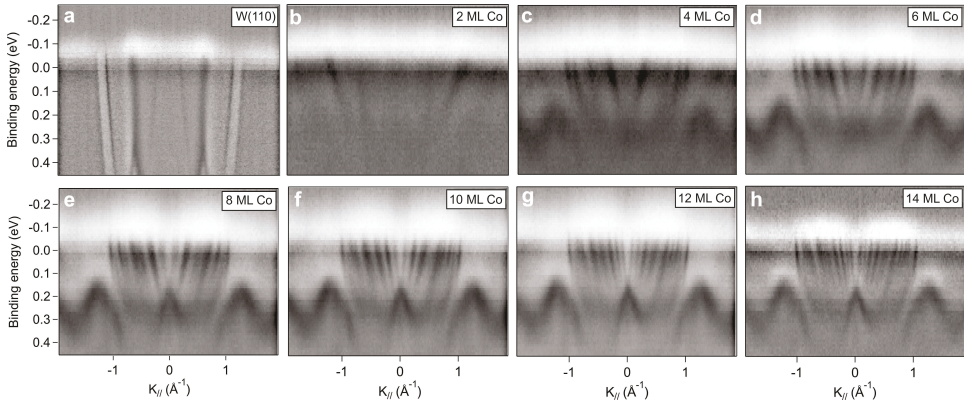


Figure 4.13: Momentum maps acquired along $K\Gamma K$ direction of clean $W(110)$ single crystal and of cobalt films of various thickness (as indicated in the image) deposited on $W(110)$. All the maps were acquired using 56 eV p-polarized photons.

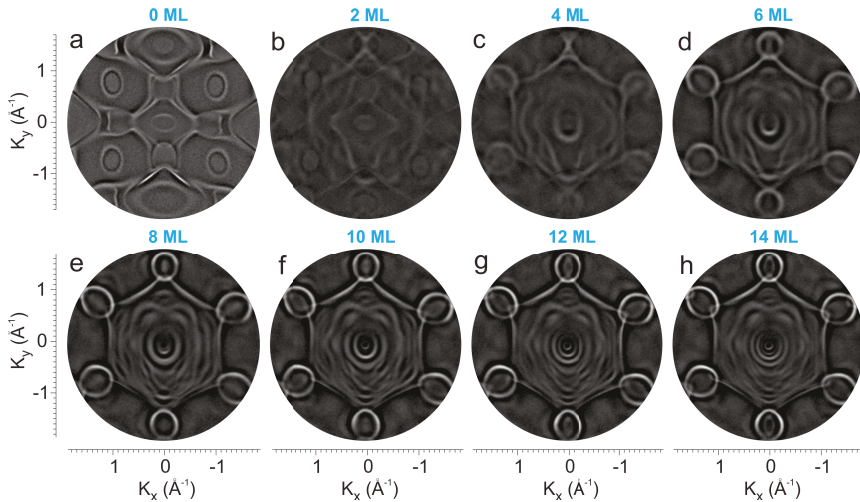


Figure 4.14: Constant binding energy maps of a) Clean $W(110)$ b) $Co(2\text{ ML})/W(110)$ c) $Co(4\text{ ML})$ d) $Co(6\text{ ML})$ e) $Co(8\text{ ML})$ f) $Co(10\text{ ML})$ g) $Co(12\text{ ML})$ h) $Co(14\text{ ML})$. All the images were acquired using $h\nu = 56\text{ eV}$, p-polarization, at 150 meV binding energy.

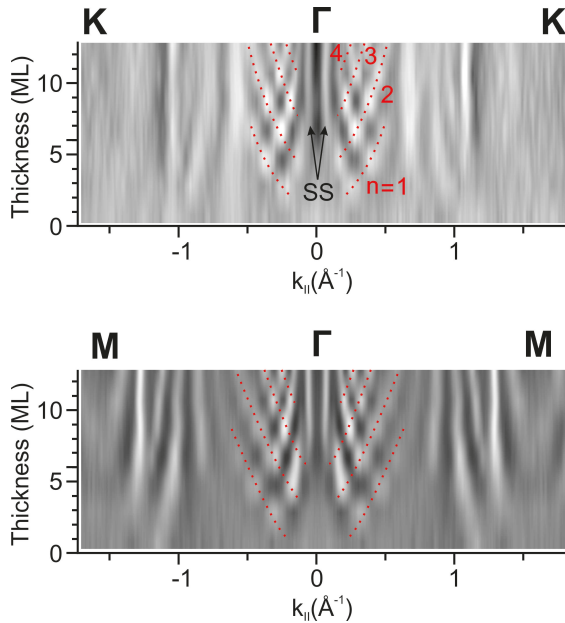


Figure 4.15: Momentum maps KTK and MFM acquired at different cobalt film thicknesses (at 150 meV below the Fermi level) and interpolated along the y axis. $h\nu = 56$ eV.

deposition of further amount of material results in the disappearance of features with rectangular symmetry. The appearance of a surface state, visible as a ring with smallest radius around the Γ point, is also observed starting from a thickness of 8 ML, meaning that the annealing temperature used in that sample is sufficient for an optimal ordering of the crystal, resulting in the formation of the surface state.

The appearance of the surface state is easily observed in the momentum maps acquired along KTK and MFM directions (Fig. 4.15), which does not vary its position in momentum at varying film thickness. The evolution of the quantum well states, together with sp -like bands at larger $k_{||}$ values, depending on the film thickness and position in the reciprocal space can be appreciated in Fig. 4.15. The dotted lines indicate the equivalent quantum number depending on the film thickness.

The study of the electronic structure on the cobalt wedge allowed us to estimate that the use of a 10 ML thin film is suitable for the study of its spin-resolved band structure. The characterization of the electronic structure of the film has been performed by means of conventional ARPES using a hemispherical analyzer and spin-dependent momentum mapping using the photoelectron microscope. As stated in the third chapter, in a photoemission experiment, the perpendicular component of the photoelectron momentum is not conserved upon surface transmission. This phenomenon allows for the observation of photon energy-dependent momentum maps, spanning the three-dimensional Brillouin zone. However, depending on the system, some features can have a two-dimensional behavior in photoemission, meaning that its observation is independent on the photon energy used for excitation. This is the case for particular systems in which some bands

are formed at the surface-vacuum interface (surface states) or in the thin film regime by electron confinement (quantum well states).

Using spin resolved momentum mapping (performed with vertically polarized 56 eV photons as excitation source, corresponding to the center of the FBZ) we characterized the band structure near the Fermi level of a 10 monolayer cobalt film, which prior to measurements has been magnetized along the $[1\bar{1}0]$ direction of the underlying W(110) substrate. First of all, the band structure has been mapped using spin-integrated momentum spectroscopy, in the $[0, 0.5]$ eV binding energy range, as visible in the momentum *vs.* energy distribution along KTK and MGM directions of the surface Brillouin zone (Fig. 4.16a and b).

Three different binding energies were selected for the acquisition of 2D spin-resolved momentum maps, namely 0.07, 0.17 and 0.27 eV, which corresponds to particular band fingerprints in the valence band. The spin-integrated maps at those energies are displayed in and in Fig. 4.16c, f and i.

The spin resolved maps of majority and minority spin character are displayed in Fig. 4.16 d, g, j and Fig. 4.16 e, h, k, respectively. Considering the majority spin channel, as visible in Fig. 4.16d, two groups of features can be identified, circular concentric bands with the center around the Γ point (identified by U1) and a well-defined contour, with a hexagonal symmetry (identified by U2), characterized by a value of spin polarization of +62%. At higher binding energies instead, the appearance of an intense feature can be observed, having a triangular shape (marked as U3), characterized by a spin polarization of +78%.

In the minority channel instead, at lower binding energies (Fig. 4.16e), six circular shaped features, centered at the Γ point are identified (marked by D7), with a spin polarization of 88%, while a group of states having an overall “flower” shape (Fig. 4.16e), centered at the Γ point, is observed (marked as D2, D4 and D6), with a spin polarization of -54%.

In order to decouple the contribution of the bands formed in the thin film regime, photon dependent band mapping has been performed on a cobalt slab of 15 ML at the VUV beamline (Elettra Trieste), using a conventional ARPES equipment. In Fig. 4.17, the experimental momentum maps acquired along ΓK (a-e) and ΓM (f) directions are shown.

Fig. 4.17(a) shows ARPES spectra taken on a 15 ML Co film along the ΓK high symmetry direction with 56 eV photon energy. In the proximity of the Fermi level we can observe a number of quantized states. Most of them have nearly linear dispersion and are spread between 0 and 0.2 eV binding energy. We evidence one of them by a red dashed line and marked by U1. The same states were previously observed at this photon energy and attributed to the Co-derived QWSs [105]. Since these QWSs are two-dimensional, the variation of the photon energy excitation does not influence their position in energy, while the variations of matrix elements may increase the relative intensity of other states which have a different symmetry. For example, the change of the photon energy to 50 eV (and the geometry to off normal), part of the U1 states, located closer to Γ point, becomes less intense, while other similar states from the same U1 group can be seen more clearly (Fig. 4.17(b)). The rightmost intense state U2 curves towards Γ point forming a flat part, which is also visible in (Fig. 4.17(a)). The presence of a bright low-dispersive state in the proximity of 0.2 eV close to K point can be observed, which is marked as U3. The U3 state is more visible using 75 eV photon energy (Fig. 4.17(c)), while the U1 and U2 states in the proximity of the Fermi level can be hardly distinguished. As it will be shown below, these three states have clear majority spin character and will serve us as reference points for the comparison with the theory.

Other bands with a dispersion different from that of U1-U3 can be observed. A curved state

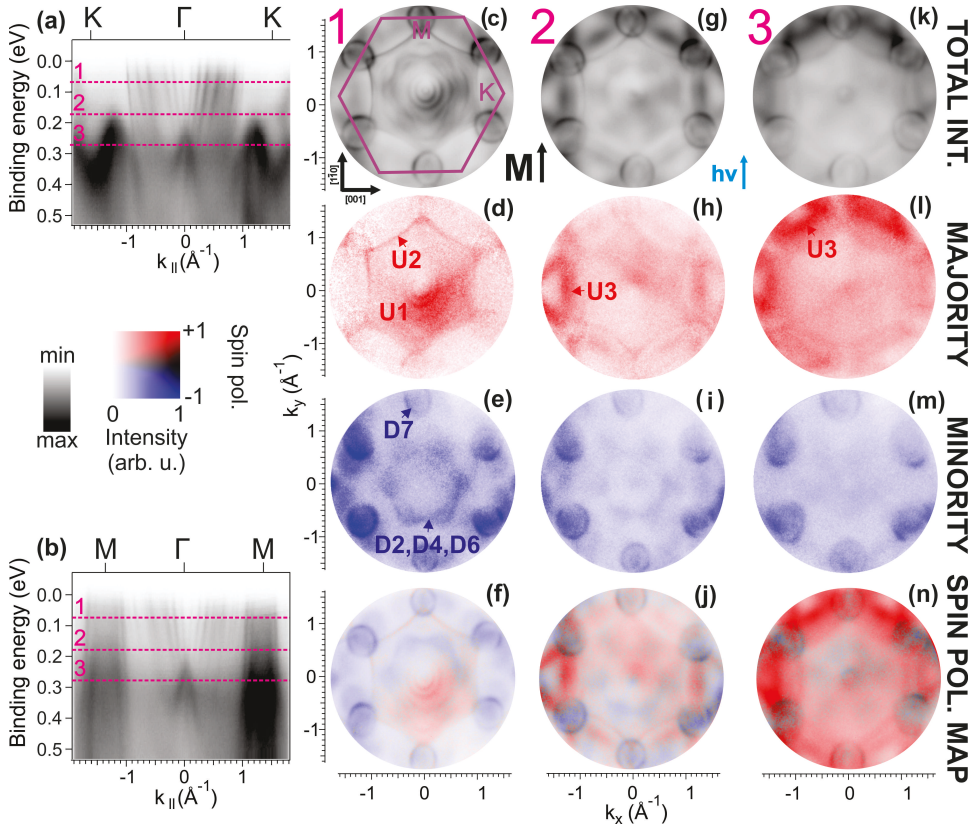


Figure 4.16: Energy vs. momentum map of a 10 ML Co film taken along K Γ K (a) and M Γ M (b) directions. (c) Spin integrated 2D momentum map taken at 0.07 eV binding energy (dashed line 1 in (a) and (b)). (d-e) spin-resolved 2D momentum map of the image in (c). (f) 2D spin polarization map of the image in (c). (g) Spin integrated 2D momentum map taken at 0.17 eV binding energy (dashed line 2 in (a) and (b)). (h-i) spin-resolved 2D momentum map of the image in (f). (j) 2D spin polarization map of the image in (g). (k) Spin integrated 2D momentum map taken at 0.27 eV binding energy (dashed line 3 in (a) and (b)). (l-m) spin-resolved 2D momentum map of the image in (i). (n) 2D spin polarization map of the image in (c). The arrow below image in (c) indicates the magnetization direction of the sample before performing spin-resolved measurements, while the blue one indicates the direction of light incidence. $h\nu = 56$ eV, $T = -140$ °C.

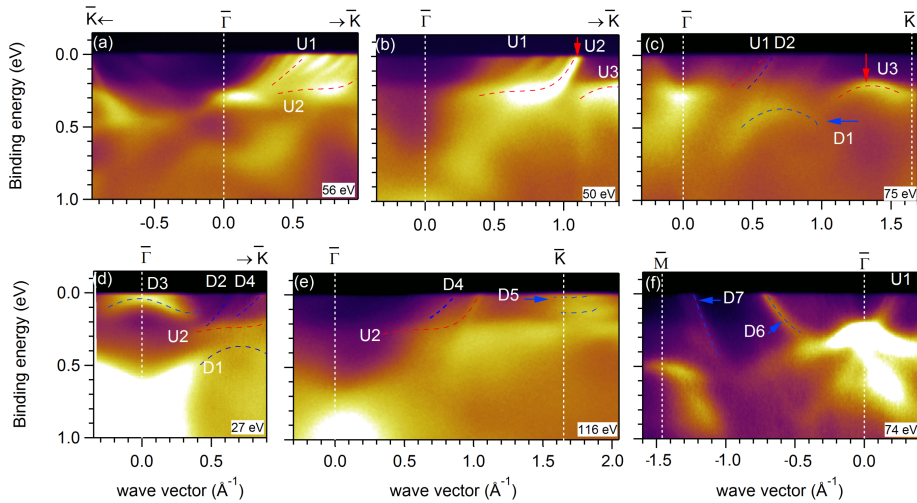


Figure 4.17: ARPES spectra of a 15ML Co film on W(110) along (a-e) $\Gamma\bar{K}$ direction using photon energies of: (a) 56 eV, (b) 50 eV (c) 75 eV (d) 27 eV (e) 116 eV. (f) Spectra acquired along $\Gamma\bar{M}$ direction using $h\nu = 74$ eV. $T = -260$ °C.

marked D1, is observed at lower binding energies in Fig. 4.17(c), and close to the Fermi level there is a nearly linear state D2. Its dispersion is rather different from that of the U1 states, as shown by a dashed red line plotted nearby, therefore it does not belong to U1-U2 group of states. At 27 eV photons (Fig. 4.17(d)) we can observe an intense W-shaped D3 state, which appears at the Γ point.

The flat part of U2 state is visible, and there is a weak intensity corresponding to D2 and D4 states at 0.5 and 0.8 \AA^{-1} . At 116 eV photon energy (Fig. 4.17(e)) the D4 state is more clear, and we can see some part of U2 states and flat broad D5 states close to the Fermi level at the K point. Looking along the $\Gamma\bar{M}$ direction (Fig. 4.17(f)) we can mark two other states, D6 and D7. We can distinguish them from the U1-U2 states due to their higher spread in energy and relative intensity. These elements will be used to make a correspondence to the calculated band structure.

Density functional theory (DFT) calculations were employed as one of the simplest approaches allowing for the identification of the experimentally observed electronic structure. Fig. 4.18 shows the calculated band structure for a 19 ML film of Co, with *hcp* and *fcc* lattice arrangements. One can notice a similarity in the band structure for both structures especially for the majority channel along $\Gamma\bar{K}$. We trace the U1, U2 and U3 dispersions on top of the majority channel for *fcc* and *hcp* along the $\Gamma\bar{K}$ direction by black dashed lines. We can see that the U1 and U2 states have similarities to the *sp*-derived states. The U2, the most intense one can be clearly assigned to the border of the *sp*-derived states and has also the same wave vector position. The U3 state has a shape similar to a *d*-derived state, marked by arrow. None of the states, however, is correctly reproduced: the theoretical slopes of the U1 and U2 state are much higher than the experimental ones, as well as the binding energy of the U3 state and flat part of the U2 state. This discrepancy for the majority spin channel is not surprising, since it has been proven that only including of the correlation effects one may reproduce the correct band position [106].

The many-body electron correlations effects are spin, energy and momentum dependent. While this effect is less pronounced at the Fermi level, at higher binding energies the correlation

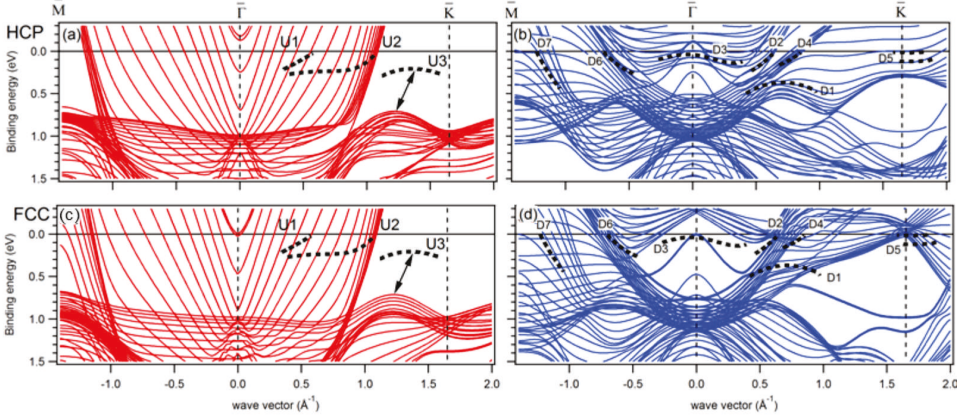


Figure 4.18: DFT band structure calculations for 19 ML Co film (a) *hcp*, majority channel (b) *hcp*, minority channel (c) *fcc*, majority channel (d) *fcc*, minority channel. The dashed lines indicate the experimentally determined bands.

leads to the broadening of the electronic bands [107]. In the 3d ferromagnets, the correlation effects are spin dependent since the filling of spin up and spin down bands is not equivalent, therefore being more pronounced in the majority with respect to its minority counterpart. There are also more differences between the theoretical band structure of *hcp* and *fcc* minority spin channels along the Γ K direction. The *hcp* structure presents, in particular, W-shaped states below the Fermi level at Γ point (there are no such states for *fcc*) and flat states at the Fermi level around the K point (the *fcc* states there have different shape). We put on top of the calculated band structure the D1-D5 states dispersion. Looking at the minority channel at the K point near the Fermi level, there is a very good agreement in the position and shape of the bands for the *hcp* arrangement, while there is no match for the *fcc* minority spin channel.

Along the Γ M direction there are fewer differences in the band structure, so the dispersion of the D6 and D7 states can find the correspondence for both *fcc* and *hcp*. One can, however, notice that there are no (clear) majority states at the M point in the experiment, while the calculations for the *fcc* show some. The constant energy contours close to the Fermi level the *hcp* reproduces better the flower-like minority channel shape in the center, deriving from the D2, D4 and D6 states. We can therefore conclude that the surface electronic features which we observe correspond to the *hcp* atom arrangement, and there is a strong need to include correlation effects to reproduce the position of the U1-U3 features.

Therefore, DFT+DMFT calculation were performed for a 5 ML slab *hcp* cobalt. The U and J potentials were varied among several values, leading to the best fit with the experiment of $U = 3.5$ eV and $J = 0.75$ eV. The optimized DFT+DMFT simulated band dispersions, together with the band fit from Fig. 4.17 in the 15 ML films is shown in Fig. 4.19. The agreement of the calculations with the experimentally determined bands is quite good, especially regarding the slope of the quantum well states U1 which in the DFT calculations showed a different E vs. k dependence.

The spin-down band structure shows features which are also in a good agreement with the dispersion and binding energy of the D1 and D2 states.

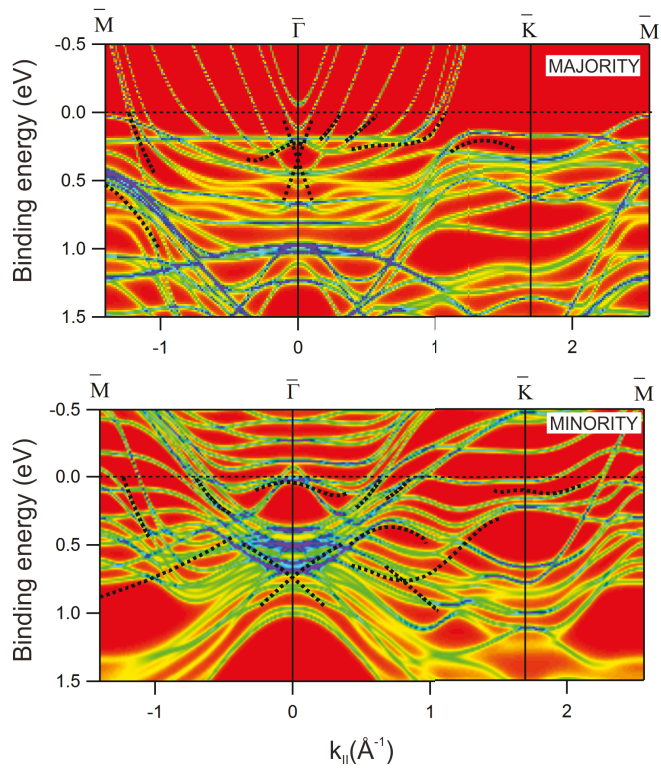


Figure 4.19: Spin resolved DMFT calculations for a 5 ML Co slab.

4.3.2 Thick Co film

In order to avoid the alloying effects observed in the low thickness regime, a sample with 50 Co monolayers has been prepared. The deposition of the cobalt layer, at a rate of 1ML/50s has been performed in the LEEM preparation chamber and afterwards transferred in front of the microscope. The sample has been characterized by μ -LEED measurements whose patterns are characterized by blurred diffraction spots with an additional presence of a (2×2) reconstruction (Fig. 4.20a). This surface reconstruction has been ascribed to the presence of oxygen during the deposition of the cobalt film. The oxygen contamination cannot be avoided since the metal deposition is done after a W(110) oxygen cleaning procedure. Therefore, an after-growth cleaning procedure has been applied to the sample, using a hydrogen back-pressure ($p = 1.5 \cdot 10^{-7}$ mbar) in the main chamber. The experiment has been performed, while following the changes in μ -LEED. It has been observed that the oxygen removal starts at 190 °C and is completed when the temperature of 250 °C has been achieved, with a linear temperature ramp. The change in the diffraction pattern before (Fig. 4.20a) and at 250 °C (Fig. 4.20b) during the treatment, shows up in the profile acquired along the $[1\bar{1}00]$ direction, as plotted in Fig. 4.20c. We note that after the treatment the (2×2) reconstruction vanishes, while the (00) spot and the first order spots present a reduced width and a lowered background, indicating an improvement of the crystalline quality of the cobalt film with the removal of surface contaminants.

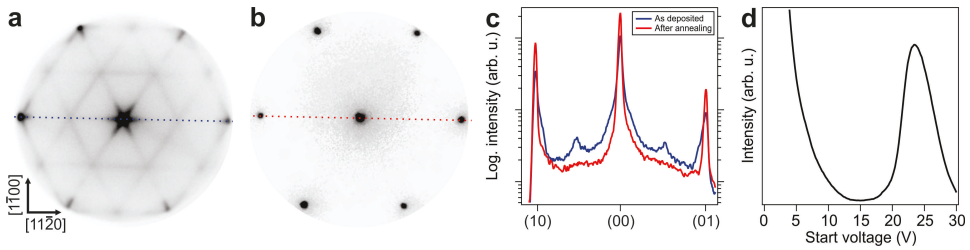


Figure 4.20: a) LEED pattern ($E_{kin} = 40$ eV) of a 50 ML cobalt film, acquired immediately after deposition. b) LEED pattern ($E_{kin} = 40$ eV) of the surface in a) after a hydrogen annealing treatment. c) LEED intensity profiles acquired along the dashed lines as indicated in a) and b), showing the enhancement of the cobalt related spots (zero and first order) and the removal of the (2×2) reconstruction, indicating the removal of the surface contaminants and the improving of the crystalline order of the cobalt film. d) LEEM-IV curve of the Co film in b).

After ensuring the removal of the surface contaminants, the sample has been cooled down to room temperature and LEEM-IV measurements have been performed. As visible in Fig. 4.20d, the IV curve of the 50 ML Co film presents a single Bragg peak. The corresponding μ -LEED pattern (not shown) shows six sharp diffraction spots, as expected from the *hcp* crystalline arrangement. The sample has been annealed afterwards, while following the changes in LEEM ($V_{st} = 22$ V), at the onset of the Bragg peak. Upon annealing, the image contrast in LEEM raises when the sample temperature reaches about 420 °C (Fig. 4.21a-b), due to the better crystalline arrangement of the Co film. Immediately after, at sample temperature of about 440 °C the LEEM contrast starts to change further. The change starts on the sample regions with a higher density of step bunches, *i.e.* where the atoms with lower coordination are located. Successively, the change in contrast propagates also on the flat regions of the sample, being complete in a couple of minutes if the sample temperature is kept constant, or very fast (dozens of seconds) if the temperature is further raised, as in Fig. 4.21.

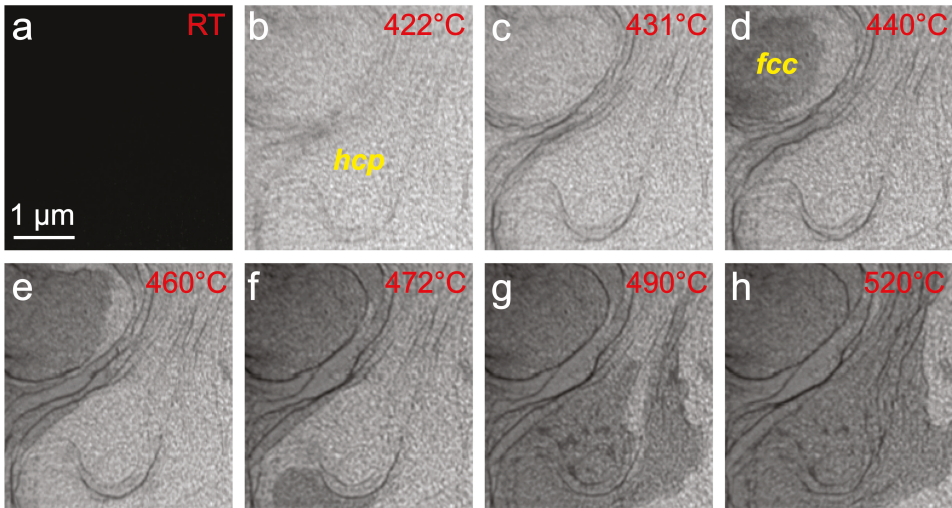


Figure 4.21: LEEM images ($V_{st} = 18$ V) acquired during the annealing of a 50 ML cobalt film. The change in image contrast is associated with the occurrence of the *hcp-fcc* transition.

μ -LEED patterns acquired at high temperature, after a complete change in the image contrast on the entire surface, shows a threefold pattern. The reflectivity curve acquired at high temperature reveals the shape of the one observed after the thermal treatment of the 15 ML film. By comparing the reflectivity curve obtained here, with the simulations performed for *fcc* silver (chapter 3), and by comparing the behavior of similar *fcc* materials, the observed behavior can be ascribed to the martensitic phase transformation of Co, changing its stacking from low-temperature *hcp* to high-temperature *fcc*. This conclusion is further supported by the fact that during the thermal treatment of the film the temperature of 420 °C, corresponding to the *hcp-fcc* transition occurring in bulk cobalt, was exceeded.

After having characterized the phase transition occurring in the cobalt film at high temperature, the sample has been cooled down to room temperature. During the cooling ramp, the image contrast in LEEM ($V_{st} = 22$ V) changes again. Differently from annealing, the contrast change exhibits a hysteresis like behavior, *i.e.* happening at much lower temperature. We observed that the transformation occurring on the surface begins around 230 °C, with a patch type of mechanism, involving small portions of the surface, apparently corresponding to crystalline domains in the cobalt film. After reaching room temperature, the image contrast on the surface is heterogeneous, while the corresponding μ -LEED pattern presents six sharp diffraction spots. This behavior suggest that the observed martensitic phase transformation is reversed, leading to the restoring of the initial *hcp* crystalline arrangement.

The heterogeneous appearance of the surface is furthermore reflected in dark-field LEEM images, acquired using first order diffraction spots, at varying kinetic energy (Fig. 4.23). It can be immediately noted that the two images at lower electron energies (a/d and b/e), acquired using two adjacent diffraction spots at exactly the same electron energy present an inverse image contrast. The one at 230 V electron energy resembles the overall behavior observed at 40 V, with the additional appearance of domains showing different dark/bright contrast. Since at 230 V the

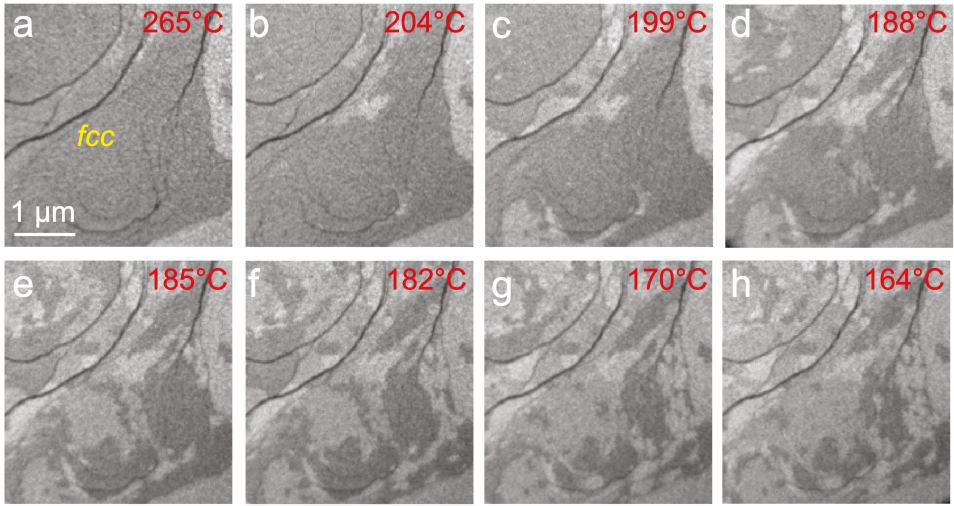


Figure 4.22: LEEM images ($V_{st} = 18$ V) acquired during the cooling down process of a sample where the *hcp*-*fcc* transition occurred. A transformation reverting the image contrast to a brighter one can be observed with lowering temperature.

calculated electron mean free path is 60% than in the 40 V case (3.8 \AA vs. 6.0 \AA), the probing depth at this higher energy is larger. Therefore, the additional contrast observed at 230 V derives from both, surface and buried layers.

The reflectivity curves acquired on different patches, presenting a distinct image contrast at $V_{st} = 18$ V are displayed in Fig. 4.24b. All of them are characterized by a prominent Bragg peak centered at 23-24 V, similar to the case before the high-temperature treatment, indicating the presence in the surface/subsurface layers with an *hcp* arrangement of the cobalt film. However, two (B, C) out of the three curves identified in our sample, exhibit a shoulder on the onset of the Bragg peak, indicating the presence of *fcc* stacked layers, which manifests in the form of stacking faults. The remaining one (A) presents the characteristic shape of the *hcp* stacked film.

Using the characteristic shape of the reflectivity curves it becomes possible to determine the relative abundance of the structures presenting different stacking sequence. We determined that the prevalent structure (48%) present on the surface after the high temperature annealing treatment is the one with a *fcc* layer, while the bulk is *hcp*. The structure presenting a full *hcp* phase instead is present on 45% of the surface. The remaining part (7%) is occupied by a structure formed by two *fcc* stacking faults lying on top of a bulk *hcp* cobalt phase.

Regarding the electronic structure, the presence of an elevated number of cobalt layers does no longer allow for the observation of discretized quantum well states. Instead, a continuum of states is observed at the same E vs. k position in the momentum maps.

The spin-integrated and spin-resolved momentum mapping on this film reveals that the behavior of the rest of the electronic structure, except the quantum well states is substantially equal.

In Fig. 4.25 top row, the constant binding energy maps of the cobalt film are presented, showing a behavior as observed in the low thickness regime. The different behavior with respect

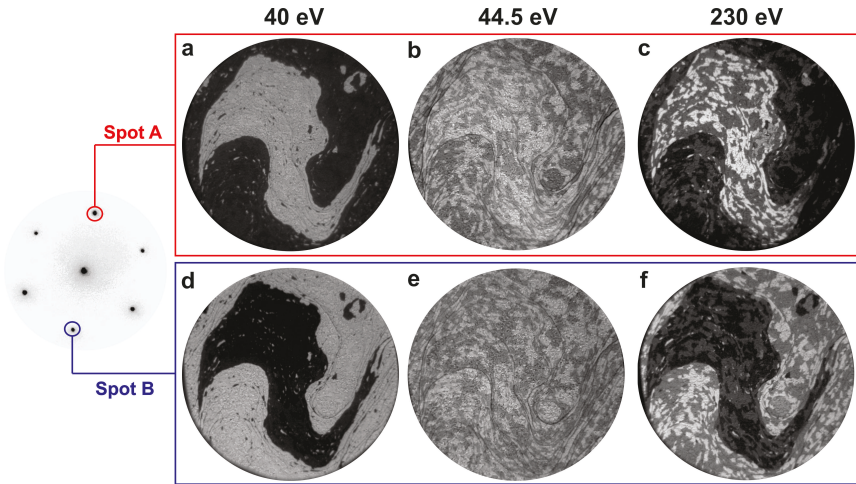


Figure 4.23: Darkfield LEEM images (using alternated first order Co spots) at varying kinetic energy acquired at RT after the *fcc-hcp* transition occurred.

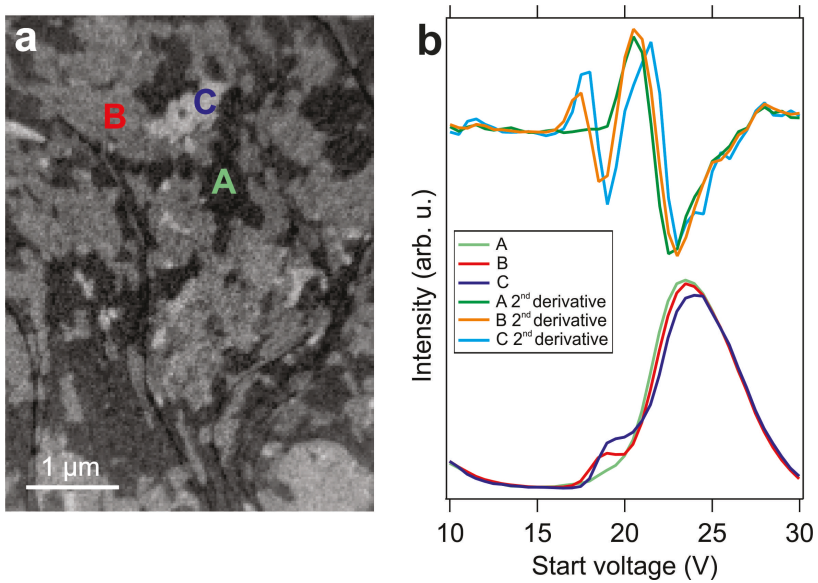


Figure 4.24: a) LEEM image ($V_{st} = 18.5$ V) acquired at RT, after the *fcc-hcp* transition occurred. b) LEEM-IV curves acquired in the regions as indicated in a), along with its respective second derivative.

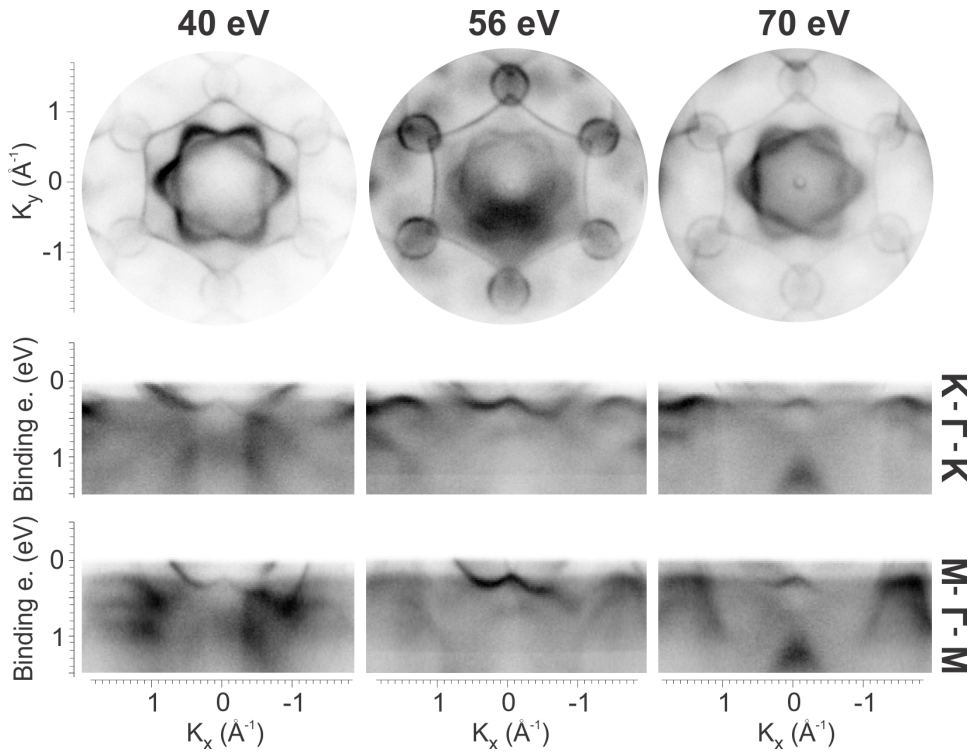


Figure 4.25: Top row: constant binding energy maps of a 50 ML cobalt film acquired at 70 meV binding energy, at varying photon energy. Middle and bottom rows: Momentum maps corresponding to the top row images, acquired along K- Γ -K and M- Γ -M directions, respectively. $T = -140$ °C.

to the photon energy indicates that the crystal starts to become bulk-like, therefore having a k_z dependence of the electronic states. This leads to the appearance of different momentum patterns at the center of the FBZ, and at different points in the Brillouin zone. The momentum maps acquired along high symmetry directions show in more detail the k_z behavior. It can be also noted that the bands exhibit a left-right asymmetry, which can be assigned to magnetization effects (magnetic dichroism), since before the measurements the sample has been remanently magnetized along the k_y direction. This is confirmed by the acquisition of the momentum maps with inverse magnetization, showing a mirrored spectrum with respect to the one presented.

The study of the electronic character generally requires the use of several photon energies, capable of spanning the full Brillouin zone in the k_{\perp} direction. Thanks to our identification of the orbital and spin character of the cobalt bands, performed in the thin film regime (10 ML), we were able to easily recognize and correctly interpret the observed features in thick film regime. This has been achieved through spin-resolved momentum mapping and dedicated theoretical calculations, underlying the importance of including energy-dependent correlation effects to correctly assign the orbital and spin character of the experimentally observed bands. As it will be shown in the following chapter, the identification of the cobalt bands behavior will be of fundamental importance for understanding the hybridization processes between cobalt, which will serve as a substrate, and the graphene overlayer grown on top.

Chapter 5

CVD growth of graphene on cobalt: an in-situ study

In the previous chapter the characterization of the morphological and electronic properties of three different metals exhibiting ferromagnetic behavior at room temperature has been performed, with the goal of finding a suitable substrate for graphene growth, with the goal of transferring the substrate ferromagnetic properties to it. The CVD growth has been performed on top of Fe, Ni, and Co. Cobalt has been chosen as the substrate for the majority of the work performed in this thesis, preferring it with respect to the other two both from geometrical reasons as well as for the better suitability to the experimental setup used.

In order to characterize the graphene CVD growth on top of cobalt thin films, the synthesis procedure has been performed at different hydrocarbon (ethylene) pressures and varying sample temperatures (scheme in Fig. 5.26). The procedures used are divided in two groups: the low temperature (LT), where the hydrocarbon partial pressure is introduced at room temperature on top of a clean cobalt film and the high temperature (HT), where the hydrocarbon is introduced on a preheated cobalt sample [108]. As will be in detail explained in the following, the LT procedure leads to the formation of a defective and misoriented graphene, which will be denoted as Gr-A. The annealing of this graphene leads to a carbon recondensation procedure which improves both its quality and alignment resulting in a Gr-B structure. The HT procedure allows for the formation of a misoriented graphene of high crystallographic quality (Gr-C), which through a similar transformation procedure leads to the formation of a high-quality epitaxially aligned graphene single layer (Gr-D).

5.1 Low temperature growth - formation of Gr-A

5.1.1 Ethylene exposure at low temperature

Cobalt films displaying *hcp* stacking and high crystalline quality were grown on W(110). The deposition conditions were set to obtain a minimum thickness of about 50 atomic layers (~ 10 nm), in order to avoid the possible de-wetting from the substrate, which might occur during the high temperature CVD process for graphene growth, as it has been discussed in the previous chapter. As can be seen in Fig. 5.1a, the resulting cobalt film exhibited a sharp (1×1) LEED pattern. No

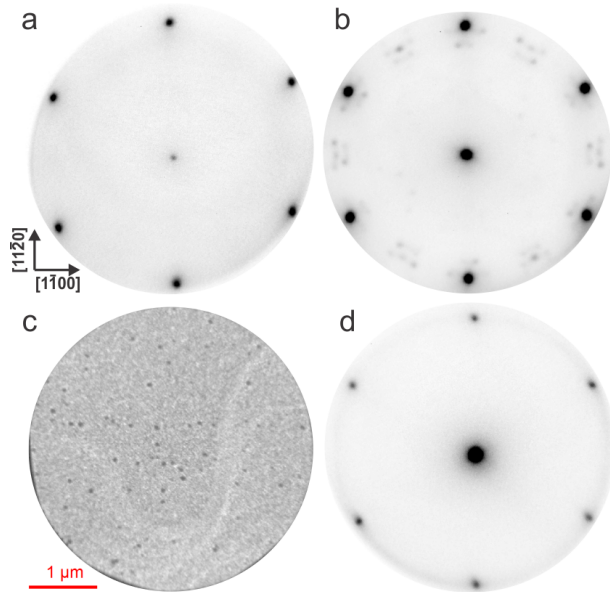


Figure 5.1: (a-c) LEED images illustrating the surface structure of the Co film at different stages of graphene preparation: a) after Co deposition and UHV annealing; b) after exposure to 100 L C_2H_4 and subsequent annealing at $T=130$ °C; c) LEEM image ($V_{st} = 7$ V) after graphene formation (Gr-A phase) at 400 °C; LEED of the Gr-A phase shown in c). Electron energy: 40 eV.

$W(110)$ substrate spots could be detected in LEED, nor the emission from $W 4f_{7/2}$ core level (Fig. 5.2a), confirming the uniform lateral continuity of the Co film.

The CVD process was initiated by exposing the cobalt surface to 100 L of ethylene (C_2H_4) at room temperature. A steady decrease of the zero-order diffraction intensity was observed in LEED during uptake, which we attribute to the disorder in the adlayer accompanying the fragmentation of ethylene [109, 110]. Subsequently, the sample was annealed at C_2H_4 partial pressure of $1 \cdot 10^{-6}$ mbar. At a sample temperature of 130 °C, following the dehydrogenation of ethylene and its fragments [109], an ordered superstructure appears in LEED. The pattern, shown in Fig. 5.1b, closely resembles that of carbides on Ni(111) [111], which has been interpreted as due to a clock reconstructed $fcc(100)$ oriented structure characterized by a carbon coverage of 0.5 ML [112]. At the final temperature of 400 °C, after a dose of 900 L of C_2H_4 , the Co film is covered to a large extent by a new structure, characterized by a higher reflectivity in LEEM, as visible in Fig. 5.1c. At this stage, however, the surface appear to be inhomogeneous. As can be seen in the figure, small dark spots with dimension less than 50 nm interrupt the lateral continuity of the dominant phase (bright). These spots are defined as the precursor phase of epitaxial graphene. Their role in the realignment of the overlayer will be elucidated in the following.

To chemically and structurally characterize the film we performed μ -XPS and μ -LEED measurements. We found that the $C 1s$ spectrum is peaked at 284.5 eV, a value that suggests that the carbon overlayer has a graphitic nature. As will be seen later in more detail when discussing Fig. 5.7, the $C 1s$ line shape is rather broad at this stage. The spectrum exhibits in fact a shoulder

at low binding energy, compatible with the presence of carbidic species and possibly defects. The accumulation of carbon on the surface is further confirmed by the Co $3p$ spectrum, which displays reduced intensity with respect to that of the as-grown Co film (Fig. 5.2b). The measured signal attenuation is compatible with that produced by a single layer of graphene. The lateral continuity and structural integrity of the Co film after graphene growth was verified by measuring the photoemission intensities of the W $4f$ core levels. As shown in Fig. 5.2a, the W $4f$ emission is below the detection level, confirming that there was no de-wetting from the cobalt substrate.

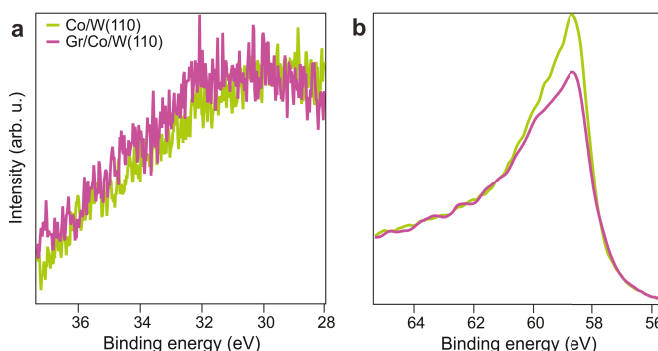


Figure 5.2: Photoemission spectra before and after graphene growth. a) W $4f$; b) Co $3p$; all measurements were performed at RT with photon energy of 400 eV.

Coming now to discuss the LEED of the graphene/cobalt system, this is not very different from that of Co(0001), as observed in Fig. 5.1d. The most notable aspect is the faint diffraction ring with a radius which is compatible with the graphene unit vector. A similar feature is frequently observed when nanometric graphene crystals are oriented with a random azimuthal angle with respect to the underlying substrate, that is, when the graphene film is rotationally incoherent [113]. Based on the above XPS and LEED data, we identify the new overlayer as a defective, rotationally incoherent graphene layer. In the following, we will refer to it as graphene phase A (Gr-A).

It should be noted that the C_2H_4 partial pressure is the key to obtain the Gr-A phase. The sole exposure to ethylene at room temperature, in fact, does not provide sufficient carbon to form graphene upon subsequent annealing to 400 °C in UHV.

In order to access the chemical state of adsorbed carbon during UHV annealing of the *hcp* Co film, C $1s$ spectra at the sample temperatures of 25, 250, 330 and 400 °C were acquired. In this separate experiment, a freshly prepared Co film was successively exposed to 100 L C_2H_4 while keeping the sample at room temperature (RT). In the first spectrum, acquired at room temperature after exposure, the C $1s$ emission is characterized by a main component centered at 283.5 eV (Fig. 5.3, top), due to dehydrogenated ethylene, which in turn transforms into acetylene, adsorbed with the C-C bond parallel to the surface [114]. A second, smaller component can be noted at 284.3 eV, which we attribute to sp^2 carbon formed upon the dehydrogenation of the hydrocarbons. Heating to 250 °C causes the complete decomposition of the hydrocarbon, producing a broader spectral component peaked at 283.15 eV, which we ascribe to the formation of surface carbides [115]. Further annealing to 330 °C leads to a substantial decrease of the overall C $1s$ intensity, with the appearance of a new feature at 284.7 eV. This component is ascribed to formation of small patches of rotationally incoherent graphene. By raising the temperature to 400 °C, the complete

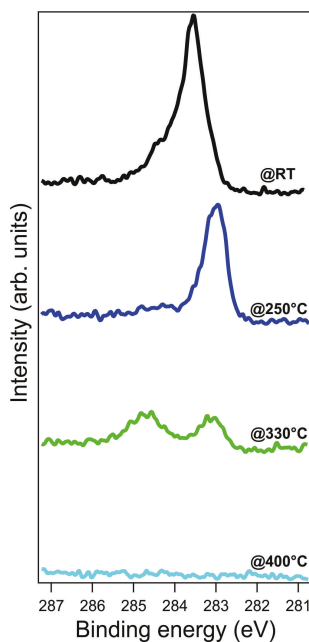


Figure 5.3: C 1s photoemission spectra (offset for clarity) after ethylene deposition at room temperature, followed by UHV step annealing to 250, 330 and 400 °C, as indicated by the labels. The spectra are measured in normal emission at a photon energy of 400 eV.

bulk dissolution of the surface carbon can be observed (spectrum at the Figure 5.3 bottom).

The chemical interaction between graphene and the underlying cobalt substrate is quite strong. The reason for this behavior can be explained considering geometrical factors of the interface. First, the presence of an epitaxial match of graphene with the underlying substrate leads to the break of the symmetry in the graphene unit cell, with the preferential adsorption configuration being the “*fcc-top*” configuration, the one with lowest adsorption energy among all considered (see Table 5.1).

Second, the interlayer spacing between the carbon layer and the first surface layer is reduced upon adsorption. In the optimized “*fcc-top*” configuration, from the DFT calculations emerged that the distance between the top located carbon atom and the underlying Co atom is 2.12 Å, while the distance between the *fcc* located carbon atom and the underlying Co atom is 2.14 Å (see Table 5.2). This relatively low distance allows for a strong overlap of the Co 3*d* bands with C 2*p_z* bands, leading to a strong chemisorptive behavior. This is expected by comparing similar graphene-metal interfaces, such as Gr/Pd, Gr/Pt and Gr/Ni, which depending on the relative distance between graphene and the substrate leads to chemisorption or physisorption at the graphene-substrate interface [116].

Gr-A is characterized by the presence of misoriented domains and defective structures, as shown previously. As visible in Fig. 5.4, the momentum map of Gr-A (centered at the K point of the SBZ) is characterized by two main features: one at low binding energies near the Fermi level and a reverse V-shaped one, so-called Dirac cone, at higher binding energies.

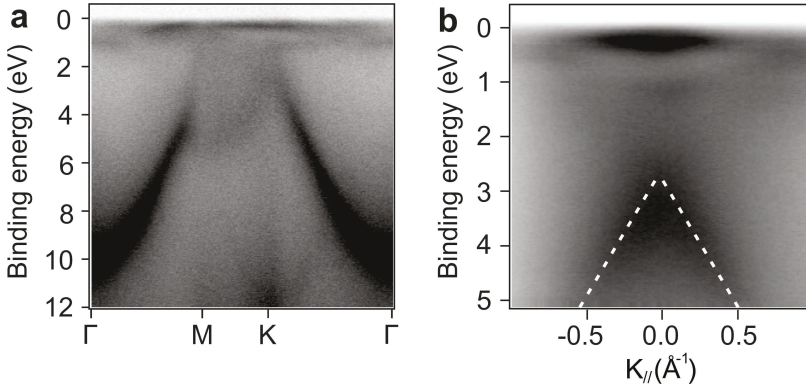


Figure 5.4: a) Momentum map of LT grown graphene (Gr-A) extracted along Γ MKT. b) Momentum map, centered at the K point of SBZ, of Gr-A. All the spectra were acquired using p-polarized 40 eV photons, at sample temperature of -140 °C.

The interaction of graphene with the underlying Co substrate induces mixing of the graphene π states with the d states of the Co support. The interaction is strong and leads to a shift of the graphene π and σ states towards higher binding energies with respect to the free-standing case.

In order to determine the speed of the charge carriers and the position of the π band crossing at the K point, the following fit procedure has been performed. On a momentum map (centered at the K point of the SBZ) MDC curves are extracted and successively, fitted with convoluted Gaussian and Lorentzian profiles (Voigt). Their position is recorded with respect to the binding energy and then plotted on a graph. The fit so-plotted peak maxima allow for the determination of the crossing of the graphene-related bands at the K point.

For Gr-A, the crossing of the π bands at the K point is found at 2.83 ± 0.08 eV. However, by visual inspection of the momentum map, the center seems to be positioned at higher binding energies, approximately at 3 eV. This phenomenon has been already observed in strongly interacting graphene-metal systems, such as Ru(0001) and Ni(111). In those cases the Dirac cone apex is rounded off, like in the Co case, due to the opening of a gap between the π and π^* bands which hybridize with the substrate, indicating a strong graphene-substrate interaction.

Regarding the Fermi velocity instead, which is a measure of the speed of the charge carriers, from a linear fit of the center of the graphene bands, we find that $v_F = 0.96 \cdot 10^6$ m/s. This value is slightly lower of experimentally measured Fermi velocities for other strongly interacting graphene-transition metal systems.

5.1.2 Transformation from Gr-A to Gr-B

In general, the use of CVD temperatures between 600 °C and 1000 °C is known to dramatically improve the crystallographic quality of graphene [60, 21]. Under these conditions, the increased mobility and bulk exchange of carbon atoms provide additional means to order the crystalline lattice. Previous studies have also shown that the annealing improves the epitaxial relation of both defective and rotationally incoherent graphene grown on Ni and Co substrates [117, 118]. By adopting a similar approach, we heated the Gr-A to high temperatures in distinct experiments

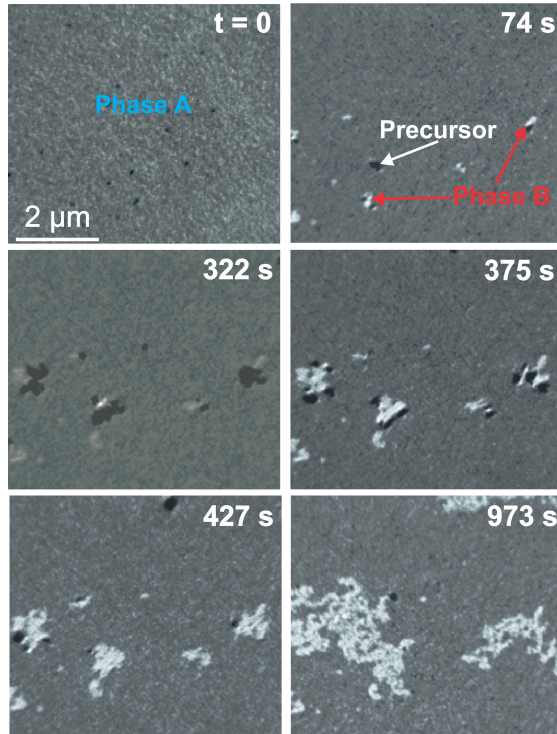


Figure 5.5: LEEM image sequence at $V_{st} = 7$ V illustrating the transformation from the rotationally incoherent Gr-A (neutral gray) to the epitaxial layer of Gr-B (bright), mediated by a precursor (small dark regions). The sample temperature was kept constant at 530 °C; the ethylene partial pressure was $1 \cdot 10^{-6}$ mbar.

performed in ethylene partial pressure and under UHV conditions.

Figure 5.5 shows a set of selected LEEM images taken during the annealing of Gr-A at about 530 °C in $1 \cdot 10^{-6}$ mbar C_2H_4 . Most interestingly, the sequence shows the occurrence of a structural transformation in the film. In the initial phase, the nanometric dark spots observed in LEEM (Fig. 5.1c) become suddenly larger. This process is illustrated in the top row of Fig. 5.5. Shortly afterwards, they start to move across the surface, following a self-avoiding random walk. They leave behind their path a new phase, exhibiting a much higher intensity in LEEM than Gr-A, which we will refer to as phase B graphene (Gr-B). Notably, the transformation from Gr-A to Gr-B was also observed in an annealing experiment performed under UHV conditions. The fact that the recrystallization occurs either in UHV or in ethylene ambient is in disagreement with previous experiments by Usachov *et al.*, who observed it only during UHV annealing [118].

In order to quantitatively assess the structural differences between Gr-A and Gr-B, we interrupted the graphene transformation at the formation of sizable regions suitable for spectro-microscopic and microspot diffraction measurements (Fig. 5.6a). These regions were characterized using LEEM-IV and μ -LEED. The LEEM-IV spectra acquired on the two phases are shown in Fig. 5.6b. The shape of the reflectivity curves indicates that both phases can be identified as single-layer graphene [119]. As can be seen, Gr-B exhibits an increased electron reflectivity, which

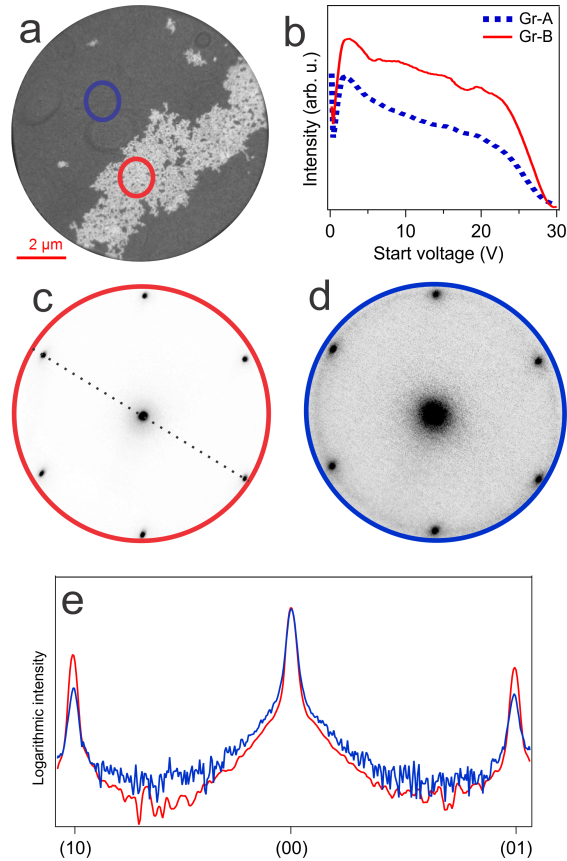


Figure 5.6: Room temperature characterization of the Gr-A and Gr-B phases, corresponding to rotationally incoherent and epitaxial graphene, respectively: a) LEEM image at $V_{st} = 7$ V showing at the center a domain of Gr-B (bright), formed upon the transformation of Gr-A (neutral gray) surrounding it. The blue and red contours depict the area probed in the LEEM-IV and μ -LEED measurements shown in b-e; b) LEEM-IV curves taken from Gr-B and from the surrounding Gr-A. The higher electron reflectivity of Gr-B determines the image contrast. b-c) LEED patterns ($V_{st} = 40$ V) taken on Gr-A and Gr-B. Note that Gr-B shows sharper and more intense spots compared to Gr-A. d) LEEM-IV curves taken on Gr-A and Gr-B. e) Cross-sectional plots of the LEED intensities acquired along the $(1\bar{1}20)$ direction, as indicated by the dotted line in b). Note the logarithmic scale.

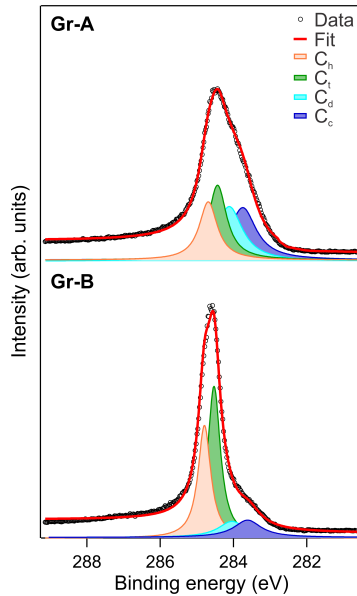


Figure 5.7: Comparison of the C $1s$ core level emission on Gr-A and Gr-B; photon energy: 400 eV. The spectra were acquired at RT, after freezing the transformation process from Gr-A to Gr-B by quickly cooling the sample to RT.

indicates a higher degree of order. The LEED patterns recorded on Gr-B and Gr-A are shown in Fig. 5.6c-d (the images are normalized to the same levels). The better structural quality of the Gr-B can be readily appreciated from the enhanced intensity of first order spots, accompanied by the disappearance of the blurred ring due to rotationally incoherent graphene. Moreover, the background in the μ -LEED pattern is substantially reduced, as demonstrated by the cross sectional plots displayed in Fig. 5.6e.

We note that the Co film did not break-up during treatment, as we could verify using LEEM and XPS. The morphological stability of the Co film is favored by the presence of graphene, which is known to have a surfactant effect, preventing the cobalt layer from islanding and de-wetting [16, 120]. Accordingly, we have observed a complete phase transformation from Gr-A to Gr-B over microscopically extended regions of the Co film without degradation of the film morphology.

The chemical state of graphene was characterized by μ -XPS. The C $1s$ core level spectra were collected separately from Gr-A and Gr-B, using a $2\ \mu\text{m}$ wide field-limiting aperture to select the region of interest. The experimental data and Voigt line shape fits are shown in Fig. 5.7. To favor a qualitative interpretation of the data, the core level spectra were fitted using 4 components: two graphene peaks representing the non-equivalent adsorption sites in the “*fcc-top*” carbon adsorption geometry (C_t and C_h) [121] and two peaks at lower binding energies (C_d and C_c) accounting for the emission from carbon atoms in proximity of defects [122] and carbidic species, respectively. For the case of Gr-A, all four components have similar intensity. The two graphene components, C_h and C_t , centered at 284.88 eV and 284.62 eV binding energy, are characterized by a Lorentzian full width at half maximum (FWHM) of 0.6 eV. On Gr-B, instead, the intensity of the low binding energy components has significantly reduced as compared to Gr-A. On the

other hand, the graphene components (C_t and C_h) have become more prominent. Moreover, a chemical shift to higher binding energies of the graphitic components can be observed, becoming centered at 284.95 eV for C_h and 284.72 eV for C_t . The chemical shift was accompanied by a notable narrowing of the peaks (down to 0.42 eV), confirming the improved lattice order of the epilayer.

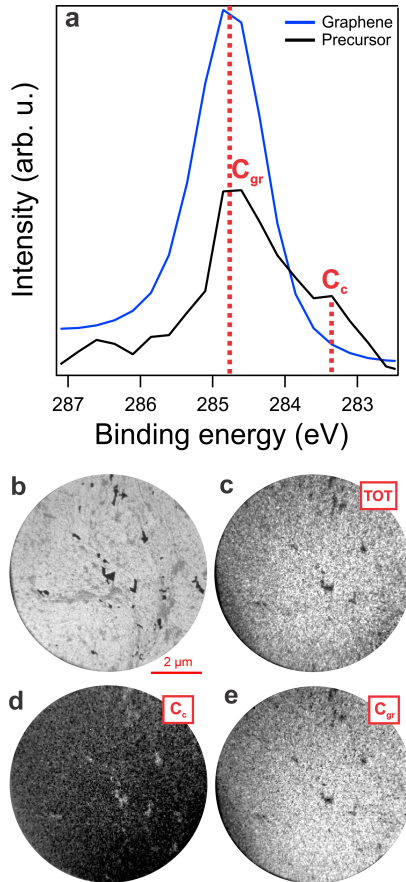


Figure 5.8: a) $C\ 1s$ XPEEM spectra acquired on rotationally incoherent graphene (Gr-A) (blue) and the precursor islands (black) b) LEEM image of the Gr-A and precursor islands at $V_{st} = 40$ V. c) Integrated XPEEM intensity over the entire $C\ 1s$ emission. d) XPEEM map of the carbidic component centered at 283.3 eV B.E. e) XPEEM map of the graphitic component at $E_B = 284.8$ eV. All measurements were performed at RT; $h\nu = 400$ eV.

Since the precursor regions are much smaller than the μ -XPS probe area, they were characterized using XPEEM (Fig. 5.8). At variance with the Gr-B, which shows a smeared out version of peaks C_h and C_t as a broad peak centered at 284.8 eV, the precursor exhibits a pronounced shoulder at 283.3 eV. This shift of about 1.2 eV towards lower binding energies can be ascribed to carbidic species located in the topmost Co layers, in analogy with previous observations [114].

The annealing of Gr-A induces changes also in the appearance of the valence band states near

the Fermi level, as visible in Fig. 5.9a and b. This includes an improvement of the sharpness of graphene states, both π , and σ , reflected in a sensible reduction of the momentum width of the bands. Moreover, their intensity with respect to the overall background becomes much higher, pointing out that the amount of incoherent emitters has been significantly diminished (*i.e.* a lower amount of defective structures). By acquiring the EDC at the Γ point, the presence of the top of the σ band can be identified in the spectra (Fig. 5.9d). The center of the σ band is found at 4.8 eV, which is 1.1 eV lower than in the case of graphite, being much less affected upon adsorption with respect to the π band. This is justified since the interaction of the Co d bands is stronger with the π states than with the σ states. Instead, in the region near the Fermi level, no changes can be observed, as expected since the intensity in this region originates from cobalt d states. However, the enhanced quality of the graphene film reflects also in the intensity raise of the π -band bottom, found at around 10 eV binding energy.

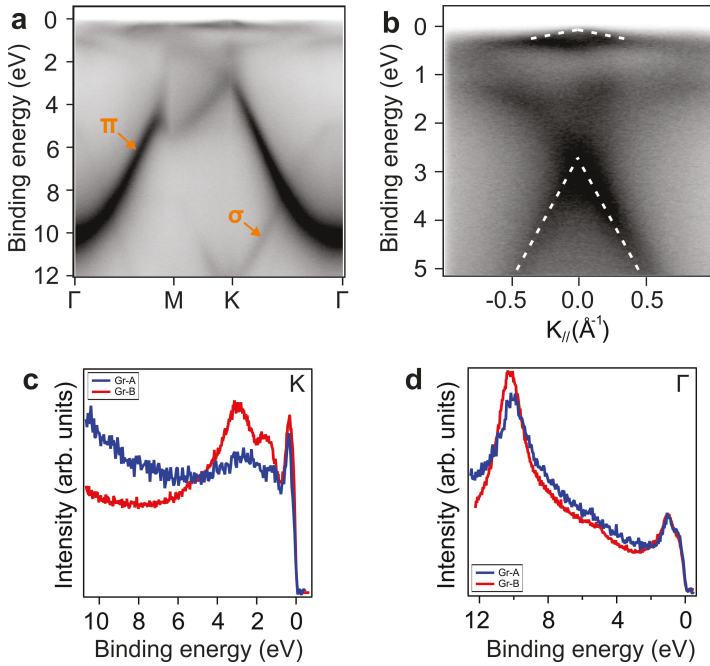


Figure 5.9: a) MDC of Gr-B extracted along $\Gamma\text{MK}\Gamma$. b) Momentum map, centered at the K point of SBZ, of Gr-B. c) Comparison of EDCs acquired at the K point of Gr-A and Gr-B. d) Comparison of EDC acquired at the Γ point of Gr-A and Gr-B. All the spectra were acquired using p-polarized 40 eV photons, at sample temperature of -140°C .

By acquiring EDCs at the K point of the SBZ, the enhancement of the features in the $E_B = [0, 4]$ eV regime can be noted upon transformation (Fig. 5.9c). The peak present at lower binding energies, originating from the Co $3d$ and C $2p_z$ hybridization and forming of a single-spin polarized band, the so-called minicone [21], presents an enhanced intensity. The observation of the minicone feature (which will be characterized in detail in the following) has been reported to be strongly dependent on the crystalline quality of the graphene layer, which upon annealing increases. Moreover, the two peaks located between 1 and 3 eV binding energy, which derives

from the graphene π bands are also enhanced after the transformation process, accompanied, as in the previous case, by a reduction of the background.

The fit of the graphene π bands allowed for the determination of the Dirac cone apex position which turns out to be 2.81 ± 0.05 eV, therefore being essentially at the same binding energy position as before the transformation. The Fermi velocity instead slightly increments, yielding in $v_F = 1.03 \cdot 10^6$ m/s.

In summary, we find that the transformation of graphene enhances the electronic properties of the carbon overlayer, with the visible formation of the minicone feature and with enhanced speed of the charge carriers.

5.2 High temperature growth - formation of Gr-C

The growth temperature in a CVD process emerged as the most important parameter influencing the crystalline quality of a graphene film. It was shown that an increased substrate temperature during growth leads to the formation of a graphene with reduced defects and grain boundaries with respect to the one grown at lower temperatures. However, the growth temperatures have to be wisely chosen with respect to the substrate used. This is especially important in the growth of graphene on thin metallic films, which are usually deposited on top of a support. An elevated temperature gives the means for the wetting of deposited metallic film. Therefore the study at elevated temperatures has to be followed by imaging techniques, which can study the growth temperature limits in the CVD process.

5.2.1 Ethylene exposure at high temperature

After growing a 10 nm thick Co film, the high temperature CVD growth of graphene has been followed qualitatively and quantitatively using imaging and diffraction techniques, in two separate experiments. In the diffraction experiment, we followed the changes in the low energy electron diffraction pattern during a high-temperature graphene growth (Fig. 5.10). As a starting point, after deposition of the cobalt film, the LEED pattern is characterized by a hexagonal pattern (Fig. 5.10a), as observed before. Upon annealing, the crystalline quality of the substrate improves, as observed from the intensity rise of the first order cobalt spots. At a temperature of about 250 °C, the cobalt first order spots reach a plateau in intensity, meaning that the surface reached its maximum degree of order (Fig. 5.10b). At this point, ethylene is introduced in the microscope chamber ($p = 1 \cdot 10^{-6}$ mbar), while the sample temperature is ramped. Ethylene molecules which impact towards the heated surface layer immediately dehydrogenate, leading to the accumulation of carbon monomers/dimers. The exposure of the surface to the hydrocarbon leads to an intensity drop of the first order spots, since a disordered phase forms on the surface upon adsorption. The increased mobility at this temperature leads to the rearrangement of the accumulated carbon on the surface into an ordered structure. This allows for the formation of a surface carbide, which is clearly observed in the LEED pattern (Fig. 5.10c) and in the relative intensity profile. The ramp in temperature leads to the disappearance of the carbide phase with the carbon atoms dissolving into the bulk, as it has been demonstrated in the previous section. This is further confirmed in this case by inspecting the intensity of the first order spots of the substrate. As visible from the profile, the drop in intensity of the carbide related spots is accompanied by a rise in intensity of the first order substrate spots, indicating that the surface carbon structure is dissolved.

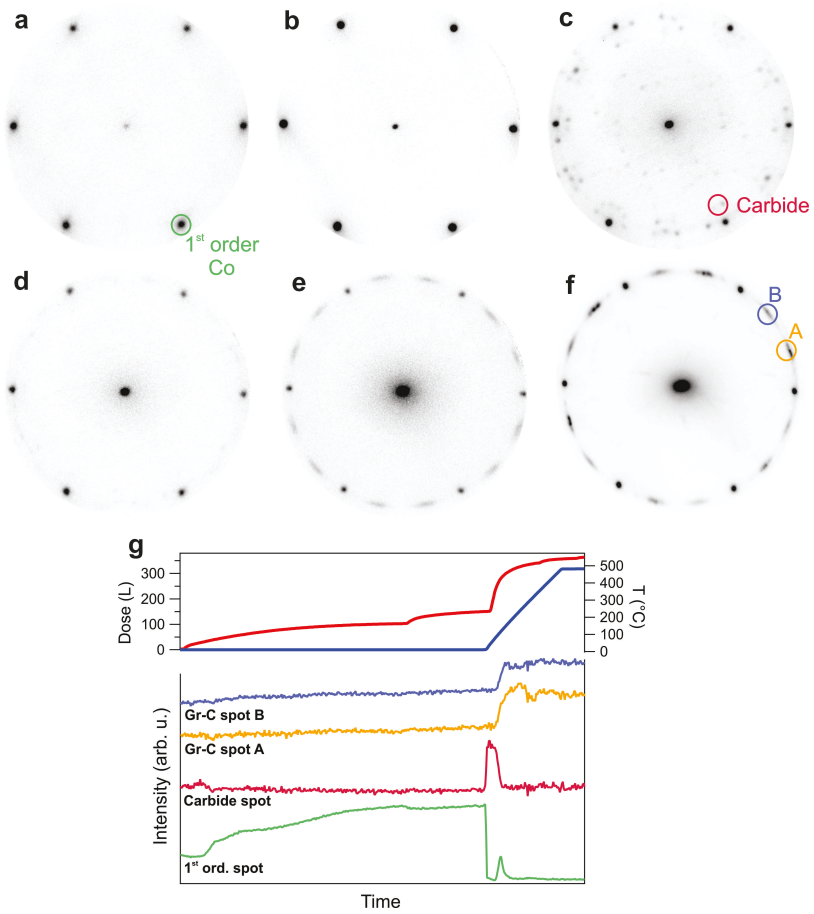


Figure 5.10: a-f) LEED patterns acquired during Gr-C growth process. g) LEED intensity profile during the Gr-C growth, acquired on the spots as indicated in the legend.

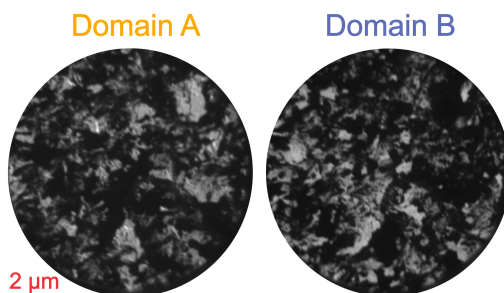


Figure 5.11: Darkfield LEEM images ($V_{st} = 7$ V) acquired from the two arch features in the LEED pattern of Gr-C.

The ramp in temperature up to 550 °C at constant ethylene partial pressure, leads to the formation of an ordered surface structure, with a faint diffraction ring with a radius equal to the first order substrate spots. By further increasing the ethylene total dose and keeping the temperature around 500 °C, the LEED pattern is characterized by the appearance of arc-shaped intensities with a rotation angle of $\pm 18 \pm 8^\circ$ from the first order spots of the Co substrate (Fig. 5.10e), which become even more evident after cooling down the sample to RT (Fig. 5.10f). In the following we will refer to this structure as graphene phase C (Gr-C).

The post-growth characterization has been performed with LEEM and LEED. Using bright field imaging the amount of ordered structures has been quantified, being 98.6%. The remaining percentage up to full coverage is occupied by the carbidic islands, whose nature has been discussed in the previous section. Using dark-field LEEM imaging, it was possible to spatially resolve the structures giving rise to the arcs in the LEED pattern. As visible from Fig. 5.11, by acquiring DF-LEEM images separately from the two arcs enclosed between two first-order Co spots, we have determined the ratio between the two groups of rotational domains, being quantitatively almost equal, namely 48.9% *vs.* 49.7%.

In order to reveal the relative angle between graphene and the cobalt substrate, a LEED profile was acquired along the arc enclosed between two first order spots of cobalt. As visible in Fig. 5.12, the LEED profile was fitted using 5 components. The 0 of the angular scale has been set in correspondence of the first order substrate spot. The fit reveals that the graphene orientations with respect to the substrate are 9.6° , 16.5° , 19.2° and 22.4° . The abundance of the observed domains in that particular region of Gr-C under analysis was 4.7%, 38.2%, 40.6% and 16.5%, respectively. By taking the weighted average of the abundance of the different angular configurations, we find that the mean rotational angle can be determined to be 18.25° , a result that will be important in electronic structure analysis.

The elevated crystallographic quality of graphene (as observed by XPS) grown by exposing the hot cobalt surface to ethylene results also in the formation of sharp graphene-related bands in momentum space. The presence of rotational domains is reflected also in the band structure, with the SBZ presenting features centered at the same angle as observed in the LEED pattern. Since the size of the domains is smaller than the portion of the surface illuminated by the photon beam, the momentum maps at constant binding energy contain the contribution from both kinds of rotated domains. Moreover, since the domains of the discrete graphene-substrate rotational configurations (as determined by LEED analysis above) are small with respect to the dimension of the photon beam, the SBZ of the rotated domains are expected to be rotated on average by

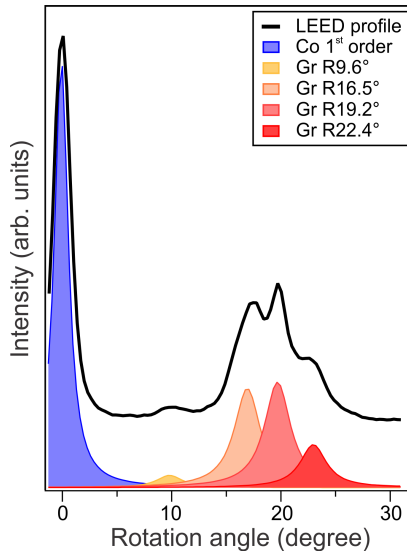


Figure 5.12: Analysis of the LEED profile acquired along the arch enclosed between two consecutive first order Co spots after the growth of Gr-C (Fig. 5.10f). The fit reveals the presence of four discrete angles of the graphene lattice with respect to the cobalt lattice vector: 9.6° , 16.5° , 19.2° and 22.4° .

$\pm 18.25\%$ with respect to the epitaxial case.

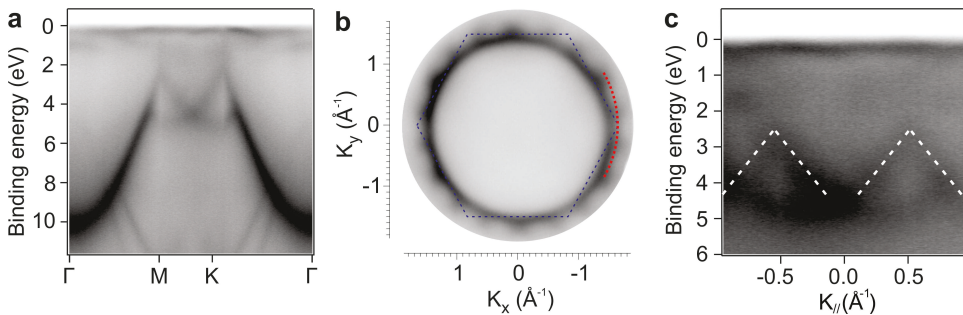


Figure 5.13: a) Momentum map of Gr-C extracted along $\Gamma MK\Gamma$. b) 2D momentum map acquired at $E_B = 3.2$ eV with superimposed the substrate Brillouin zone. c) Momentum map of Gr-C acquired along the dashed arch as indicated in b). All the spectra were acquired using p-polarized 40 eV photons, at sample temperature of 135 K.

The momentum maps acquired for each Brillouin zone along the $\Gamma MK\Gamma$ (Fig. 5.13a) direction of the Co substrate, show that the two branches of the π bands are almost equal in position and shape. This can be explained since the overlap of two Brillouin zones relative to the two groups of rotational domains makes impossible to distinguish the bands of different domains, leading to the formation of a π band continuum, characterized by a circle in the momentum maps at constant energy. The fit of the π bands allowed for the estimation of the $v_F = 0.95 \cdot 10^6$ m/s and the position of the Dirac cone apex at 2.45 eV. The position of the apex is, therefore, shifted 0.38 eV towards

lower binding energies with respect to the position of the Dirac cone in epitaxial graphene. This shift to lower binding energies with respect to the epitaxial case indicates a lower interaction between graphene and cobalt, which is expected since no preferential site is occupied. Similar behavior has been observed also in rotated graphene grown on Ni(111) [119].

At the same azimuthal angle with respect to the substrate Brillouin zone ($\approx 18^\circ$), the apex of the main Dirac cones, formed by the intersection of the π bands, are observed. As visible in Fig. 5.13b, the momentum map, acquired along an arc of the circumference with the radius of the K point, is plotted. In this map, two Dirac cones, relative to the two rotational domains are observed (Fig. 5.13c). The absence of epitaxial domains can be deduced since no Dirac cone is observed at the K point of the substrate Brillouin zone.

Graphene growth on a multiphased substrate: *hcp* vs. *fcc*

Knowing that Co undergoes a phase transition from *hcp* to *fcc* stacking, we considered the possible influence of the substrate stacking on the transformation from Gr-A to Gr-B. In principle, the graphene transformation can be related to the well-known martensitic *hcp-fcc* transition of cobalt occurring in the bulk above 420°C [123] and in surface layers at about 500°C [124]. Those temperatures are in the same temperature range of the graphene phase transformation as we described in the previous section.

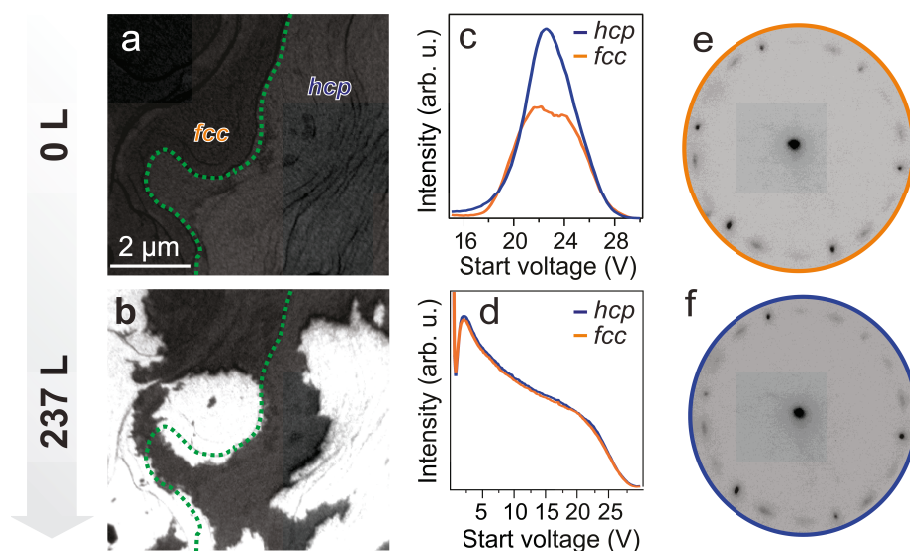


Figure 5.14: a) LEEM image showing structural domains on clean cobalt at 430°C . At the chosen energy ($V_{st} = 22\text{ V}$), the *fcc* region appears slightly darker than *hcp*; b) LEEM image of the same region taken after dosing 237 L of C_2H_4 . The white regions correspond to the growing graphene overlayer; c) LEEM-IV curves for *fcc* and *hcp* cobalt. The splitting of the Bragg peak at 23 eV explains the LEEM contrast in a); d) Room temperature LEEM-IV curves for graphene grown on *fcc* and *hcp* cobalt. The two curves are basically identical; μ -LEED ($V_{st} = 22\text{ V}$) for e) *fcc* and f) *hcp* cobalt. Note the presence of 22° rotated graphene.

In order to assess the influence of the substrate stacking on the graphene crystalline quality, a fresh cobalt film with homogeneous thickness of about 50 atomic layers was prepared. The film,

which exhibits *hcp* stacking at room temperature, was annealed at a temperature of 450 °C. The thermal treatment resulted in the formation of microscopically extended *fcc* domains inside the dominant *hcp* phase, which were then stabilized by decreasing the sample temperature to 430 °C. By using LEEM, it was possible to readily visualize the *hcp* and *fcc* stacking domains, the latter appearing slightly darker than the former at $V_{st} = 22$ V, as visible in Fig. 5.14a. The observed image contrast arises from a slight difference in the LEEM-IV spectra of the *hcp* and *fcc* cobalt phases. As can be seen in Fig. 5.14c, *fcc* cobalt exhibits a splitting of the Bragg peak at electron energy of 20 V, as explained in detail in the previous chapter.

Subsequently, we exposed the structurally heterogeneous *hcp-fcc* film to ethylene at partial pressures of about $1 \cdot 10^{-6}$ mbar while monitoring the growth using LEEM. As can be seen from the LEEM image in Fig. 5.14b, graphene (bright regions) starts to nucleate in both the *hcp* and *fcc* domains, quickly expanding over the entire Co film until a complete monolayer is formed. Notably, the nucleation and growth processes take place on both *hcp* and *fcc* cobalt in a very similar manner. As a matter of fact, LEEM-IV measurements taken after growth (Fig. 5.14d) on the same regions initially exhibiting *hcp* and *fcc* stacking are identical. Moreover, we note that the same LEED pattern exhibiting domains of 18° rotated graphene (Gr-C) was observed in both regions (Fig. 5.14e-f), nicely confirming that the overlayer configuration is independent of the substrate structural conformation.

The fact that the graphene growth is not influenced by the cobalt structural conformation brings up the into question the relative stability of graphene on *hcp* and *fcc* cobalt. In order to compare the relative adsorption energies of the carbon atoms on Co(111) and Co(0001), *ab-initio* density-functional theory calculations were performed by our collaborators. In the simulations, we considered three adsorption sites for both *hcp*(0001) and *fcc*(111): the “*fcc-top*” (AC site), “*hcp-top*” (AB site) and the “*bridge*” site, as shown in Fig. 5.15. In the “*fcc-top*” adsorption (Fig. 5.15(a)), one carbon atom is placed on top of the surface Co atom (“T” position) and the other carbon atom in the hollow site in the “F” stacking position. Similarly, for the “*hcp-top*” adsorption (Fig. 5.15(b)), one C atom is on top of the surface Co atom and the other in the hollow site in the “H” stacking position. The “*hcp-top*” adsorption sites can be obtained from “*fcc-top*” by rotation by 60° and translation by the graphene lattice parameter. In the “*bridge*” adsorption (Fig. 5.15(c)), the middle of the C-C bond is above the topmost Co atom.

The results of the calculations are summarized in Table 5.1. The strongest adsorption occurs on Co(0001) on the “*fcc-top*” site. Notably, this bond is only 13.78 meV per C atom stronger than for the graphene adsorption on Co(111). Further, the energy difference between “*fcc-top*” and “*hcp-top*” sites is relatively small for both surfaces, amounting to ~ 3 meV per C atom, while the bridge adsorption site is roughly 20 meV per C atom weaker. The energy ordering of adsorption site preferences, as well as numerical values of the differences are in agreement with the previous studies for *fcc*(111) and *hcp*(0001) cobalt [21, 125, 126, 127].

Table 5.1: Relative adsorption energies in meV per C atom on Co(0001) and Co(111) with respect to the strongest adsorption energy configuration (“*fcc-top*” site on Co(0001)). The values are converged to better than 1 meV per C atom.

	“ <i>fcc-top</i> ”	“ <i>hcp-top</i> ”	“ <i>bridge</i> ”
Co(0001)	0.0	3.3	22.4
Co(111)	13.8	16.3	37.5

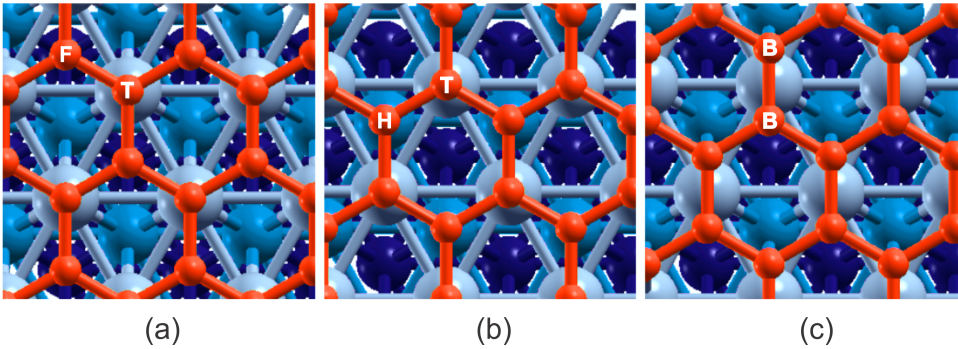


Figure 5.15: Adsorption sites considered for adsorption of graphene on *fcc*(111) and *hcp*(0001) Co: a) “*fcc-top*”, b) “*hcp-top*” and c) “*bridge*” site. Graphene on *fcc*(111) Co is shown. The red spheres represent C atoms, gray spheres top layer of Co, light blue the subsurface Co layer and dark blue third layer of Co.

Moreover, in Table 5.2 the distances between the optimized graphene and the topmost Co layer for different adsorption sites on *fcc*(111) and *hcp*(0001) Co are compared. The difference in distances between the top and hollow sites indicates that the graphene layer is buckled.

Although the differences are small, we see that the distance between the C and Co atom for *hcp*(0001) in “*fcc-top*” and “*hcp-top*” is the smallest, indicating the strongest interaction, in agreement with the adsorption energy analysis. Furthermore, the distance between C and Co atoms in the top position is the largest in all cases.

Table 5.2: Distance in Å between the relaxed carbon atoms and the Co *fcc*(111) and *hcp*(0001) surfaces .

	<i>hcp</i> (0001)	“ <i>fcc-top</i> ”	“ <i>hcp-top</i> ”	“ <i>bridge</i> ”
1 st site (top)		2.14	2.14	2.11
2 nd site (<i>fcc/hcp</i>)		2.12	2.12	2.11
<hr/>				
<i>fcc</i> (111)				
1 st site (top)		2.16	2.16	2.14
2 nd site (<i>fcc/hcp</i>)		2.14	2.14	2.14

Regarding the graphene adsorption on *fcc*(111) and *hcp*(0001), we can deduce that their energy difference is virtually negligible compared to the thermal energy at the graphene growth temperature ($kT = 60$ meV at $T = 430$ °C). This conclusion, along with the experimental evidence, demonstrates that the graphene transformation reported in the previous section is not driven by the changes in the cobalt stacking underneath graphene, but is to be attributed to the dissolution and recondensation process observed in LEEM. Vice versa, we cannot rule out that a change in stacking of the underlying cobalt accompanies the recrystallization of graphene.

5.2.2 Transformation from Gr-C to Gr-D

The same procedure used in the transformation of the Gr-A was applied in the case of Gr-C. The sample was annealed under the same UHV conditions and monitored by LEEM as in the

previous case. The annealing produced no changes until the sample temperature reached 630 °C. By annealing over 630 °C, it was observed that the carbidic islands start to laterally increase in size. At the same time small precursors enlarge in size, mostly in the regions where two growing fronts meet during the growth procedure, *i.e.* along the grain boundaries, where the concentration of defects is highest. As in the previous case, the moving precursors spaced almost all the surface area, transforming the Gr-C in a new phase, which in the following it will be referred as graphene phase D, Gr-D (Fig. 5.16).

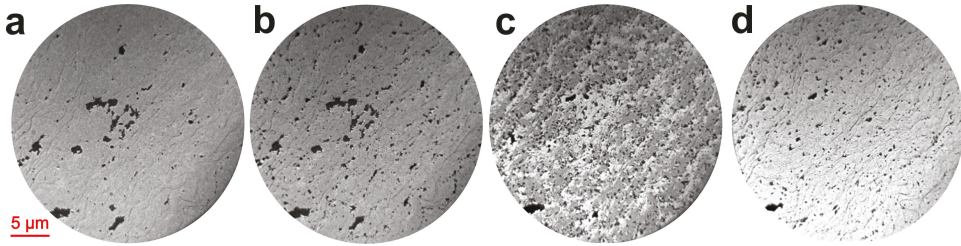


Figure 5.16: LEEM image sequence ($V_{st} = 7\text{eV}$) acquired during the transformation Gr-C to Gr-D at 650 °C.

It has been observed that, the transformation process converted the misoriented graphene domains into epitaxial (1x1) graphene. This fact is immediately visible comparing the LEED patterns on the bright and grey surface area (Fig. 5.17b and c) and furthermore supported by comparing the LEED pattern logarithmic intensity profile taken from a LEED pattern along the curve as indicated in Fig. 5.17d), which leads to the conclusion that almost all the misoriented graphene has been transformed in an epitaxial one.

From the spectroscopic point of view (Fig. 5.17e), the change is not as abrupt as in the LT case. Since Gr-C is grown at higher temperatures, its structural quality is already good, as observed in the previous section. However, since the transformed graphene is aligned with the substrate, following the same fitting procedure as for Gr-A and Gr-B, it is possible to fit the core level with the two components related to the two non-equivalent adsorption sites, C_h and C_t , centered at 284.93 and 284.69 respectively, in very good agreement with the values obtained for the Gr-B. Moreover, the FWHM of those peaks passed from 0.54 eV of the single component in Gr-C to 0.28 eV of the two components in Gr-D. This is because, as mentioned above, the transformation process allow to pass from a random match of the graphene carbon atoms with the underneath substrate to a one to one match, removing the small chemical shifts that gave rise to a larger FWHM. After the transformation, no carbidic components could be observed, removing completely the C_c peak. In addition, the overall peak area of the transformed phase is about 3.5% less than the one before the process, which is comparable with the dissolution of the initial quantity of carbide present on the surface (5%).

The changes observed in LEED are also reflected in the band structure, where the bands formed by the rotational domains are reverted to the bands of perfectly aligned graphene with no contribution leftover from the rotated phase (Fig. 5.18a-c). The Gr-D presents the bands with highest sharpness and with lowest background among all the preparation in this thesis.

The transformation of graphene can be visualized also by acquiring an EDC along the K point of the SBZ (Fig. 5.18d). The density of states in the $E_B = [1, 5]$ eV drastically changes, where the apex of the Dirac cone shifts to higher binding energies. A closer inspection to the region near the

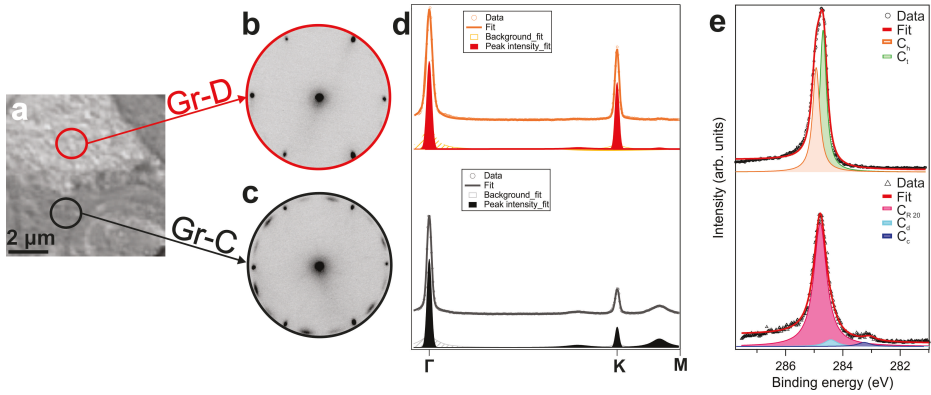


Figure 5.17: a) LEEM image ($V_{st} = 7$ V) acquired at RT after partial Gr-C to Gr-D transformation. The bright surface area represents Gr-D regions. b-c) LEED patterns ($E_{kin} = 40$ eV) taken on the flake and outside respectively. It is clearly visible that the misoriented graphene domains are transformed in epitaxial one. d) Logarithmic plots of the LEED intensities acquired on along the direction as indicated on bottom scale. e) Comparison of the C $1s$ core levels on Gr-C (g) and on Gr-D (h).

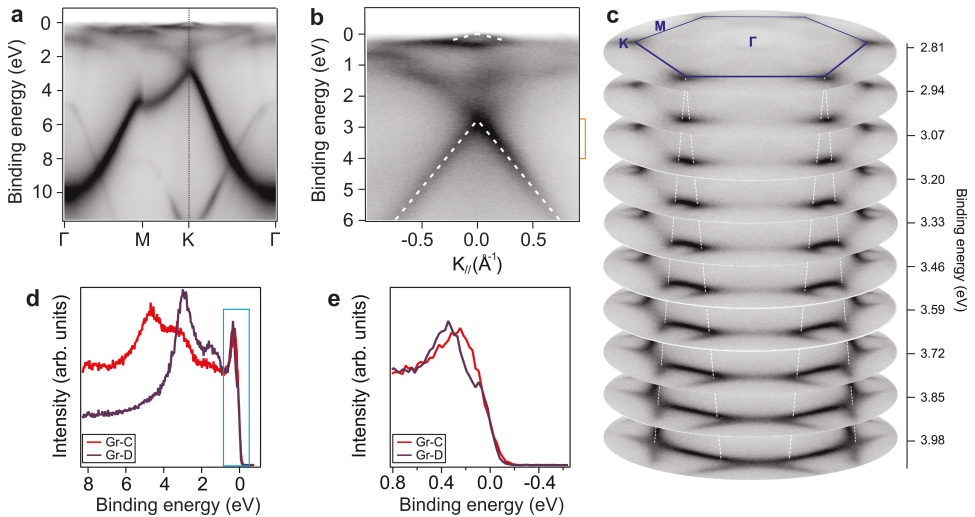


Figure 5.18: a) Momentum map of Gr-D extracted along Γ MK Γ . b) Momentum map, centered at the K point of SBZ, of Gr-D. c) 3D visualization of the SBZ (as indicated in the top image) in the range as indicated on the right side of b), in the range of the Dirac cone. d) Comparison of EDC acquired at the K point of Gr-C and Gr-D. e) Zoom-in of the two EDC curves in the range as indicated by the light blue box in d). All the spectra were acquired using p-polarized 40 eV photons, at sample temperature of -140 °C.

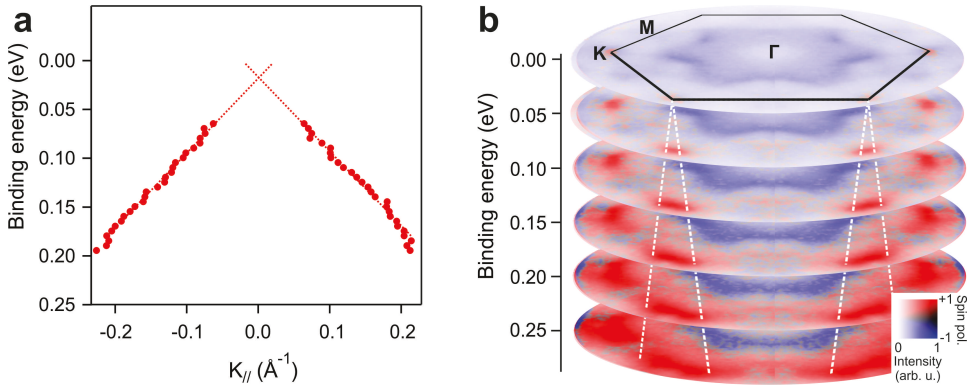


Figure 5.19: a) Fit of E vs. k position of the minicone band: it can be observed that the crossing of the cone can be found in the proximity of the Fermi level. b) 3D spin resolved band structure near the Fermi level, highlighting the single spin behavior of the minicone band. $h\nu = 40$ eV, $T = -140$ °C.

Fermi level reveals that upon transformation the minicone feature shifts by ≈ 80 meV to higher binding energies (Fig. 5.18e).

Minicone

As stated before, the minicone feature is a band, which is formed by the hybridization of C $2p_z$ and Co $3d$ bands. Its peculiarity lies in the fact that it has a conical dispersion similar to the Dirac cone, but with a slope (and therefore also the Fermi velocity) 10 times smaller. The apex of the minicone band is found at the K point of the graphene Brillouin zone, with the crossing lying in the proximity of the Fermi level (Fig. 5.19a). This feature is localized in a narrow energy window, which goes from the Fermi level down to 0.3 eV binding energy. However the most intriguing property lies in the spin character of those bands, which are single spin-polarized, with a majority character. The nature of the minicone is two-dimensional, since we observed that its appearance does not change with varying photon energy. In analogy with the Dirac cone, the apex of the minicone is rounded. Therefore, this band has all the characteristics of the main interacting cone.

In order to get further insight into the nature of the minicone, in the case of epitaxial match at the graphene-cobalt interface, DFT calculations revealed that, by considering an “*fcc-top*” adsorption geometry, the minicone feature is formed upon hybridization of the C $2p_z$ orbitals occupying an *fcc* position in the unit cell and of Co d orbitals (d_{zx} , d_{zy} , d_{xy} and $d_{x^2-y^2}$) from the topmost substrate layer. As visible from Fig. 5.20 top, the minicone has prevalently a carbon-character, since the density of states is dominated by the carbon atoms occupying the *fcc* site of the cobalt substrate. The reduced slope of the band can be justified since the hybridization involves the “heavy” d -electrons of the cobalt substrate, therefore reducing the speed of the charge carriers.

The single spin behavior of the minicone band has been confirmed by spin-resolved momentum mapping. As visible from the figure 5.19, the band presents the same spin polarization along with the entire band, with an exclusively majority spin polarization behavior. We verified that upon reversal of the sample magnetization, the projection of the minicone spin flips also its direction, therefore behaving ferromagnetically. Using the procedure described in Appendix B, we were

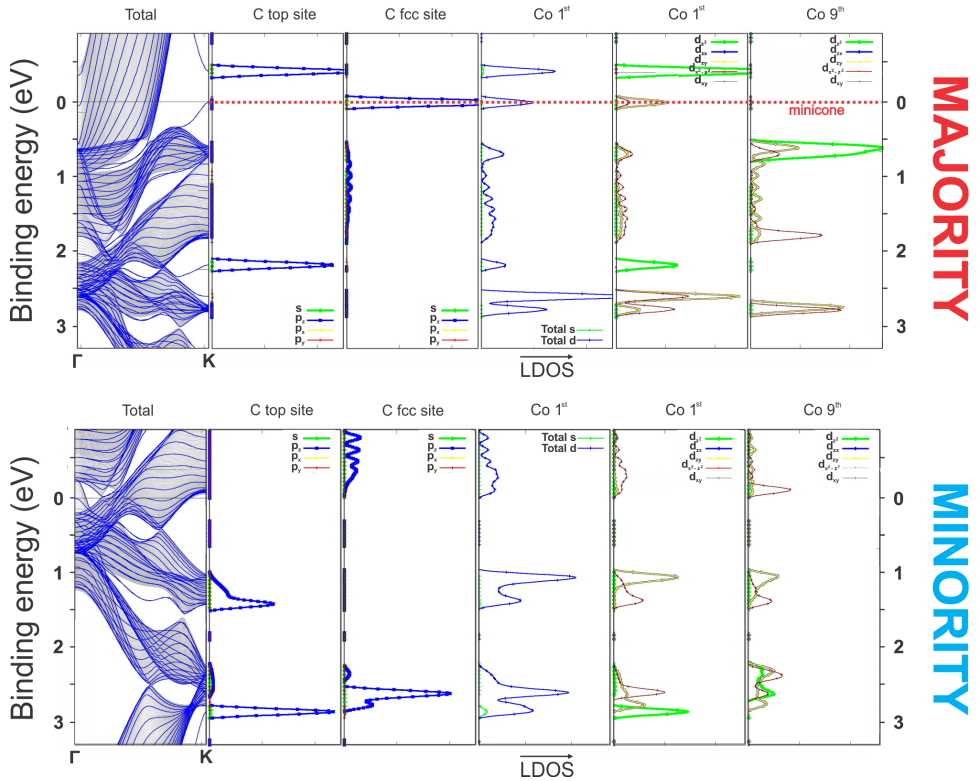


Figure 5.20: Momentum resolved projected local density of states for the majority (top) and the minority (bottom) spin channels for graphene on Co(0001), considering an “*fcc-top*” adsorption geometry.

able to estimate the value of spin polarization on the minicone states, being $+53\pm 8\%$.

On contrary to what has been stated in the literature [21], the formation of minicone is observed also in Gr-C, characterized by misoriented graphene domains. Since the orientation of misoriented domains with respect to the high symmetry directions of the cobalt substrate span over a wide window, centered at $\approx \pm 18$ degrees, the center of the minicone band is found at ± 18 azimuthal angle from the Co K point. Therefore, near the Fermi level, the momentum map is characterized by 12 bands whose azimuthal distribution is spread, leading to the formation of arc-shaped bands. The spin-resolved momentum imaging over the binding energies near the Fermi level revealed that the minicone bands are single spin-polarized. The single-spin behavior is observed in both domains, the ones oriented at -18 and the ones at $+18$ degrees from the Co K point. (Fig. 5.21). The measured degree of spin polarization of the minicones belonging to the misoriented graphene domains is about $+47\pm 7\%$, in both ± 18 oriented domains, being comparable to the value obtained on solely epitaxial graphene.

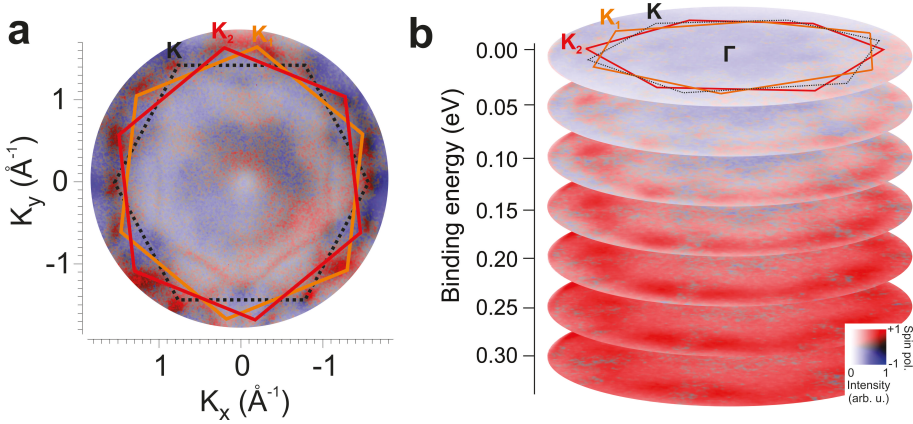


Figure 5.21: 3D spin resolved plot of the SBZ near the Fermi level $E_B = [0, 250]$ meV of a Gr-C sample. The presence of rotational domains reflects in the band structure, where two Brillouin zones (red and orange) corresponding to the ± 18 degrees domains with respect to the substrate (black) are observed. $h\nu = 40$ eV.

By acquiring two distinct momentum maps in the region near the Fermi level, one along the ΓK direction of Gr-C SBZ (Fig. 5.22a) and another along ΓK direction of the Gr-D SBZ (Fig. 5.22b) we compare appearance of the minicone band in Gr-C and Gr-D. The fit of the minicone band of both domains, reveal that the slope of the band is equivalent in the two cases. The only difference observed is the relative position of the band with respect to the Γ point of the Brillouin zone (Fig. 5.22c). Quantitatively, in the case of Gr-C, the apex of the minicone band is found at 1.9% larger k values with respect to the apex in Gr-D. Regarding the momentum width, the minicone band in Gr-C are characterized by a 5.4% larger FWHM with respect to the one in Gr-D.

A question which comes up at this point is which is the mechanism standing behind the observed behavior of the minicone states in the misoriented graphene domains. For explaining that, theoretical calculations were performed on the graphene/cobalt system, considering additional two adsorption geometries. In the first one, the “*hcp-top*” (Fig. 5.15b), one carbon atom in the unit cell is placed on top of a cobalt atom of the substrate, while the other one is placed in an *hcp* site. In the second considered adsorption geometry, both carbon atoms in the unit cell are placed on a

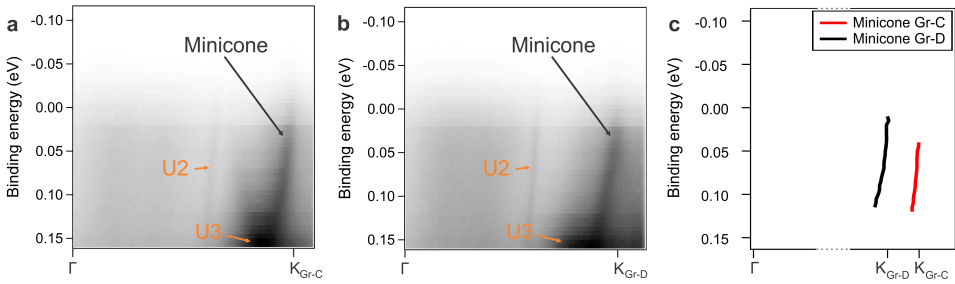


Figure 5.22: a) Momentum map acquired along ΓK direction of Gr-C in the region near the Fermi level, showing the minicone graphene state. b) Momentum map acquired along ΓK direction of Gr-D in the region near the Fermi level, showing the minicone graphene state. c) Comparison of the fitted slopes of minicone bands in Gr-C and Gr-D. $h\nu = 56$ eV, $T = -140$ °C.

bridge site (Fig. 5.15c), *i.e.* one carbon atom is placed between a *top* and a *fcc* site, while the other one between a *top* and an *hcp* cobalt site.

In the “*hcp-top*” graphene adsorption geometry (Fig. 5.23a), the appearance of the bands is very similar as in the case of the “*fcc-top*” geometry considered in the epitaxial case as the energetically most stable one. The main graphene Dirac cone is found at around 3 eV, characterized by a minority spin behavior on its apex, as in the “*fcc-top*” case. The minicone band is found also in this case, with its apex shifted to higher binding energies.

In the “*bridge*” adsorption geometry (Fig. 5.23b), the graphene main Dirac cone is found at lower binding energies, slightly below 3 eV. The minicone band is formed also in this adsorption geometry, but with no gap opening at the K point. This can be justified since the two atoms in the graphene unit cell occupy similar positions with respect to the substrate and therefore, there is no symmetry breaking leading to gap opening. In this geometry, the slope of the minicone band is higher with respect to the “*hcp-top*” and “*fcc-top*” adsorption geometries.

The three adsorption geometries considered above show that the minicone band is formed in all the cases. In the case of Gr-C, the analysis of the adsorption sites of the carbon atoms with respect to the substrate does not show any abundance of one between the selected ones. Therefore, it would be almost straightforward to assume that the minicone band is formed also in graphene C. However, an additional fact should be considered, which is the symmetry and the momentum dispersion of the cobalt substrate band which hybridize upon the formation of the minicone. Since from LEED analysis emerge that the SBZ of Gr-C is rotated by ± 18 degrees, the K point is also found at this angle with respect to the epitaxial case. Therefore, by analyzing the symmetry of the Co *3d* band, which hybridize with the graphene overlayer originating the minicone band, we were able to determine that at 18 degrees from the K point of the Co substrate, the same *3d* band is found. Its distance from the Γ point is slightly larger with respect to the ΓK distance, which can justify also the larger k value of the minicone band in Gr-C with respect to Gr-D. Consequently, we can state that the minicone band in Gr-C originates from the same hybridization process which was found for epitaxial graphene and therefore, this single-spin band can be considered to be a general feature of the graphene/cobalt interface, which is not influenced by the epitaxial or misoriented relation at the interface.

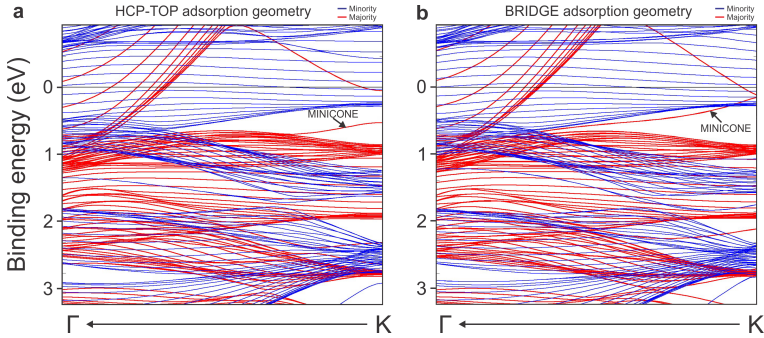


Figure 5.23: a) DFT band structure calculations for the graphene/cobalt system with a “hcp-top” adsorption geometry. b) DFT band structure calculations for the graphene/cobalt system with a “bridge” adsorption geometry. The minicone graphene band is indicated in both images.

5.3 Characterization of the graphene transformation procedure

The Gr-A to Gr-B and the Gr-C to Gr-D transformations were studied in LEEM experiments performed at sample temperatures in the range 555 to 580 °C, and 630 to 680 °C respectively. The observed temperature dependence allowed us to estimate the activation energy of the process. The reaction rate was determined by measuring the change in fractional area of Gr-B as a function of time at constant temperature. This quantity, denoted as α (Fig. 5.24 top), shows an Arrhenius temperature dependence. By fitting $\ln(\alpha)$ with respect to the inverse temperature (Fig. 5.24 bottom), we could estimate the value of the activation energy of the process, being 1.84 ± 0.11 eV in the Gr-A to Gr-B transformation, while 1.71 ± 0.08 eV in the Gr-C to Gr-D transformation. The activation energy in this range is compatible with the detachment of a graphene edge from the cobalt [128, 129, 130].

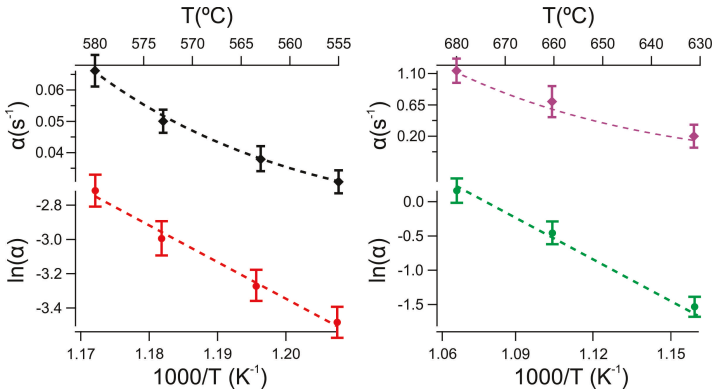


Figure 5.24: Arrhenius plot of the LT (left) and HT (right) graphene transformation. Top: Dependence of α on the sample temperature. Bottom: Arrhenius plot of the $\ln(\alpha)$ versus $1000/T$. The activation energy of the transformation process is extracted from the slope of the line fit.

Moreover, as mentioned previously, the precursor phase (tiny dark structures in LEEM) was

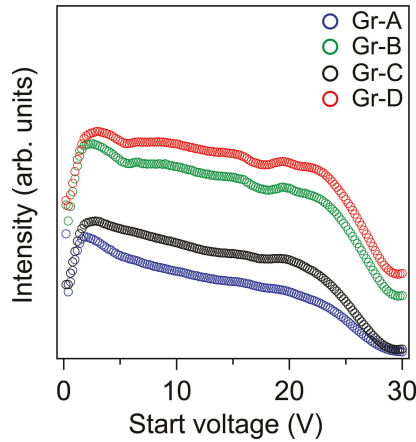


Figure 5.25: LEEM-IV curves of the different graphene phases: Gr-A, Gr-B, Gr-C, Gr-D.

shown to have a carbidic nature. We also found that the carbidic species dissolve into subsurface layers above 400 °C. Considering this evidence, we suggest that a supersaturation between carbon dissolution and recondensation occurs within the area occupied by the precursor. This is not surprising since the dissolution process has a lower activation energy (1.5 eV) [131] compared to the barrier found above. Therefore, the transformation propagates by detachment of carbon atoms on one side (Gr-A, Gr-C), dissolution and re-attachment on the other side (Gr-B, Gr-D).

The precursor path is self-terminated whenever its direction crosses a previously traced path. The particular labyrinthine path (Fig. 5.5 and 5.16) traced by the precursor phase resembles the patterns observed in Pd growth on Ru [132], as well as Sn on Cu [133]. In the case of Pd/Ru the patterns are reported to originate from the surface alloy forming around the islands. In analogy to that case, we propose that the particular motion of the precursor islands in this work is related to the changing bulk carbon density at island boundaries.

In order to compare the different graphene phases, before and after the transformation process, LEEM-IV curves were acquired at each stage (Fig. 5.25). It can be noted that the Gr-C has a higher reflectivity with respect to the Gr-A. By comparing the two reflectivity curves after transformation (Gr-B and Gr-D), it can be noted that the shape and intensity of the two structures is almost similar. This means that the graphene obtained via the two transformation processes described above leads to the formation of an equivalent structure (as it was previously determined by LEED and XPS). Therefore the formation of a monolayer graphene layer with elevated crystallographic quality can be obtained by both procedures, having a very similar outcome.

In conclusion, a complete diagram resuming the processes studied in this work can be outlined (Fig. 5.26). Either by passing through a low temperature process, which is more suitable for graphene growth on lower thickness films, or passing through a high temperature process, the outcome is similar, namely a graphene layer with low amount of defects, with a thickness of a single atomic layer.

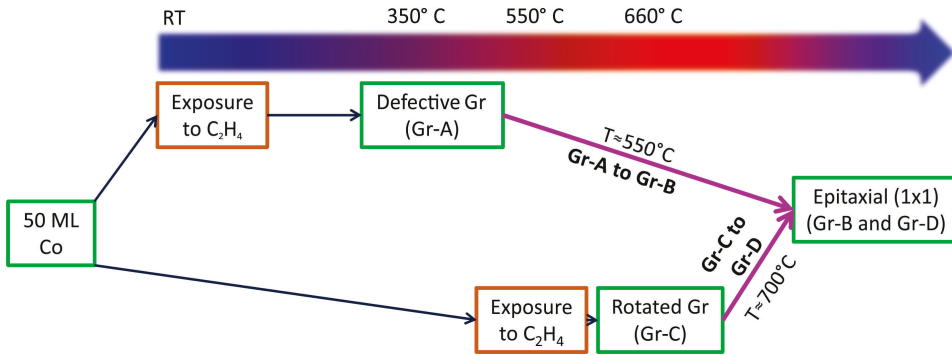


Figure 5.26: Diagram resuming the CVD growth procedures used in this work.

5.4 Exposure of the graphene/cobalt interface to air

In order to make a further step towards the practical applicability of the graphene-metal interface, the Gr-D has been exposed to atmosphere, with the aim to verify if the peculiar properties of the interface are preserved in realistic working conditions. In practice, Gr-D has been exposed to air for 20 min, after which the sample has been re-inserted in UHV, and shortly annealed to 250 °C to remove surface contaminants.

Momentum maps (in the region near the Fermi level) were measured in the two cases: after Gr-D growth and after reinserting the same sample after air exposure followed by a short annealing. In Fig. 5.27a and b, the momentum maps, centered at the K point of the SBZ, measured prior and after air exposure are presented. By fitting the graphene-related features, using Lorentzian functions as described in the previous chapter, it was possible to estimate that the position and the slope of the mini-Dirac cone feature do not change upon treatment. This is also confirmed by angle integrated valence band spectra (not shown), acquired near the Fermi level, whose shape and intensity remains unchanged. The only appreciable difference can be observed in the momentum width (MW) of the mini-Dirac cone (Fig. 5.27c and d). The fit reveals that the MW at the apex of the conical feature increases by around 8%, indicating the presence of incoherent scattering targets due to the residual oxygen present on top and bottom of the graphene layer.

Photoemission spectra of the carbon, cobalt, and oxygen core levels were measured in order to confirm the results observed in reciprocal space mapping (Fig. 5.27e, f, g). By comparing the photoemission intensities measured immediately after CVD growth and after air exposure, it can be appreciated that the O 1s spectra show a small rise in intensity (Fig. 5.27e). This intensity could derive both from the presence of residual oxygen on top of the graphene network or from the intercalation of oxygen at grain boundaries and defects in the network. This residual oxygen reflects in a slight modification of the C 1s spectra (Fig. 5.27f), which presents a shift (lower than 50 meV) towards lower binding energies of the single components C_{ii} and C_i . The fit of the C 1s intensities reveals that the total quantity of carbon remains unchanged, and the FWHM of the single components is not modified upon air treatment. As a final proof, the photoemission intensity was measured at the substrate Co 3p level. It is observed that the shape, the position, and the intensity are almost the same upon the treatment (Fig. 5.27g).

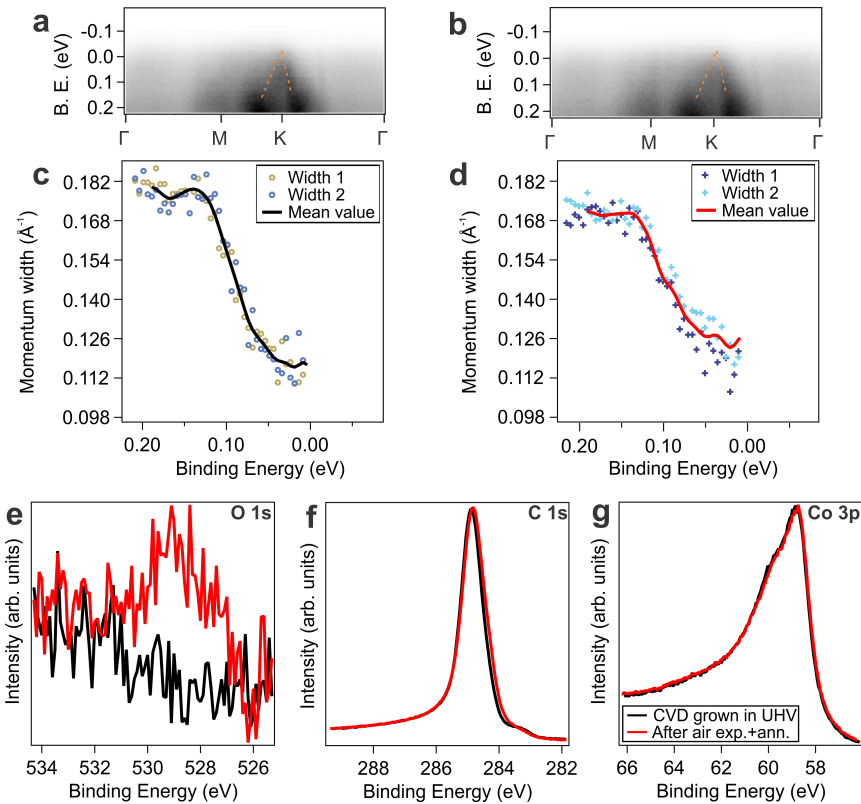


Figure 5.27: a) Momentum map ($h\nu = 56$ eV) of CVD grown graphene acquired near the Fermi level in the region of the minicone graphene band. b) Momentum map ($h\nu = 56$ eV) of graphene after air exposure, reinsertion in UHV and 250°C annealing. c) Momentum width and its mean value obtained by fitting two minicone bands of the SBZ from the sample in a). d) Momentum width and its mean value of the sample in b). e) O $1s$ ($h\nu = 650$ eV) f) C $1s$ ($h\nu = 380$ eV) g) Co $3p$ ($h\nu = 150$ eV) spectra before and after air exposure and reinsertion in UHV followed by an annealing to 250°C .

Chapter 6

Modification of the graphene/cobalt interface: atomic substitution and intercalation

Despite the demonstrated application potential, it should be noted that free-standing graphene possesses a nearly zero band gap as well as the inertness to reactions, which does not necessarily favor its application in the field of semiconductors and sensors. This is one of the reasons motivating the research aimed at modifying the electronic properties of graphene, including reactions of graphene with organic and inorganic molecules and chemical modification of the graphene layer. A band gap opening of graphene by doping, intercalation, and striping would be helpful for the application in functional nanoelectronic devices. In this regard, considering the graphene/cobalt interface, the possibility to alter the properties of the single- spin polarized minicon band would be potentially appealing for applications. Therefore, we will show how the graphene/cobalt interface can be modified in order to achieve desired properties of the nanocomposite.

In practice, the modification of the electronic and magnetic properties of substrate-supported graphene can be achieved via the addition of gaseous or solid compounds, which can be deposited on top, incorporated in the carbon network or intercalated at the graphene/substrate interface. Among the most common compounds, nitrogen and oxygen emerge as two of the most important elements to be considered in the test of real applications of graphene-based devices, since they compose 99% of the Earth's atmosphere.

6.1 Oxygen exposure

We have already proven the efficiency of the graphene layer as passivation barrier towards metal layer oxidation at room temperature in the previous chapter. In order to intercalate oxygen at the graphene/substrate interface, the exposure to O₂ should be therefore performed at higher sample temperature. The intercalation has been achieved on a sample composed of epitaxial graphene with an additional presence of small rotated domains. After stabilizing the sample temperature within values in the 200 - 230 °C range, the system was exposed to a partial pressure

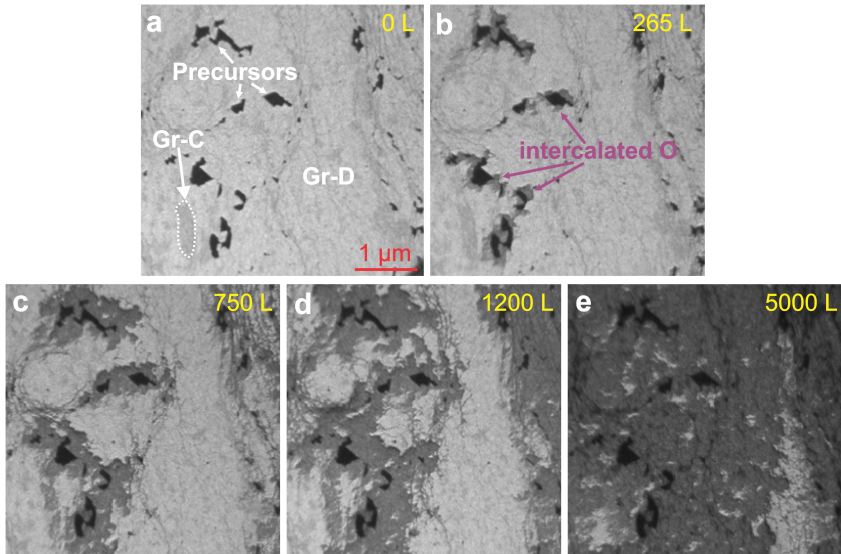


Figure 6.1: Series of LEEM images ($V_{st} = 13$ eV) showing the intercalation process during O_2 exposure ($p=1\cdot 10^{-6}$ mbar) at $T = 220$ °C. a) Surface as prepared, consisting of heterogeneous Gr/Co and holes in the layer (black). Epitaxial regions, characterized by brighter contrast, cover the majority of the surface, while small rotated island (Gr-C) have a gray contrast. b-d) Sequence of images showing the key role of holes, rotational domain boundaries and steps in the intercalation process. The intercalated and not intercalated (pristine) area have dark gray and white contrasts respectively; holes in the graphene are visible as black island. The O_2 dose is indicated in the images. e) Surface after 10000 L O_2 exposure at 220 °C.

of $5\cdot 10^{-6}$ mbar of oxygen.

In order to evaluate real-time changes, *i.e.* to understand the intercalation kinetics, the process was imaged by LEEM [134]. The sequence of LEEM images in Fig. 6.1 shows the evolution of the system during the intercalation process. Initially, at low O_2 dose, the changes are observed near the precursors in the epitaxial regions of the layer, which act as catalytic centers for the O_2 dissociation, promoting the production of atomic oxygen. The development of a new phase, corresponding to the intercalated regions, appears as dark gray contrast in the images. This new phase isotropically extends over the epitaxial regions, following the step morphology of the film. On rotated graphene domains, the oxygen intercalation initiates spontaneously at the boundary with the epitaxial phase, while its activation needs higher dose with respect to the epitaxial phase (Fig. 6.1c-d). However, once started, the intercalation is faster as compared to the epitaxial case, meaning that the diffusion of oxygen atoms below the rotated phase is favored over the epitaxial one. This behavior is most likely due to the lower adhesion of the rotated graphene to the substrate, also resulting in an increased graphene/substrate distance, as it was also observed in the graphene/nickel case [135]. We note that the intercalation proceeds only in O_2 atmosphere and hence the extent of the intercalated area can be controlled by varying the oxygen dose. The intercalation rate in our experimental condition is $0.01 \mu m^2/s$, as estimated from the time-dependent coverage of the intercalated areas, visible in the LEEM sequence.

After intercalation, the integrity of the graphene layer and the characterization of the oxygen

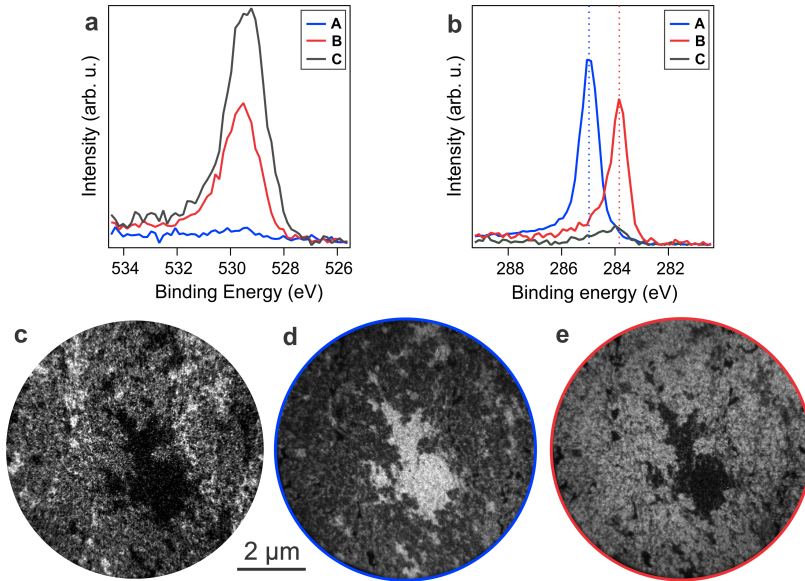


Figure 6.2: a, c) local spectra and XPEEM image at the O $1s$ core level ($h\nu = 650$ eV) acquired after intercalation, evidencing the inhomogeneous O enrichment: for not-intercalated regions (A), intercalated areas (B) and O-rich areas (C) located close to the holes (*i.e.* the intercalation starting points). b) local spectra at the C $1s$ core level ($h\nu = 400$ eV) for the pristine (not intercalated) regions (A) and intercalated regions (B intercalation is related to the shift of the BE by -1.16 eV, and of O-rich areas (C). d, e) XPEEM images obtained at the non-interacting peak (A) and at the interacting peak (B) characterized by a clear inversion of contrast.

lateral distribution was verified using XPEEM. The extent of the intercalated/non-intercalated regions was sufficiently large in order to separate their contributions with spatially resolved techniques within the same field of view of an image.

The intercalation process is associated with subsurface oxygen enrichment. The spatially resolved measurements at the O $1s$ core level highlights that the oxygen is inhomogeneously distributed across the surface, being mostly absent in the “pristine regions” (*i.e.* non-intercalated), while a higher concentration is localized close to the holes and domain boundaries (Fig. 6.2a-b). The oxygen photoemission spectrum in all the oxygen intercalated regions is single peaked and centered at $E_B = 529.6$ eV with a FWHM of 1.6 eV. The quite high width of the oxygen photoemission intensity indicates the presence of oxygen atoms in different chemical environments, *i.e.* different binding sites with respect to the cobalt substrate. The absence of the oxygen XPS signal in the “pristine regions” demonstrates that the graphene layer itself is impermeable to O₂ and that the intercalation proceeds by the diffusion of the oxygen atoms from the exposed metal patches (which are not covered by graphene), where they are initially adsorbed (and dissociated).

Besides the O $1s$ spectrum, also the C $1s$ core level exhibits significant changes in the intercalated regions (Fig. 6.2c). The C $1s$ peak of graphene, centered at 285.0 eV binding energy, shifts by 1.2 eV towards lower binding energy (283.8 eV), which is a typical fingerprint of the graphene decoupling from its support [136, 137, 138, 139, 140]. The binding energy shift derives from the charge redistribution due to the presence of oxygen, which suppresses the charge transfer

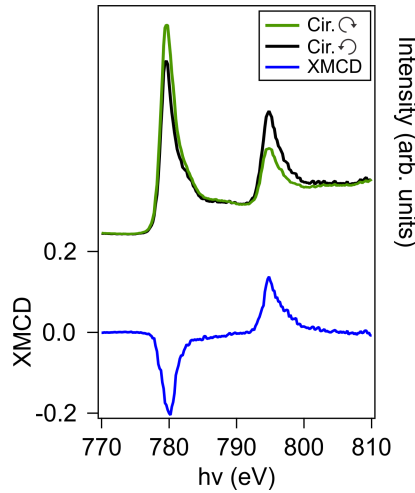


Figure 6.3: XMCD absorption spectra at the Co $L_{2,3}$ edges of an oxygen intercalated region, at varying polarization and sample magnetization. In the bottom XMCD spectra it can be observed that the ferromagnetic behavior of the cobalt substrate is preserved upon oxidation.

between the graphene and the metal substrate (quasi-free-standing graphene). The intensity of photoemission spectra remains identical as in the pristine regions and unchanged with respect to the measurements before the intercalation procedure, meaning that the amount of C possibly removed during the treatment is below the XPS detection limit.

To get an insight into the quantity of oxygen trapped below the graphene network the intensity of the photoemission spectra of the carbon and oxygen core levels are compared. However, several factors should be taken into account, like attenuation length, electron damping, and photoionization cross section correction. Considering the above-listed factors, the ratio between oxygen and carbon atoms is 1:4. Furthermore, it is fundamental to investigate the effect of the presence of oxygen on the substrate chemical properties. The oxidation of the Co substrate can be excluded on the base of Co $3p$ photoemission spectrum and the absorption spectra at the Co L-edge (Fig. 6.3). In fact, in both cases, the oxide component, absent in our experiments, should appear at higher binding energies (XPS) and result in a different shape of the adsorption spectra (XAS).

To investigate the magnetic coupling behavior at the graphene/cobalt interface and to obtain quantitatively the related magnetic moments of the system, X-ray Magnetic Circular Dichroism (XMCD) is employed (Fig. 6.3). The XMCD spectrum (blue line in lower part of Fig. 6.3) is obtained by the difference $I_{XMCD} = I_{C-right} - I_{C-left}$, leading to a negative signal at the Co L_3 edge and positive at the L_2 edge. Following the sum rules reported in [141], the orbital and spin magnetic moments were calculated. The values ($\mu_L = 0.18\mu_B$ and $\mu_S = 1.40\mu_B$, where $\mu_B = e\hbar/2m_e$ is the Bohr magneton) are comparable with the values obtained for metallic cobalt [141].

In order to get an insight into the effects of oxygen intercalation on the electronic structure of the system, momentum mapping has been performed, using the band structure of the Gr/Co surface acquired before intercalation as a reference. As discussed in the previous chapter, the

interaction of graphene with Co leads to the formation of two Dirac-like features.

Oxygen intercalation dramatically alters the electronic structure of the system in the region near the Fermi level. By acquiring momentum maps on a partially intercalated region, the effect on the band structure induced by the presence of oxygen can be appreciated (Fig. 6.4b). In the partially intercalated regions, a new feature visible as additional states crossing the Fermi level can be observed. This feature originates from the lifting of the π - d hybridization, leading to a shift of the graphene π band towards lower binding energies. The Dirac point of the new states is at 0.43 eV above the Fermi level (*vs.* $E_B = 2.83$ eV of the pristine case), indicating a net hole doping of the graphene layer. Moreover, upon intercalation the Fermi velocity increases its value by the $\approx 9\%$ with respect to the pristine case, ($v_F = 1.09 \cdot 10^6$ m/s), that is closer to the value found for free-standing graphene [142].

In a region of fully oxygen intercalated graphene (Fig. 6.4c), the carbon overlayer is completely decoupled from the substrate. This turns into the complete disappearance of both, the Dirac cone present at 2.8 eV binding energy and the minicone at the Fermi energy, with the remanence of the graphene bands assigned to the decoupled graphene. The fitting of the π bands in the range [0, 4] eV allows us to estimate that the values of the Dirac point and Fermi velocity of the new features upon O₂ intercalation are about the same as determined in the partially intercalated case.

The dispersion of the graphene bands can be assumed as linear, therefore the momentum width (extracted from the Lorentzian fit as described before) is proportional to the electronic scattering rate deriving from the many-body interactions such as electron-electron, electron-phonon and electron-defect interactions. The reduced width of graphene Dirac cone, at the same $E_D - E_B$ point (*i.e.* corresponding to the energy scale referred to the Dirac point) in the case of oxygen-intercalated graphene confirms the free-standing tendency of the system (Fig. 6.4d).

We notice that the value of FWHM and v_F for the intercalated graphene obtained in our measurements is in good agreement with those obtained on a similar work performed on Ni(111) [135]. Finally, we note that the spectra acquired in normal emission, around the Γ point (Fig. 6.4e), show that the intensity of the Co $3d$ bands is reduced upon damping after O₂ intercalation. This effect appears differently for the two $3d$ bands (majority and minority). The band present at $E_B = 1.25$ eV (majority) is almost fully attenuated, while the other feature present at 0.32 eV (minority) remains almost unaffected. This result is in agreement to previous spin-resolved studies performed on an oxygen covered cobalt surface [143], where in normal emission, the intensity lowering is more pronounced in the majority channel. At the same time, the relative intensity difference between the two spin channels also decreases.

Our measurements point out that oxygen intercalation decouples the graphene electronically from the Co substrate, which may lead to modifications of the peculiar spin polarization induced in the pristine graphene by the interaction with Co (disappearance of the single spin graphene minicone band).

Reversibility of the intercalation process

After having characterized the oxygen-intercalated system, the possibility of cycling the process, *i.e.* removing the oxygen from the surface and restoring the pristine graphene layer was investigated.

Studies on similar oxygen intercalated graphene hybrids showed that the oxygen trapped below graphene could be removed from the interface by UHV annealing in the range between 250 °C and

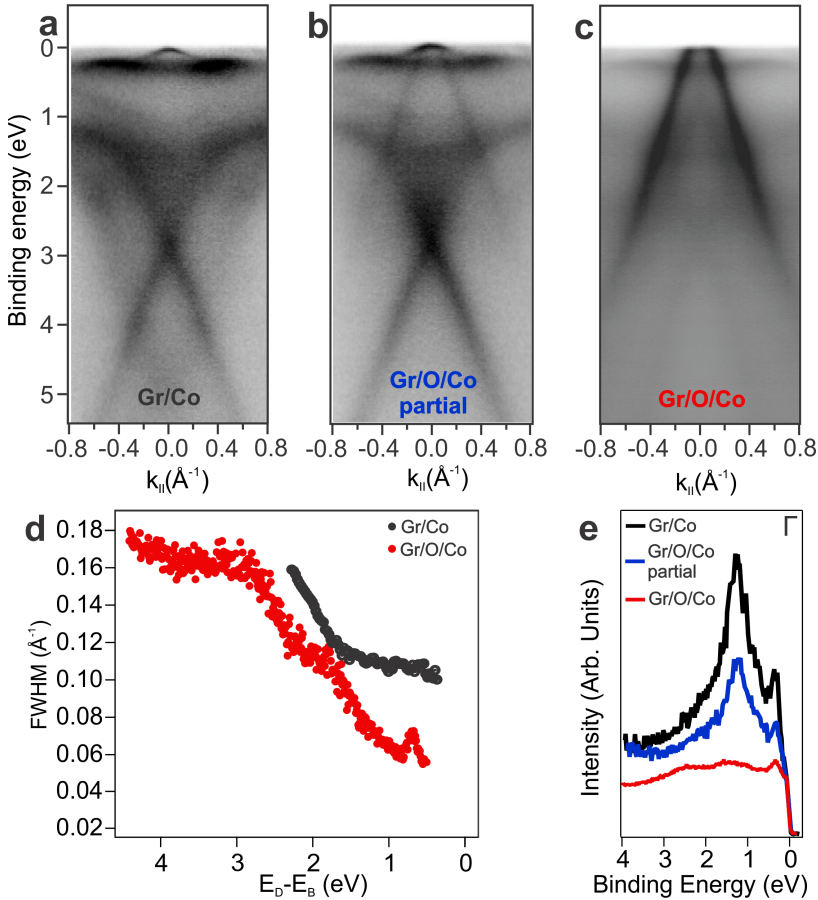


Figure 6.4: Momentum map acquired at the K point of: a) pristine Gr/Co interface b) partially oxygen intercalated region c) fully oxygen intercalated region. d) Energy dependence of the momentum width of the graphene related features in the electronic structure. E_D indicates the position of the Dirac cone in the two cases. e) VB photoemission spectra acquired in normal emission of the three phases listed above. All spectra were acquired at $-140\text{ }^\circ\text{C}$, using p-polarized photons of $h\nu = 56\text{ eV}$.

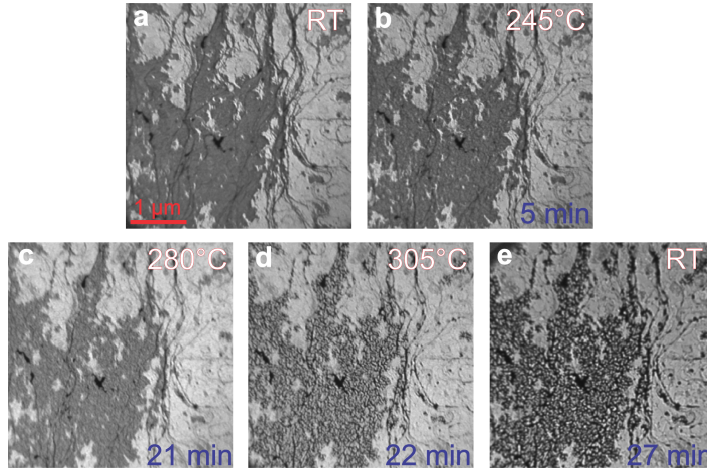


Figure 6.5: a-e) sequence of images LEEM images ($V_{st} = 14$ V) showing the surface changes during UHV annealing of a partially oxygen intercalated area. Temperature and annealing time are indicated.

420 °C [136, 137]. However, in this temperature range also falls the graphene etching temperature, a process which irreversibly damages the graphene network, leading to the formation of defects [136, 137, 140].

In order to investigate the condition for oxygen desorption from the graphene/cobalt interface, a partially oxygen-intercalated sample was annealed in UHV up to 425 °C, in two annealing ramps, while following the changes in real-time LEEM imaging (see sequence Fig. 6.5). After the first ramp (rate = 0.5 °C/s), the sample temperature was kept constant at 370 °C for 21 min, observing no visible changes. During the second ramp up to 420 °C (rate = 0.16 °C/s), severe modifications can be observed in the intercalated region within a small temperature window. The image contrast in the intercalated regions started to change at a temperature of about 410 °C, reaching a steady state after 5 minutes at a constant temperature of 420 °C. The LEEM image (Fig. 6.5a) shows in those regions an inhomogeneous contrast, while the initially O-free regions remain essentially unchanged after the UHV annealing treatment.

XPEEM at O $1s$ core level demonstrates that oxygen has been almost completely removed from the intercalated regions (Fig. 6.6b). Contextually, the C $1s$ peak (Fig. 6.6c) shifts back to its original value (pristine graphene), *i.e.* at higher binding energy. Only a minor component associated to a residual intercalated island or unsaturated carbon (dangling bonds) is present at $E_B = 284.0$ eV. The total C $1s$ intensity decreased by 20% as compared to the O-free regions, indicating a deterioration of the carbon layer during oxygen removal. In the C $1s$ spectrum, no carbidic contribution at lower binding energies is detected, suggesting that the surface carbon is present as graphene patches. As an explanation for the deterioration of the graphene layer, we suggest that during desorption, the oxygen atoms recombine partially with the C atoms from the graphene. In the limiting case that no other channel for C removal is accessible, it could be expected that oxygen desorbs principally as CO and CO₂, while O₂ production should be much scarcer given the relative atomic density (C:O = 1:4). However, other channels for carbon removal are available in the temperature range used, such as carbidic bulk segregation, as observed in the

previous chapter, and therefore the relative abundances of desorbing gases could be different.

In order to restore the starting conditions, *i.e.* obtain a continuous and uniform graphene layer, the damaged regions were locally “healed” via ethylene CVD, using the same conditions as for the preparation. This procedure induces the re-growth in the C-poor regions, and no second layer nucleation is observed. In this way, a full graphene layer is created, allowing for the intercalation process to be repeated multiple times. After a full graphene re-growth, oxygen was successfully intercalated again at the interface, proving that the process can be cycled.

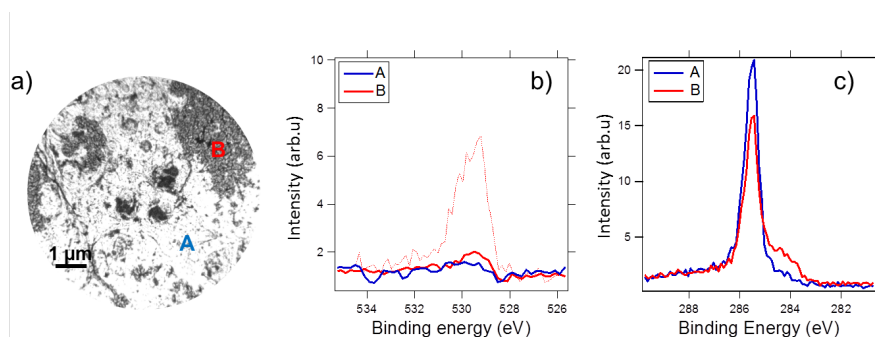


Figure 6.6: a) LEEM image ($V_{st} = 5$ V) acquired after UHV annealing for oxygen removal. b) Local spectra for not-intercalated regions (A), and the intercalated areas (B); for comparison the O $1s$ spectrum ($h\nu = 650$ eV) prior to the treatment is shown (thin red dotted line). c) corresponding local spectra at the C $1s$ core level ($h\nu = 400$ eV) for the not intercalated regions (A) and intercalated regions (B).

Formation of a cobalt oxide phase

The oxygen intercalation process has been continued obtaining a full oxygen intercalated graphene phase across the entire sample. In a second step, such a sample has been exposed to an additional oxygen dose, while keeping its temperature in the range between 200-250 °C, being able to trap an increased quantity of oxygen atoms at the graphene/substrate interface. LEEM images after a 20000 L of total oxygen exposure show that the sample is heterogeneous (Fig. 6.7a). The LEEM-IV analysis reveals that three different regions can be identified based on the shape of the reflectivity curve (Fig. 6.7b). It can be noted that the spectra from the region 1 resemble the one observed immediately after the intercalation described in the previous paragraph, indicating the presence of an oxygen physisorbed phase underneath graphene. The reflectivity curves of the two phases are, however, different from the one in 1. The phase 2 is a different phase that forms upon the second oxygen intercalation step. The phase 3 instead is the phase that separates the phase 1 from the phase 2, acting as the precursor of the formation of phase 2 expanding over the phase 1.

XPEEM characterization at O $1s$ edge shows that the oxygen coverage is not uniform. The integration of the photoemission intensity across all the O $1s$ region (Fig. 6.7c) allows identifying the three different structures observed by LEEM imaging, each having a different quantity of oxygen. The lowest quantity of oxygen is present in the oxygen physisorbed phase, the one obtained after the first intercalation step. The highest quantity of intercalated oxygen is present in the phase 3. This precursor phase is rich of oxygen and allows for the formation of the neo-formed

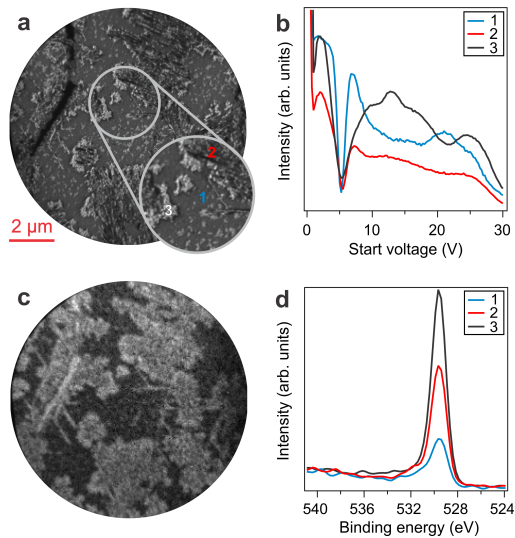


Figure 6.7: LEEM image ($V_{st} = 4$ V) of the sample after second oxidation procedure showing the heterogeneous behavior of the surface. b) LEEM-IV curves of the different phases indicated in the inset in a). c) Integrated XPEEM image along the O $1s$ core level of the region in a) showing the inhomogeneous distribution of oxygen across the surface. d) Local O $1s$ spectra ($h\nu = 650$ eV) of the three different regions in a).

phase B, which has an intermediate oxygen quantity with respect to the 1 and 3 case. However, in all three cases, the binding energy at the O $1s$ edge is peaked at the same energy, being 529.6 eV, with a FWHM of the peaks of about 1.2 eV. This value indicates the presence of oxygen in its atomic form, while the large value of the FWHM (for comparison: 0.7 eV for Co_3O_4 and 1 eV for CoO [144]) suggest the presence of multiple adsorption sites for the oxygen atoms (Fig. 6.7d).

Since the oxygen core level mapping is not sensitive to the presence of oxide species, Co $3p$ and Co L-edge spectra were acquired to verify the oxidation state of the substrate. While the system exhibits metallic behavior in phase 1, the composition of cobalt changes in the neo-formed phase 2. Photoemission measurements at Co $2p$ level (Fig. 6.8a) reveal that underneath the phase 2, the cobalt layer has been oxidized. The oxidation shifts the intensity of the Co $2p$ level to higher binding energies of about 1.98 eV [144]. The oxidation is also confirmed by XAS measurements at the Co L-edge (Fig. 6.8b), where the appearance of a small shoulder at lower photon energies can be observed. Moreover, the shape of the XAS spectra in the region around 782 eV changes with respect to the one measured on the phase 1 (Fig. 6.3b), indicating the formation of an oxide phase [145]. The values of orbital and spin magnetic moments derived from the XMCD spectrum (blue spectra in Fig. 6.8b) after the second intercalation are $\mu_L = 0.18\mu_B$ and $\mu_S = 0.84\mu_B$. The reduced value of the magnetic circular dichroism and of the total magnetic moment confirms the presence of an antiferromagnetic CoO phase [146].

From the spectroscopic point of view, the presence of cobalt oxide as graphene support also affects the graphene/substrate interaction. The C $1s$ spectrum acquired on the phase 2 shows that the emission is peaked at 284.5 eV, a value which is intermediate between the pristine and the oxygen intercalated phase.

In order to discriminate the factor influencing further oxidation of the sample, the dependence

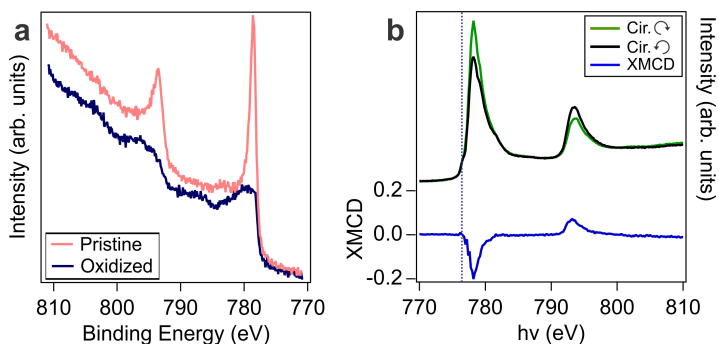


Figure 6.8: a) Co $3p$ spectra ($h\nu = 920$ eV) of the sample before and after the second oxidation procedure (acquired on a region indicated as 2 in Fig. 6.7). b) X-ray absorption spectra at the Co $L_{2,3}$ edge of the phase 2. The additional presence of a shoulder at low photon energies can be observed, suggesting the presence of cobalt oxide. In the bottom XMCD spectra it can be observed that the ferromagnetic behavior of the cobalt substrate is preserved upon oxidation, while the oxide shoulder at lower and higher excitation energies with respect to the main peak at 778.2 eV, behave antiferromagnetically.

of the oxidation outcome has been studied with varying graphene coverage. In the previous chapter, it was shown that the coverage of graphene could be controlled by varying the growth conditions (ethylene pressure and temperature) and therefore favoring the presence of uncovered substrate regions and black carbidic islands.

A sample with lower coverage of graphene ($\Theta = 0.75$ ML), characterized by the alternation of extended graphene patches and uncovered substrate areas (Fig. 6.9a) was prepared. Subsequently, this sample has been exposed to an oxygen dose of about 7200 L, while keeping its temperature at 210 °C. This procedure completely changed the morphology of the sample, leading to the formation of a cobalt oxide phase both underneath the graphene covered and on the bare cobalt regions.

The electronic structure of graphene is affected by the presence of the cobalt oxide underneath. As visible from the Fig. 6.9b-c, a feature with a conical shape appears centered at the K point, whose apex is located at 0.54 ± 0.06 eV binding energy. The apex position is consistent with the shift of the C $1s$ peak for the new graphene phase, which was determined to be as intermediate between the pristine and the intercalated layer. The outer cone resembles the electronic structure as observed after the first intercalation procedure. The Fermi velocity of this cone is comparable to the one found after the first intercalation procedure. The inner cone instead has a Fermi velocity which is about 18% lower with respect to the one of the outer cone, with a value of $v_F = 0.95 \cdot 10^6$ m/s. This lowering can be ascribed to the fact that the sample regions giving rise to the inner cone in the valence band are characterized by a graphene which is more interacting with the underlying substrate with respect to the result obtained after the first intercalation procedure. The inner cone bands FWHM is 50% higher with respect to the outer cone. The increased value of the momentum width can be ascribed to: emission from zone with higher surface roughness and due to the stronger interaction at the graphene/cobalt interface. Considering the facts listed above, we suggest that the inner cone is formed by graphene lying on cobalt oxide with an irregular morphology. At the present state, it cannot be excluded that, under the regions giving rise to the outer cone (graphene with intercalated oxygen), the cobalt is metallic or oxidated.

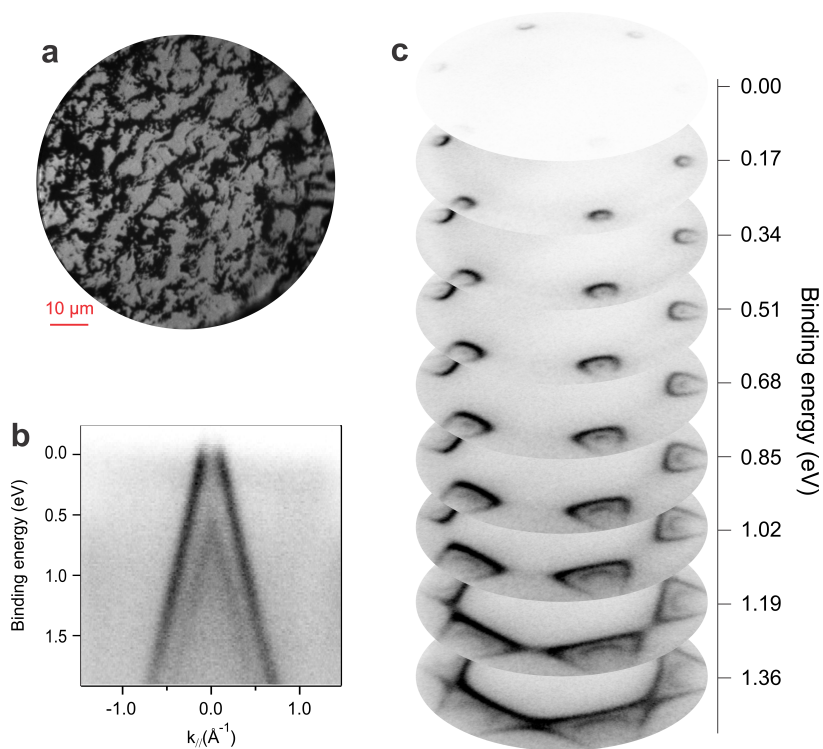


Figure 6.9: a) PEEM image (acquired at 4.65 eV kinetic energy) of an epitaxial graphene layer (white contrast) alternated to bare cobalt/cobalt carbide regions (black). b) Momentum map of the sample subjected to two oxidation procedures, showing the appearance of a second Dirac-like feature with respect to the one already present after first oxidation (Fig. 6.4). c) 3D visualization of the SBZ of the sample after second oxidation. The momentum maps were acquired at room temperature, using p-polarized photons of $h\nu = 56$ eV, $T = \text{RT}$.

6.2 Nitrogen substitutional doping

As reported above, the modification of the electronic properties of supported graphene layers can be achieved via the intercalation or on-top deposition of different compounds. However, an alternative route to modify the electronic, magnetic, and reactivity properties of the graphene layer can be substitutional doping of the carbon atoms with different species. This can be achieved by adding a gaseous precursor during the CVD growth or by means of low-energy ion implantation. It has been shown that when such dopants are present, a magnetic moment can be induced [147], or an enhanced chemical activity [148], catalyzing the reactivity of the graphene layer with gaseous molecules of environmental importance.

Therefore, in order to get an insight into the effects of nitrogen substitutional doping on graphene grown on cobalt, monolayer graphene with an epitaxial match to the underlying cobalt substrate has been prepared. The nitrogen implementation procedure has been started by introducing a nitrogen partial pressure in the preparation chamber, while keeping the sample at room temperature. Afterward, the ion gun has been tuned in order to produce ionized plasma with an energy of 50 eV, allowing for the irradiation of the sample with low-energy N^{2+}/N^+ ions. This procedure has been demonstrated in few works as an efficient technique to implement in the carbon network nitrogen atoms [149].

After 720 s of ion sputtering, with an ion current of 140 nA measured on the sample, the sample has been characterized using XPS at N $1s$ and C $1s$ core levels. The presence of nitrogen is observed as a broad feature in the N $1s$ spectra, having a multiple substructure. Following the interpretation from the literature, three different contributions in the N $1s$ spectra can be identified: pyridine-like, twofold coordinated nitrogen ($E_B = 397.5$ eV), pyrrole-like, threefold coordinated nitrogen ($E_B = 398.8$ eV) and substitutional nitrogen, graphitic ($E_B = 400.4$ eV), which is in agreement with previous studies for N-doped suspended and epitaxial graphene. It should be noted that nitrogen atoms can also be intercalated or implemented into the cobalt substrate, locally leading to the formation of cobalt nitride. As reported in the literature, cobalt nitride has a N $1s$ emission peaked in a range between 397.4 eV and 398.0 eV [150], a contribution that cannot be separated from the graphitic one, therefore being unable to distinguish them in the spectrum.

Before irradiation with nitrogen ions, the C $1s$ spectrum from pristine graphene has been collected as a reference for the upcoming treatment. As shown in the previous chapter, the spectrum can be fitted with two components due to the non-equivalent carbon adsorption geometry. C $1s$ spectra after nitrogen irradiation present two main changes, visible as the formation of two shoulders at higher, and lower binding energy, relative to the main graphene peak (Fig. 6.10a).

The broadening at lower binding energies is assigned to the formation of dangling bonds in the graphene network, due to the collision of nitrogen ions with the graphene atoms, causing carbon removal. A quantitative analysis of the spectrum reveals that the shoulder at lower binding energies has a contribution of about 5% to the total C $1s$ intensity, indicating that the graphene layer undergoes notable damage upon treatment.

The broadening at higher binding energies, is ascribed to the formation of carbon-nitrogen bonds. As reported above, several binding sites are available for the doping nitrogen atoms. Due to the low amount of such atoms and the limited resolution of the experimental setup, the contributions from different binding scenarios cannot be separated. Our quantitative analysis allows determining that a quantity of about $8 \pm 1.6\%$ of carbon atoms are bound with the imple-

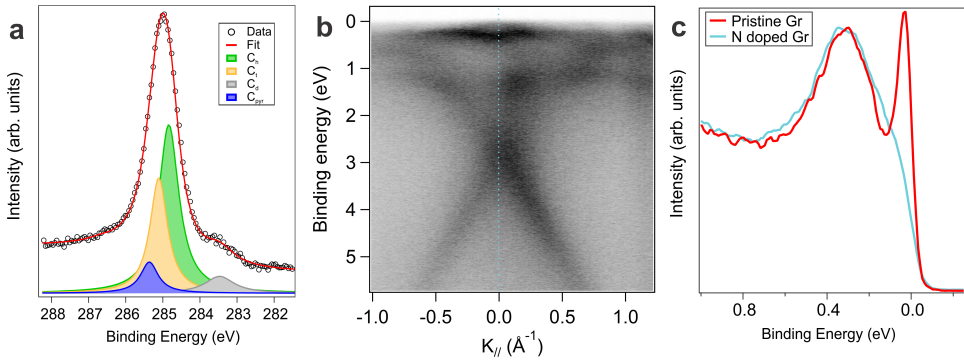


Figure 6.10: a) C $1s$ spectrum ($h\nu = 400$ eV) and relative fit of the Gr/Co sample after nitrogen implantation followed by 550 °C annealing. b) Momentum map ($h\nu = 40$ eV) acquired at the K point of the sample in a). EDC acquired at the K point (as indicated by the dashed line in b)) of the sample before and after nitrogen implantation. The disappearance of the feature near the Fermi level (relative to the graphene minicone band) can be observed after nitrogen implantation.

mented nitrogen atoms. By combining the results from N $1s$ and C $1s$ photoemission spectra, we quantified that the coverage of nitrogen atoms is about 0.08 ML.

The stability of the implemented nitrogen atoms has been tested by annealing the sample up to 550 °C, which is the temperature used for the CVD graphene growth. The N $1s$ spectrum, after the annealing process, reduces the multiple substructure as observed immediately after ion implementation into a single peak with lowered intensity with a small contribution at higher binding energies. The main peak is centered at 398.8 eV, corresponding to pyridinic nitrogen, while the small contribution at 400.4 eV corresponds to graphitic one. The observed reduction in intensity of the other components can be ascribed to the lower thermal stability of those structures, which are removed during the post-annealing of the treated sample, in agreement with previous studies [149]. The evaluation of nitrogen quantity after thermal treatment revealed that a residual quantity of 0.035 ± 0.011 ML remained trapped in the carbon network.

The above-mentioned modifications induced by nitrogen implementation, both the presence of embedded nitrogen atoms and the formation of defects in the carbon network, reflects on the electronic structure of the system. As observed in the previous chapter, the electronic structure of epitaxial graphene is characterized by a strongly hybridized π band whose crossing is shifted down to 2.83 eV binding energy, and by a minicone feature, deriving from the Co $3d$ - C $2p$ hybridization. After ion implementation and annealing, the electronic structure of graphene changes. The momentum map acquired after irradiation is shown in Fig. 6.10b. As visible from the EDC in Fig. 6.10c, the graphene π band after irradiation is broadened, with an overall higher background. This fact is ascribed to the formation of defective structures due to the ion irradiation procedure. The Fermi velocity of the charge carriers instead does not significantly change with respect to the pristine case ($2 \pm 0.9\%$ higher). Regarding the position of the apex of the Dirac cone, it shifts by about 120 meV to higher binding energies at 2.95 ± 0.03 eV, therefore having an n-doping behavior with respect to the pristine case. The resulting n-doping can be ascribed to the presence of an extra electron per nitrogen substitutional atom, trapped into the carbon network. However, also the vacancies created by irradiation affect the overall electronic structure of the system. As it was demonstrated by Jee et al. [151], the presence of vacancies, *i.e.* dangling

bonds, in the graphene network induces p-type doping, whose effect appears as a shoulder at lower binding energies in the C 1s photoemission spectra, and a shift to lower binding energies of the Dirac cone. Consequently, we can interpret the observed shift in the electronic structure as a balance between the n-doping induced by the presence of embedded nitrogen and the p-doping induced by the defects in the graphene network.

One of the most evident modifications concerns the region near the Fermi level in the proximity of the K point of the graphene Brillouin zone. A close inspection of Fig. 6.10b reveals that upon nitrogen implantation, the minicone feature disappears. In order to reveal a possible shift of the minicone feature, which may overlap with the substrate 3d bands, a line profile along a line centered at the K point has been extracted, before and after nitrogen implementation (Fig. 6.10c). It can be observed that after the treatment, the peak corresponding to the minicone feature at the Fermi level has completely disappeared. The driving force for this behavior of the minicone can be the following: a different hybridization of carbon and substrate bands due to the charge transfer induced by doping and/or a different interaction between doped graphene and substrate, leading to a different distance between them.

If the disappearance of the minicone feature would derive from the n-doping, then a similar downward shift that has been observed in the main Dirac cone should also be noted near the Fermi level. This effect can be excluded since the intensity, the shape, and the width of the Co 3d related state at 0.3 eV binding energy remain unchanged after nitrogen doping.

The above-mentioned motivation moves the attention to the evaluation of the difference in graphene-substrate distance upon doping. As it has been demonstrated in [152], the graphene-substrate distance is influenced by the density of the charge carriers, it is inversely proportional with the distance. Since the doping of the graphene layer with nitrogen atoms leads to an enhanced density of charge carriers, it can be expected that the graphene-substrate is reduced upon doping. This decrease of distance reflects remarkably in the band structure of the cobalt supported graphene, as it was demonstrated in [21]. DFT calculations performed at varying graphene-substrate distance showed that when graphene approaches the surface, the formation of the minicone and main Dirac cone is observed. Moreover, by progressively reducing the graphene-substrate distance, the Dirac cone is shifted towards higher binding energies and the minicone undergoes a shift to lower binding energies. A reduced graphene-substrate distance with respect to the pristine case allows us to explain the observed behavior in the nitrogen irradiated sample.

6.3 Intercalation of an Au monolayer

In order to study the possibility of decoupling the graphene layer from the substrate, the intercalation of a gold monolayer can be employed, since the interaction between graphene and Au atoms is weak.

Therefore, after preparing an epitaxial graphene layer on top of the cobalt substrate, gold has been evaporated on top of the surface. During deposition, we monitored the Au 4f core level, observing no shift in binding energy of the gold core levels, with the values being compatible with the bulk ones (Fig. 6.11a).

The valence band spectra after 6 min of gold deposition present a convolution of graphene/Co feature (π band, as indicated in Fig. 6.11b blue) and Au valence band features (Fig. 6.11b red).

The characteristic intensity in the valence band for Au is dominated by the emission from the Au $5d$ orbitals, spanning the intensity in two sub-regions determined by the spin-orbit splitting of the d states in the energy range between 2 eV and 7 eV. The observation of mostly Au $5d$ features at the selected photon energy (80 eV) derives also from the dominating cross-section of this orbital with respect to the s and p states. At the same time, the graphene π band, after the deposition of gold on top, presents a reduced intensity. Following the procedure in the literature, in order to intercalate the above-deposited layer, the sample has been annealed to temperatures over 400 °C. Following the changes in LEEM imaging during the annealing ramp, it can be appreciated that the gold atoms present on top of the surface, visible as bright contrast in the LEEM image, start to disappear from the top surface layer at a temperature above 320 °C. The ramp up to 400 °C lead to a uniform surface contrast, with no residual gold atoms atop the graphene layer. The valence band spectra measured after the annealing ramp (Fig. 6.11b green) shows that the graphene π band presents enhanced intensity with respect to the previous stage, due to the removal of the deposited gold layer, as it was observed by LEEM imaging. The proof of intercalation comes from Au $5d$ related features, whose intensity is reduced compared to the case before annealing, where the single peaks are not anymore distinguishable (Fig. 6.11b green).

However, this procedure did not lead to a completely decoupled layer, as determined by checking the momentum map at the K point, which shows the coexistence of two graphene-related π bands, indicating the presence of pristine and gold intercalated regions. In order to completely decouple the layer, additional Au has been deposited on top. Immediately after deposition, the sample has been annealed to about 320 °C as for the first intercalation stage. The valence band spectra acquired after this procedure shows that the cobalt related features are not present anymore (doublet in the region near the Fermi level), while the Au $5d$ features became dominant at higher binding energy values. The graphene π band presents a shift towards lower binding energies of about 2 eV. Three main peaks are observed in the valence band after the last treatment (Fig. 6.11b black). The one at higher binding energies is a convolution of graphene π band and Au $5d_{3/2}$, while the second one at about 2 eV lower energy is assigned to the emission from Au $5d_{5/2}$ levels. The peak at the Fermi level derives from the formation of an Au derived surface state, meaning that the intercalated layer presents a high crystalline order.

The characterization of the intercalated system has been initiated by measuring the photoemission at the C $1s$ core level. The spectrum measured before intercalation is the characteristic one of high-quality epitaxial graphene, with the presence of two features in C $1s$ emission due to the “*fcc-top*” adsorption geometry. After the second intercalation step instead, the system presents a p-doping character with respect to the pristine case, with a shift of the graphene π bands of ≈ 0.64 eV. The fit of the C $1s$ emission allows to separate two features: the main assigned to the sp^2 carbon in the graphene network, lying on the gold monolayer, and a smaller one, present at about 0.5 eV lower binding energy, assigned to the carbon atoms with dangling bonds, derived from the presence of graphene domain boundaries and graphene lying on stepped regions. This contribution at lower binding energies demonstrates that a successful intercalation at the graphene/substrate interface is largely facilitated in the presence of defects in the network, acting as channels for intercalation.

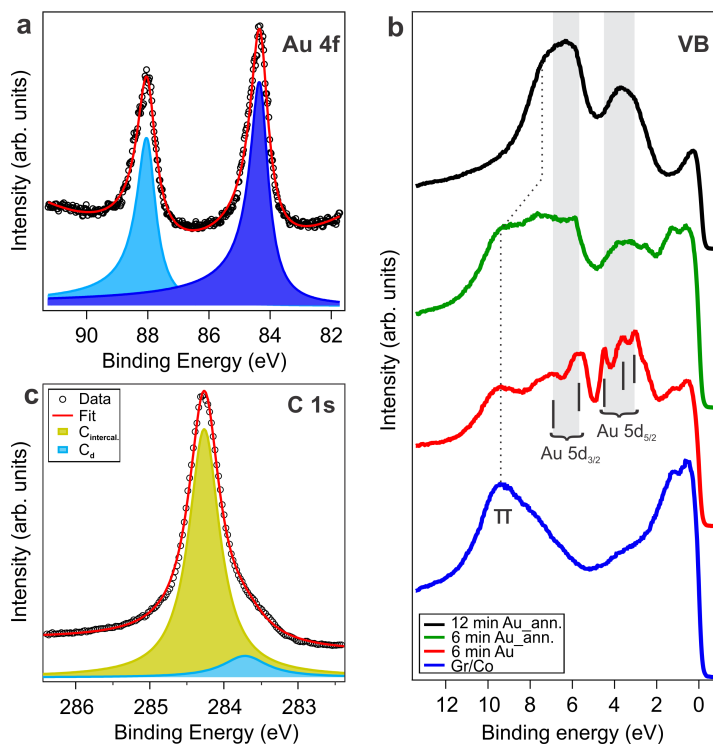


Figure 6.11: a) Au 4f core level ($h\nu = 200$ eV) acquired after the intercalation of a gold monolayer at the Gr/Co interface, showing the presence of two features relative to the spin-orbit splitting. b) Integrated valence band spectra ($h\nu = 80$ eV) acquired during the intercalation procedure of gold at the Gr/Co interface. c) C 1s spectra ($h\nu = 380$ eV) of the sample after intercalation, showing the presence of a broad peak (centered at ≈ 0.6 eV lower binding energy with respect to pristine case) and of a peak at lower binding energies assigned to defects present in the graphene network.

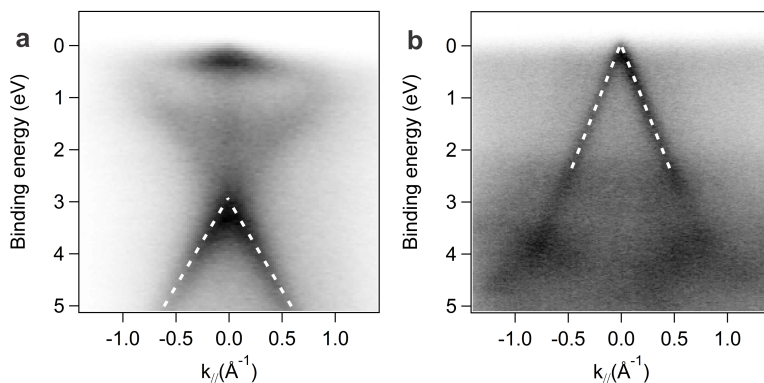


Figure 6.12: Momentum map acquired at the K point of the sample a) before and b) after the last intercalation step of the gold monolayer at the Gr/Co interface (Fig. 6.11b black). The maps were acquired at room temperature, using p-polarized photons of $h\nu = 40$ eV.

From the electronic structure point of view instead, the presence of a single layer of gold between cobalt support and graphene leads to the decoupling of the graphene layer from the substrate, as visible from momentum map measurements. Before intercalation, a reference of the momentum map has been measured, confirming the presence of high-quality epitaxial graphene (Fig. 6.12a). After the second intercalation procedure instead, when a full gold monolayer is present at the graphene/cobalt interface, the graphene π band is shifted towards lower binding energies, with the crossing of the K point present near the Fermi level (Fig. 6.12b), as in the free-standing case. By fitting the momentum distribution curves in the range from the Fermi level to 4 eV binding energy, it has been possible to determine that the crossing of the π bands, within the experimental resolution, is found at the Fermi level. The fitting of the MDC also allows determining that the momentum width has not changed, indicating that no defects are induced upon intercalation. Moreover, it should be noted that the presence of gold at the interface inhibits the observation of the minicone feature.

Furthermore, the comparison of photoemission intensities of the Co $3p$ peak indicates that no chemical modification occurred to the cobalt layer in contact with the gold single layer, excluding any possibility of intermixing or alloying. The Co $3p$ spectrum acquired after gold intercalation presents only a reduced intensity, due to the photoemission screening effect.

Summary and conclusions

In this thesis, a combination of real-time surface-sensitive spectromicroscopy techniques was used along with theoretical calculations in order to give a comprehensive picture of the graphene growth and electronic properties on ferromagnetic supports of choice. Fe, Co and Ni were considered as substrates for graphene growth being the only elemental ferromagnets at room temperature. The respective thin films of these elemental metals were deposited on the W(110) single crystal. The crystallographic order in the films was optimized as it constitutes a crucial step in the subsequent growth and study of the graphene overlayer. In particular, the martensitic *hcp-fcc* transition (at about 420 °C) was studied in cobalt films, showing a large thermal hysteresis and the presence of mixed structural phases under certain conditions. Nevertheless, films with enhanced crystallographic order were obtained and exhibited sharp bands in the momentum space in the region near the Fermi level. These bands were experimentally investigated using spin-resolved momentum mapping. Dedicated DFT and DMFT calculations were performed in collaboration with ICTP and University of Hamburg, respectively, helping in the interpretation of the observed bands, especially regarding their majority/minority spin character. The identification of the corresponding band features in the experiment and theory allowed also for an understanding of the most suitable model for reproducing the observed spectral features.

Among the listed materials, cobalt was selected as the main substrate for the graphene CVD synthesis, as it shows a better epitaxial match to graphene compared to Fe and it has a larger magnetic moment compared to Ni. We demonstrated that the room temperature exposure of the cobalt film to ethylene, followed by a temperature ramp to 400 °C leads to the formation of a defective and azimuthally-disordered graphene (termed as “Gr-A” in the preceding chapters). This was accompanied with the formation of carbidic islands. It is important to note that above 250 °C, carbon dissolves into the cobalt support. Thus, the formation of Gr-A involves both the bulk and surface carbon. At higher temperatures (above 530 °C), a bulk dissolution and recondensation procedure allows to transform Gr-A to an epitaxial graphene with higher crystallographic quality (termed as “Gr-B”). Real-time LEEM imaging, performed at 530 °C, revealed that this transformation proceeds following a procedure involving the carbidic islands (as precursors) which expand laterally at the expense of the surrounding rotationally incoherent graphene. This is balanced by the re-segregation of bulk carbon favoring the growth of epitaxial graphene. The result is an effective lateral movement of the precursor island, following a self-avoiding random walk path. This process results in an overall transformation of graphene into an epitaxial layer. From the spectroscopical point of view, this transformation manifest as a sharper C 1s core level, also indicating a better structural order.

Instead, by varying the growth pathway, it was possible to obtain a graphene composed

predominantly by well-defined rotational domains. The exposure of a preheated (above 350 °C) cobalt surface to ethylene induces the formation of graphene domains with various moiré patterns (Gr-C) along with carbide islands similar to the precursor phase mentioned above. Note that Gr-C consists of domains with well-defined azimuthal angles with respect to cobalt (9.6°, 16.5°, 19.2°, 22.4°). Through a similar procedure as in the Gr-A to Gr-B conversion, Gr-C can be converted to an epitaxial graphene (Gr-D) at sufficiently high temperatures (over 700 °C). Although qualitatively similar to Gr-B, Gr-D shows a better crystalline quality. The estimated activation energies of both transformation processes are similar, indicating that they share the same mechanism.

In order to address whether the cobalt stacking has a potential influence on the graphene structure, graphene was also grown on top of a thermally stabilized heterogeneous cobalt surface composed both by *hcp* and *fcc* domains. It was thus determined that graphene growth (Gr-C) does not depend on the substrate stacking, a result also substantiated by the DFT calculations.

On these well-characterized graphene structures, electronic structure measurements were performed. A single spin polarized band near the Fermi level, termed as “minicone”, was observed. Together with the calculations, the results presented in this thesis show that the minicone is formed upon hybridization of carbon and cobalt orbitals. DFT calculations reveal that the minicone band is mostly localized on the carbon atoms. In this respect, having well-defined rotational domains was crucial in the experimental observation of the minicone feature. While in Gr-A only a faint intensity can be observed near the Fermi level, upon Gr-A to Gr-B transformation, the minicone band becomes visible. In Gr-C instead, contrary to what has been stated in the literature [21], the same spin-polarized minicone band near the Fermi level was observed at the corresponding momentum points. Upon Gr-C to Gr-D transformation, leading to the formation of epitaxial graphene, all the band features became even more pronounced due to the improved crystalline order. Consequently, the presence of the minicone band is a general feature originating upon the interaction between cobalt and carbon, independent of the relative Gr-Co orientation at the interface.

Interestingly from an application point of view, I showed that even atmospheric exposure of the graphene/cobalt system, the peculiar properties of the interface are preserved, allowing to extend the range of application of the graphene/cobalt system also to ambient working conditions.

On the other hand, oxygen intercalation was observed to take place at sample temperatures above room temperature, by exposing the surface to molecular oxygen at pressures well-below the ambient regime. Thus, a controlled intercalation of different species as a function of temperature was employed to verify the nature of the minicone. We observed that the presence of atomic oxygen at the interface strongly depends on the concentration of the carbidic regions (*i.e.* catalytic sites), acting as active sites for oxygen adsorption and decomposition. The presence of oxygen at the interface induces not only a decoupling of the graphene layer from the substrate, but also, a p-doping of the graphene bands, as observed in the momentum maps. Moreover, we demonstrated the possibility to cycle the oxygen intercalation, using a combined annealing and regrowth procedure. In the first step, the annealing (over 300 °C) allows us to remove the intercalated oxygen; in the second instead the limited damage formed by oxygen induced carbon removal was healed via ethylene CVD.

Another way used for decoupling the graphene from its support was the intercalation of a gold monolayer. The momentum mapping revealed that upon the presence of gold underneath, graphene shows a free-standing character. In the case of both intercalants, gold and oxygen, we observed the disappearance of the minicone band.

An alternative way to modify the graphene/cobalt interface is identified as substitutional nitrogen doping of the graphene lattice. This was accomplished by low-energy nitrogen ion irradiation. Post-treatment annealing leads to the modification of the graphene atomic structure (by substitutional doping of nitrogen), changing the electronic properties near the Fermi level. While the main Dirac cone (2.8 eV below the Fermi level) does not alter its position or width, the minicone feature disappears. This behavior can be tentatively ascribed to the limited damage upon irradiation and/or to charge transfer phenomena from nitrogen to the graphene layer.

To conclude, in this thesis, using a multi-technique approach, we used the CVD method for producing graphene layers on top of a cobalt support. Spectromicroscopical studies revealed that a graphene obtained via the recrystallization of a preexisting graphene layer composed by misoriented domains present the best crystallographic quality with an epitaxial relation with the underlying substrate. This type of graphene present the sharpest fingerprint in the band structure among all the others preparations used in this thesis. The strong interaction between graphene and cobalt leads to a 2.8 eV binding energy up-shift of the π band crossing with respect to the free-standing case. In addition, the graphene-cobalt system is characterized by a peculiar electronic state, having a cone-like dispersion, with the crossing at the Fermi level. This state, commonly referred to as minicone, is formed upon the hybridization of carbon p_z orbitals with cobalt d states. We observed that the minicones are a general characteristic of the graphene-cobalt interface which does not depend on the epitaxial relation at the interface, while spin-resolved momentum mapping for the first time revealed that its single-spin behavior is found also in the misoriented graphene domains. The use of intercalants and dopants on the graphene-cobalt system leads to the disappearance of the minicone feature, a fact that can be exploited for the building of next-generation spin circuits.

Outlook

Using three-fold symmetry substrates in fundamental graphene adsorption studies allows for a deeper understanding of the interface's fundamental interactions, but does not reflect the complexity found in an arbitrary surface termination. This is because usually the materials found in nature are polycrystalline, therefore exposing faces with multiple orientations. Consequently, applying the knowledge gained from model systems to realistic systems is not always trivial. Therefore, for a given material, the study of graphene adsorption on all possible surface terminations is required.

Comparative works in the literature on symmetry-dependent graphene-metal interfaces are quite scarce. The works performed on Cu(100), Ir(100), Ni(100), Fe(110) and Ni(110) show that the graphene-substrate lattice mismatch and symmetry induces the formation of one or two-dimensional moiré patterns, depending on the interaction at the interface.

On cobalt instead, the growth of graphene has been performed mainly on surfaces exposing the hexagonal phase, while up to now, no dedicated works have been performed using the rectangular or quadratic phase of cobalt as substrate for graphene synthesis. However, these phases were revealed to be present in Co substrates even after graphene synthesis (Fig. O.1).

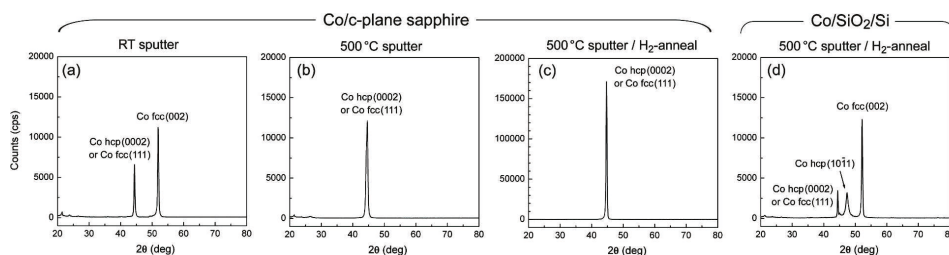


Figure O.1: a-d) X-ray Diffraction (XRD) profiles measured after CVD at 1000 °C, using Co samples with varying treatment. Reprinted with permission from [60]. Copyright 2010 American Chemical Society.

In this context, we have performed preliminary studies of CVD graphene synthesis on top of a cobalt film (30 ML) exposing a surface with square symmetry. For this purpose, the cobalt film has been grown on top of a clean Cu(100) single crystal. The epitaxial growth on the Cu(100) substrate stabilizes the cobalt film in the *fcc* phase, exposing the (100) surface phase.

On top of that surface, graphene has been synthesized via ethylene CVD. XPS measurements at the C 1s core level reveal a substantial difference with respect to the synthesis performed on the hexagonal phase, as shown in Chapter 5. While upon graphene synthesis on the hexagonal phase a single peak is observed, the synthesis on the quadratic phase leads to the formation of

three prominent peaks (Fig. O.2). The position of the leftmost peak is assigned to the interacting graphene layer with the substrate, consistent with what found in Chapter 5. The peak at about 0.6 eV lower binding energy is characteristic of sp^2 carbon, which can be either from lifted moiré patches or decoupled via a carbidic layer, whose emission is visible as a prominent peak at low binding energies.

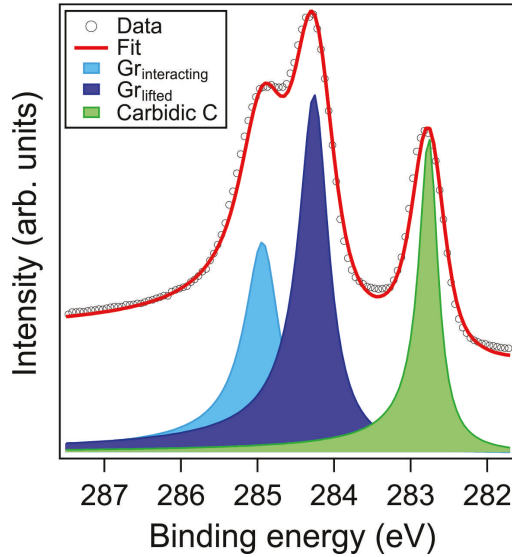


Figure O.2: XPS at the C $1s$ core level after graphene synthesis on Co film exposing the (100) surface. $h\nu = 380$ eV.

This result motivate further studies on this system, which show different characteristics with respect to graphene grown on substrate with hexagonal symmetry, in order to draw a complete picture of graphene adsorption on top of polycrystalline cobalt surface.

Appendix

A Theoretical methods

A.1 Density functional theory - DFT

A stable electronic system is composed both by electrons and positively charge nuclei. But due to the large difference in mass of electrons and nuclei, the kinetic energy of the nuclei can be neglected, considering the nuclei frozen and the nucleus-nucleus repulsion term becomes only an energy shift, as stated by the Born-Oppenheimer approximation.

This model allows for the description of the electronic system by assuming a potential created by the nuclei and the interaction with an electron cloud. Density functional theory (DFT) provides the theoretical background for studying the electronic structure by deducing from the ground-state electronic density the features of many-electron systems. DFT is based on two theorems formulated by Hohenberg and Kohn [153] in 1964. The starting point of an electronic system is to write the Hamiltonian:

$$\hat{H} = \hat{T} + \hat{V}_{ee} + \hat{V}_{ext} \quad (\text{G.1})$$

Where \hat{T} is the kinetic energy operator, \hat{V}_{ee} describes the electron-electron interaction and \hat{V}_{ext} the operator corresponding to the external potential.

In order to unravel the Hamiltonian in G.1, the two Hohenberg-Kohn theorems are stated:

- For a system of interacting particles in an external potential v_{ext} , the potential v_{ext} is determined uniquely, apart from a constant, by the ground state particle density ρ_0 ;
- A universal functional for the energy $E[\rho]$ in terms of the density $\rho(\mathbf{r})$ can be defined, valid for any external potential $v_{ext}(\mathbf{r})$. For any particular $v_{ext}(\mathbf{r})$, the exact ground state energy of the system is the global minimum value of this functional, and the density $\rho(\mathbf{r})$ that minimizes the functional is the exact ground state density $\rho_0(\mathbf{r})$.

Kohn and Sham proposed an ansatz for expressing the energy functional, assuming that the ground state density of the original interacting system is equal to that of some chosen non-interacting system, leading to [154]:

$$E[\rho] = T_S[\rho] + U_H[\rho] + E_{XC}[\rho] + E_{ext}[\rho] \quad (\text{G.2})$$

Where T_S and U_H are the electron kinetic energy and the Hartree energy (nuclei-electron interaction) of a non interacting system. E_{XC} is defined as the exchange-correlation functional and

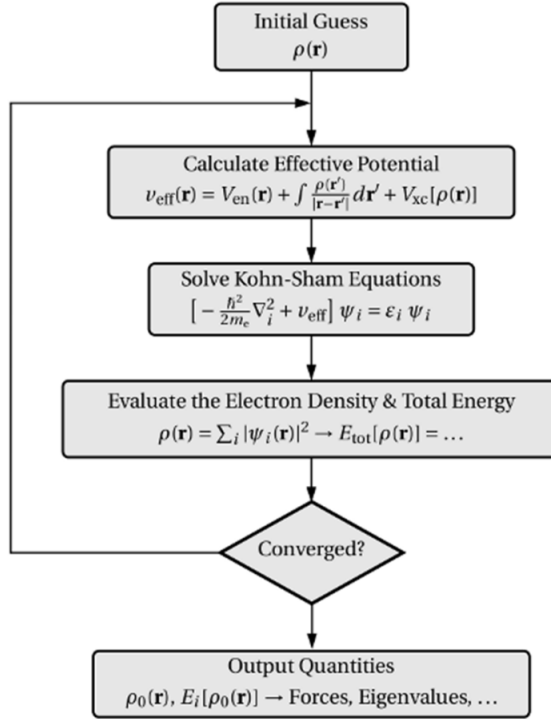


Figure A.1: The iteration scheme in the DFT calculation. Adapted from [155].

E_{ext} the energy derived from the interaction with the external potential. In order to obtain the ground state energy, the variational principle is used, minimizing the total energy functional of a given number of electrons, leading to an exact system of single particle Kohn-Sham equations. These equations describe a system of non-interacting particles in an effective potential at zero temperature. The system must be solved self-consistently since the effective potential depends on the charge density $\rho(\mathbf{r})$, which is in turn determined by the sum over the N_e wave functions of lowest energy. A new charge density is thus obtained at each iteration and the process is repeated until convergence is reached as shown in the flow chart in Figure A.1. When the self-consistent charge density is known, the ions can be optionally relaxed to their equilibrium positions.

In principle, the eigenvalues of the Kohn-Sham equations do not have a physical meaning. However, it has become standard practice to interpret the eigenvalues as estimates of the excitation energies and compare them in solids with experimental band structures, where the ground state density and the total energy are well described.

The solution of the E_{XC} term is non-trivial, so several approximations are used, based on the local effect of the potential. In local density approximation (LDA), the E_{XC} is approximated as a nearly local functional of the density. This turns that the total exchange-correlation energy $E_{XC}[\rho]$ is given by locally applying the exchange-correlation energy calculated for a uniform gas of electrons:

$$E_{XC}[\rho] = \int d^3r \rho(\mathbf{r}) \epsilon_{XC}(\rho(\mathbf{r})) \quad (\text{G.3})$$

The presence of the spin in the electronic system is accounted in DFT by considering the kinetic and exchange-correlation terms to be dependent of the single spin charge densities ρ , while the other terms in the equation G.2 are not spin-dependent. Usually the electron spin is introduced in the local spin density approximation (LSDA), where the E_{XC} term is distinct for each spin channel through the respective local density of up and down electrons. However, the spin-orbit coupling (SOC) is not considered in this model since it leads to spin intermixing and therefore gives different values as compared to experimental ones.

An improvement to LDA requires the use of non-local exchange-correlation functionals. The general gradient approximation (GGA) considers parametrizes the functionals using not only the charge density ρ , but also its gradient $\nabla\rho$.

The presence of positively charged nuclei should, however, be accounted in the description of the system. For a crystal with atoms located at $R + t_j$, where R is a Bravais lattice vector and t_j gives the position of the atom within the unit cell, the all-electron external potential is:

$$v_{ext}(\mathbf{r}) = - \sum_{R,j} \frac{1}{|\mathbf{r} - \mathbf{R} - \mathbf{t}_j|} \quad (\text{G.4})$$

The solution of the Hamiltonian describing the valence and core electrons in the unit cell, which are moving in this external potential is a challenging task. This is because, considering the divergence of the Coulomb potential, not only the electronic energies are spread over a very wide range, but the characteristic length scales of the various wave functions are also broadly distributed.

However, the deep core-electron wave functions are tightly bound to the nuclei and their spatial distribution remains almost unchanged from one chemical environment to another. On the contrary, the valence electrons are higher in energy and are strongly influenced by the neighboring atoms. This lead to the development of pseudopotentials, which replace the influence of frozen core states on the valence electrons by an effective external potential. The crystalline Hamiltonian then describes only the valence electrons in an effective potential, a substantial save of computational time.

A.2 Dynamic mean field theory - DMFT

The DFT approach for the simulation of real electronic systems tends to give altered results when considering strongly correlated systems. The Hamiltonian believed to describe the physics of strongly correlated systems is the well-known Hubbard model [156]:

$$H_{\text{Hubbard}} = t \sum_{\langle ij \rangle \sigma} c_{i\sigma}^\dagger c_{j\sigma} + U \sum_i n_{i\uparrow} n_{i\downarrow} \quad (\text{G.5})$$

where $c_{i\sigma}^\dagger$ ($c_{i\sigma}$) is the creation (annihilation) operator in the second quantization picture for a lattice site i , spin σ and $n_i = c_i^\dagger c_i$ is the corresponding number operator.

In equation G.5, t represents the hopping parameter, which is proportional to overlap between the orbitals of nearest neighbor sites and gives the electronic bandwidth, and U is the on-site Coulomb repulsion strength. This model describes the competition between electron hopping at

different sites, favoring the formation of delocalized metallic states and the tendency for electronic localization and insulating behavior due to U .

Although the model is easily formulated, the solution of this many-body problem is not trivial. Dynamical mean field theory (DMFT) is the approach used to solve this issue [157]. Two assumptions are made:

- Only one orbital is contributing to the electronic properties
- The orbitals are so localized that only nearest-neighbor hopping t is considered, therefore being easy to generalize to longer-range hopping.

The Anderson impurity model (AIM) [158] is hence considered as an approximation of the electronic system, where one site (called impurity) is interacting with a bath of electronic levels, through a hybridization function. This function describes the dynamics of electrons hopping in and out of the bath. It should reproduce the lattice dynamics such that the impurity Green's function coincides with the local lattice Green's function. One of the possible solutions to this problem is to couple the DFT approach with DMFT, using the AIM. To describe a bulk material, the AIM is used in a self-consistency loop. The computational solution of the problem include several steps, where the Green's functions for the impurity and the bath are determined, resulting in new self energy at each calculation step. These steps are iterated until self-consistency in the Green's function or the self-energy is reached. The self-consistency loop in the DFT+DMFT approach can be extended to include the electronic charge density $\rho(\mathbf{r})$. In such a calculation, the resulting charge density $\rho(\mathbf{r})$ is used as a starting point for a new DFT calculation, which subsequently serves as starting point for the successive DMFT calculation. Those steps are iterated until self-consistency in both the self-energy and the charge density are achieved. In practice, however, most applications of the DFT+DMFT method, so far, are restricted to calculations obtaining self-consistency only in the self-energy.

Double counting problem in DFT+DMFT approach

The combination of DFT and DMFT approaches leads to an overestimation of the electronic correlation effect, which is included, with different weight, in both methods. Therefore the electronic correlation effects, which are included in DFT, have to be subtracted from the Hamiltonian (the double-counting correction). A good agreement between the experimental and simulated spectral function has been obtained only when considering the double-counting correction as an adjustable parameter [159].

In the community, two different approximations are used for the accounting of the double-counting problem, namely the around-mean-field correction (AMF) and the fully-localized limit (FLL) approaches. Those approximations were initially intended to serve as a correction in the LDA+U approach [160, 161]. The LDA+U method introduces the Hubbard U -kind of interaction between the localized atomic orbitals. This method separates the electrons into localized d - or f -electrons and delocalized s - and p -electrons. While for the latter an orbital independent electron potential suits well, a Hartree-Fock like interaction better describes the strongly localized valence electrons. This interaction is proportional to:

$$\frac{1}{2} \sum_{i,j(\neq i)} n_i n_j \quad (\text{G.6})$$

with n_i the occupancies of the localized shells. Assuming that the Coulomb energy for the electron-electron interaction, as a function of the total number of electrons

$$N = \sum_i n_i \quad (\text{G.7})$$

is well represented by LDA, then LDA already contains part of this energy. Therefore this part has to be subtracted from the total energy:

$$E_{LDA+U} = E_{LDA} + E_{HF} - E_{DC} \quad (\text{G.8})$$

In the AMF approach, the double-counting term is written as:

$$E_{DC}^{AMF} = UN_{\uparrow}N_{\downarrow} + \frac{1}{2} \left(N_{\uparrow}^2 + N_{\downarrow}^2 \right) \frac{2l}{2l+1} (U - J) \quad (\text{G.9})$$

where U and J are the Coulomb and exchange interaction respectively, N_{\uparrow} and N_{\downarrow} are the occupation at each spin (up and down), and l the angular momentum.

However, it emerged that for strongly correlated electronic systems, the AMF approach leads to unrealistic results. Therefore, the FLL approach has been introduced, in which the localized d - and f -electrons have an atomic character (localized orbitals). This leads to the double counting term to become:

$$E_{DC}^{FLL} = \frac{U}{2} N(N-1) - \frac{J}{2} (N_{\uparrow}(N_{\uparrow}-1) + N_{\downarrow}(N_{\downarrow}-1)) \quad (\text{G.10})$$

Most of the modern LDA calculations rely on one of the two above-mentioned approaches, although in real materials, the occupation numbers are found between these two limits, therefore neither AMF nor FLL are correctly reproducing real systems, instead an interpolation between those limits should be used [162].

B Image processing of spin-resolved momentum maps

In order to obtain the information about spin polarization using the information acquired at two scattering energies (E_S) as described by Tusche *et al.* [95], the following procedure is used. Considering the elastic scattering of an electron from an atom, the cross sections can be written as:

$$\sigma(\theta, \phi) = R(\theta)(1 + S(\theta)\mathbf{P} \cdot \hat{n}) \quad (\text{G.11})$$

where θ and ϕ are the polar and azimuthal angles, respectively, \hat{n} is the scattering plane normal, $R(\theta)$ is the spin integrated scattering amplitude and $S(\theta)$ is the spin sensitivity, also termed Sherman function.

At a solid surface, dynamical theory and experimental proof show that R and S depend on the polar and azimuthal angles, due to multiple scattering [163, 164].

The scattering cross section is proportional to the ratio of the scattered to incident photoelectron current. Only the component of the polarization vector \mathbf{P} parallel to the scattering plane normal \hat{n} can be measured. In the case of scattering from a $W(100)$ crystal, two characteristic energies are selected (26.5 and 30.5 eV), corresponding to local maxima in reflectivity and different spin sensitivity, higher (at 26.5 eV) and lower (at 30.5 eV). The photoelectron current at the two scattering energies can be written as:

$$I_H = T(1 + S_H P)R_H \quad (\text{G.12})$$

$$I_L = T(1 + S_L P)R_L \quad (\text{G.13})$$

Where I_H and I_L are the intensities at higher (30.5 eV) and lower scattering energy (26.5 eV), respectively (Fig. B.1a,b). S_H , S_L and R_H , R_L indicate the relative spin sensitivity and reflectivity values at the two scattering energies, while T is the total, spin-integrated current.

In order to obtain information about the spin polarization in the images, the ratio between the two equations is taken:

$$\frac{I_H}{I_L} = \frac{(1 + S_H P) R_H}{(1 + S_L P) R_L} \quad (\text{G.14})$$

Since the electron reflectivity is almost equal at the two scattering energies, its influence can be neglected. By solving the equation G.14 for P :

$$P = \frac{I_L - I_H}{I_H S_L - I_L S_H} \quad (\text{G.15})$$

it is possible to obtain the spin polarization at every image point (Fig. B.1c). By taking the difference between the two equations in G.12 and G.13 and insert the above derived equation G.15, we obtain:

$$T = \frac{I_H S_L - I_L S_H}{S_L - S_H} \quad (\text{G.16})$$

which gives the total spin-integrated image intensity (Fig. B.1d).

Considering that the spin integrated current is obtained by the sum of spin up and spin down

components:

$$T = N_{\uparrow} + N_{\downarrow} \quad (\text{G.17})$$

and that the spin polarization is calculated as difference between the spin up and spin down components weighted on the total intensity:

$$P = \frac{N_{\uparrow} - N_{\downarrow}}{T} \quad (\text{G.18})$$

it is possible to obtain two expressions for each spin channel (Fig. B.1e,f):

$$N_{\downarrow} = \frac{PT - T}{2} = \frac{T}{2}(1 - P) \quad (\text{G.19})$$

$$N_{\uparrow} = \frac{PT + T}{2} = \frac{T}{2}(1 + P) \quad (\text{G.20})$$

The quantification of the spin polarization can be performed by considering constant the spin sensitivity, being 0.42 for the 26.5 eV scattering energy and 0.05 for the 30.5 eV one [95]. Therefore the spin polarization P can be given in an interval ranging from -100% (fully spin-down) and +100% (fully spin-up). By analyzing the image in Fig. B.1c, therefore it is possible to estimate the value of the spin polarization of selected bands in the momentum space. However, in the experiments, the maximal and minimal values for the spin polarization are very hardly found, depending on many factors which lower its detected value.

For the representation of the 2D spin polarized photoemission map (Fig. B.1g), the total (spin-integrated) intensity and spin polarization are mapped on a two dimensional color code as given on the right-hand side of Fig. B.1g. In that way, the intensity shown in the momentum map is easily recognized as predominantly spin-up (red), spin-down (blue) or as unpolarized (gray).

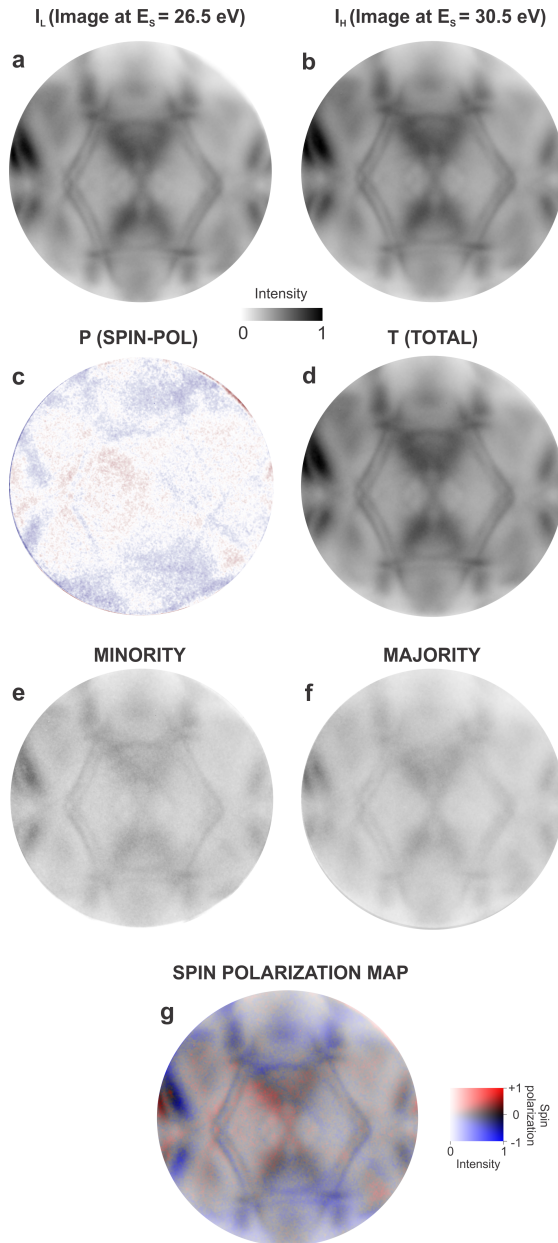


Figure B.1: Steps in the spin-resolved analysis of 2D momentum maps. a) 2D momentum map acquired at $E_s = 26.5$ eV. b) 2D momentum map acquired at $E_s = 30.5$ eV. c) Spin-polarized map obtained as in equation G.15. d) Spin-integrated total intensity map, obtained as in equation G.16. e) Spin down channel, obtained through equation G.19. f) Spin up channel, obtained through equation G.20. g) 2D spin-resolved momentum map, obtained by equally averaging the two spin channels. The images are acquired on a 9 ML Ni film deposited on W(110). $h\nu = 52.5$ eV, s-polarization, $T = -140$ °C.

C Graphene on Fe(110) films

The Fe(110) substrate for graphene growth has been prepared by depositing 60 ML of iron on top of the clean W(110) surface, following the procedure described in Chapter 4, resulting in a well-ordered metal film, characterized by a rectangular unit cell. Graphene synthesis was performed by exposing the preheated metal surface (≈ 550 °C) to ethylene pressure ($p = 5 \cdot 10^{-6}$ mbar) for 600 s. Subsequently, the sample temperature was lowered and post-growth characterization was performed.

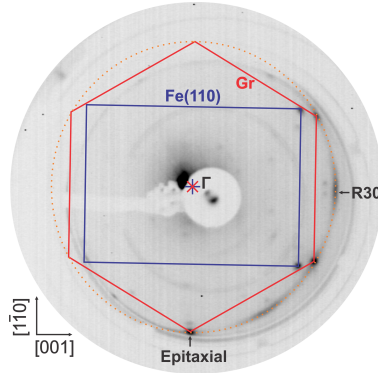


Figure C.1: LEED pattern ($E_{kin} = 55$ eV) acquired after graphene growth on 60 ML Fe(110) film. The blue rectangle indicates the substrate unit cell, while the red hexagon the unit cell of graphene aligned with the substrate lattice vector. The orange circle, having a radius compatible with the graphene unit vector, denotes the misaligned domains, characterized by a random orientation at the graphene-substrate interface.

The LEED analysis after graphene growth reveals that the synthesized graphene is characterized by multiple configurations. The resulting LEED pattern (Fig. C.1) is dominated by the (7×17) reconstruction, as previously observed in the literature [165], originating from the lattice mismatch between graphene and Fe(110). This moiré structure is characterized by the alignment of graphene and substrate lattice vectors, resulting in the overlap of first-order graphene spots and second order substrate spots (Fig. C.1). In addition, a faint diffraction ring with a radius compatible with the graphene unit vector can be observed in the LEED pattern, with a majored intensity in the central region enclosed between two consecutive graphene spots. This majored intensity derives from a graphene lattice that present a rotation of 30° with respect to the cobalt substrate.

Using a μ -spot beam, a spectroscopic characterization of the different structures observed in LEED was possible. On a region composed mainly by aligned graphene domains with respect to the substrate (substrate), *C 1s* core level is characterized by a main peak centered at 284.9 eV binding energy (Fig. C.2a). In addition, a shoulder at lower binding energies is visible ($E_B = 283.25$ eV), spectroscopic fingerprint of iron carbide structures. By performing momentum mapping on this region, the characteristic fingerprint of single domain graphene lattice can be observed. This turns into the observation of six Dirac cones, with a strong interaction with the underlying substrate, which shifts the Dirac point to 2.58 ± 0.03 eV binding energy (Fig. C.2c). The bottom of the π band is found at 10.22 ± 0.06 eV binding energy, while the top of the σ and band at $E_B = 4.8 \pm 0.05$ eV (Fig. C.2b).

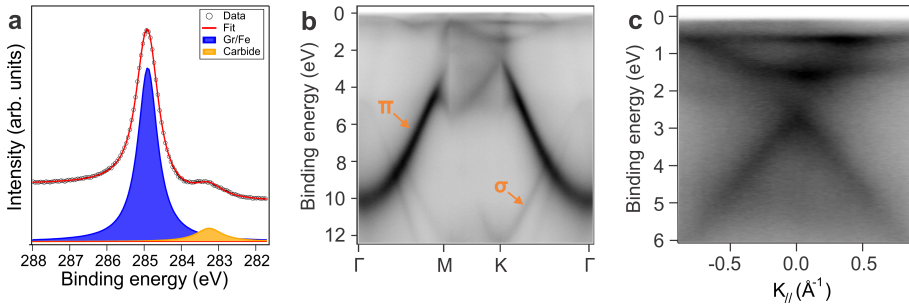


Figure C.2: a) C $1s$ spectra ($h\nu = 380$ eV) acquired on a region mainly composed by aligned graphene. b) Momentum map ($h\nu = 40$ eV) acquired along Γ MK Γ of the sample in a). c) Momentum map acquired at the K point of the sample in a), where the Dirac cone with its apex at 2.58 ± 0.03 eV is clearly visible.

The spectroscopic characterization of a region mainly composed by misaligned domains (rotated by 30°) unravel that the C $1s$ core level (Fig. C.3a) has its main peak at the same energy position but with a FWHM 13% higher with respect to the aligned case. As in the previous case, evidence of iron carbides is found at $E_B = 283.3$ eV. The acquisition of a 2D momentum map (Fig. C.3b) at the binding energy corresponding to the region of the Dirac cone ($E_B = 2.65 \pm 0.03$ eV) unveils that the size of the μ -spot probing beam is bigger than the extension of misaligned graphene domains, therefore leading to the observation of features corresponding to both domains (aligned and misaligned). By scanning across the entire surface of graphene with the procedure described above, we were not able to independently image the misaligned graphene domains, thus having each time also the contribution in the momentum maps of the aligned graphene domains. This observation confirms the hypothesis based on the LEED pattern, concluding that the majority of the surface is composed by graphene domains aligned with the substrate lattice vector.

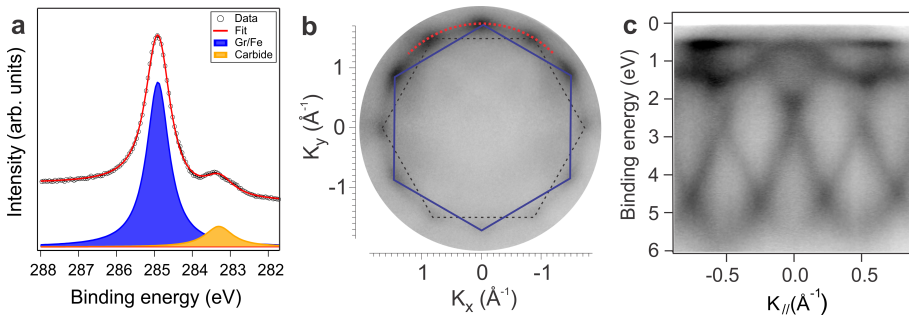


Figure C.3: a) C $1s$ spectra ($h\nu = 380$ eV) acquired on a region composed by graphene both aligned and rotated by 30° with respect to the Fe(110) lattice vector. b) 2D momentum map ($h\nu = 40$ eV) acquired at $E_B = 2.65$ eV of the sample in a). The Brillouin zone of the rotated graphene is superimposed in blue, while the one of the aligned one in dashed black line. c) Momentum map acquired along the arch as indicated in b), showing the simultaneous presence of Dirac cones deriving from aligned and misaligned graphene domains.

In order to characterize the Dirac cones of the misaligned domains and compare them to the ones of aligned graphene, the momentum map was acquired along the red dashed arc (of 80°) as

indicated in Fig. C.3b. The simultaneous presence of both graphene domains allows us to observe 3 Dirac cones along the considered arc: the central one corresponding to the misaligned graphene domains, while the two on the side stem from the aligned graphene. The fit of graphene π bands in the two cases reveals that the Dirac point of misaligned graphene (rotated by 30°) is located at 50 meV lower binding energies, *i.e.* $E_B = 2.53 \pm 0.04$ eV.

For aligning the misoriented graphene domains, and therefore obtain a full epitaxial layer, the sample was subjected to high-temperature annealing. As observed in the literature [166], the annealing of the graphene/iron interface leads to the dissolution of carbon inside the iron lattice, leading to its carburization. Therefore, the method applied for the alignment of the graphene/cobalt interface, cannot be applied for the alignment of graphene grown on iron.

D Graphene on Ni(111) films

The growth of graphene on top of the Ni(111) surface was performed by exposing a 30 ML Ni film to ethylene pressure of $p = 1 \cdot 10^{-6}$ mbar, during an annealing ramp from room temperature to 550 °C. As reported by Patera *et al.* [167], this growth recipe leads to the formation of an epitaxial graphene layer characterized by the presence of defects in the network. These defects are composed by vacancies, which incorporate nickel atoms from the substrate [168]. The epitaxial match at the graphene/nickel interface favors the alignment of graphene with respect to the lattice vectors of the substrate, leading to the observation of a LEED pattern, where only a (1x1) structure is visible D.1.

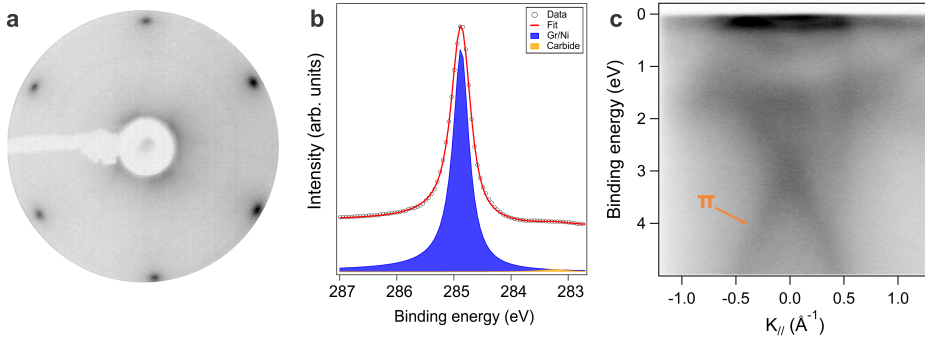


Figure D.1: a) LEED pattern ($E_{kin} = 70$ eV) acquired after graphene growth on a 15 ML Ni film b) C $1s$ spectra ($h\nu = 380$ eV) acquired on the sample in a). c) Momentum map ($h\nu = 52.5$ eV) acquired at the K point of the sample in a), where a faint Dirac cone with its apex at 2.81 eV is present.

The spectroscopic fingerprint at the C $1s$ core level is a peak centered at 284.87 eV binding energy with small contribution of carbidic carbon at lower binding energies ($E_B = 283.24$ eV).

Momentum mapping reveals that graphene is highly hybridized with the underlying substrate, resulting in a 2.81 ± 0.05 eV downshift of the π bands (Fig. D.1c). As expected from the LEED pattern, the SBZ of the graphene aligned with the substrate is observed. Moreover, in the region near the Fermi level, an intensity is revealed, corresponding to the formation of a new state which resembles the minicone feature observed for the graphene/cobalt interface, albeit with a lowered intensity. The difficulty to observe it can be also ascribed to the higher density of states of the $3d$, which are found in the region very close to the Fermi level, therefore being hard to distinguish from the substrate bands.

Abbreviations

- AES** Auger Electron Spectroscopy
- ARPES** Angle Resolved Photoelectron Spectroscopy
- BCC** Body Centered Cubic
- BE** Binding Energy
- BF** Bright-field
- CVD** Chemical Vapor Deposition
- DF** Dark-field
- DFT** Density Functional Theory
- DMFT** Dynamic Mean Field Theory
- DOS** Density of States
- FBZ** First Brillouin Zone
- FCC** Face Centered Cubic
- FWHM** Full-width at Half-maximum
- GGA** General Gradient Approximation
- HCP** Hexagonal Close Packed
- HSA** Hemispherical Sector Analyzer
- E_{kin} Kinetic Energy
- LDA** Local Density Approximation
- LEED** Low Energy Electron Diffraction
- LEEM** Low Energy Electron Microscopy
- ML** Monolayer
- PDOS** Projected Density of States
- PEEM** Photoemission Electron Microscopy

PES Photoemission Electron Spectroscopy

PMA Perpendicular magnetic anisotropy

RT Room temperature

SBZ Surface Brillouin Zone

SPELEEM Spectroscopic Photoemission and Low Energy Electron Microscope

V_{st} Start Voltage

UHV Ultra High Vacuum

UPS Ultraviolet Photoelectron Spectroscopy

VB Valence Band

XAS X-ray Absorption Spectroscopy

XMCD X-ray Magnetic Circular Dichroism

XPEEM X-ray PhotoEmission Electron Microscopy

XPS X-ray PhotoElectron Spectroscopy

Curriculum Vitae

Personal Data

Name	Matteo Jugovac
Address	Babići 1d, Umag, 52470, Croatia
Email	m.jugovac@fz-juelich.de, matteo.jugovac@trieste.ism.cnr.it
Date of Birth	29 th January 1992
Place of Birth	Koper, Slovenia
Nationality	Italian

Education

09/2019-present	Post-Doc position at CNR ISM Trieste <u>Supervisor:</u> Dr. Carlo Carbone
03/2016-08/2019	Ph.D. at Forschungszentrum Jülich (PGI-6) <u>Advisor:</u> Prof. Dr. Claus M. Schneider
09/2013-11/2015	Master Degree in Physics, University of Trieste <u>Thesis:</u> "Characterization and growth of graphene on metal surfaces of technological interest." <u>Advisor:</u> Prof. Giovanni Comelli
09/2010-09/2013	Bachelor Degree in Physics, University of Trieste <u>Thesis:</u> "Structural defects and chemical reactivity of graphene on Ni(111)." <u>Advisor:</u> Prof. Giovanni Comelli
2006-2010	Liceo Scientifico (Highschool diploma)

Publications and conference contributions

Publications

H. M. Sturmeit, I. Cojocariu, **M. Jugovac**, A. Cossaro, A. Verdini, L. Floreano, A. Sala, G. Comelli, S. Moro, M. Stredansky, M. Corva, E. Vesselli, P. Puschnig, C. M. Schneider, V. Feyer, G. Zamborlini and M. Cinchetti.

Molecular anchoring stabilizes low valence Ni(I)TPP on copper against thermally induced chemical changes. Journal of Materials Chemistry C, **8** (2020) 8876.

M. Jugovac, F. Genuzio, T. O. Mendes, A. Locatelli, G. Zamborlini, V. Feyer, and C. M. Schneider. *Tunable coupling by means of oxygen intercalation and removal at the strongly interacting graphene/cobalt interface.*

Carbon, **163** (2020) 541-347.

N. Haag, D. Lüftner, F. Haag, J. Seidel, L. L. Kelly, G. Zamborlini, **M. Jugovac**, V. Feyer, M. Aeschlimann, P. Puschnig, M. Cinchetti and B. Stadtmüller.

Signatures of an atomic crystal in the band structure of a C₆₀ thin film.

Physical Review Review B, *accepted* (2020).

M. Stredansky, S. Moro, M. Corva, **M. Jugovac**, G. Zamborlini, V. Feyer, C. M. Schneider, I. Cojocariu, H. M. Sturmeit, M. Cinchetti, A. Verdini, A. Cossaro, L. Floreano and E. Vesselli.

Vibronic Fingerprints of the Nickel Oxidation States in Surface-Supported Porphyrin Arrays.

The Journal of Physical Chemistry C, **124** (2020) 6297-6303.

Z. Zou, V. Carnevali, L. L. Patera, **M. Jugovac**, C. Cepek, M. Peressi, G. Comelli and C. Africh.

Operando atomic-scale study of graphene CVD growth at steps of polycrystalline nickel.

Carbon, **161** (2020) 528-534.

I. Cojocariu, H. M. Sturmeit, G. Zamborlini, A. Cossaro, A. Verdini, L. Floreano, E. D'Incecco, M. Stredansky, E. Vesselli, **M. Jugovac**, V. Feyer, M. Cinchetti, and C. M. Schneider.

Evaluation of molecular orbital symmetry via oxygen-induced charge transfer quenching at a metal-organic interface.

Applied Surface Science, **504** (2020) 144343.

M. Jugovac, F. Genuzio, E. L. Gonzalez, N. Stojić, G. Zamborlini, V. Feyer, T. O. Montes, A. Locatelli and C. M. Schneider.

Role of carbon dissolution and recondensation in graphene epitaxial alignment on cobalt.

Carbon, **152** (2019) 489-496.

P. Kliuiev, G. Zamborlini, M. Jugovac, Y. Gurdal, K. von Arx, K. Waltar, S. Schnidrig, R. Alberto, M. Iannuzzi, V. Feyer, M. Hengsberger, J. Osterwalder and L. Castiglioni.

Valence electronic structure of a hydrogen evolution catalyst: orbital tomography of Co-pyrphyrin.

Nature Communications, **10** (2019) 5255.

X. Yang, L. Egger, J. Fuchsberger, M. Unzog, D. Lüftner, F. Hajek, P. Hurdax, M. Jugovac, G. Zamborlini, V. Feyer, G. Koller, P. Puschnig, F. S. Tautz, M. G. Ramsey and S. Soubatch.

Coexisting Charge States in a Unary Organic Monolayer Film on a Metal.

The Journal of Physical Chemistry Letters, **10** (2019) 6438-6445.

V. R. Nallagatla, T. Heisig, C. Baeumer, V. Feyer, M. Jugovac, G. Zamborlini, C. M. Schneider, R. Waser, M. Kim, C. U. Jung and R. Dittmann *Topotactic phase transition driving memristive behavior.*

Advanced Materials, (2019) 1903391.

V. Carnevali, L. L. Patera, G. Prandini, M. Jugovac, S. Modesti, G. Comelli, M. Peressi and C. Africh.

Doping of epitaxial graphene by direct incorporation of nickel adatoms.

Nanoscale, **11** (2019) 10358.

E. Mlynczak, M. C. T. D. Müller, P. Gospodaric, T. Heider, I. Aguilera, G. Bihlmayer, M. Gehlmann, M. Jugovac, G. Zamborlini, C. Tusche, S. Suga, V. Feyer, L. Plucinski, C. Friedrich, S. Blügel and C. M. Schneider.

Kink far below the Fermi level reveals new electron-magnon scattering channel in Fe.

Nature Communications, **10** (2019) 505.

M. Grimm, C. Metzger, M. Graus, M. Jugovac, G. Zamborlini, V. Feyer and F. Reinert.

Molecular orbital imaging beyond the first monolayer: Insights into the pentacene/Ag(110) interface.

Physical Review B, **98** (2018) 195412.

M. Giesen, M. Jugovac, G. Zamborlini, V. Feyer, F. Gunkel and D. N. Mueller.

Principal component analysis: Reveal camouflaged information in x-ray absorption spectroscopy photoemission electron microscopy of complex thin oxide films.

Thin Solid Films, **665** (2018) 75-84.

P. Kliuiev, T. Latychevskaia, G. Zamborlini, M. Jugovac, C. Metzger, M. Grimm, A. Scöll, J. Osterwalder, M. Hengsberger and L. Castiglioni.

Algorithms and image formation in orbital tomography.

Physical Review B, **98** (2018) 085426.

M. T. Dau, M. Gay, D. Di Felice, C. Vergnaud, A. Marty, C. Beigne, G. Renaud, O. Renault, P. Mallet, T. Le Quang, J.-Y. Veuillen, L. Huder, V. T. Renard, C. Chapelier, G. Zamborlini, M. Jugovac, V. Feyer, Y. J. Dappe, P. and M. Jamet.

Beyond van der Waals Interaction: The Case of MoSe₂ Epitaxially Grown on Few-Layer Graphene.

ACS Nano, **12** (2018) 2319-2331.

Z. Zou, V. Carnevali, **M. Jugovac**, L. L. Patera, A. Sala, M. Panighel, C. Cepek, G. Soldano, M. M. Mariscal, M. Peressi, G. Comelli and C. Africh.

Graphene on nickel (100) micrograins: Modulating the interface interaction by extended moiré superstructures.

Carbon, **130** (2018) 441-447.

G. Zamborlini, **M. Jugovac**, A. Cossaro, A. Verdini, L. Floreano, D. Lüftner, P. Puschnig, V. Feyer and C. M. Schneider.

On-surface nickel porphyrin mimics the reactive center of an enzyme cofactor.

Chemical Communications, **54** (2018) 13423-13426.

G. Zamborlini, D. Lüftner, Z. Feng, B. Kollmann, P. Puschnig, C. Dri, M. Panighel, G. di Santo, A. Goldoni, G. Comelli, **M. Jugovac**, V. Feyer and C. M. Schneider.

Unexpected multi-orbital charge transfer at highly oriented organic/metal interfaces.

Nature Communications, **8** (2017) 1949.

Talks

M. Jugovac, G. Zamborlini, V. Feyer, E. L. Gonzalez, N. Stojic, F. Genuzio, T. O. Menteş, A. Locatelli and C. M. Schneider.

Optimized pathways for obtaining epitaxial graphene on cobalt.

Materials, Bologna (IT), 22.-26.10.2018.

M. Jugovac, G. Zamborlini, V. Feyer, F. Genuzio, T. O. Menteş, A. Locatelli and C. M. Schneider.

Temperature induced transformation of graphene on cobalt films.

FisMat, Trieste (IT), 01.-05.10.2017.

Poster contributions

M. Jugovac, G. Zamborlini, A. Locatelli, T. O. Menteş, F. Genuzio, V. Feyer and C. M. Schneider.

Carbon dissolution and recondensation drives graphene epitaxial alignment on cobalt.

VUVX 2019, San Francisco (USA), 01.-05.07.2019.

M. Jugovac, V. Feyer, G. Zamborlini, F. Genuzio, T. O. Menteş, A. Locatelli and C. M. Schneider.

Optimized pathways for obtaining epitaxial graphene on cobalt.

LEEM/PEEM 11, Chongqing (CHI), 30.10.-03.11.2018.

M. Jugovac, G. Zamborlini, A. Locatelli, T. O. Menteş, F. Genuzio, V. Feyer and C. M. Schneider.

Spectro-microscopic studies of CVD graphene growth on cobalt films. Awarded with 3rd prize

Graphene Study 2018, Göteborg (SWE), 29.06.-05.07.2018.

M. Jugovac, G. Zamborlini, P. Puschnig, D. Lüftner, V. Feyer and C. M. Schneider.

Charge transfer phenomena at NiTPP/Ag(110)&CoTPP/Ag(110).

Technologically relevant Quantum Materials: growth, experiments and theory, Trieste (IT), 19.-20.12.2016.

M. Jugovac, G. Zamborlini, C. Tusche, P. Puschnig, D. Lüftner, V. Feyer and C. M. Schneider.
Molecular Orbital Tomography studies of NiTPP on Ag(110).
LEEM/PEEM 10, Monterey (USA), 11.-15.09.2016.

Erklärung

Hiermit erkläre ich, dass ich die vorliegende Arbeit selbstständig und ohne fremde Hilfe verfasst habe. Ferner habe ich außer den angegebenen Quellen keine anderen Hilfsmittel benutzt. Die dem Sinn oder Wortlaut nach entnommenen Textpassagen oder Abbildungen habe ich in jedem Einzelfall kenntlich gemacht. Dieser Dissertation geht weder ein erfolgloser Promotionsversuch voraus, noch wurde sie in einem weiteren Promotionsverfahren eingereicht. Abgesehen von den angegebenen Publikationen sind die Ergebnisse dieser Dissertation unveröffentlicht.

Diese Dissertation, die den Doktorgrad "Dr. rer. nat." anstrebt, wurde von Prof. Dr. C. M. Schneider betreut.

Jülich, 31/03/2020

Matteo Jugovac

Acknowledgments

At the end of this work, but in general, of this life chapter, I would like to express my gratitude to the people who allowed me to come to this point and paved my way to it.

First of all, many thanks to my advisor, Prof. Claus M. Schneider, for letting me crown my student career with the Ph.D. title. Even if the occasions to talk were limited, I would like to thank him for his valuable suggestions and support during this period.

My heartfelt thanks go to the supervisor, Dr. Vitaliy Feyer, who supported me from the very beginning and throughout all this period and learned me how hard can be being a part of a beamline crew. A sincere gratitude goes to my colleagues in this period; Dr. Giovanni Zamborlini, through which I came to know this world, and who was during the worktime a reliable teammate but in general a trusted friend; and to Iulia Cojocariu, with whom I shared a short period, but in which I appreciated her willing to help and for being a trustworthy friend.

A deep thanks goes to the benchline friends more than colleagues, Dr. Francesca Genuzio, Dr. T. Onur Montes and Dr. Andrea Locatelli. In these years I understood your extraordinary ability in being great scientists, but more than that for the constant assistance both in science and life. Many thanks to the theoreticians Dr. Nataša Stojić, Eduardo L. Gonzalez, for the many fruitful discussions we had and for being patient to listen all our intricate ideas. Many thanks also to Prof. Alexander Liechtenstein and to Prof. Jan Ingo Flege for performing and providing the requested simulations.

I would like to thank also Dr. Alessandro Sala and Dr. Polina M. Sheverdyayeva, who helped me with the scientific issues encountered on the way and Dr. Paolo Moras for his proof-reading. A special thanks goes to the colleagues at the Elettra synchrotron, technicians and scientists, for your help to solve the day-to-day issues encountered. I would also like to thank Dr. Patrick Zeller for proofreading the German version of the introduction.

Moreover, I thank my colleagues from the PGI-6 in Jülich, and in particular Tristan, Pika, and Cristoph, for being warm hosts during the visits to Germany and for the very nice time spent together.

I would not be here to write this work without the unconditional lifetime support given from my parents, Roberto and Danijela, and the one from my beloved Arianna, a special thanks for her patience throughout all this period.

Bibliography

- [1] A. Lavoisier, "Premier mémoire sur la destruction du diamant par le feu," *Histoire de l'Académie royale des sciences. Avec les Mémoires de Mathématique & de Physique.*, vol. 2, pp. 564–591, 1772.
- [2] C. W. K. Scheele, "Versuche mit Wasserbley; Molybdaena," *Svenska Vetensk. Academ. Handlingar*, no. 40, p. 238, 1779.
- [3] H. W. Kroto, J. R. Heath, S. C. O'Brien, R. F. Curl, and R. E. Smalley, "C₆₀: Buckminsterfullerene," *Nature*, vol. 318, no. 6042, p. 162, 1985.
- [4] P. R. Wallace, "The band theory of graphite," *Physical Review*, vol. 71, no. 9, p. 622, 1947.
- [5] J. W. McClure, "Diamagnetism of graphite," *Physical Review*, vol. 104, no. 3, p. 666, 1956.
- [6] G. W. Semenoff, "Condensed-matter simulation of a three-dimensional anomaly," *Physical Review Letters*, vol. 53, no. 26, p. 2449, 1984.
- [7] K. S. Novoselov, A. K. Geim, S. V. Morozov, D. Jiang, Y. Zhang, S. V. Dubonos, I. V. Grigorieva, and A. A. Firsov, "Electric field effect in atomically thin carbon films," *Science*, vol. 306, no. 5696, pp. 666–669, 2004.
- [8] "The nobel prize in physics 2010.." <http://www.nobelprize.org/nobelprizes/physics/laureates/2010/>. Accessed: 2019-08-22.
- [9] X. Li, L. Colombo, and R. S. Ruoff, "Synthesis of Graphene Films on Copper Foils by Chemical Vapor Deposition," *Advanced Materials*, vol. 28, no. 29, pp. 6247–6252, 2016.
- [10] X. Chen, L. Zhang, and S. Chen, "Large Area CVD Growth of Graphene," *Synthetic Metals*, vol. 210, pp. 95 – 108, 2015. Reviews of Current Advances in Graphene Science and Technology.
- [11] A. Dahal and M. Batzill, "Graphene-Nickel Interfaces: a Review," *Nanoscale*, vol. 6, pp. 2548–2562, 2014.
- [12] M. Chen, R. C. Haddon, R. Yan, and E. Bekyarova, "Advances in Transferring Chemical Vapour Deposition Graphene: a Review," *Materials Horizons*, vol. 4, pp. 1054–1063, 2017.
- [13] D. Sander, S. O. Valenzuela, D. Makarov, C. H. Marrows, E. E. Fullerton, P. Fischer, J. McCord, P. Vavassori, S. Mangin, P. Pirro, B. Hillebrands, A. D. Kent, T. Jungwirth, O. Gutfleisch, C. G. Kim, and A. Berger, "The 2017 Magnetism Roadmap," *Journal of Physics D: Applied Physics*, vol. 50, no. 36, p. 363001, 2017.

- [14] B. Dlubak, M.-B. Martin, R. S. Weatherup, H. Yang, C. Deranlot, R. Blume, R. Schloegl, A. Fert, A. Anane, S. Hofmann, P. Seneor, and J. Robertson, "Graphene-Passivated Nickel as an Oxidation-Resistant Electrode for Spintronics," *ACS Nano*, vol. 6, no. 12, pp. 10930–10934, 2012.
- [15] E. Cobas, A. L. Friedman, O. M. J. van't Erve, J. T. Robinson, and B. T. Jonker, "Graphene As a Tunnel Barrier: Graphene-Based Magnetic Tunnel Junctions," *Nano Letters*, vol. 12, no. 6, pp. 3000–3004, 2012.
- [16] P. Genoni, F. Genuzio, T. O. Mentes, B. Santos, A. Sala, C. Lenardi, and A. Locatelli, "Magnetic Patterning by Electron Beam-Assisted Carbon Lithography," *ACS Applied Materials & Interfaces*, vol. 10, no. 32, pp. 27178–27187, 2018.
- [17] F. Ajejas, A. Gudin, R. Guerrero, A. Anadón Barcelona, J. M. Diez, L. de Melo Costa, P. Olleros, M. A. Nino, S. Pizzini, J. Vogel, M. Valvidares, P. Gargiani, M. Cabero, M. Varela, J. Camarero, R. Miranda, and P. Perna, "Unraveling Dzyaloshinskii-Moriya Interaction and Chiral Nature of Graphene/Cobalt Interface," *Nano Letters*, vol. 18, no. 9, pp. 5364–5372, 2018.
- [18] A. D. Vu, J. Coraux, G. Chen, A. T. N'Diaye, A. K. Schmid, and N. Rougemaille, "Unconventional Magnetisation Texture in Graphene/Cobalt Hybrids," *Scientific Reports*, vol. 6, p. 24783, 2016.
- [19] H. Yang, A. D. Vu, A. Hallal, N. Rougemaille, J. Coraux, G. Chen, A. K. Schmid, and M. Chshiev, "Anatomy and Giant Enhancement of the Perpendicular Magnetic Anisotropy of Cobalt-Graphene Heterostructures," *Nano Letters*, vol. 16, no. 1, pp. 145–151, 2016.
- [20] H. Yang, G. Chen, A. A. C. Cotta, A. T. N'Diaye, S. A. Nikolaev, E. A. Soares, W. A. A. Macedo, K. Liu, A. K. Schmid, A. Fert, *et al.*, "Significant Dzyaloshinskii-Moriya interaction at graphene-ferromagnet interfaces due to the Rashba effect," *Nature materials*, vol. 17, no. 7, p. 605, 2018.
- [21] D. Usachov, A. Fedorov, M. M. Otrokov, A. Chikina, O. Vilkov, A. Petukhov, A. G. Rybkin, Y. M. Koroteev, E. V. Chulkov, V. K. Adamchuk, A. Grüneis, C. Laubschat, and D. V. Vyalikh, "Observation of Single-Spin Dirac Fermions at the Graphene/Ferromagnet Interface," *Nano Letters*, vol. 15, no. 4, pp. 2396–2401, 2015.
- [22] "Graphene band structure." <https://www.uni-muenster.de/Physik.PI/Zacharias/en/research/graphene/graphene.html>. Accessed 2019-08-29.
- [23] K. S. Novoselov, A. K. Geim, S. V. Morozov, D. Jiang, M. I. Katsnelson, I. V. Grigorieva, S. V. Dubonos, and A. A. Firsov, "Two-dimensional gas of massless Dirac fermions in graphene," *Nature*, vol. 438, no. 7065, pp. 197–200, 2005.
- [24] A. K. Geim, "Graphene: Status and Prospects," *Science*, vol. 324, no. 5934, pp. 1530–1534, 2009.
- [25] A. H. Castro Neto, F. Guinea, N. M. R. Peres, K. S. Novoselov, and A. K. Geim, "The electronic properties of graphene," *Reviews of Modern Physics*, vol. 81, pp. 109–162, 2009.
- [26] P. Blake, E. W. Hill, A. H. Castro Neto, K. S. Novoselov, D. Jiang, R. Yang, T. J. Booth, and A. K. Geim, "Making graphene visible," *Applied Physics Letters*, vol. 91, no. 6, p. 063124, 2007.

-
- [27] A. Grüneis, T. Pichler, H. Shiozawa, C. Attaccalite, L. Wirtz, S. L. Molodtsov, R. Follath, R. Weber, and A. Rubio, "Low energy quasiparticle dispersion of graphite by angle-resolved photoemission spectroscopy," *Physica status solidi (b)*, vol. 244, no. 11, pp. 4129–4133, 2007.
- [28] K. I. Bolotin, K. J. Sikes, Z. Jiang, M. Klima, G. Fudenberg, J. Hone, P. Kim, and H. L. Stormer, "Ultrahigh electron mobility in suspended graphene," *Solid State Communications*, vol. 146, no. 9, pp. 351 – 355, 2008.
- [29] L. Britnell, R. V. Gorbachev, R. Jalil, B. D. Belle, F. Schedin, M. I. Katsnelson, L. Eaves, S. V. Morozov, A. S. Mayorov, N. M. R. Peres, A. H. Castro Neto, J. Leist, A. K. Geim, L. A. Ponomarenko, and K. S. Novoselov, "Electron Tunneling through Ultrathin Boron Nitride Crystalline Barriers," *Nano Letters*, vol. 12, no. 3, pp. 1707–1710, 2012. PMID: 22380756.
- [30] X. Li, W. Cai, J. An, S. Kim, J. Nah, D. Yang, R. Piner, A. Velamakanni, I. Jung, E. Tutuc, S. K. Banerjee, L. Colombo, and R. S. Ruoff, "Large-Area Synthesis of High-Quality and Uniform Graphene Films on Copper Foils," *Science*, vol. 324, no. 5932, pp. 1312–1314, 2009.
- [31] Z. Han, A. Kimouche, D. Kalita, A. Allain, H. Arjmandi-Tash, A. Reserbat-Plantey, L. Marty, S. Pairis, V. Reita, N. Bendiab, J. Coraux, and V. Bouchiat, "Homogeneous Optical and Electronic Properties of Graphene Due to the Suppression of Multilayer Patches During CVD on Copper Foils," *Advanced Functional Materials*, vol. 24, no. 7, pp. 964–970, 2014.
- [32] A. Reina, X. Jia, J. Ho, D. Nezich, H. Son, V. Bulovic, M. S. Dresselhaus, and J. Kong, "Large Area, Few-Layer Graphene Films on Arbitrary Substrates by Chemical Vapor Deposition," *Nano Letters*, vol. 9, no. 1, pp. 30–35, 2009.
- [33] K. S. Kim, Y. Zhao, H. Jang, S. Y. Lee, J. M. Kim, K. S. Kim, J.-H. Ahn, P. Kim, J.-Y. Choi, and B. H. Hong, "Large-scale pattern growth of graphene films for stretchable transparent electrodes," *Nature*, vol. 457, pp. 706 EP –, 2009.
- [34] Y. Zhang, Y.-W. Tan, H. L. Stormer, and P. Kim, "Experimental observation of the quantum Hall effect and Berry's phase in graphene," *Nature*, vol. 438, no. 7065, pp. 201–204, 2005.
- [35] C. Lee, X. Wei, J. W. Kysar, and J. Hone, "Measurement of the Elastic Properties and Intrinsic Strength of Monolayer Graphene," *Science*, vol. 321, no. 5887, pp. 385–388, 2008.
- [36] A. A. Balandin, S. Ghosh, W. Bao, I. Calizo, D. Teweldebrhan, F. Miao, and C. N. Lau, "Superior Thermal Conductivity of Single-Layer Graphene," *Nano Letters*, vol. 8, no. 3, pp. 902–907, 2008.
- [37] W. Cai, A. L. Moore, Y. Zhu, X. Li, S. Chen, L. Shi, and R. S. Ruoff, "Thermal Transport in Suspended and Supported Monolayer Graphene Grown by Chemical Vapor Deposition," *Nano Letters*, vol. 10, no. 5, pp. 1645–1651, 2010.
- [38] E. Pop, D. Mann, Q. Wang, K. Goodson, and H. Dai, "Thermal Conductance of an Individual Single-Wall Carbon Nanotube above Room Temperature," *Nano Letters*, vol. 6, no. 1, pp. 96–100, 2006.
- [39] P. Kim, L. Shi, A. Majumdar, and P. L. McEuen, "Thermal Transport Measurements of Individual Multiwalled Nanotubes," *Physical Review Letters*, vol. 87, p. 215502, 2001.

- [40] Y.-M. Lin, K. A. Jenkins, A. Valdes-Garcia, J. P. Small, D. B. Farmer, and P. Avouris, "Operation of Graphene Transistors at Gigahertz Frequencies," *Nano Letters*, vol. 9, no. 1, pp. 422–426, 2009.
- [41] Y.-M. Lin, C. Dimitrakopoulos, K. A. Jenkins, D. B. Farmer, H.-Y. Chiu, A. Grill, and P. Avouris, "100-GHz Transistors from Wafer-Scale Epitaxial Graphene," *Science*, vol. 327, no. 5966, pp. 662–662, 2010.
- [42] L. Liao, J. Bai, R. Cheng, Y.-C. Lin, S. Jiang, Y. Huang, and X. Duan, "Top-Gated Graphene Nanoribbon Transistors with Ultrathin High-k Dielectrics," *Nano Letters*, vol. 10, no. 5, pp. 1917–1921, 2010.
- [43] Y. Yang, C. Han, B. Jiang, J. Iocozzia, C. He, D. Shi, T. Jiang, and Z. Lin, "Graphene-based materials with tailored nanostructures for energy conversion and storage," *Materials Science and Engineering: R: Reports*, vol. 102, pp. 1 – 72, 2016.
- [44] J.-H. Ding, H.-R. Zhao, and H.-B. Yu, "A water-based green approach to large-scale production of aqueous compatible graphene nanoplatelets," *Scientific Reports*, vol. 8, no. 1, p. 5567, 2018.
- [45] J. Chen, W. Shi, Y. Chen, Q. Yang, M. Wang, B. Liu, Z. Tang, M. Jiang, D. Fang, and C. Xiong, "Eco-friendly exfoliation of graphite into pristine graphene with little defect by a facile physical treatment," *Applied Physics Letters*, vol. 108, no. 7, p. 073105, 2016.
- [46] M. Coroş, F. Pogăcean, M.-C. Roşu, C. Socaci, G. Borodi, L. Mageruşan, A. R. Biriş, and S. Pruneanu, "Simple and cost-effective synthesis of graphene by electrochemical exfoliation of graphite rods," *RSC Advances*, vol. 6, pp. 2651–2661, 2016.
- [47] J. M. Munuera, J. I. Paredes, M. Enterría, A. Pagán, S. Villar-Rodil, M. F. R. Pereira, J. I. Martins, J. L. Figueiredo, J. L. Cenis, A. Martínez-Alonso, and J. M. D. Tascón, "Electrochemical Exfoliation of Graphite in Aqueous Sodium Halide Electrolytes toward Low Oxygen Content Graphene for Energy and Environmental Applications," *ACS Applied Materials & Interfaces*, vol. 9, no. 28, pp. 24085–24099, 2017.
- [48] H. Wang, C. Wei, K. Zhu, Y. Zhang, C. Gong, J. Guo, J. Zhang, L. Yu, and J. Zhang, "Preparation of Graphene Sheets by Electrochemical Exfoliation of Graphite in Confined Space and Their Application in Transparent Conductive Films," *ACS Applied Materials & Interfaces*, vol. 9, no. 39, pp. 34456–34466, 2017.
- [49] C.-T. Hsieh and J.-H. Hsueh, "Electrochemical exfoliation of graphene sheets from a natural graphite flask in the presence of sulfate ions at different temperatures," *RSC Advances*, vol. 6, pp. 64826–64831, 2016.
- [50] P. C. Shi, J. P. Guo, X. Liang, S. Cheng, H. Zheng, Y. Wang, C. H. Chen, and H. F. Xiang, "Large-scale production of high-quality graphene sheets by a non-electrified electrochemical exfoliation method," *Carbon*, vol. 126, pp. 507 – 513, 2018.
- [51] M. T. H. Aunkor, I. M. Mahbul, R. Saidur, and H. S. C. Metselaar, "The green reduction of graphene oxide," *RSC Advances*, vol. 6, pp. 27807–27828, 2016.
- [52] K. K. H. D. Silva, H. H. Huang, R. K. Joshi, and M. Yoshimura, "Chemical reduction of graphene oxide using green reductants," *Carbon*, vol. 119, pp. 190 – 199, 2017.

-
- [53] R. Ortega-Amaya, Y. Matsumoto, E. Díaz-Torres, C. D. Gutierrez-Lazos, M. A. Pérez-Guzmán, and M. Ortega-López, "Green Routes for Graphene Oxide Reduction and Self-Assembled Graphene Oxide Micro- and Nanostructures Production," in *Graphene Materials* (G. Z. Kyzas and A. C. Mitropoulos, eds.), ch. 6, IntechOpen, 2017.
- [54] X. Qin, X. Chen, F. Zhang, L. Xiao, X. Xie, X. Yang, X. Xu, X. Hu, and P. Yu, "Polarized Raman Scattering of Epitaxial Graphene Prepared by Thermal Decomposition of SiC," *ECS J. Solid State Sci. Technol.*, vol. 7, no. 3, pp. M35–40, 2018.
- [55] F. Mitsuhashi, M. Okada, Y. Tateno, T. Nakabayashi, M. Ueno, H. Nagasawa, H. Fukidome, and M. Suemitsu, "Extremely uniform epitaxial growth of graphene from sputtered SiC films on SiC substrates," *MRS Advances*, vol. 2, no. 1, p. 51–56, 2017.
- [56] C. Moreno, M. Vilas-Varela, B. Kretz, A. Garcia-Lekue, M. V. Costache, M. Paradinas, M. Panighel, G. Ceballos, S. O. Valenzuela, D. Peña, and A. Mugarza, "Bottom-up synthesis of multifunctional nanoporous graphene," *Science*, vol. 360, no. 6385, pp. 199–203, 2018.
- [57] V. H. R. Souza, M. M. Oliveira, and A. J. G. Zarbin, "Bottom-up synthesis of graphene/polyaniline nanocomposites for flexible and transparent energy storage devices," *Journal of Power Sources*, vol. 348, pp. 87 – 93, 2017.
- [58] X. Li, W. Cai, L. Colombo, and R. S. Ruoff, "Evolution of Graphene Growth on Ni and Cu by Carbon Isotope Labeling," *Nano Letters*, vol. 9, no. 12, pp. 4268–4272, 2009. PMID: 19711970.
- [59] M. P. Lavin-Lopez, L. Sanchez-Silva, J. L. Valverde, and R. A., "CVD-graphene growth on different polycrystalline transition metals," *AIMS Materials Science*, vol. 4, no. 1, pp. 194–208, 2017.
- [60] H. Ago, Y. Ito, N. Mizuta, K. Yoshida, B. Hu, C. M. Orofeo, M. Tsuji, K. ichi Ikeda, and S. Mizuno, "Epitaxial Chemical Vapor Deposition Growth of Single-Layer Graphene over Cobalt Film Crystallized on Sapphire," *ACS Nano*, vol. 4 12, pp. 7407–14, 2010.
- [61] Y. Yao, Z. Li, Z. Lin, K.-S. Moon, J. Agar, and C. Wong, "Controlled Growth of Multilayer, Few-Layer, and Single-Layer Graphene on Metal Substrates," *The Journal of Physical Chemistry C*, vol. 115, no. 13, pp. 5232–5238, 2011.
- [62] M. E. Ramón, A. Gupta, C. Corbet, D. A. Ferrer, H. C. P. Movva, G. Carpenter, L. Colombo, G. Bourianoff, M. Doczy, D. Akinwande, E. Tutuc, and S. K. Banerjee, "CMOS-Compatible Synthesis of Large-Area, High-Mobility Graphene by Chemical Vapor Deposition of Acetylene on Cobalt Thin Films," *ACS Nano*, vol. 5, no. 9, pp. 7198–7204, 2011. PMID: 21800895.
- [63] H. An, W.-J. Lee, and J. Jung, "Graphene synthesis on Fe foil using thermal CVD," *Current Applied Physics*, vol. 11, no. 4, Supplement, pp. S81 – S85, 2011. International Conference on Electronic Materials and Nanotechnology for Green Environment.
- [64] A. Locatelli, G. Zamborlini, and T. O. Mentes, "Growth of single and multi-layer graphene on Ir(100)," *Carbon*, vol. 74, pp. 237 – 248, 2014.
- [65] J. Coraux, A. T. N'Diaye, C. Busse, and T. Michely, "Structural Coherency of Graphene on Ir(111)," *Nano Letters*, vol. 8, no. 2, pp. 565–570, 2008. PMID: 18189442.

- [66] E. V. Rut'kov, A. V. Kuz'michev, and N. R. Gall', "Carbon interaction with rhodium surface: Adsorption, dissolution, segregation, growth of graphene layers," *Physics of the Solid State*, vol. 53, no. 5, pp. 1092–1098, 2011.
- [67] P. Sutter, J. T. Sadowski, and E. Sutter, "Graphene on Pt(111): Growth and substrate interaction," *Physical Review B*, vol. 80, p. 245411, 2009.
- [68] E. Miniussi, M. Pozzo, T. O. Mentes, M. A. Niño, A. Locatelli, E. Vesselli, G. Comelli, S. Lizzit, D. Alfè, and A. Baraldi, "The competition for graphene formation on Re(0001): A complex interplay between carbon segregation, dissolution and carburisation," *Carbon*, vol. 73, pp. 389 – 402, 2014.
- [69] T. Oznuluer, E. Pince, E. O. Polat, O. Balci, O. Salihoglu, and C. Kocabas, "Synthesis of graphene on gold," *Applied Physics Letters*, vol. 98, no. 18, p. 183101, 2011.
- [70] J. Wintterlin and M.-L. Bocquet, "Graphene on metal surfaces," *Surface Science*, vol. 603, no. 10, pp. 1841 – 1852, 2009. Special Issue of Surface Science dedicated to Prof. Dr. Dr. h.c. mult. Gerhard Ertl, Nobel-Laureate in Chemistry 2007.
- [71] G. Giovannetti, P. A. Khomyakov, G. Brocks, V. M. Karpan, J. van den Brink, and P. J. Kelly, "Doping Graphene with Metal Contacts," *Physical Review Letters*, vol. 101, no. 2, p. 026803, 2008.
- [72] T. Enoki and K. Takai, "The edge state of nanographene and the magnetism of the edge-state spins," *Solid State Communications*, vol. 149, no. 27-28, pp. 1144–1150, 2009.
- [73] O. V. Yazyev and L. Helm, "Defect-induced magnetism in graphene," *Physical Review B*, vol. 75, no. 12, p. 125408, 2007.
- [74] P. O. Lehtinen, A. S. Foster, Y. Ma, A. V. Krasheninnikov, and R. M. Nieminen, "Irradiation-induced magnetism in graphite: a density functional study," *Physical review letters*, vol. 93, no. 18, p. 187202, 2004.
- [75] D. Eom, D. Prezzi, K. T. Rim, H. Zhou, M. Lefenfeld, S. Xiao, C. Nuckolls, M. S. Hybertsen, T. F. Heinz, and G. W. Flynn, "Structure and Electronic Properties of Graphene Nanoislands on Co(0001)," *Nano Letters*, vol. 9, no. 8, pp. 2844–2848, 2009.
- [76] S. Hüfner, *Photoelectron spectroscopy: principles and applications*. Springer Science & Business Media, 2013.
- [77] B. Feuerbacher and R. F. Willis, "Photoemission and electron states at clean surfaces," *Journal of Physics C: Solid State Physics*, vol. 9, no. 2, p. 169, 1976.
- [78] C. N. Berglund and W. E. Spicer, "Photoemission Studies of Copper and Silver: Theory," *Physical Review*, vol. 136, pp. A1030–A1044, 1964.
- [79] G. D. Mahan, "Theory of Photoemission in Simple Metals," *Physical Review B*, vol. 2, pp. 4334–4350, 1970.
- [80] J. E. Ortega, F. J. Himpsel, G. J. Mankey, and R. F. Willis, "Quantum-well states and magnetic coupling between ferromagnets through a noble-metal layer," *Physical Review B*, vol. 47, pp. 1540–1552, 1993.

-
- [81] T. C. Chiang, "Photoemission studies of quantum well states in thin films," *Surface Science Reports*, vol. 39, no. 7, pp. 181 – 235, 2000.
- [82] M. Jałochowski, "Experimental evidence for quantum size effects in ultrathin metallic films," *Progress in Surface Science*, vol. 48, no. 1, pp. 287 – 297, 1995. Proceedings of the Seventeenth International Seminar on Surface Physics.
- [83] M. Jałochowski, M. Hoffman, and E. Bauer, "Quantized Hall Effect in Ultrathin Metallic Films," *Physical Review Letters*, vol. 76, pp. 4227–4229, 1996.
- [84] B. G. Orr, H. M. Jaeger, and A. M. Goldman, "Transition-Temperature Oscillations in Thin Superconducting Films," *Physical Review Letters*, vol. 53, pp. 2046–2049, 1984.
- [85] W. Weber, A. Bischof, R. Allenspach, C. Würsch, C. H. Back, and D. Pescia, "Oscillatory Magnetic Anisotropy and Quantum Well States in Cu/Co/Cu(100) Films," *Physical Review Letters*, vol. 76, pp. 3424–3427, 1996.
- [86] J. B. Pendry, *Low energy electron diffraction: the theory and its application to determination of surface structure*, vol. 2. Academic Press, 1974.
- [87] M. A. Van Hove and S. Y. Tong, *Surface crystallography by LEED: theory, computation and structural results*, vol. 2. Springer Science & Business Media, 2012.
- [88] K. Radican, S. I. Bozhko, S.-R. Vadapoo, S. Ulucan, H.-C. Wu, A. McCoy, and I. V. Shvets, "Oxidation of W(110) studied by LEED and STM," *Surface Science*, vol. 604, no. 19-20, pp. 1548–1551, 2010.
- [89] J. Lachnitt and D. Mazur, "in preparation."
- [90] A. Barbieri and M. A. V. Hove, "private communication." <http://www.icts.hkbu.edu.hk/vanhove/>.
- [91] N. F. Materer, "Layer stacking implementation of tensor low energy electron diffraction," *Surface Science*, vol. 491, no. 1, pp. 131 – 139, 2001.
- [92] E. Bauer, *Surface microscopy with low energy electrons*, vol. 23. Springer, 2014.
- [93] M. C. Patt, *Bulk and surface sensitivity energy-filtered photoemission microscopy using synchrotron radiation for the study of resistive switching memories*. PhD thesis, Universität Duisburg-Essen, 2016.
- [94] C. Wiemann, M. Patt, I. P. Krug, N. B. Weber, M. Escher, M. Merkel, and C. M. Schneider, "A New Nanospectroscopy Tool with Synchrotron Radiation: NanoESCA@Elettra," *e-Journal of Surface Science and Nanotechnology*, vol. 9, pp. 395–399, 2011.
- [95] C. Tusche, M. Ellguth, A. Krasnyuk, A. Winkelmann, D. Kutnyakhov, P. Lushchik, K. Medjanik, G. Schönhense, and J. Kirschner, "Quantitative spin polarization analysis in photoelectron emission microscopy with an imaging spin filter," *Ultramicroscopy*, vol. 130, pp. 70–76, 2013.
- [96] G. Zamborlini, *Organic-Metal Hybrid Interfaces at the Mesoscopic Scale*. PhD thesis, Universität Duisburg-Essen, 2017.

- [97] U. Gradmann, J. Korecki, and G. Waller, "In-plane magnetic surface anisotropies in Fe(110)," *Applied Physics A*, vol. 39, no. 2, pp. 101–108, 1986.
- [98] M. Przybylski, U. Gradmann, and J. Korecki, "Magnetic hyperfine fields near the W(110)/Fe(110)-interface," *Journal of Magnetism and Magnetic Materials*, vol. 69, no. 2, pp. 199 – 205, 1987.
- [99] M. Albrecht, T. Furubayashi, M. Przybylski, J. Korecki, and U. Gradman, "Magnetic step anisotropies," *Journal of Magnetism and Magnetic Materials*, vol. 113, no. 1, pp. 207 – 220, 1992.
- [100] J. Schäfer, M. Hoinkis, E. Rotenberg, P. Blaha, and R. Claessen, "Spin-polarized standing waves at an electronically matched interface detected by Fermi-surface photoemission," *Physical Review B*, vol. 75, p. 092401, 2007. 10.1103/PhysRevB.75.092401.
- [101] M. Farle, A. Berghaus, Y. Li, and K. Baberschke, "Hard axis magnetization of ultrathin Ni(111)/W(110) in UHV a new set-up for SMOKE," *Journal of Magnetism and Magnetic Materials*, vol. 93, pp. 215 – 219, 1991.
- [102] E. Bauer, "Growth of thin films," *Journal of Physics: Condensed Matter*, vol. 11, no. 48, p. 9365, 1999.
- [103] B. Santos, J. M. Puerta, J. I. Cerda, T. Herranz, K. F. McCarty, and J. de la Figuera, "Structure of ultrathin Pd films determined by low-energy electron microscopy and diffraction," *New Journal of Physics*, vol. 12, no. 2, p. 023023, 2010.
- [104] R. C. Jaklevic and L. C. Davis, "Band Signatures in the Low-Energy-Electron Reflectance Spectra of fcc Metals," *Physical Review B*, vol. 26, pp. 5391–5397, 1982.
- [105] P. Moras, G. Bihlmayer, P. M. Sheverdyaeva, S. K. Mahatha, M. Papagno, J. Sánchez-Barriga, O. Rader, L. Novinec, S. Gardonio, and C. Carbone, "Magnetization-dependent Rashba splitting of quantum well states at the Co/W interface," *Physical Review B*, vol. 91, no. 19, p. 195410, 2015.
- [106] J. Sánchez-Barriga, J. Minár, J. Braun, A. Varykhalov, V. Boni, I. Di Marco, O. Rader, V. Bellini, F. Manghi, H. Ebert, M. I. Katsnelson, A. I. Lichtenstein, O. Eriksson, W. Eberhardt, H. A. Dürr, and J. Fink, "Quantitative determination of spin-dependent quasiparticle lifetimes and electronic correlations in hcp cobalt," *Physical Review B*, vol. 82, p. 104414, 2010.
- [107] C. Tusche, M. Ellguth, V. Feyer, A. Krasnyuk, C. Wiemann, J. Henk, C. M. Schneider, and J. Kirschner, "Nonlocal electron correlations in an itinerant ferromagnet," *Nature Communications*, vol. 9, no. 1, p. 3727, 2018.
- [108] M. Jugovac, F. Genuzio, E. L. Gonzalez, N. Stojić, G. Zamborlini, V. Feyer, T. O. Mentes, A. Locatelli, and C. M. Schneider, "Role of carbon dissolution and recondensation in graphene epitaxial alignment on cobalt," *Carbon*, vol. 152, p. 4, 2019.
- [109] C. J. Weststrate, I. M. Ciobîcă, J. van de Loosdrecht, and J. W. Niemantsverdriet, "Adsorption and Decomposition of Ethene and Propene on Co(0001): The Surface Chemistry of Fischer-Tropsch Chain Growth Intermediates," *The Journal of Physical Chemistry C*, vol. 120, no. 51, pp. 29210–29224, 2016.

-
- [110] H. Tetlow, J. Posthuma de Boer, I. J. Ford, D. D. Vvedensky, D. Curcio, L. Omiciuolo, S. Lizzit, A. Baraldi, and L. Kantorovich, "Ethylene Decomposition on Ir(111): Initial Path to Graphene Formation," *Physical Chemistry Chemical Physics*, vol. 18, pp. 27897–27909, 2016.
- [111] C. Klink, I. Stensgaard, F. Besenbacher, and E. Lægsgaard, "An STM Study of Carbon-Induced Structures on Ni(111): Evidence for a Carbodic-Phase Clock Reconstruction," *Surface Science*, vol. 342, no. 1, pp. 250 – 260, 1995.
- [112] I. M. Ciobîcă, R. A. van Santen, P. J. van Berge, and J. van de Loosdrecht, "Adsorbate Induced Reconstruction of Cobalt Surfaces," *Surface Science*, vol. 602, no. 1, pp. 17 – 27, 2008.
- [113] F. Wang, K. Shepperd, J. Hicks, M. S. Nevius, H. Tinkey, A. Tejada, A. Taleb-Ibrahimi, F. Bertran, P. Le Fèvre, D. B. Torrance, P. N. First, W. A. de Heer, A. A. Zakharov, and E. H. Conrad, "Silicon intercalation into the graphene-SiC interface," *Physical Review B*, vol. 85, p. 165449, 2012.
- [114] T. Ramsvik, A. Borg, H. J. Venvik, F. Hansteen, M. Kildemo, and T. Worren, "Acetylene Chemisorption and Decomposition on the Co(1 $\bar{1}$ 20) Single Crystal Surface," *Surface Science*, vol. 499, no. 2, pp. 183 – 192, 2002.
- [115] C. J. Weststrate, A. C. Kızılkaya, E. T. R. Rossen, M. W. G. M. Verhoeven, I. M. Ciobîcă, A. M. Saib, and J. W. H. Niemantsverdriet, "Atomic and Polymeric Carbon on Co(0001): Surface Reconstruction, Graphene Formation, and Catalyst Poisoning," *The Journal of Physical Chemistry C*, vol. 116, no. 21, pp. 11575–11583, 2012.
- [116] M. A. O. Quiroga and G. F. Cabeza, "Role of Van der Waals Forces in Graphene Adsorption over Pd, Pt, and Ni," *Brazilian Journal of Physics*, vol. 43, no. 3, pp. 126–129, 2013.
- [117] P. Zeller, M. Weinl, F. Speck, M. Ostler, A.-K. Henß, T. Seyller, M. Schreck, and J. Wintterlin, "Single Crystalline Metal Films as Substrates for Graphene Growth," *Annals of Physics*, vol. 529, no. 11, p. 1700023, 2017.
- [118] D. Y. Usachov, K. A. Bokai, D. E. Marchenko, A. V. Fedorov, V. O. Shevelev, O. Y. Vilkov, E. Y. Kataev, L. V. Yashina, E. Rühl, C. Laubschat, and D. V. Vyalikh, "Cobalt-Assisted Recrystallization and Alignment of Pure and Doped Graphene," *Nanoscale*, vol. 10, pp. 12123–12132, 2018.
- [119] C. Africh, C. Cepek, L. L. Patera, G. Zamborlini, P. Genoni, T. O. Montes, A. Sala, A. Locatelli, and G. Comelli, "Switchable Graphene-Substrate Coupling Through Formation/Dissolution of an Intercalated Ni-Carbide Layer," *Scientific Reports*, vol. 6, p. 19734, 2016.
- [120] N. Rougemaille, A. T. N'Diaye, J. Coraux, C. Vo-Van, O. Fruchart, and A. K. Schmid, "Perpendicular Magnetic Anisotropy of Cobalt Films Intercalated under Graphene," *Applied Physics Letters*, vol. 101, no. 14, p. 142403, 2012.
- [121] D. Y. Usachov, A. V. Fedorov, O. Y. Vilkov, A. E. Petukhov, A. G. Rybkin, A. Ernst, M. M. Otrokov, E. V. Chulkov, I. I. Ogorodnikov, M. V. Kuznetsov, L. V. Yashina, E. Y. Kataev, A. V. Erofeevskaya, V. Y. Voroshnin, V. K. Adamchuk, C. Laubschat, and D. V. Vyalikh, "Large-Scale Sublattice Asymmetry in Pure and Boron-Doped Graphene," *Nano Letters*, vol. 16, no. 7, pp. 4535–4543, 2016.

- [122] P. Lacovig, M. Pozzo, D. Alfè, P. Vilmercati, A. Baraldi, and S. Lizzit, "Growth of Dome-Shaped Carbon Nanoislands on Ir(111): The Intermediate between Carbide Clusters and Quasi-Free-Standing Graphene," *Physical Review Letters*, vol. 103, p. 166101, 2009.
- [123] E. Votava, "Electron Microscopic Investigation of the Phase Transformation of Thin Cobalt Samples," *Acta Metallurgica*, vol. 8, no. 12, pp. 901 – 904, 1960.
- [124] M. Erbudak, E. Wetli, M. Hochstrasser, D. Pescia, and D. D. Vvedensky, "Surface Phase Transitions during Martensitic Transformations of Single-Crystal Co," *Physical Review Letters*, vol. 79, pp. 1893–1896, 1997.
- [125] P. A. Khomyakov, G. Giovannetti, P. C. Rusu, G. Brocks, J. van den Brink, and P. J. Kelly, "First-Principles Study of the Interaction and Charge Transfer between Graphene and Metals," *Physical Review B*, vol. 79, p. 195425, 2009.
- [126] J. C. W. Swart, E. van Steen, I. M. Ciobîcă, and R. A. van Santen, "Interaction of graphene with FCC-Co(111)," *Physical Chemistry Chemical Physics*, vol. 11, pp. 803–807, 2009.
- [127] A. Varykhalov, D. Marchenko, J. Sánchez-Barriga, M. R. Scholz, B. Verberck, B. Trauzettel, T. O. Wehling, C. Carbone, and O. Rader, "Intact Dirac Cones at Broken Sublattice Symmetry: Photoemission Study of Graphene on Ni and Co," *Physical Review X*, vol. 2, p. 041017, 2012.
- [128] L. Wang, X. Zhang, H. L. W. Chan, F. Yan, and F. Ding, "Formation and Healing of Vacancies in Graphene Chemical Vapor Deposition (CVD) Growth," *Journal of the American Chemical Society*, vol. 135, no. 11, pp. 4476–4482, 2013.
- [129] H. Shu, X. Chen, X. Tao, and F. Ding, "Edge Structural Stability and Kinetics of Graphene Chemical Vapor Deposition Growth," *ACS Nano*, vol. 6, no. 4, pp. 3243–3250, 2012.
- [130] N. R. Gall', N. P. Lavrovskaya, E. V. Rut'kov, and A. Y. Tontegode, "Thermal Destruction of Two-Dimensional Graphite Islands on Refractory Metals (Ir, Re, Ni, and Pt)," *Technical Physics*, vol. 49, no. 2, pp. 245–249, 2004.
- [131] R. B. McLellan, C. Ko, and M. L. Wasz, "The Diffusion of Carbon in Solid Cobalt," *Journal of Physics and Chemistry of Solids*, vol. 53, no. 10, pp. 1269 – 1273, 1992.
- [132] N. Rougemaille, F. El Gabaly, R. Stumpf, A. K. Schmid, K. Thürmer, N. C. Bartelt, and J. de la Figuera, "Labyrinthine Island Growth during Pd/Ru(0001) Heteroepitaxy," *Physical Review Letters*, vol. 99, p. 106101, 2007.
- [133] A. K. Schmid, N. C. Bartelt, and R. Q. Hwang, "Alloying at Surfaces by the Migration of Reactive Two-Dimensional Islands," *Science*, vol. 290, no. 5496, pp. 1561–1564, 2000.
- [134] M. Jugovac, F. Genuzio, T. O. Menteş, A. Locatelli, G. Zamborlini, V. Feyer, and C. M. Schneider, "Tunable coupling by means of oxygen intercalation and removal at the strongly interacting graphene/cobalt interface," *Carbon*, vol. 163, pp. 341–347, 2020.
- [135] L. Bignardi, P. Lacovig, M. M. Dalmiglio, F. Orlando, A. Ghafari, L. Petaccia, A. Baraldi, R. Larciprete, and S. Lizzit, "Key role of rotated domains in oxygen intercalation at graphene on Ni(111)," *2D Materials*, vol. 4, no. 2, p. 025106, 2017.

-
- [136] R. Larciprete, S. Ulstrup, P. Lacovig, M. Dalmiglio, M. Bianchi, F. Mazzola, L. Hornekær, F. Orlando, A. Baraldi, P. Hofmann, *et al.*, "Oxygen switching of the epitaxial graphene-metal interaction," *ACS Nano*, vol. 6, no. 11, pp. 9551–9558, 2012.
- [137] R. Blume, P. R. Kidambi, B. C. Bayer, R. S. Weatherup, Z.-J. Wang, G. Weinberg, M.-G. Willinger, M. Greiner, S. Hofmann, A. Knop-Gericke, *et al.*, "The influence of intercalated oxygen on the properties of graphene on polycrystalline Cu under various environmental conditions," *Physical Chemistry Chemical Physics*, vol. 16, no. 47, pp. 25989–26003, 2014.
- [138] E. Granas, J. Knudsen, U. A. Schroeder, T. Gerber, C. Busse, M. A. Arman, K. Schulte, J. N. Andersen, and T. Michely, "Oxygen intercalation under graphene on Ir(111): energetics, kinetics, and the role of graphene edges," *ACS Nano*, vol. 6, no. 11, pp. 9951–9963, 2012.
- [139] S. Sahu and G. C. Rout, "Band gap opening in graphene: a short theoretical study," *International Nano Letters*, vol. 7, no. 2, pp. 81–89, 2017.
- [140] Y. Dedkov, W. Klesse, A. Becker, F. Späth, C. Papp, and E. Voloshina, "Decoupling of graphene from Ni(111) via formation of an interfacial NiO layer," *Carbon*, vol. 121, pp. 10–16, 2017.
- [141] C. T. Chen, Y. U. Idzerda, H.-J. Lin, N. V. Smith, G. Meigs, E. Chaban, G. H. Ho, E. Pellegrin, and F. Sette, "Experimental Confirmation of the X-Ray Magnetic Circular Dichroism Sum Rules for Iron and Cobalt," *Physical Review Letters*, vol. 75, pp. 152–155, 1995.
- [142] D. C. Elias, R. V. Gorbachev, A. S. Mayorov, S. V. Morozov, A. A. Zhukov, P. Blake, L. A. Ponomarenko, I. V. Grigorieva, K. S. Novoselov, F. Guinea, *et al.*, "Dirac cones reshaped by interaction effects in suspended graphene," *Nature Physics*, vol. 7, no. 9, p. 701, 2011.
- [143] M. Getzlaff, J. Bansmann, and G. Schönhense, "Spin resolved photoemission study of oxygen on thin cobalt films," *Journal of Electron Spectroscopy and Related Phenomena*, vol. 77, no. 2, pp. 197 – 207, 1996.
- [144] M. C. Biesinger, B. P. Payne, A. P. Grosvenor, L. W. M. Lau, A. R. Gerson, and R. S. C. Smart, "Resolving surface chemical states in XPS analysis of first row transition metals, oxides and hydroxides: Cr, Mn, Fe, Co and Ni," *Applied Surface Science*, vol. 257, no. 7, pp. 2717–2730, 2011.
- [145] A. Tuxen, S. Carencio, M. Chintapalli, C.-H. Chuang, C. Escudero, E. Pach, P. Jiang, F. Borondics, B. Beberwyck, A. P. Alivisatos, G. Thornton, W.-F. Pong, J. Guo, R. Perez, F. Besenbacher, and M. Salmeron, "Size-Dependent Dissociation of Carbon Monoxide on Cobalt Nanoparticles," *Journal of the American Chemical Society*, vol. 135, no. 6, pp. 2273–2278, 2013. PMID: 23339635.
- [146] J. Bansmann, M. Getzlaff, A. Kleibert, F. Bulut, R. K. Gebhardt, and K. H. Meiwes-Broer, "Mass-filtered cobalt clusters in contact with epitaxially ordered metal surfaces," *Applied Physics A*, vol. 82, no. 1, pp. 73–79, 2006.
- [147] R. Babar and M. Kabir, "Ferromagnetism in nitrogen-doped graphene," *Physical Review B*, vol. 99, p. 115442, 2019.

- [148] X. Duan, Z. Ao, H. Sun, S. Indrawirawan, Y. Wang, J. Kang, F. Liang, Z. H. Zhu, and S. Wang, "Nitrogen-Doped Graphene for Generation and Evolution of Reactive Radicals by Metal-Free Catalysis," *ACS Applied Materials & Interfaces*, vol. 7, no. 7, pp. 4169–4178, 2015. PMID: 25632991.
- [149] A. Sala, G. Zamborlini, T. O. Menteş, and A. Locatelli, "Fabrication of 2D heterojunction in graphene via low energy N_2^+ irradiation," *Small*, vol. 11, no. 44, pp. 5927–5931, 2015.
- [150] W. De La Cruz, O. Contreras, G. Soto, and E. Perez-Tijerina, "Cobalt nitride films produced by reactive pulsed laser deposition," *Revista mexicana de fisica*, vol. 52, no. 5, pp. 409–412, 2006.
- [151] H.-g. Jee, K.-H. Jin, J.-H. Han, H.-N. Hwang, S.-H. Jhi, Y. D. Kim, and C.-C. Hwang, "Controlling the self-doping of epitaxial graphene on SiC via Ar ion treatment," *Physical Review B*, vol. 84, no. 7, p. 075457, 2011.
- [152] J. M. Caridad, F. Rossella, V. Bellani, M. Maicas, M. Patrini, and E. Díez, "Effects of particle contamination and substrate interaction on the Raman response of unintentionally doped graphene," *Journal of Applied Physics*, vol. 108, no. 8, p. 084321, 2010.
- [153] P. Hohenberg and W. Kohn, "Inhomogeneous Electron Gas," *Physical Review*, vol. 136, pp. B864–B871, 1964.
- [154] W. Kohn and L. J. Sham, "Self-Consistent Equations Including Exchange and Correlation Effects," *Physical Review*, vol. 140, pp. A1133–A1138, 1965.
- [155] W. Widayani, T. D. K. Wungu, S. E. Marsha, and S. Suprijadi, "Study of Target Recognition of MAA-based Molecularly Imprinted Polymer (MIP) Using Density Functional Theory (DFT) Computation on the Interaction of Methacrylic Acid (MAA)-D-Glucose," *Journal of Polymer and Biopolymer Physics Chemistry*, vol. 5, no. 1, pp. 10–12, 2017. doi: 10.12691/jpbpc-5-1-2.
- [156] J. Hubbard and B. H. Flowers, "Electron correlations in narrow energy bands," *Proceedings of the Royal Society of London. Series A. Mathematical and Physical Sciences*, vol. 276, no. 1365, pp. 238–257, 1963.
- [157] A. Georges, G. Kotliar, W. Krauth, and M. J. Rozenberg, "Dynamical mean-field theory of strongly correlated fermion systems and the limit of infinite dimensions," *Review of Modern Physics*, vol. 68, pp. 13–125, 1996.
- [158] P. W. Anderson, "Localized magnetic states in metals," *Physical Review*, vol. 124, no. 1, p. 41, 1961.
- [159] M. Karolak, G. Ulm, T. Wehling, V. Mazurenko, A. Poteryaev, and A. Lichtenstein, "Double counting in LDA+DMFT—The example of NiO," *Journal of Electron Spectroscopy and Related Phenomena*, vol. 181, no. 1, pp. 11 – 15, 2010. Proceedings of International Workshop on Strong Correlations and Angle-Resolved Photoemission Spectroscopy 2009.
- [160] V. I. Anisimov, J. Zaanen, and O. K. Andersen, "Band theory and Mott insulators: Hubbard U instead of Stoner I," *Physical Review B*, vol. 44, pp. 943–954, 1991.
- [161] V. I. Anisimov, F. Aryasetiawan, and A. I. Lichtenstein, "First-principles calculations of the electronic structure and spectra of strongly correlated systems: the LDA+U method," *Journal of Physics: Condensed Matter*, vol. 9, no. 4, pp. 767–808, 1997.

-
- [162] A. G. Petukhov, I. I. Mazin, L. Chioncel, and A. I. Lichtenstein, "Correlated metals and the LDA + U method," *Physical Review B*, vol. 67, p. 153106, 2003.
- [163] J. Kirschner and R. Feder, "Spin polarization in double diffraction of low-energy electrons from W(001): experiment and theory," *Physical Review Letters*, vol. 42, no. 15, p. 1008, 1979.
- [164] R. Feder, "Spin-polarised low-energy electron diffraction," *Journal of Physics C: Solid State Physics*, vol. 14, no. 15, p. 2049, 1981.
- [165] N. A. Vinogradov, A. A. Zakharov, V. Kocevski, J. Ruzs, K. A. Simonov, O. Eriksson, A. Mikkelsen, E. Lundgren, A. S. Vinogradov, N. Mårtensson, and A. B. Preobrajenski, "Formation and Structure of Graphene Waves on Fe(110)," *Physical Review Letters*, vol. 109, p. 026101, 2012.
- [166] N. A. Vinogradov, K. A. Simonov, A. V. Generalov, J. Drnec, F. Carla, A. S. Vinogradov, A. B. Preobrajenski, N. Martensson, and R. Felici, "The structural evolution of graphene/Fe(110) systems upon annealing," *Carbon*, vol. 111, pp. 113 – 120, 2017.
- [167] L. L. Patera, C. Africh, R. S. Weatherup, R. Blume, S. Bhardwaj, C. Castellarin-Cudia, A. Knop-Gericke, R. Schloegl, G. Comelli, S. Hofmann, and C. Cepek, "In Situ Observations of the Atomistic Mechanisms of Ni Catalyzed Low Temperature Graphene Growth," *ACS Nano*, vol. 7, no. 9, pp. 7901–7912, 2013. PMID: 23924234.
- [168] V. Carnevali, L. L. Patera, G. Prandini, M. Jugovac, S. Modesti, G. Comelli, M. Peressi, and C. Africh, "Doping of epitaxial graphene by direct incorporation of nickel adatoms," *Nanoscale*, vol. 11, pp. 10358–10364, 2019.

Band / Volume 210

Quantum Technology

Lecture Notes of the 51st IFF Spring School 2020

23 March – 03 April 2020, Jülich, Germany

ed. by H. Bluhm, T. Calarco, D. DiVincenzo (2020), ca. 700 pp

ISBN: 978-3-95806-449-2

Band / Volume 211

Interaction of physical fields with nanostructured materials

(2020), 255 pp

ISBN: 978-3-95806-450-8

Band / Volume 212

First-principles study of collective spin excitations in noncollinear magnets

F.J. dos Santos (2020), 270 pp

ISBN: 978-3-95806-459-1

Band / Volume 213

Direct measurement of anisotropic resistivity in thin films using a 4-probe STM

T. Flatten (2020), viii, 129 pp

ISBN: 978-3-95806-460-7

Band / Volume 214

The guided self-assembly of magnetic nanoparticles into two- and three- dimensional nanostructures using patterned substrates

W. Ji (2020), VI, 140 pp

ISBN: 978-3-95806-462-1

Band / Volume 215

Molecular layer deposition and protein interface patterning for guided cell growth

M. Glass (2020), iv, 81 pp

ISBN: 978-3-95806-463-8

Band / Volume 216

Development of a surface acoustic wave sensor for in situ detection of molecules

D. Finck (2020), 63 pp

ISBN: 978-3-95806-464-5

Band / Volume 217

Detection and Statistical Evaluation of Spike Patterns in Parallel Electrophysiological Recordings

P. Quaglio (2020), 128 pp

ISBN: 978-3-95806-468-3

Band / Volume 218

Automatic Analysis of Cortical Areas in Whole Brain Histological Sections using Convolutional Neural Networks

H. Spitzer (2020), xii, 162 pp
ISBN: 978-3-95806-469-0

Band / Volume 219

Postnatale Ontogenesestudie (Altersstudie) hinsichtlich der Zyto- und Rezeptorarchitektur im visuellen Kortex bei der grünen Meerkatze

D. Stibane (2020), 135 pp
ISBN: 978-3-95806-473-7

Band / Volume 220

Inspection Games over Time: Fundamental Models and Approaches

R. Avenhaus und T. Krieger (2020), VIII, 455 pp
ISBN: 978-3-95806-475-1

Band / Volume 221

High spatial resolution and three-dimensional measurement of charge density and electric field in nanoscale materials using off-axis electron holography

F. Zheng (2020), xix, 182 pp
ISBN: 978-3-95806-476-8

Band / Volume 222

Tools and Workflows for Data & Metadata Management of Complex Experiments

Building a Foundation for Reproducible & Collaborative Analysis in the Neurosciences
J. Sprenger (2020), X, 168 pp
ISBN: 978-3-95806-478-2

Band / Volume 223

Engineering of *Corynebacterium glutamicum* towards increased malonyl-CoA availability for polyketide synthesis

L. Milke (2020), IX, 117 pp
ISBN: 978-3-95806-480-5

Band / Volume 224

Morphology and electronic structure of graphene supported by metallic thin films

M. Jugovac (2020), xi, 151 pp
ISBN: 978-3-95806-498-0

Weitere **Schriften des Verlags im Forschungszentrum Jülich** unter
<http://www.zb1.fz-juelich.de/verlagextern1/index.asp>

Schlüsseltechnologien / Key Technologies

Band / Volume 224

ISBN 978-3-95806-498-0